AFOSR-TR-95

~~(td)~~ 0621

Final Technical Report

on

ADVANCED DIAGNOSTICS FOR REACTING FLOWS

Grant AFOSR 89-0067

DTIC
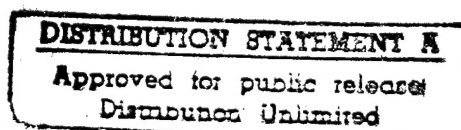SELECTED
OCT 1 3 1995
F

Prepared for

AIR FORCE OFFICE OF SCIENTIFIC RESEARCH

For the Period

October 1, 1990 to October 31, 1994

Submitted by

R. K. Hanson, Principal Investigator

HIGH TEMPERATURE GASDYNAMICS LABORATORY
Mechanical Engineering Department
Stanford University

REPORT DOCUMENTATION PAGE

Public reporting burden for this collection of information is estimated to average 1 hour per response, including the time for reviewing instructions, searching existing data sources, gathering and maintaining the data needed, and completing and reviewing the collection of information. Send comments regarding this burden estimate or any other aspect of this collection of information, including suggestions for reducing this burden, to Washington Headquarters Services, Directorate for Information Operations and Reports, 1215 Jefferson Davis Highway, Suite 1204, Arlington, VA 22202-4302, and to the Office of Management and Budget, Paperwork Reduction Project (0704-0188), Washington, DC 20503.

1. AGENCY USE ONLY (Leave blank)	2. REPORT DATE 12 January 1995	3. REPORT TYPE AND DATES COVERED Final Report 10/1/90 - 10/31/94

4. TITLE AND SUBTITLE

(U)Advanced Diagnostics for Reacting Flows

5. FUNDING NUMBERS

PE - 61102F
PR - 2308
SA - CS
G - AFOSR 89-0067

6. AUTHOR(S)

R. K. Hanson

7. PERFORMING ORGANIZATION NAME(S) AND ADDRESS(ES)

Stanford University
Mechanical Engineering Department
Stanford, CA 94305-3032

8. PERFORMING ORGANIZATION REPORT NUMBER

9. SPONSORING/MONITORING AGENCY NAME(S) AND ADDRESS(ES)

AFOSR/NA
110 Duncan Avenue, Suite B115
Bolling AFB DC 20332-0001

10. SPONSORING/MONITORING AGENCY REPORT NUMBER

11. SUPPLEMENTARY NOTES

12a. DISTRIBUTION/AVAILABILITY STATEMENT

Approved for public release; distribution is unlimited

12b. DISTRIBUTION CODE

13. ABSTRACT (Maximum 200 words)

Progress is summarized for the past four years of a research program on advanced diagnostic techniques for combustion gases and plasmas. The parameters of interest are species concentrations, temperature, density, pressure, velocity, mass flow rate and thrust. The techniques studied are based on laser spectroscopy, particularly laser absorption and laser-induced fluorescence. Sources include tunable cw diode lasers and tunable pulsed lasers. The cw lasers are spectrally narrow, allowing study of new techniques based on spectral lineshapes and shifts, while the pulsed lasers provide intense bursts of photons needed for techniques based on light-scattering phenomena. Accomplishments of note include: the first use of diode lasers for absorption and fluorescence measurements in combustion gases and plasmas; development of an optical diagnostic for mass flux and thrust; the first use of laser absorption to monitor atomic nitrogen and oxygen; development of wavelength-multiplexing to allow multiple-species absorption measurements along a common optical path; demonstration of quantitative PLIF methods for temperature and velocity imaging in supersonic flows; development of acetone seeding for improved PLIF imaging; and the first application of PLIF to shock tunnel flows.

14. SUBJECT TERMS
Laser, Imaging, Combustion, Velocity, Pressure, Absorption,
Temperature, Fluorescence, Reacting, Flow, Plasma, Diagnostics

15. NUMBER OF PAGES
147

16. PRICE CODE

17. SECURITY CLASSIFICATION OF REPORT	18. SECURITY CLASSIFICATION OF THIS PAGE	19. SECURITY CLASSIFICATION OF ABSTRACT	20. LIMITATION OF ABSTRACT
Unclassified	Unclassified	Unclassified	UL

Final Technical Report

on

ADVANCED DIAGNOSTICS FOR REACTING FLOWS

Grant AFOSR 89-0067

Prepared for

AIR FORCE OFFICE OF SCIENTIFIC RESEARCH

For the Period

October 1, 1990 to October 31, 1994

Accesion For		
NTIS CRA&I		☑
DTIC TAB		☐
Unannounced		☐
Justification		
By		
Distribution /		
Availability Codes		
Dist	Avail and / or Special	
A-1		

Submitted by

R. K. Hanson, Principal Investigator

High Temperature Gasdynamics Laboratory

Mechanical Engineering Department

Stanford University

Stanford, California 94305

TABLE OF CONTENTS

1.0 INTRODUCTION

Progress is summarized for the past four years of a research program on advanced diagnostic techniques for combustion gases and plasmas. The parameters of interest are species concentrations, temperature, density, pressure, velocity, mass flow rate and thrust. The techniques studied are based on laser spectroscopy, particularly laser absorption and laser-induced fluorescence. Sources include tunable cw diode lasers and tunable pulsed lasers. The cw lasers are spectrally narrow, allowing study of new techniques based on spectral lineshapes and shifts, while the pulsed lasers provide intense bursts of photons needed for techniques based on light-scattering phenomena. Accomplishments of note include: the first use of diode lasers for absorption and fluorescence measurements in combustion gases and plasmas; development of an optical diagnostic for mass flux and thrust; the first use of laser absorption to monitor atomic nitrogen and oxygen; development of wavelength-multiplexing to allow multiple-species absorption measurements along a common optical path; demonstration of quantitative PLIF methods for temperature and velocity imaging in supersonic flows; development of acetone seeding for improved PLIF imaging; and the first application of PLIF to shock tunnel flows.

1

2.0 PROJECT SUMMARIES

Included in this section are summaries of progress in each of nine project areas. Additional descriptions of this work may be found in the publications listed in Sections 3.1 and 3.2. Reprints of these papers are available on request. Personnel involved in these projects are listed in Section 4.0.
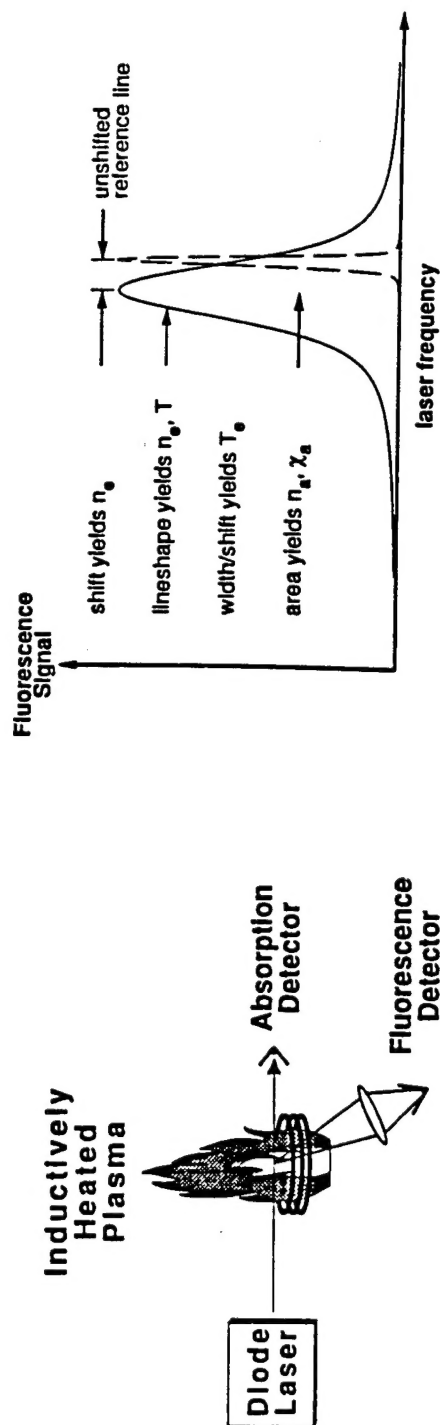
2.1 Plasma Diagnostics

Over the past four years we have maintained a steady effort to explore the use of cw semiconductor diode lasers as light sources for absorption and fluorescence diagnostics of temperature, species concentration, velocity and electron number density in laboratory plasmas. These low-cost lasers are evolving rapidly owing to their numerous practical applications (compact disc players, supermarket scanners, etc.), but they also offer significant prospects for scientific applications. With regard to spectroscopic diagnostics, these lasers can be viewed as economical, rugged and compact sources of low power, cw, tunable wavelength light with relatively narrow spectral linewidths. Thus they represent possible replacements for currently employed cw dye lasers. Unfortunately, diode lasers were initially developed for use at near-infrared wavelengths (especially 1.3 and 1.5 microns), and only in the past few years have lasers become readily available at wavelengths below 1 micron where most electronic transitions of interest in atoms and molecules are located. At the present time, cw diode lasers are available for use in selected wavelength bands down to about 650 nm.

Particular accomplishments in the first two years of the program include: the first application of diode lasers for single-point fluorescence measurements in atmospheric pressure plasmas, and the first studies of partially-saturated fluorescence as a possible method of measuring electronic quench rates in plasmas. The flow facility, in all cases, was an RF-excited, atmospheric-pressure plasma torch operating on argon. More recent accomplishments include extension of diode-laser absorption and fluorescence diagnostics to atomic oxygen and xenon.

A simplified form of the experimental arrangement used to develop diode laser techniques for plasmas is indicated in Fig. 1, together with a sketch of representative data which illustrates the features of our spectrally-resolved-lineshape strategy for inferring plasma properties. The measurements are made in an atmospheric pressure, inductively-coupled RF plasma torch (assembled in the early phase of this program) which provides a controlled, high temperature plasma with convenient optical access. In the experiment, the

Spectrally-Resolved Plasma Diagnostics using Tunable Diode Lasers

Fluorescence Signal

unshifted reference line

shift yields n_e

lineshape yields n_e, T

width/shift yields T_e

area yields n_a, χ_a

laser frequency

Inductively Heated Plasma

Diode Laser

Absorption Detector

Fluorescence Detector

- Spatially-resolved fluorescence detection obviates need for Abel inversion

- New spectral strategy provides simultaneous determination of electron density and temperature

- First application of diode lasers to high-pressure plasmas

Figure 1. Overview of plasma diagnostic strategy based on spectrally-resolved fluorescence.

diode laser is rapidly swept in wavelength across an individual absorption transition of interest, providing a fully resolved record of the absorption lineshape; either line-of-sight absorption or single-point fluorescence recording may be used, but our primary goal was to establish LIF, since it provides spatially-resolved data. The lineshape data can be used to infer gas temperature (through Doppler broadening of the line) and electron density (through the Stark-induced shift in the line position). Since the lineshape also is influenced by Stark broadening, the linewidth data can be interpreted to yield a second, independent determination of the electron density. In general, excellent agreement is found between the two measurements of electron density. Inferred temperatures in the plasma are typically in the range 6000-8000 K, for both absorption and fluorescence measurements, thereby illustrating the power of this diagnostic for probing very high temperature gases. The development of a diode-based plasma diagnostic based on LIF is significant, because most past plasma diagnostics have been based on line-of-sight emission approaches which require use of Abel inversion methods to establish spatial distributions; inversion methods are applicable only to plasmas with radial symmetry while LIF diagnostics have no symmetry limitation.

Our most recent research has been aimed at extending these techniques, previously demonstrated in argon and oxygen, to xenon plasmas. Xenon's high molecular weight and low ionization potential make it the optimal choice as a propellant in ion thrusters for satellite electric propulsion. An understanding of the operation of these thrusters for performance enhancement will require non-intrusive plasma diagnostics capable of probing their exhausts.

Particular accomplishments in our work with xenon include accurate modeling of an isotopically and nuclear spin-split xenon lineshape obtained by single-point laser-induced fluorescence (LIF), and with this the demonstration of a kinetic temperature diagnostic in a low pressure DC glow discharge. This work is discussed briefly in the following paragraphs.

The extension of our previously developed diode-laser diagnostics to xenon is complicated by the existence of several strong isotopes and the hyperfine splitting of most energy levels. Xenon is a relatively heavy inert gas with nine stable isotopes. The two isotopes, ^{129}Xe and ^{131}Xe, with an odd number of neutrons (atomic number 54 = even number of protons) have a nuclear spin which causes a splitting of the fine structure energy levels. Figure 2 summarizes the energy level structure for neutral xenon and the nuclear spin-splitting which must be considered for one of the 6s-6p transitions currently being studied (at 823 nm). The energetic nature of the plasma environments under study makes excited-state spectroscopy appropriate. The absorption lineshape of this overall transition thus involves a convolution of 21 individual lines which are each broadened and, possibly, shifted according to the local gas properties.
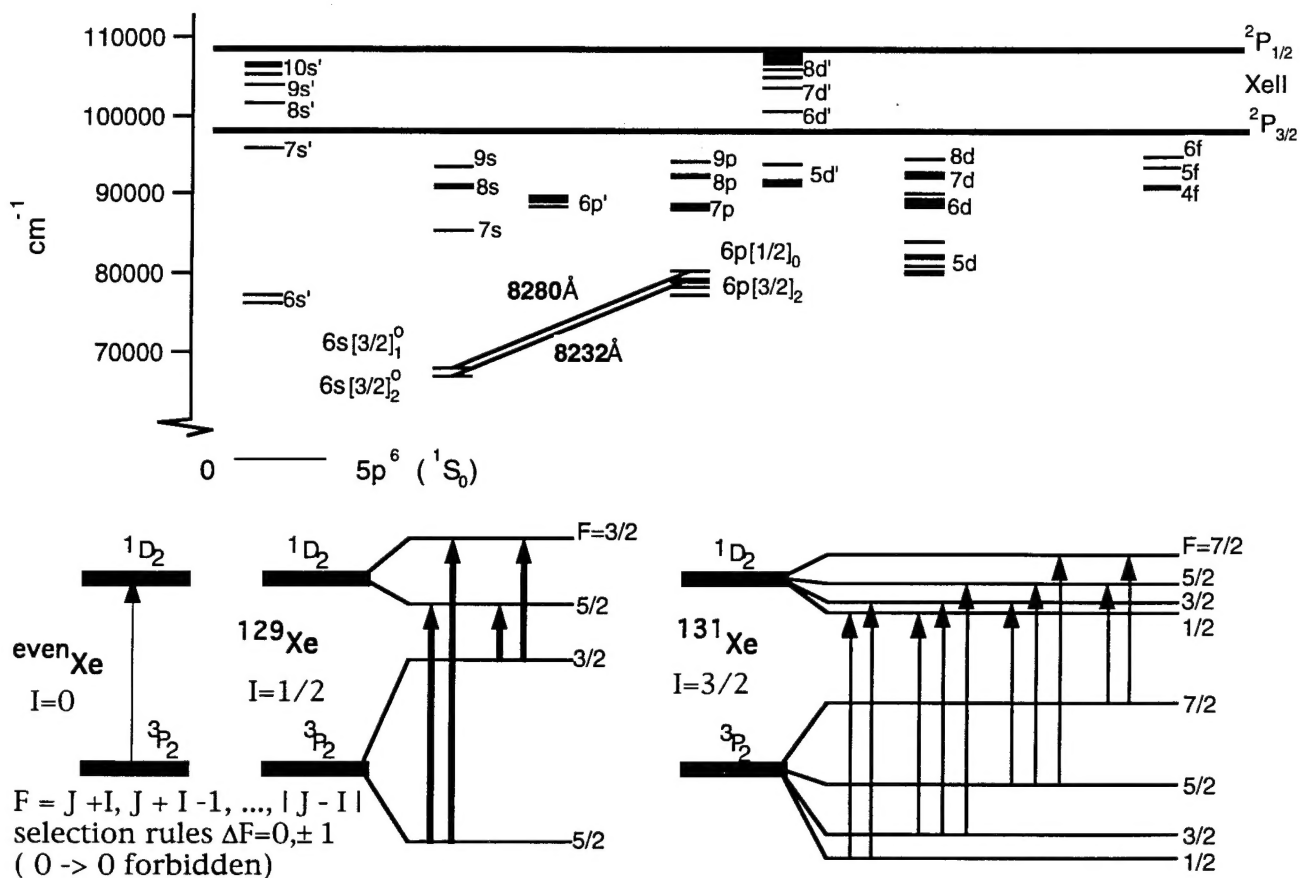
4

Figure 2. Xenon energy level diagram. Nuclear spin splitting of the $6s[3/2]^o_2$-$6p[3/2]_2$ ($^3P_2$-$^1D_2$) transition for even and odd (129 and 131 amu) atomic weights.

In the experiment, the diode laser is directed through the plasma and is swept in wavelength across the overall transition providing highly resolved spectral lineshapes. The line-of-sight absorption and the LIF are simultaneously recorded, but the LIF is of greater interest to us because of its spatial resolution capabilities. Figure 3 shows a sample data trace of a 60 second LIF scan over the 823 nm transition. The relative positions and relative intensities of the 21 hyperfine-split lines contributing to this lineshape are included in Figure 3. Each of the 21 theoretical lines can be individually broadened and the resulting intensities added to construct an excitation spectrum similar to the LIF data. The results of a curve-fitting procedure that optimizes T_{kin} (Doppler broadening) and the Lorentzian broadening (laser-linewidth and collisional effects) halfwidth Δv_{lor} to most closely match the data is also shown in Figure 3. The 21 line positions and relative intensities are fixed, with the overall amplitude, T_{kin}, and Δv_{lor} being the three parameters to the fit.

5

A second 6s-6p transition (828 nm) has also been studied by line-of-sight absorption. The lower state of this transition is optically coupled to the ground state of xenon causing the lineshape to be significantly affected by resonance broadening. The amount of resonance broadening is proportional to the ground state number density N_g and the oscillator strength f_{g1} of the resonant transition. Thus, the investigation of this transition by LIF affords the possibility of a spatially resolved pressure diagnostic.
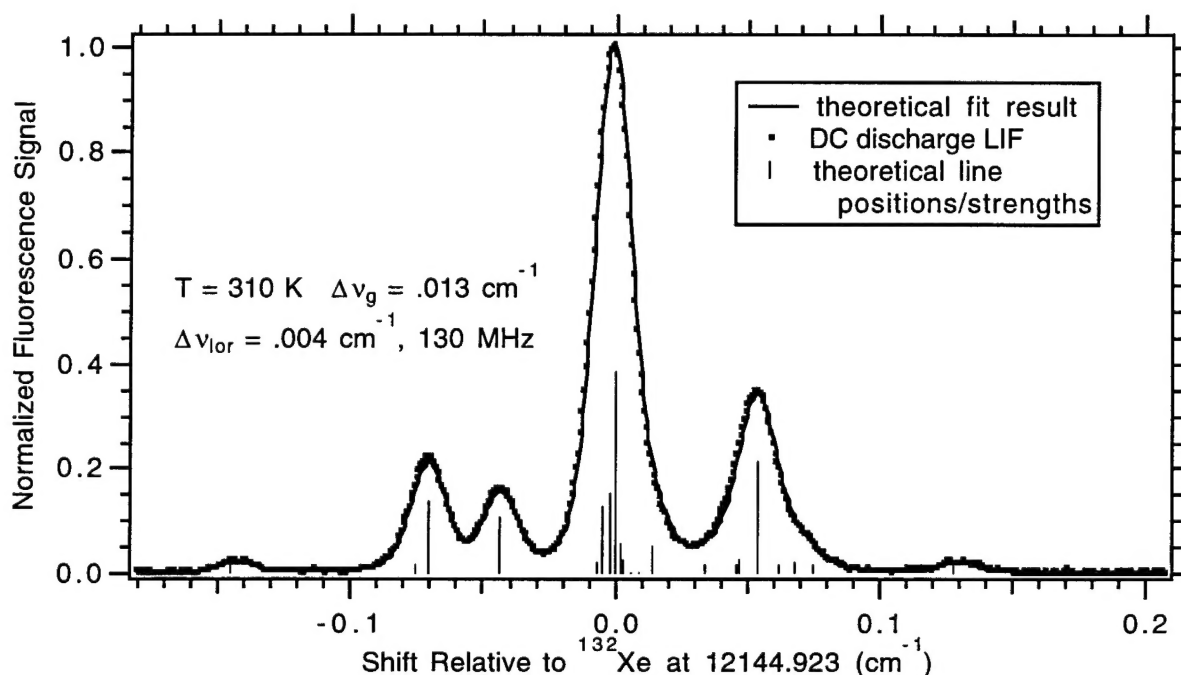

Figure 3. Comparison of measured xenon LIF $6s[3/2]^o_2$-$6p[3/2]_2$ spectrum to calculated fit result.

The use of this LIF diagnostic for velocity measurements in xenon plasmas is currently being investigated. A search for an appropriate xenon ion transition for similar lineshape analyses is also underway.

Details of our work on diode-laser plasma diagnostics are available in several papers (see Secs. 3.1 and 3.2).

## 2.2 Atomic Species Measurements in High-Enthalpy Flows

For gases at combustion temperatures, i.e. up to about 3000 K, spectroscopic diagnostics for temperature typically probe molecular species, such as OH, O_2, NO and N_2.

6

Such temperature measurements can be made using a number of experimental methods that are currently available including LIF, Raman scattering and CARS. At higher temperatures, however, as may be found in various high-enthalpy hypersonic air flows and propulsion plasmas, it will be necessary to establish new techniques which recognize that the major species present are neutral and ionized atoms. For example, in equilibrium air at 1 atm, the mole fraction of O-atoms exceeds that of molecular oxygen above 3500 K, and above about 7000 K, the atomic species O and N are the primary components of air. Ionic species, such as O^+ and N^+, become important above approximately 12000 K. It is thus apparent that spectroscopic diagnostics intended for gases at very high temperatures should be based on atomic rather than molecular species.

We have been pursuing two approaches in developing diagnostics for very high temperature flows. The first approach is based on spectrally resolved absorption of excited-state transitions of atomic nitrogen and oxygen. The laser source is a tunable cw diode laser, and the experimental procedure involves rapidly recording at least one fully resolved absorption lineshape. At high temperatures, the width of the line is dominated by Doppler broadening, and thus a measurement of linewidth is easily converted to a value for the translational (i.e., kinetic) temperature of the gas. The integrated area under the measured spectral absorption coefficient curve yields the number density of atoms in the absorbing (i.e., lower) state, from which we can invoke a Boltzmann distribution to infer an "electronic" or population temperature, assuming that the density of the species is known. (The density of a species is known from theory once the translational temperature and pressure are specified for a mixture of known atomic proportions.) It is important to note that the two temperatures inferred with these methods, i.e. the kinetic and electronic temperatures, may differ in gases at very high temperatures where radiative and collisional transfer processes are not in balance, and such difficulties motivate the need for diagnostics sensitive to these different temperatures in gases with very high enthalpies. The elements of these ideas are illustrated in Fig. 4 which shows a representative lineshape and the key theoretical relationships.

The second approach uses fixed-frequency linecenter absorption of excited-state transitions of atomic oxygen and nitrogen to monitor the number density of the atoms in the absorbing state. An example application is to measure the time evolution of the excited-state atom concentration following passage of a strong shock wave simulating conditions of hypersonic flight. By quantitatively determining the number density of the atomic species in the electronically excited-state probed, we can infer which kinetic processes (i.e., dissociation, ionization, and/or recombination) are important during different stages of the test time, as well as gain insight into whether electronic nonequilibrium exists in the flow. Such

7

Measurement Approach

- Beer's Law

$$I/I_0 = \exp\left(-\alpha_\nu L\right)$$

- $\Delta\nu_D \propto \sqrt{T_{kin}}$

- Boltzmann Equation
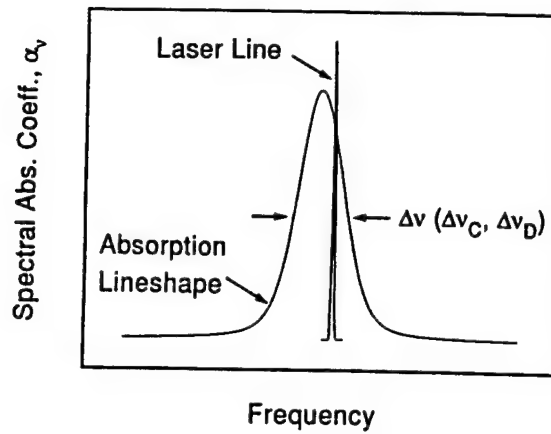
$$\frac{n_i}{n_a} = \frac{g_i}{Z_a} \exp\left(\frac{-E_i}{kT_{pop}}\right)$$

Laser Linewidth	$\approx$ MHz
Absorption Linewidth	$\approx$ GHz

Figure 4. Measurement concept for spectral lineshape thermometry.
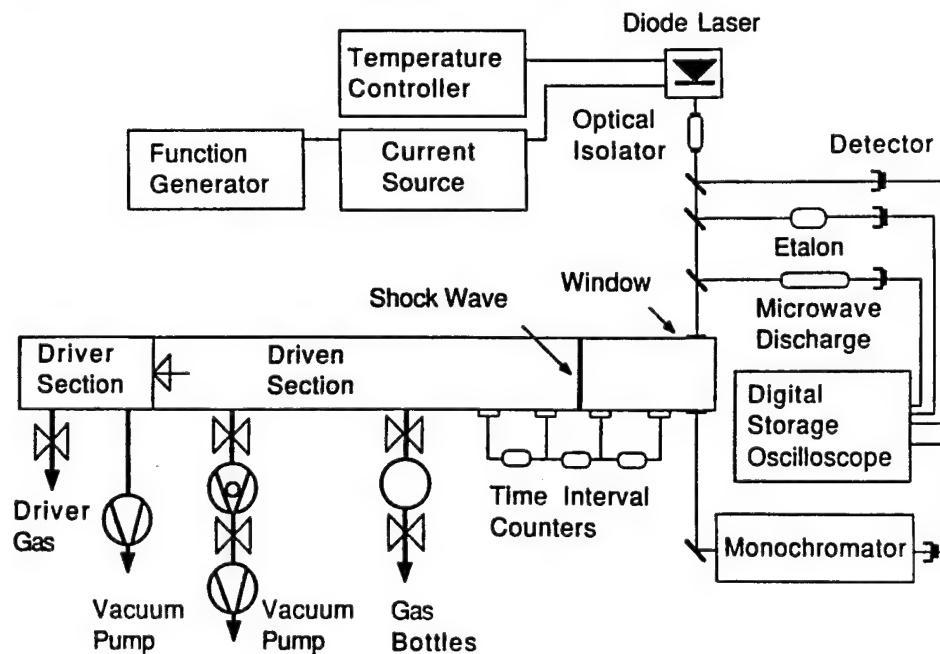
Experimental Setup

Figure 5. Experimental set-up for diode laser thermometry at high temperatures.

understanding is presently lacking for strong shock waves in air and is critical to the development of quantitative kinetic models applicable to hypersonic flight and atmospheric reentry.

Our work to explore high-temperature laser thermometry has been carried out in a conventional pressure-driven shock tube, using reflected shock waves to provide a wide range of known gas temperatures and pressures. A schematic of the experimental arrangement is shown in Fig. 5. Test gas mixtures consist of 1.5% O_2 in argon and 1.5% N_2 in krypton. The lasers utilized to probe the absorption lines (777.1 nm for O-atoms and 821.6 nm for N-atoms) are commercially available GaAlAs semiconductor lasers with an output power level of 5 to 20 mW.

An energy level diagram for the relevant N-atom transitions, and a representative single-sweep data trace (converted from time to laser frequency) are shown in Fig. 6. The laser is repetitively modulated at 8 kHz to record multiple lineshapes. The absorption data are converted through Beer's law to a plot of the spectral absorption coefficient and then best fit with a Voigt profile. This allows determination of the Gaussian component of the lineshape, which yields directly the kinetic temperature through the known Doppler-broadening relationship. The integrated area under the lineshape curve is used to infer the electronic or population temperature of the absorbing state. Note, in this case, that the temperatures are in close agreement (9000 versus 9300 K). Experiments thus far have been limited to temperatures in the range of 6000 to 13000 K, owing primarily to shock tube design limitations, but measurements of higher temperatures should be possible in larger test facilities.

An example data trace for the fixed-frequency linecenter absorption of the O-atom excited-state transition at 777.1 nm is shown in Fig. 7. The data trace represents a shock from the higher end of our temperature range with an initial pressure of 1.10 torr and a shock speed of 2.41 mm/μsec. We can follow both the fractional absorption ($(I_0-I)/I_0$; where I_0 is the incident and I is the transmitted laser intensity) of the O-atoms in the electronically excited-state and the number density determined from the fractional absorption as a function of time. O-atom absorption appears only after the reflected shock as the temperature needs to be high enough to induce not only O_2 dissociation, but excitation of the electronic states as well. Following the dissociation process, the drop in absorption is due to depletion of the excited-state O-atom population by ionization, while the rise in the absorption signal afterwards is due to recombination of the O^+ ions and electrons caused by the drop in temperature during subsequent ionization of the bath gas (Ar, in this case). Electronic relaxation finally brings the absorption level up to an "equilibrium" value. We are currently

Diode Laser Absorption Diagnostic of Atomic Nitrogen for Hypersonic Flowfields and Plasmas

- **High temperature measurements enabled by excited-state absorption**

<u>N-atom Excited-state Absorption</u>
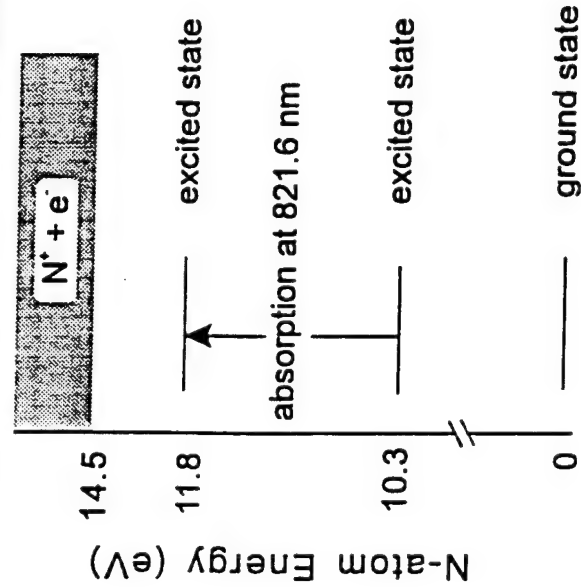
<u>Fast Repetitive Scans of N-atom Lineshape</u>
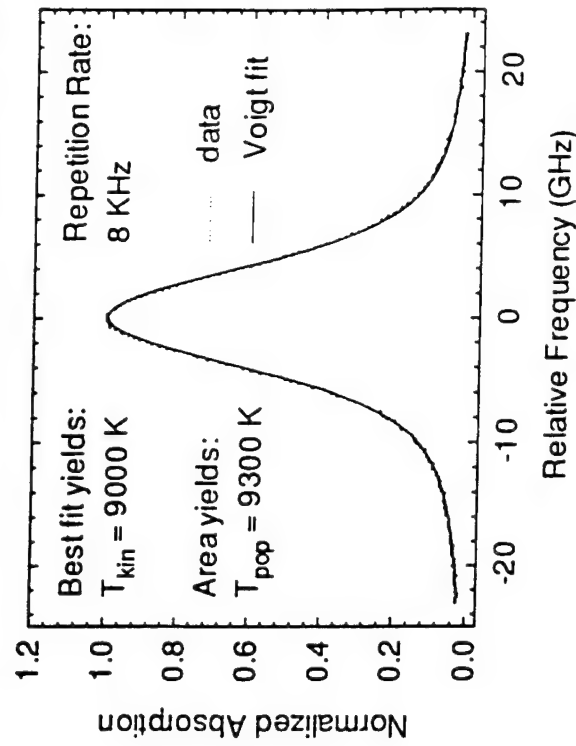
- **First use of excited N- and O-atom absorption in high-enthalpy flows**
- **Kinetic and population temperatures determined simultaneously**
- **Well-suited for remote sensing using fiberoptics**
- **Potential for monitoring velocity in high-speed flows**

Figure 6. Diode laser lineshape measurements in high-temperature gases.

Fractional Absorption of Excited-State O-Atom

1.5% O_2, 98.5% Ar

P_1 = 1.1 torr
V   = 2.4 mm/μsec

Reflected Shock

Incident Shock

y-axis: $(I_o-I) / I_o$
x-axis: Time (msec)
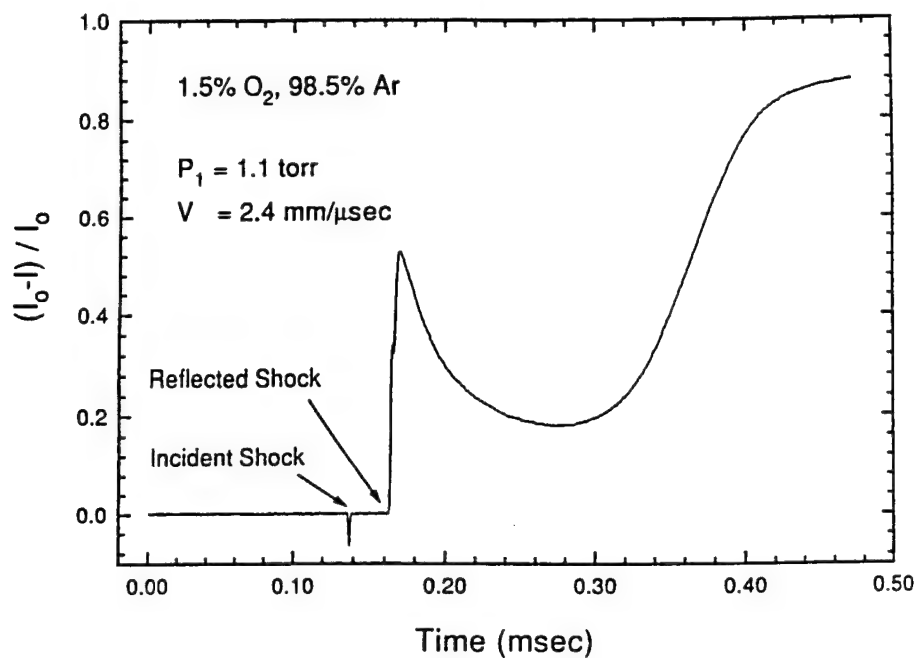
(a)

Excited-State O-Atom Number Density

1.5% O_2, 98.5% Ar

P_1 = 1.1 torr
V   = 2.4 mm/μsec

Ionization of Ar

Ionization of O

Dissociation of O_2

y-axis: n_o (cm^{-3})
x-axis: Time (msec)
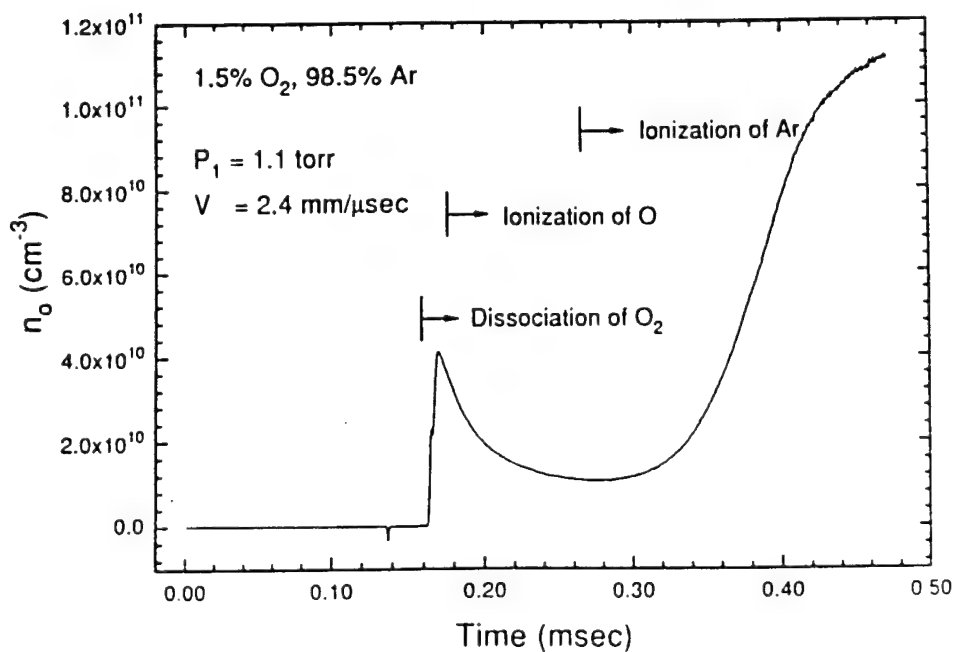
(b)

Figure 7. Diode laser fixed-frequency measurements in high-temperature gases.

11

working on a kinetics model to better understand the various reactions involved in high-enthalpy flows.

Further details of our work on diagnostics for gases at very high temperatures are available in the publications cited in Secs. 3.1 and 3.2.

The concept of using absorption between excited electronic states is versatile since the specific lower (absorbing) state used may be varied to give appropriately large fractional absorption as the temperature of interest changes. For example, as the temperature increases, we can utilize excited states with a higher electronic energy. In addition, the species selected for thermometry may be varied depending on the temperature and the specific gas mixture under study. The atomic nitrogen and oxygen studied typically have many possible absorption transitions which may be utilized.

Future research related to this project may include velocity measurements in high-speed flows using Doppler-shifted lineshapes recorded with different propagation vectors with respect to the flow direction. This diagnostic may also be suited for remote sensing applications (e.g., in flight experiments) using fiber optics.

2.3   Diode Laser Diagnostics for Mass Flux and Thrust Measurements

During the early part of this program we initiated an effort to establish a new class of diagnostic techniques based on diode laser line-of-sight absorption which would enable accurate, fast, and simultaneous measurements of multiple gasdynamic properties including velocity, temperature, pressure, density, and species concentrations in high speed gas flows. We recognized that measured values for these independent properties could be combined to yield quantitative results for important propulsion performance parameters such as mass flux (from the product of density and axial velocity) and momentum flux or thrust (from the product of mass flux and velocity). To our knowledge, these critical propulsion parameters have not previously been measured by optical techniques, and the methods developed in this program offer unique potential for both ground- and flight-based instruments.

The fundamental measurement concept is based on the known dependence of spectral lineshapes on the thermodynamic and gasdynamic state parameters of interest. This strategy, summarized schematically in Fig. 8, permits simultaneous determination of multiple flowfield variables, and with a measurement repetition rate far in excess of that possible with current diagnostic schemes based on pulsed lasers. Tunable diode lasers are attractive and highly promising sources of the narrow-linewidth radiation needed because they are (or will be) economical, rugged, compact, compatible with fiberoptic transmission, and in addition can be

12

Principle of Mass Flux, Thrust Diagnostics

Absorption Line Shapes Contain Information on Flowfield Properties

- Temperature from peak ratio

- Pressure from line width

- Total Density from P/RT

- O_2 or H_2O Concentration from area

- Velocity from Doppler shift of feature relative to static sample

- Mass Flux from $\rho \cdot V$

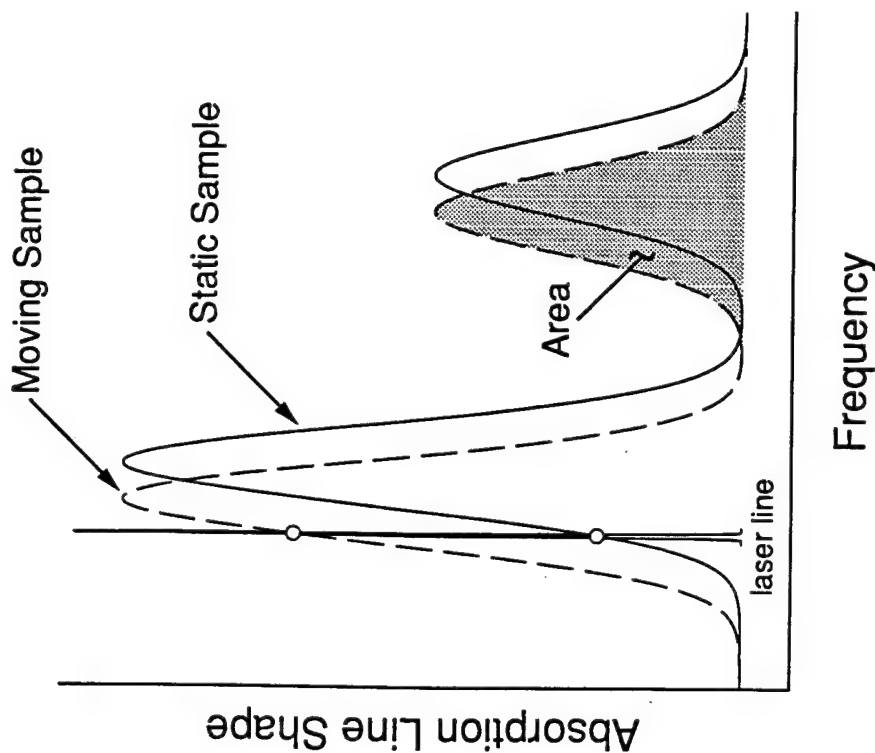- Momentum Flux (Thrust) from mass flux and velocity

Figure 8. Schematic of measurement principle for mass flux and thrust.

13

modulated in wavelength at extremely high rates. At present, diode lasers are available only in specific wavelength windows at wavelengths generally in excess of 650 nm, but the trend toward operation at shorter wavelengths and toward increasing the number of "laser wavelength windows" is clear.

Our research focused on two related efforts: one involving detection of O_2 with 760 nm laser light, as a means of measuring the mass flux of air in a supersonic stream; and the other involving H_2O detection with lasers operating near 1.4 microns, which leads to a method for monitoring momentum flux (or thrust at the exit of a supersonic combustor. These projects are discussed separately below.

We began with O_2, since there is a fortuitous spectral match between recently developed GaAlAs diode lasers which emit near 760 nm and the weakly absorbing A-band (known as the "atmospheric band") of molecular oxygen. A bench-top diode laser absorption system was assembled to establish optimum laser modulation and detection strategies. In that work, we found that the weakness of the absorption as well as various problems with noise could be overcome by modulating the laser wavelength at a high frequency f (typically 10 Mhz) and detecting the second harmonic (2f) signal while the laser was repetitively scanned across the spectral region of interest at a rate of 10 kHz. Thus a complete 2f spectrum could be recorded every 100 microseconds, and the measured spectrum compared with analytical calculations based on known spectral parameters of O_2 to infer the gas temperature (from the ratio of peak signals for the lines encompassed in the scan), pressure (from linewidths), oxygen concentration (from the area under a 2f spectrum), and velocity (from the Doppler shift of the features). Experiments were conducted first in static samples of room air, and subsequently in supersonic streams of gases containing O_2 using a shock tube as a means of preparing samples with a wide range of gasdynamic conditions. The agreement between the measured and calculated flow conditions was typically within 5% for all parameters, including mass flux. Further details of this work may be found in the papers by Philippe and Hanson cited in Secs. 3.1 and 3.2. The success of this effort led to a follow-on project to measure mass fluxes in the 16-inch hypersonic shock tunnel at NASA-Ames Research center as part of a NASP research program.

Our work with tunable diode laser absorption of H_2O followed subsequently. Initially we conducted an analytical study of water vapor absorption bands to identify possible coincidences of H_2O bands and diode laser wavelengths. We found that the strongest bands of water, especially for high temperature measurements, are near 1.4 microns, and that these bands are "combination bands," i.e. they involve simultaneous changes in two (or more) vibrational quantum numbers. Although less strong than the "fundamental"

14

vibrational bands at longer wavelengths, the combination bands near 1.4 microns still lead to usable absorption signals. Thus, in principle, the methods demonstrated for oxygen should carry over to water vapor. This is important, since it would be desirable to identify a single strategy in which O_2 could be detected in air inlets of supersonic propulsion systems (ground-based test facilities or flight systems) and H_2O measurements could be made in the engine exhausts. Further, in analogy with the use of O_2 detection to give air mass flux, one could imagine applying the same approach to infer thrust at a combustor exit plane. The fact that these diode laser strategies are compatible with optical fiber technology holds promise of applying these measurements remotely and with multiple measurement paths to allow more complete mapping of the nonuniform flows.

After identifying the optimum wavelength regions for absorption measurements, and developing the code to calculate the absorption spectra of water at any prescribed conditions, we turned our attention to acquiring a diode laser. After an extensive search, we were able to obtain two prototype lasers from a Japanese company which gave tunable single-mode output near 1.39 microns. To our knowledge, these were the only lasers in existence (at that time) which provided tunable single-mode radiation at these wavelengths, although such devices have now been produced commercially owing to demand for sensitive detection of H_2O. Following characterization of these lasers, we initiated a series of experiments to verify our detailed spectroscopic model of H_2O and to explore schemes for inferring gasdynamic parameters from H_2O spectra in low-and high-speed flows containing water vapor. In particular, we completed experiments which confirmed our ability to make quantitative measurements of water vapor concentration, temperature and pressure in room temperature air, in the combustion products produced in a flat flame burner, and in a supersonic stream containing H_2O produced by a shock tube. In the latter experiments we also measured velocity. In each of these experiments, we were able to successfully demonstrate the utility of the diagnostic concept based on spectrally resolved lineshapes. Owing to the increased strength of the absorption relative to the O_2 measurements (reported above), we were able to use direct recording of fractional absorption rather than resorting to high-frequency modulation with 2f detection.

Details of this work are available in the papers by Arroyo and Hanson cited in Secs. 3.1 and 3.2.

There were two important observations from this work which should be noted here. Firstly, we observed that the fundamental spectroscopic data base for water vapor (primarily in the form of a detailed computer listing of absorption lines, strengths, widths and positions, and known as "HITRAN" in the open literature) contains some important deficiencies, particularly when used to predict high temperature spectra of water vapor. Positions of

15

some lines near the optimum region for H_2O detection (1.40 microns) were found to be slightly in error, some lines were found to have either different strengths or widths than tabulated in HITRAN, and some lines were observed that are not in the latest tabulations. We concluded from these observations that further work with the diagnostic method should include an effort to refine the elements of HITRAN that are required to perform accurate measurements of water vapor at high temperatures.

The second important conclusion of our work is that quantitative measurements of gasdynamic parameters in high-speed streams of combustion gases, using spectrally-resolved absorption measurements of H_2O, are both feasible and attractive. In particular, this method may satisfy the need for a nonintrusive diagnostic to characterize the exhaust gas conditions in both ground-and flight-based tests of advanced propulsion devices. For example, it should be feasible to utilize line-of-sight absorption measurements of water vapor, executed through optical fibers, to provide line-of-sight-averaged flow properties in hypersonic shock tunnel tests which are in progress at Ames, Calspan, GASL and elsewhere. Such measurements might be the most direct means of verifying codes being developed to describe fuel-air mixing and combustion in the engine modules being tested, and may also provide information which confirms the chemical state (i.e., progress of recombination reactions) predicted by reactive-flow computer codes. In the longer term, the methods under study here appear to be the only feasible optical approach for flight monitoring of engine exhausts. Such off-wall measurements may prove to be a crucial complement to more standard surface-based instruments during tests of high performance hypersonic propulsion systems.

2.4 Multiplexed Diode-Laser Absorption Sensors

Following the successful completion of the diode laser sensors for O_2 and H_2O, discussed in Sec. 2.3, we began to explore diagnostic concepts which could further increase the number of gasdynamic quantities or species measured simultaneously. This line of thought led to a new strategy based on the use of multiple diode laser sources arranged to enable simultaneous absorption measurements, along a common path, at multiple wavelengths. In the past six months we have assembled such a system which combines the outputs of multiple diode/lasers into a single optical fiber using appropriate fiber splitters and couplers. This system provides a simple means of expanding the effective wavelength range and number of spectral channels which can be probed simultaneously along a single path. The use of fiber-optic components effectively obviates the need for conventional optical elements such as lenses and mirrors and thus greatly simplifies the optical alignment procedure and significantly increases the ruggedness of the system.

Initially, our strategy for combining and separating the beams of multiple lasers along a single path was based on tuning the lasers alternately in time. The system was used to accurately determine temperature and species concentration in high-temperature, high-velocity flowfields, generated in a shock tube, using measurements of high-resolution H_2O lineshapes near 1.4 μm; see paper 41 in Sec. 3.2 for details.

Quite recently, a new and improved system for combining and separating individual diode-laser beams based on wavelength-division multiplexing has been developed (see Fig. 9). In this system, light from multiple lasers propagates simultaneously in a single optical fiber; the multiple lasers are operated independently and scanned across discrete spectral regions containing the absorption transitions of species of interest. The multi-wavelength transmitted light is demultiplexed into constituent laser wavelengths by directing the beam exiting the probed region at a non-normal incidence angle onto a diffraction grating. The beams are diffracted at angles which correspond to each wavelength and subsequently monitored with appropriate detectors. The left side of Figure 9 illustrates the experimental setup used recently for simultaneous measurements of H_2O, O_2, and temperature in a heated cell and a room-temperature air path. The right side of Figure 9 shows a comparison of temperatures measured in a heated cell using the two-line method and a thermocouple. The laser data were based on single wavelength scans; the laser modulation rate, and hence temperature measurement rate, is typically 3-10 kHz. The excellent agreement between the two methods suggests that the system and method are reliable.

The multiplexed diode-laser absorption sensor system capable of nonintrusively measuring several flowfield constituents and properties along a single path may be easily extended to simultaneously monitor multiple species along many paths in order to obtain three-dimensional flow-parameter distributions using tomographic methods; to simultaneously monitor different, separated flowfields; or to determine multiple velocity components in moving gaseous flows through measurements of Doppler-shifted line positions. Ongoing work is aimed at exploring extensions of this strategy including fixed-wavelength techniques which will allow continuous *in situ* determinations of gasdynamic parameters within various flowfields.

17

MULTIPLEXED DIODE-LASER ABSORPTION SENSOR SYSTEM FOR MULTI-PARAMETER MEASUREMENTS

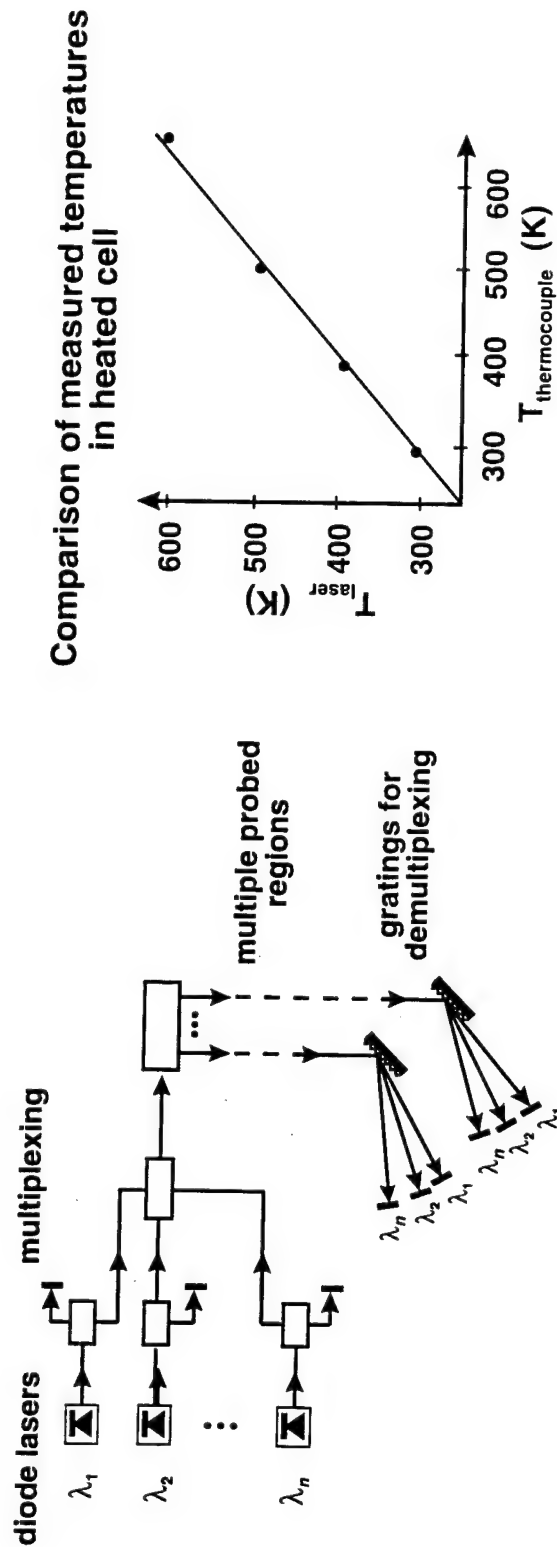- **Simultaneous measurements of species, temperature and pressure at kHz rates**

Comparison of measured temperatures in heated cell

diode lasers   multiplexing

multiple probed regions

gratings for demultiplexing

- **First measurements of multiple species (H_2O, O_2) and temperature along a common path**
- **Fiber-optic system is compact, flexible, and rugged**
- **Applicable to remote measurements in ground facilities and flight testing**
- **High potential for application in combustion control**

Hanson/Stanford

Figure 9

18

2.5 Digital Camera for 3-D and High-Speed Imaging

Advances in image-based diagnostic techniques for turbulent combustion are dependent, in part, on state-of-the-art improvements in high-speed camera systems. For this reason, a portion of our overall diagnostics program has been directed at building a unique camera with the capability for light-efficient, high-speed recording of planar flow visualizations. In concert with this effort, we have developed experimental techniques for 2-d imaging of ultrafast combustion, plasma, and laser events, and instantaneous 3-d imaging of turbulent flames and flows. During the past four years, we have assembled and characterized the camera system and have conducted a series of 2-d and 3-d experiments. Most recently, we have collected instantaneous 3-d PLIF images, and we have developed methods for correcting various camera system distortions.

Our unique flow visualization system is shown in Figure 10, and an example of the system output is shown in Figure 11. For 3-d imaging, flow visualization is provided by planar illumination from a pulsed dye laser lasting 2 μsec. During this time, the laser is swept laterally across the flow using a 30,000-RPM mirror, and an image converter camera framing at 10^7 frames/sec provides up to 20 high speed images. The images are passed from the image converter through a fiber-optic coupling and placed side-by-side on a cooled high-resolution CCD array. In this way, the system records sequential image planes within the flow and so provides a record of the instantaneous 3-d flow conditions which can be analyzed for a wide variety of information. Details of the laser and camera systems, and their characterization may be found in papers 20, 29 and 41 in Sec. 3.1.
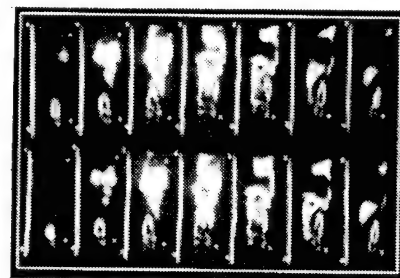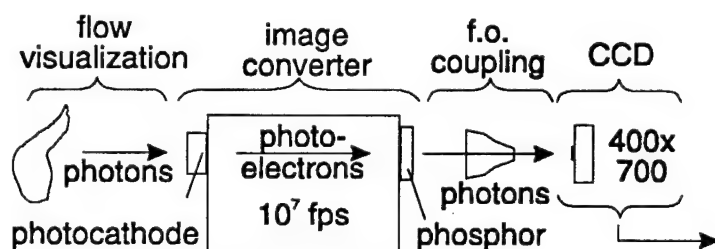

Figure 10. Exploded schematic of camera.   **Figure 11. Example of camera output.**

To demonstrate the potential of this system to provide high quality images, we collected 3-d PLIF images of an acetone-seeded air jet. Figure 12 shows several examples of such 3-d PLIF data processed into graphical volume renderings for qualitative presentation. To collect this data, our 2-μsec laser was tuned and frequency-doubled to provide intense

ultraviolet illumination suitable for acetone, which we recently identified as an excellent PLIF tracer. The results are the first instantaneous 3-d PLIF images of such high quality, and they provide us insight to the practical challenges associated with this promising 3-d technique. Further example applications of the camera system are presented in paper 37 in Sec. 3.2.
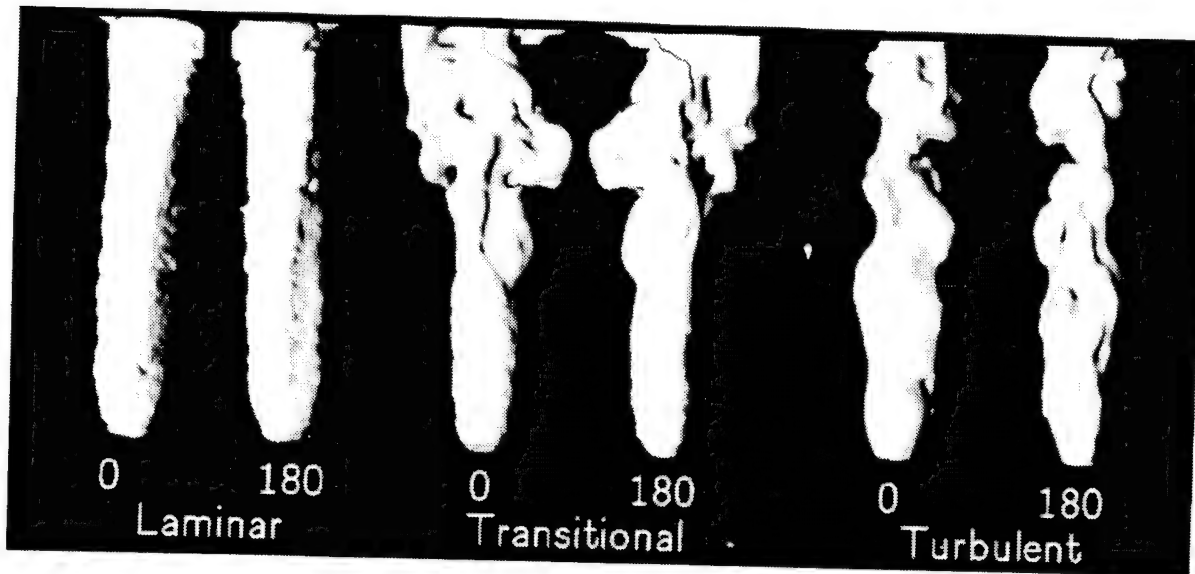
Figure 12. 3-d PLIF images of acetone-seeded air jet.

Also in the past two years, we have substantially reduced the image distortions inherent in image converter cameras operated at high framing rates. The source of the distortion has been identified as uncompensated electrodynamic forces arising from the high charge densities associated with high speed operation of the image converter. As shown in Figure 13 (a), the typical distortion appears as an inward bowing that substantially changes the shape of, in this case, a simple rectangular subject. To deal with this distortion, we have developed a unique post-processing software package which computes the electrodynamic force field for a given image. In Figure 13 (b and c) we show the electrodynamic "x" and "y" components of the force field for the case of the rectangular subject. Finally, in Figure 13 (d) we show the corrected image in which we have reversed the effects of the computed force field and thereby substantially recovered the original rectangular geometry.

This image-distortion model and our software procedures for correcting such distortions are detailed in paper 47 in Sec. 3.2, and were also presented at the 20th International Congress on High Speed Photography (see presentation 29 in Sec. 3.1). There was strong interest in our work, particularly from the Russian scientists and major camera manufacturers anxious to improve the quality of results obtained with current image-converter cameras.
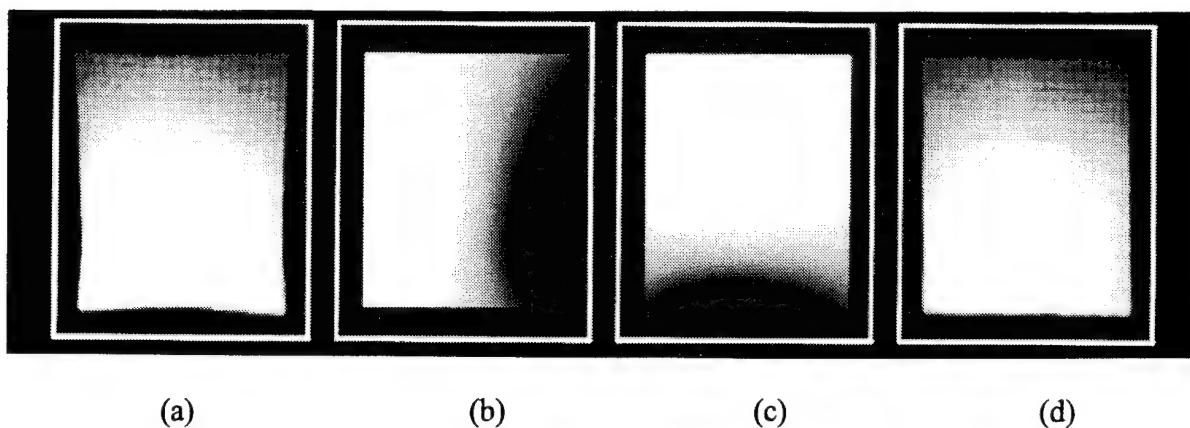
Figure 13. (a) Spatial distortion of a rectangular subject; (b and c) x and y distortion forces (black=rightward or downward force, white=leftward or upward force); (d) corrected imaging showing recovered geometry.

2.6 PLIF Imaging in High-Speed Flows

Planar laser-induced fluorescence (PLIF) imaging, pioneered at Stanford under support from AFOSR, is of growing value in high-speed propulsion research. Laser-based diagnostics are advantageous in these severe flow environments because they are nonintrusive; additionally, PLIF can yield quantitative two-dimensional property fields on a nearly instantaneous basis. In large, high-enthalpy, short-duration flow facilities, an ability to obtain information on the flow at many points simultaneously is crucial, as a day or more may be required between facility firings.

The focus of our work over the past four years has been on the development of velocimetry and thermometry strategies applicable in nonequilibrium supersonic flows relevant to advanced propulsion concepts. Two flow configurations, both based on shock tubes, have been utilized: (1) a model scramjet flow produced by pulsing a jet of gaseous (H_2) fuel into the hot supersonic flow behind an incident shock wave; and (2) a supersonic free jet produced in a reflected-shock tunnel.

A schematic of the experimental arrangement used to develop quantitative single-shot thermometry imaging in a model scramjet flowfield is shown in Fig. 14. The temperature measurement strategy is based on a ratio technique in which two independent PLIF images are acquired (essentially at an instant, but actually separated in time by about 200 nsec) using two independently tunable dye laser sources and two intensified CCD cameras. The lasers are tuned to wavelengths which excite different quantum states of NO (or alternatively OH in
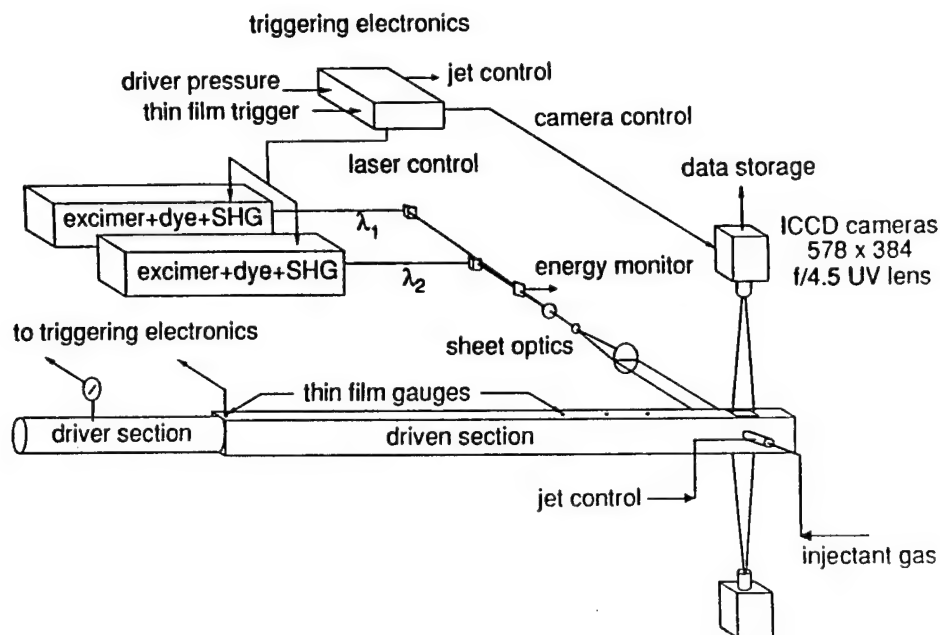
Figure 14. Schematic of the experimental facility for two-line PLIF imaging of temperature in a model scramjet flow.

related experiments), which may be seeded into either the jet alone or both the jet and crossflow. The ratio of the fluorescence signals, after proper normalization for laser energy and other proportionality factors, yields the relative populations in the two quantum states, and this can be easily converted to temperature. This methodology is known as the two-line method, and it has significant advantages over competing methods for imaging temperature. The flowfield investigated and an example result are shown in Fig. 15. Typical conditions of the freestream are 1200-2200K, 0.5 atm, and Mach 1.5, while the jet is hydrogen seeded with a low level of NO. Use of a pulsed jet minimizes the quantity of H_2 required for an experiment and the perturbation to the pre-shock test gas mixture. The results shown represent, to our knowledge, the most quantitative temperature imaging yet achieved in a supersonic flow; typical accuracy levels, set by shot noise, are 5-10% for these experiments. Improvements in the experimental arrangement, particularly in the laser pulse energy, could allow improvements in accuracy to a few percent. Further details of this work may be found in papers 30 and 34 in Sec. 3.2.

Instantaneous PLIF Temperature Imaging of Scramjet Flow

- **Use of shock tube provides access to a wide range of flow conditions**
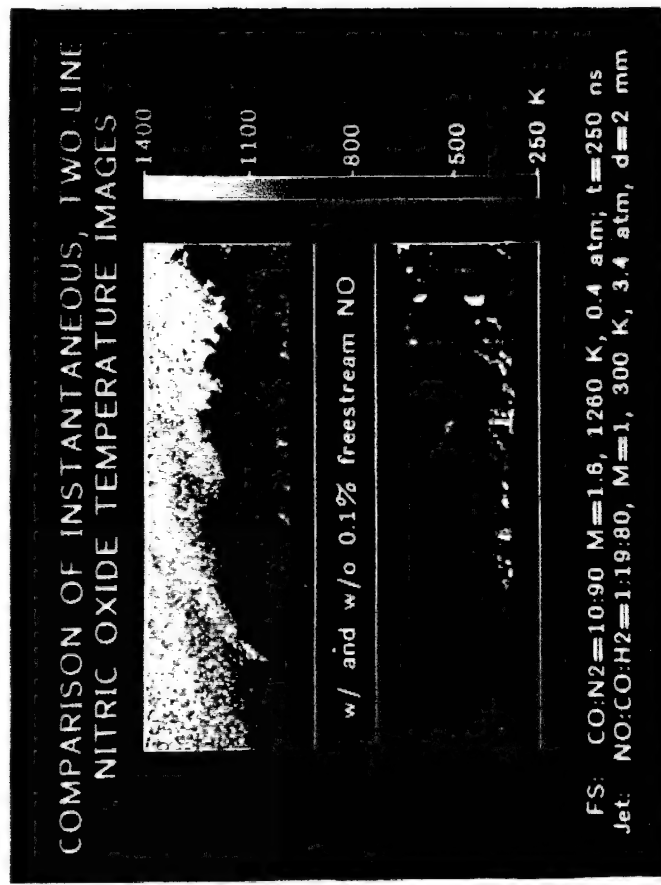
- **First instantaneous two-line (two laser/two camera) temperature images using PLIF**

- **NO temperature marks jet penetration and indicates extent of mixing**

- **Single-shot images reveal large-scale structures not apparent in averaged images**

- **Results confirm utility of PLIF measurements for scramjet research**

Figure 15.   Schematic diagram and example results for two-line PLIF imaging in a scramjet flow.

Our experiments to develop PLIF thermometry and velocimetry imaging in a supersonic free jet have been carried out in a reflection-type shock tunnel facility, constructed from a pressure-driven shock tube by adding a converging nozzle with a throat diameter of 5 mm. The shock-tunnel free jet provides a convenient, economical means of studying nonequilibrium gasdynamic phenomena and of simulating extreme flow conditions. The test gas is either seeded with nitric oxide (NO) or contains a hydrogen/oxygen mixture which forms hydroxyl radicals (OH) in the flow following combustion in the shock tunnel reservoir. PLIF measurements have been performed with both of these fluorescent species, in each case using a tunable, excimer-pumped dye laser to excite individual electronic transitions and collecting the resultant broadband fluorescence. A schematic of the experimental facility, and representative results for velocity imaging (axial and radial components), are shown in Fig. 16.

In these experiments, sequential fluorescence bursts are induced by broadband counter-propagating laser sheets directed at an angle through the axis of the jet. A single frequency-doubled dye laser pulse split into two parts forms the sheets, which therefore have identical spectral properties. A delay of 200-300 ns in one of the beams temporally separates the PLIF signals, which are captured by the gated, intensified charge coupled device (CCD) arrays mounted above and below the test section, as shown in Fig. 16. Opposite Doppler shifts of the absorption frequency with respect to the beams at each point in the flow cause a velocity dependence in the resultant image pair. A difference-to-sum combination of the images, with an analysis of the single-shot laser spectrum and the assumption of flowfield symmetry, yields the instantaneous two-component velocity field of the free jet. The rotational temperature field is obtained by taking the ratio of images acquired by exciting two different rovibrational transitions. Each image in the ratio is formed by summing images acquired simultaneously with a single laser shot for the experimental arrangement shown here. Alternatively, a single laser sheet oriented perpendicular to the jet axis has frequently been used in collecting an image which yields the rotational or vibrational temperature field, when compared with a similar image obtained by exciting a different rovibrational line. A method of characteristics (MOC) simulation of the flowfield has also been used in assessing the velocity and temperature measurements.

An example of the velocity results obtained in our work is given in Fig. 16, where we show composite velocity images based on the MOC calculation and on a single-shot PLIF measurement with the $A \leftarrow X(0,0) P_1(1.5)$ feature of NO. In each case, the upper part of the image shows the radial velocity component, while the lower shows the axial component. The images represent regions of the flowfield 43×15 mm in size, with a resolution of 0.23 mm/pixel. The test gas, composed of 4.6% NO, 8% H_2O, and 87.4 % Ar, was shock-heated to 2000 K and 4 atm in the shock tunnel. The reservoir gas then exhausted through the nozzle into the low pressure test section, yielding a free jet with a stagnation-to-ambient

INSTANTANEOUS, TWO-COMPONENT VELOCITY MEASUREMENTS IN A SUPERSONIC FREE JET USING PLIF
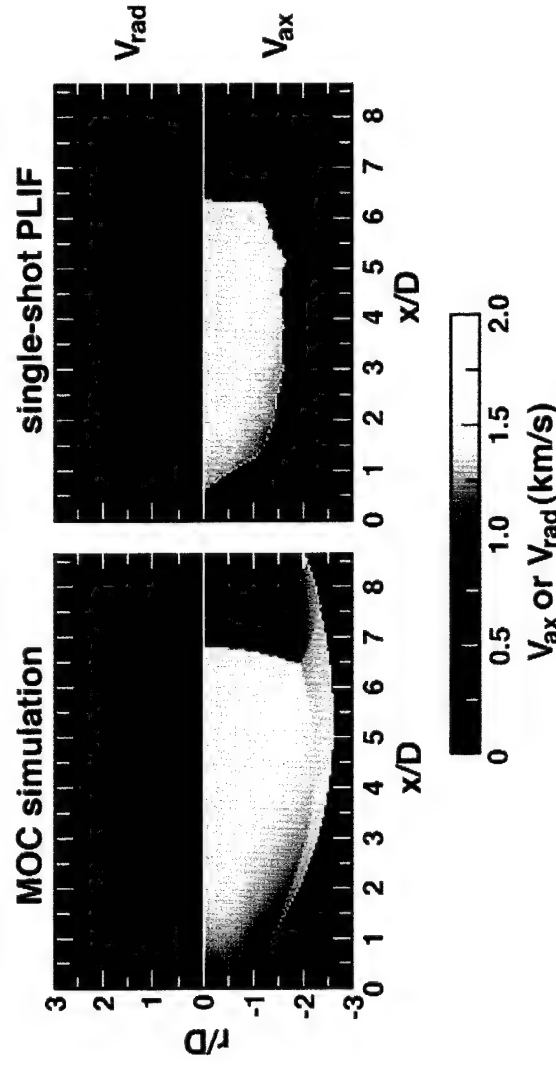
- PLIF signal depends on Doppler shift of absorbing line caused by bulk flow velocity

- Use of counter-propagating laser sheets yields radial and axial velocities simultaneously

Shock Tunnel Facility
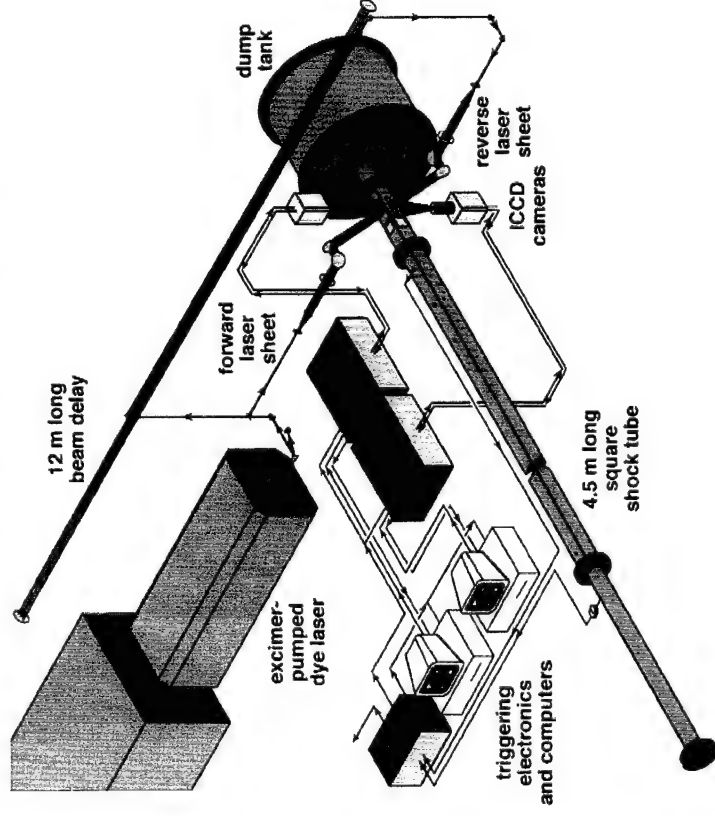
Composite Velocity Images

4.6% NO/8% H_2O/Ar, P_s = 4 atm, T_s = 2000 K image size = 188 × 128 pixels, D = 5 mm

MOC simulation

single-shot PLIF

V_{rad}

V_{ax}

V_{ax} or V_{rad} (km/s)

- Single-shot capability demonstrated in a hypersonic shock tunnel

- Found good agreement with method of characteristics (MOC) simulation

- Potential for simultaneous temperature and density measurements

Figure 16.

pressure ratio of ~95. The agreement between the measured and predicted velocity components is good throughout the jet core. The portions of the flow outside of the core, where the flow is turbulent, are not shown, as the assumption of flowfield symmetry fails there. The component of the velocity in the direction of laser propagation was, however, successfully measured throughout the imaged region.

An example of PLIF imaging of nonequilibrium for temperature is provided in Fig. 17. In this case a mixture of 4.6/8.0/85.4 $NO/H_2O/Ar$ is expanded from a 4 atm, 2000K in the free jet, and the temperature is inferred from ratios of PLIF images acquired by excitation of different rotational and vibrational states of NO. These results confirm the large differences in the rotational and vibrational temperature fields for this rapid-expansion flowfield, as may be expected for a diatomic molecule with relatively large vibrational energy-level spacing such as NO. We believe these represent the first application of PLIF thermometry to flows with vibrational nonequilibrium. It is worth noting that competing methods for temperature imaging, such as Rayleigh scattering and single-line fluorescence, would be of limited use in such flows, while PLIF can be easily tailored to give either or both the vibrational and rotational temperatures. Details are available in papers 24, 42 and 45 of Sec. 3.1.

In addition to these results, we have recently demonstrated PLIF velocimetry and thermometry in a supersonic free jet flowfield with OH, again using single-shot imaging. At present, the velocity fields are captured during a single laser pulse; while two separate runs of the tunnel are required to capture the temperature field, because only one excitation wavelength is used. However, the extension of the technique to either instantaneous temperature measurements or simultaneous, single-shot velocity and temperature measurements is straightforward. Further details of this work are provided in paper 54 in Sec. 3.1.

2.7 PLIF Imaging of Acetone-Seeded Flows

Four years ago, we initiated an effort to survey alternatives to the use of biacetyl as a flowfield tracer in PLIF studies on turbulent mixing in nonreactive flows. Until that time, biacetyl was the preferred choice as an additive owing to its relatively high vapor pressure, convenient excitation wavelength range, high fluorescence yield, and other less critical factors. The development and use of biacetyl seeding in turbulent jet mixing experiments at Stanford had previously led to the first high-quality image data for instantaneous scalar fields. These data were well received by the turbulence community owing both to their uniqueness (in providing instantaneous, full-field results for the jet mixture fraction) and to the high quality of the data, especially the high signal-to-noise ratio and high dynamic range achieved. Unfortunately, biacetyl is limited in its applicability to high-speed flows owing to the relatively long radiative decay time (about 1 millisecond) of the phosphorescent emission

26

PLIF MEASUREMENTS OF MULTIPLE TEMPERATURES IN A VIBRATIONALLY-RELAXING, SUPERSONIC FLOWFIELD

- Vibrationally-nonequilibrated flows have two temperatures: T_{rot} and T_{vib}
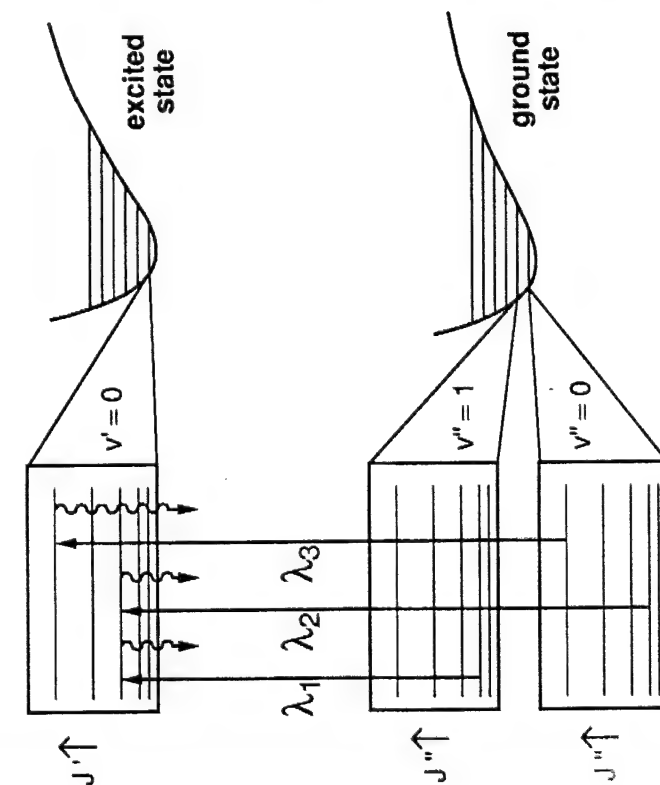
PLIF Image of Free Jet
4.6% NO/8% H_2O/Ar, P_s = 4.0 atm, T_s = 2000 K
43 × 27 mm region
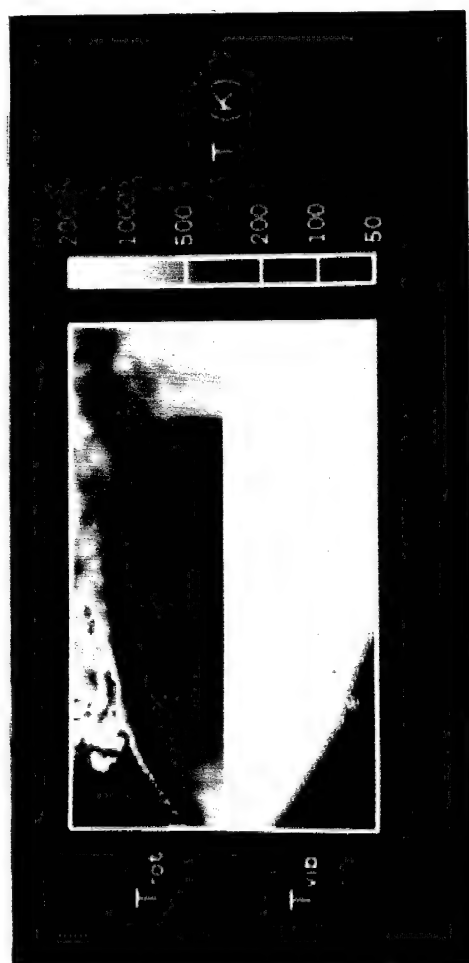
- Use of 3 excitation wavelengths yields T_{rot} and T_{vib}

- PLIF imaging technique extended to multi-temperature flows

- Single-shot capability demonstrated in hypersonic shock tunnel

Figure 17. PLIF strategy and results for thermometry imaging in vibrationally relaxing flowfield.

27

(long decay times lead to blurring in single-shot images). Thus, as the direction of our research began to emphasize high-speed and supersonic flows, we decided to review alternative molecular tracers.

Although our survey identified several attractive compounds, we eventually selected acetone as best-suited to our needs for a fluorescent tracer. Details of our analysis of acetone photophysics have been published (see paper 25 in Sec. 3.2). Here we mention only the primary advantages of acetone: (1) acetone has a high vapor pressure, about 180 torr at room temperature, so that it can be easily seeded at high levels; (2) it is economical, easily handled and non-toxic, so that safety is not a problem; (3) the peak absorption is at 275 nm, but reasonably efficient excitation occurs at the convenient laser wavelengths of 248 nm, 266 nm and 308 nm; (4) the fluorescence quantum yield is high, about 0.2%, and is independent of the presence of O_2; (5) the emission has short lifetime (4 nsec) and occurs in a wide band which peaks at 480 nm, in the visible, so that it can be recorded on an unintensified camera; and (6) we estimate that, at room temperature and with existing laser sources, the fluorescence signals achievable with acetone are only about a factor of six less than the high phosphorescence signals obtained with biacetyl. Thus it is possible to obtain both high SNR and high signal resolution (dynamic range), comparable to our past experience with biacetyl, in high speed flows seeded with acetone.

In reviewing options for exciting acetone, we realized that 308 nm light from a xenon chloride (XeCl) excimer laser offered an important advantage, namely that it could be used to simultaneously excite fluorescence of OH, which has a few absorption lines which lie under the output curve of typical (XeCl) laser output. To demonstrate this concept of simultaneous PLIF imaging of multiple species (i.e., acetone and OH), we first performed experiments in a simple diffusion flame. The fuel, nominally H_2, was seeded with acetone (about 10% by mol fraction), and burned in ambient air. Two time-gated intensified CCD cameras were used to capture the resulting PLIF images, as indicated schematically in Fig. 18. The OH images were separated from the acetone images through use of spectral filters; a 10 nm bandpass filter centered at 310 nm was used for the OH channel and a broad bandpass filter selected the 350-470 nm light from the acetone emission. Example results for a flame with jet Re = 24,000 are shown in Fig. 19. The field imaged is 6 cm x 8 cm, the bottom of which is 16 dia above the 2.2 mm nozzle. Note the capability to obtain high quality images for both species with a very simple experimental arrangement. Mie scattering from dust in the ambient air is also evident. The virtue of this diagnostic strategy is the ability to utilize a single laser while obtaining information on multiple species.
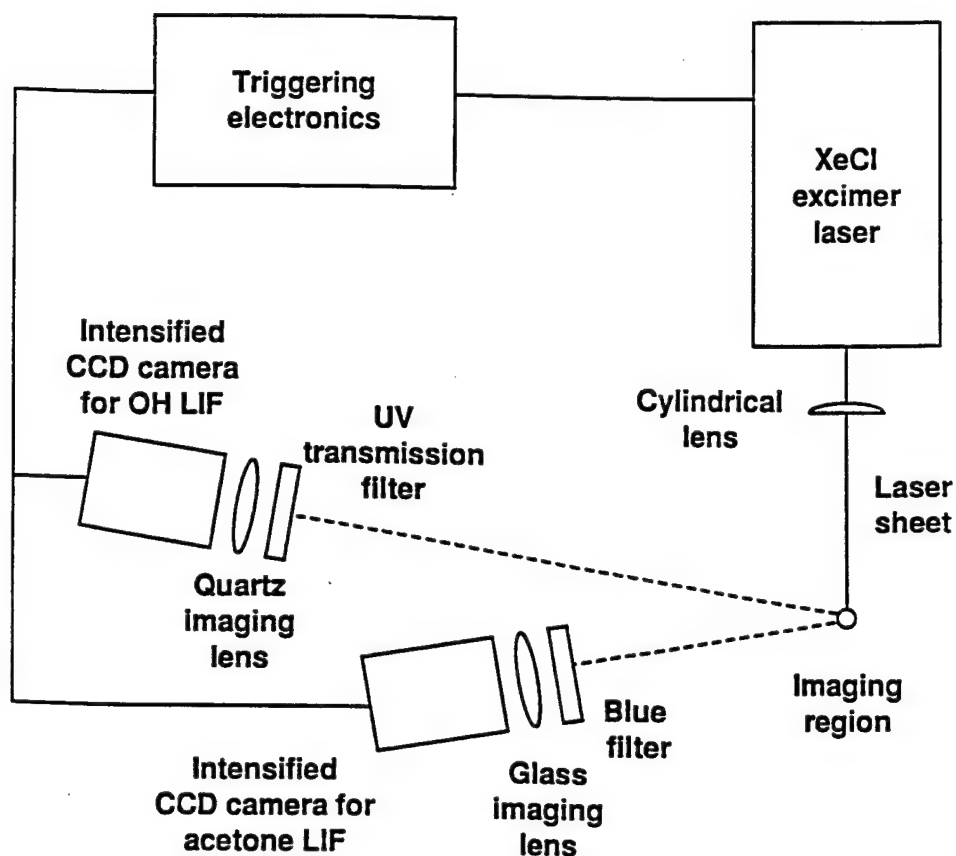
Figure 18. Experimental setup for combined OH/acetone PLIF imaging.

During the past two years we also investigated the applicability of the combined OH/acetone imaging concept for supersonic flows. A detailed analysis was carried out to establish the regimes in which acetone could serve as representative tracer of hydrocarbon fuels in reacting (combusting) flows, and this analysis pointed clearly to high-speed flows as optimum. There is good reason to believe that the primary difficulty observed in using acetone as a tracer in a low speed diffusion flame, namely the difference in thermal decomposition of the true fuel and the acetone tracer, would be eliminated in supersonic mixing layers where the time scales of interest are very short. The experiments to test this hypothesis, conducted in Stanford's supersonic mixing facility, were a collaboration involving Drs. Yip and Seitzman of our diagnostics group with Mike Miller and Toby Island, who were graduate students conducting their Ph.D. thesis work in this facility under separate AFOSR support. The flowfield under study is a planar supersonic mixing layer, with high-speed vitiated air on top and lower speed ((sonic) fuel (H_2) seeded with acetone on the bottom. The mixing and subsequent combustion of these gases, under supersonic flow

SIMULTANEOUS OH AND ACETONE FLUORESCENCE IMAGING USING ONE EXCITATION LASER

Instantaneous images acquired in an acetone/H$_2$ diffusion flame (Re = 24,000). Left: OH fluorescence and ambient air dust Mie scattering. Center: acetone fluorescence. Right: superposition of left and center.

Single-laser excitation, two-camera detection strategy enables simultaneous imaging of :

- OH fluorescence (reaction zone information)
- Acetone fluorescence (cold fuel information)
- Air dust Mie scattering (ambient air information)

Figure 19. : Simultaneous OH and acetone fluorescence imaging using one excitation laser.

30

conditions, is highly relevant to current research on scramjets. We explored two excitation strategies: (1) 308 nm light from a tunable XeCl laser; and (2) 285 nm light from a tunable dye laser. Both schemes excite both OH and acetone, but the use of 285 nm allows excitation of the 1-0 band of OH and, by use of 1-1 plus 0-0 detection, gives excellent discrimination against elastically scattered light. The result of this measurement strategy is a significant improvement in the signal-to-noise ratio of the OH images. Details of this work are available in paper 52 in Sec. 3.1 and paper 48 in Sec. 3.2.

As a last example of PLIF employing acetone, we summarize work during the past three years to develop a scheme for measuring mixing on a molecular scale. The objective is to find a way to eliminate the bias in PLIF measurements of mixing owing to the finite size of the imaged volume. (In short, our usual PLIF images are unable to resolve mixing scales below the size of the imaged volume.) Our strategy, which is a refined version of ideas put forth previously by other groups, can be described with the help of the schematic shown in Fig. 20. We imagine that the problem of interest involves the mixing between two gaseous streams, one seeded with biacetyl and the other with acetone. A pulse of laser light is used to excite the first excited singlet state of acetone, and the absorbed photons nearly all are returned to the ground state by quenching collisions. A small fraction of these absorbed photons are emitted as fluorescence, and this signal, in the blue, is directly proportional to the local concentration of acetone. However, wherever acetone molecules are in intimate contact with biacetyl molecules, a transfer of energy occurs to the first excited triplet state of biacetyl, and some of these molecules then emit fluorescence in the green. Thus, green light is only emitted when mixing has occurred to the molecular level. A typical two-color image acquired in a preliminary study of this concept appears in Fig. 20.

We have developed a detailed model to characterize the behavior of acetone-biacetyl systems as a function of the various parameters: e.g., mixture fraction, pulse energy, collisional cross-sections, radiative rates, etc. This model (see paper 43 in Sec. 3.1 and paper 38 in Sec. 3.2) confirms the feasibility of the approach and allows prediction of the signal dependences (uv and green) on the extent of molecular mixing. Although difficulties remain, we believe that this general approach has considerable merit for application in fundamental studies of mixing.

2.8　Degenerate Four-Wave Mixing

Four years ago, we initiated a study of innovative diagnostic methods based on degenerate four-wave mixing (DFWM). A relatively new diagnostic, DFWM is a spatially resolved technique which is complementary to LIF. It offers potential advantages in some

31

ACETONE-SENSITIZED BIACETYL PHOSPHORESCENCE ALLOWS MEASUREMENT OF MOLECULAR MIXING IN GASEOUS FLOWS
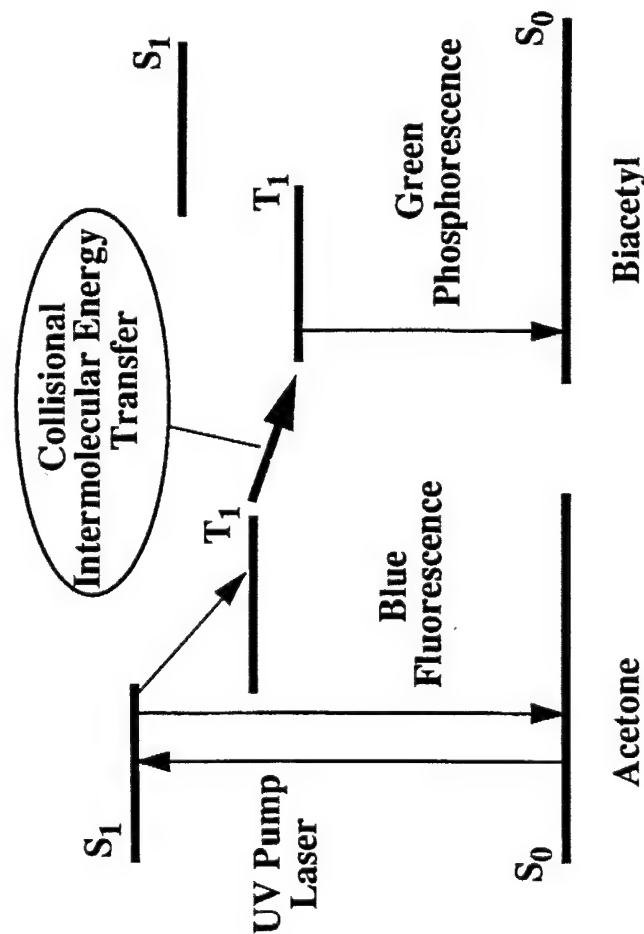
Schematic of energy diagram and photophysical processes.

Combined image of acetone fluorescence (blue) and sensitized biacetyl phosphorescence (green).

- Collisionally-induced biacetyl phosphorescence marks flowfield regions where two fluids have mixed molecularly

- Study is in progress to obtain quantitative mixing information from sensitized biacetyl phosphorescence and simultaneous acetone fluorescence

Figure 20.   Schematic diagram and example results for PLIF imaging of molecular mixing.

applications, though it is more complicated and less well understood than LIF. In particular, DFWM generates a coherent signal beam which is useful for both remote sensing and rejection of unwanted background light; and it is a Doppler-free technique allowing very highly resolved (spectrally) spectroscopic measurements. Although this technique requires absorption of light, it does not necessarily require subsequent re-emission of light. Thus, it can be used to probe non-fluorescing transitions as are commonly found in the infrared. In summary, while it is more difficult to perform and understand, DFWM has some attractive qualities when compared to LIF, and hence continued research on this subject is merited.

Over a year ago, in collaboration with researchers at Sandia National Laboratories in Livermore, CA (SNLL), we set a goal of developing improved understanding of the effects of collisional quenching on both DFWM and LIF. (The SNLL component of the effort is sponsored by DoE.) We found that DFWM has a reduced dependence on quenching compared to LIF (see paper 32 in Sec. 3.2). Another effect of collisional quenching we observed was the generation of DFWM signal from a process known as the *thermal-grating* mechanism. We believe that thermal gratings show promise as a flow diagnostic for reactive environments (see papers 57-59 in Sec. 3.1 and papers 45, 46 in Sec. 3.2).

Conventionally, DFWM diagnostic measurements have been performed using the *population-grating* mechanism. Population gratings result when an interference pattern generated by two crossed laser beams causes a spatial modulation of excited-state molecules in an absorbing medium. A portion of a third beam incident on this population modulation is diffracted by the grating in a well-prescribed direction, generating a signal beam. In the presence of rapid collisional quenching, another process known as the thermal-grating mechanism is the dominant DFWM mechanism. Thermal gratings were observed in liquids and solids for many years, but they were only identified in the gas phase recently at SNLL.

Thermal gratings arise when the energy absorbed by molecules in population-grating DFWM is collisionally converted to heat by quenching, resulting in a spatially modulated heat addition. The heat addition perturbs the gas density, which spatially modulates the refractive index of the gas. These index of refraction modulations can contribute to the DFWM signal. We developed a simple model for this process to predict the major temperature and pressure dependencies of thermal gratings. Adding more physics to the model, we were able to predict the time evolution of thermal grating, which can have a ringing structure.

Fig. 21 shows a typical measurement of this thermal-grating time evolution. The grating was written into the NO/CO_2 gas mixture by two crossed beams from a 226-nm laser tuned to the resonance of the $O_{12}(2)$ transition of nitric oxide. We read out this grating with an independent pulsed laser (the "backward-pump" beam), with a variable delay. Rapid

33

collisional quenching caused strong modulations in the thermal grating signal, as shown in the figure. Our one-dimensional hydrodynamics model accurately agrees with the measured data. The frequency of the ringing structure is dependent only upon known experimental parameters and the speed of sound in the gas. By measuring this frequency, we are able to measure the speed of sound, and can estimate the temperature. This technique could be used to measure temperature in certain environments where LIF is not applicable. In particular, this technique is likely to be especially useful under high-density conditions where strong thermal-grating DFWM signals are expected; and these signal intensities are essentially independent of the total pressure.
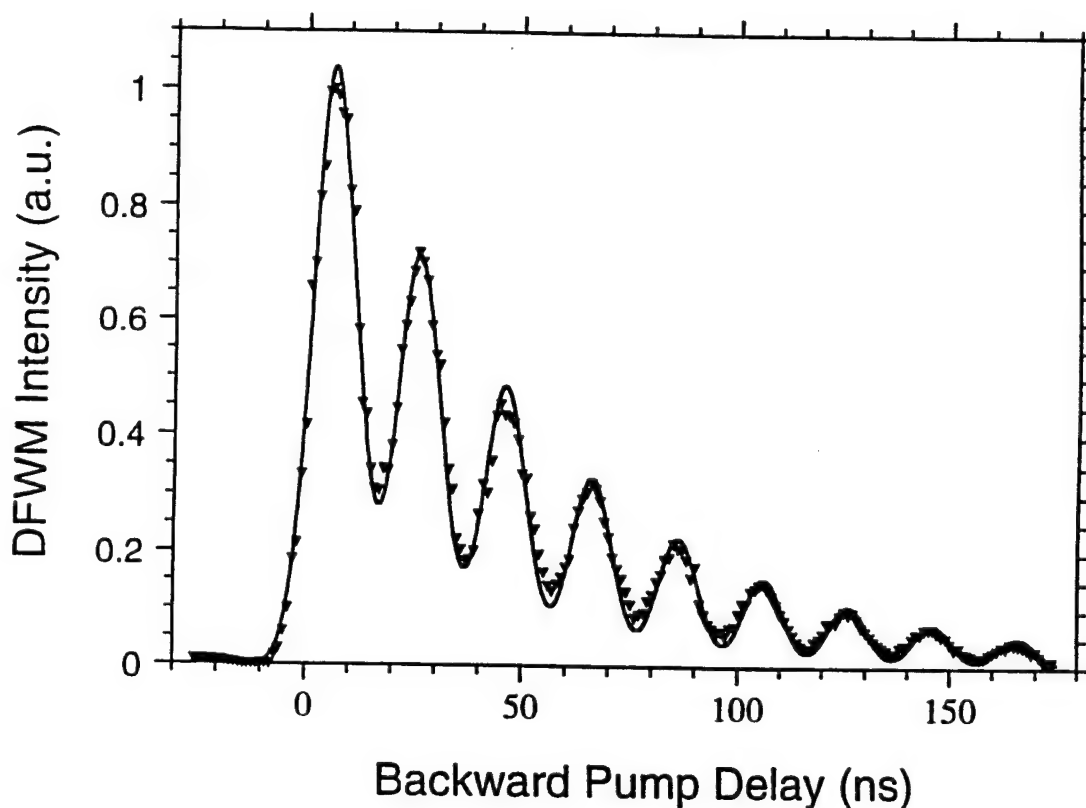
Fig. 21: **Experimental and theoretical temporal evolution of thermal gratings by excitation of nitric oxide. The gas mixture consisted of ~50 mTorr of NO in 1000 Torr of CO_2 at 295 K. The observed 20 ns oscillation period is consistent with the known grating fringe spacing, 5.4 μm, and calculated speed of sound of the gas mixture, 268 m/s.**

Another diagnostic we have developed in the past year is a velocimetry technique based on nearly-degenerate four-wave mixing (NDFWM) (paper 60 in Sec. 3.1). Again in collaboration with researchers at SNLL, we sought to develop a velocimetry technique with a collimated, coherent signal beam allowing spatially-resolved velocity measurements in

luminous environments and remote-sensing applications where optics and detectors cannot be placed near the experiment.

The technique has a simple interpretation: Two laser beams (known as the forward-pump and the probe beams) of nearly the same frequency cross in an absorbing medium forming interference fringes. Since the frequencies of the two beams are different, the fringes move with a velocity proportional to the spectral detuning of the beams. When the fringes move with the same speed as the flow, they write a population grating into the media. A third laser beam incident on this perturbation is partially diffracted, generating the signal beam. By scanning the frequency of the probe beam only, the fringes move at different velocities. When the velocity of the fringes equals the velocity of the flow, a signal maximum is observed.

We have experimentally demonstrated the technique in a simple, well-understood flow: a free jet expanding into a vacuum. Velocity measurements were performed using NDFWM and LIF at the same conditions and then compared to simple theoretical predictions. We used two independently-tunable, pulsed, single-longitudinal-mode, 226-nm lasers to probe the $R_1(0)$ line of nitric oxide. The probed volume was located 15 mm downstream from a 1-mm diameter pulsed nozzle.

The probe beam was scanned near the spectral resonance, causing the fringe pattern to move at varying velocities and leading to a two-peaked structure as indicated in Fig. 22. The left peak for LIF corresponds to the Doppler shift of the NO in the jet relative to the 18 degree probe-beam / jet crossing angle. The right peak corresponds to LIF observed from excitation by retro-reflecting the probe beam through the same observation volume. The NDFWM spectral peaks shown also correspond to the same Doppler shifts. Alternatively, they can be thought of as the frequencies which cause the fringes to move at the flow velocity. The left hand NDFWM peak was generated by the fringes described above convecting with the flow. The right hand peak was generated by retro-reflecting both the probe and forward-pump beams to generate a second moving grating. This second set of fringes moves the opposite direction of the first for a given probe tuning. By scanning the probe to the other side of the resonance, we observe a second peak. Thus, the technique is self-referencing. Analysis of these spectra showed better than 3% agreement between the theoretical and measured velocities for both techniques.

Currently, we are attempting to use diode lasers to make DFWM measurements of atomic species in a plasma. One of the goals of this experiment, which is being performed in the HTGL at Stanford University, is to make useful DFWM measurements with inexpensive and easy-to-use diode lasers. DFWM with atomic species in plasmas can potentially be used

to measure properties such as kinetic temperature and electron number density from the width and shape of the DFWM spectral feature.
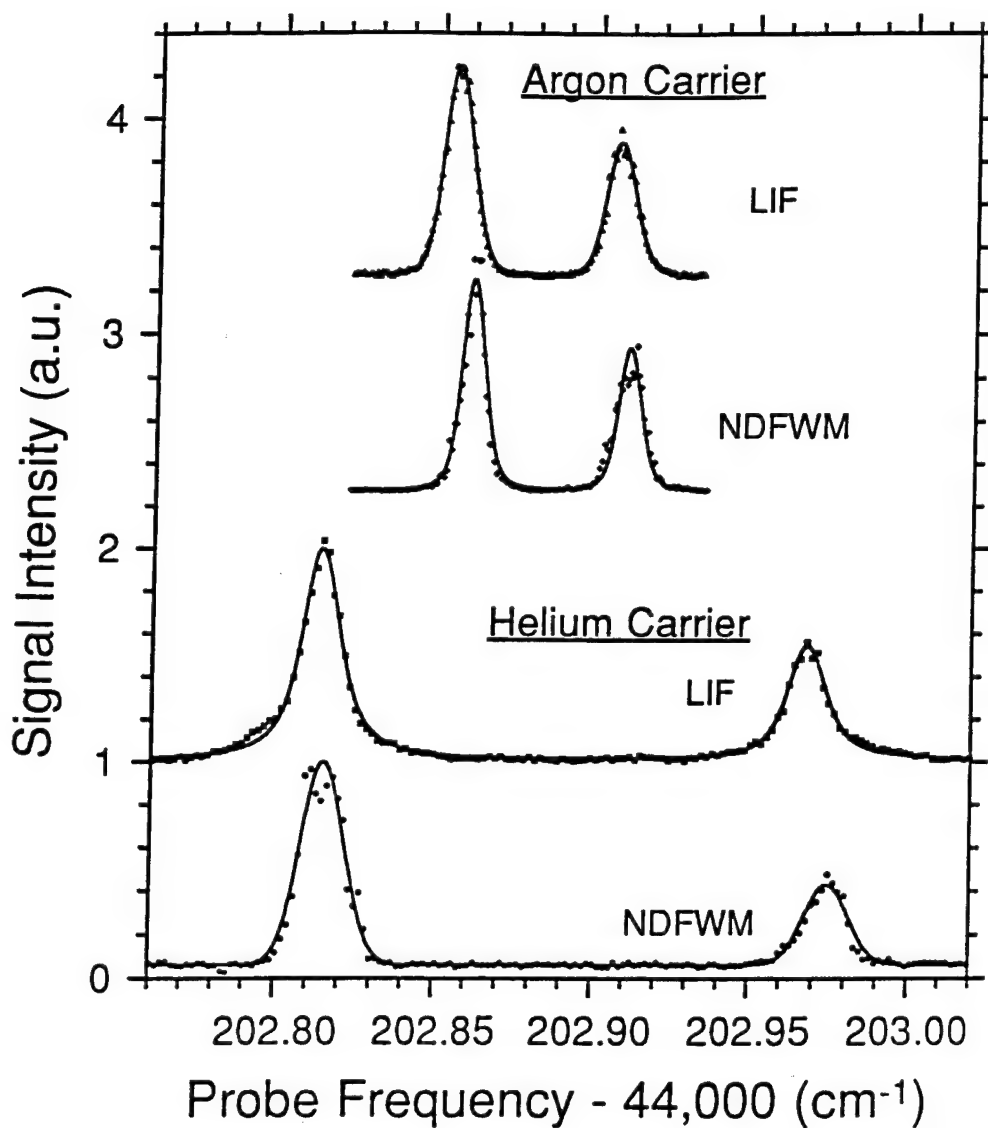
Fig. 22: **LIF and NDFWM velocity measurements in a free jet. Gas mixtures of 1% NO in carrier gases of argon and helium were used to generate different flow velocities and spectral shifts. The upper three scans are offset from the origin for clarity.**

2.9 Diagnostics for High-Pressure Systems

During the final year of this program we initiated a new research effort aimed at exploring fundamental aspects of laser-based diagnostics for high-pressure combustion systems. This work is motivated by the emerging need for nonintrusive diagnostic methods suitable for probing the advanced combustion and propulsion systems which will operate at increased pressure levels. Systems of interest include aircraft engines, the ram accelerator, chemical rockets, fuel handling systems of future aircraft (which will involve combinations of high pressure and temperature), and certain solid propellant systems. Until recently, nearly all work with laser-based diagnostics has been done at pressures near atmospheric, with the notable exception of measurements in IC engines which may involve pressure levels of 30-50 atm. Research to establish quantitative laser diagnostic methods for application in systems at higher pressures is clearly needed and timely.

Our plan has been to utilize a shock tube as a device for generating a wide range of accurately known pressures and temperatures. This is an attractive approach owing both to our long experience with shock tubes and to the fact that ONR has funded a new high-pressure shock tube in our laboratory which will be used for studies of gas-phase kinetics relevant to combustion of energetic materials. We plan to use this same facility for our AFOSR-sponsored diagnostics research. Fabrication and installation of the shock tube were completed during this past year, and testing of the system is now in progress. This facility is unique in the United States and will allow fundamental investigations of spectroscopy and diagnostic concepts over a wide range of pressure and temperature. A plot of projected test conditions accessible in reflected shock waves is given in Fig. 23. Note that pressures of up to 1000 atm are achievable at combustion temperatures.

Although there are several diagnostic methods we wish to study, including spontaneous Raman, laser-induced fluorescence, degenerate four-wave mixing (and related wave-mixing concepts), and line-of-sight absorption, we have focused our analytical work thus far on the simplest problem, namely the influence of pressure on absorption lineshapes and positions. This is a critical issue, since laser absorption is our most quantitative tool, and it will be essential to use this measurement method as we push the shock tube into an operating regime where ideal gas theories will no longer apply without corrections, e.g. for dense gas effects.

An example of calculations conducted thus far for the influence of pressure on spectral line (or peak) shifts at a temperature of 2000K is shown in Fig. 24. Two models have been utilized: a conventional line-shift model based on binary collisions which is
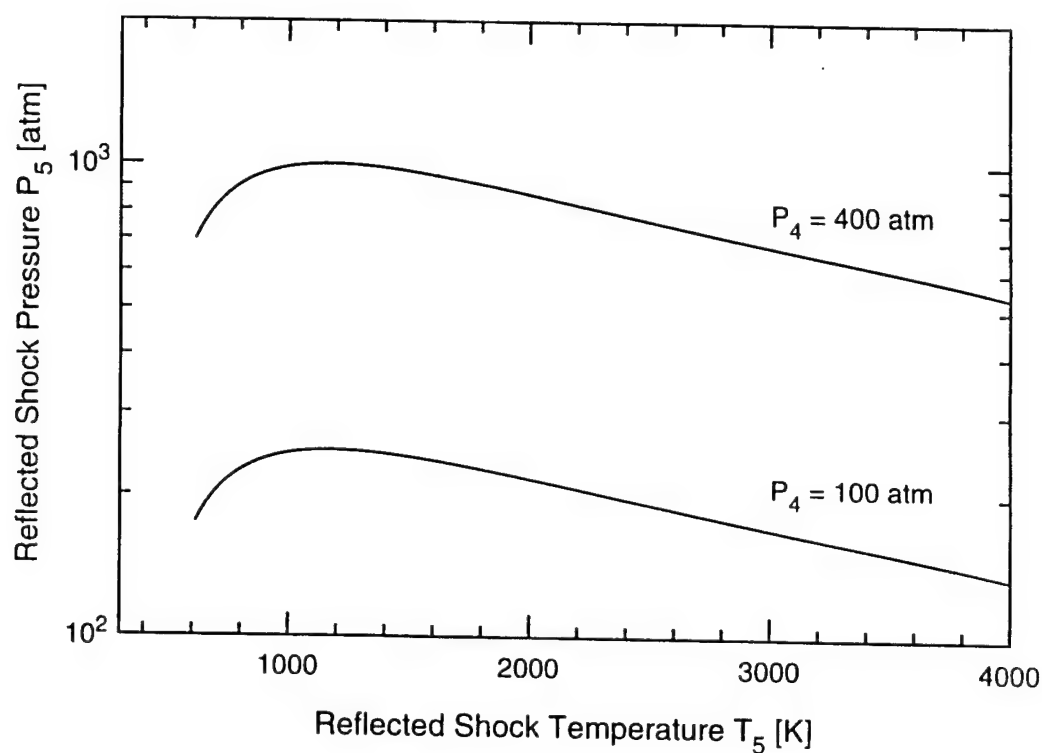
37

Fig. 23. Reflected shock wave properties in argon for two driver gas (helium) pressures.
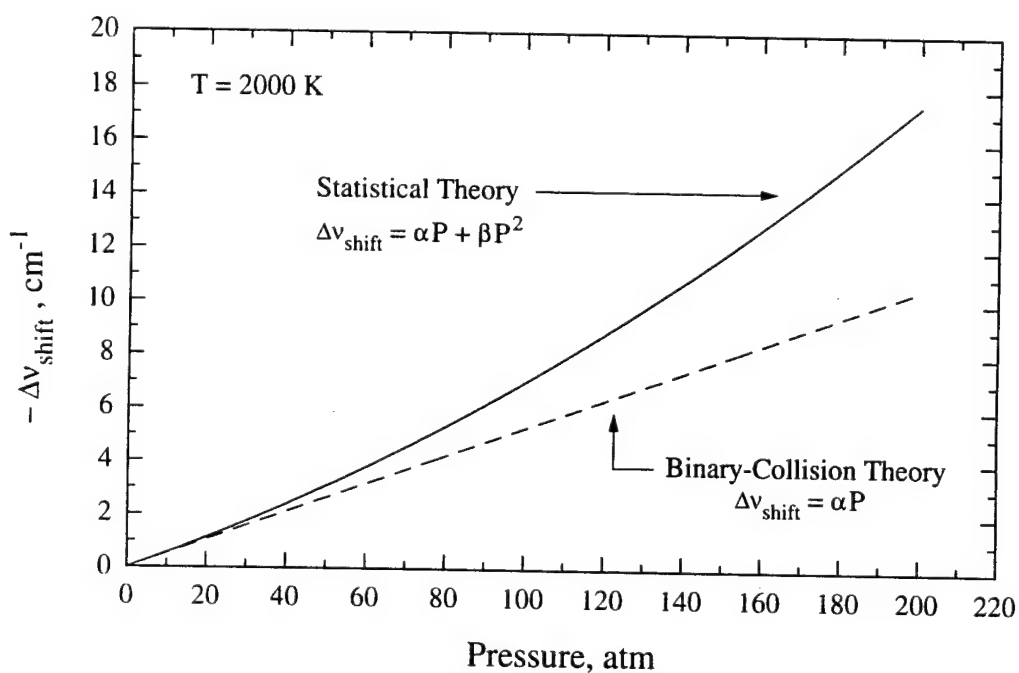

Fig. 24 Peak-shifts of NO A←X(0,0) absorption lines predicted by binary-collision and statistical theories.

38

commonly applied at atmospheric pressures; and a statistical theory, appropriate for "high pressures," which incorporates the effects of continuous perturbation of molecular energy levels. The results shown are for nitric oxide (NO), a species of particular interest owing to its importance as a combustion-generated pollutant. (We have drawn on recent work by Vyrodov et al. at the DLR in Stuttgart for elements of the curves in Fig. 24.) Although these calculations are preliminary and have not yet been validated, they reveal dramatic differences in the prediction of this spectral parameter at pressures as low as 50 atm; and results for collisionally broadened linewidths show similar characteristics. (These differences occur at even lower pressures when the temperature is decreased.) Since quantitative application of most laser diagnostic methods depends directly on the availability of accurate spectral absorption models, and these models rely in turn on knowledge of parameters such as line-broadening and -shift coefficients, it is clear that research will be needed to measure these parameters and to map out the range of applicability of candidate theoretical models. The availability of the new shock tube will allow the first detailed study of these and other spectroscopic issues as well as investigation of promising new diagnostic concepts.

3.0 PRESENTATIONS AND PUBLICATIONS

3.1 Presentations and Technical Reports (10/90 - 10/94)

1. M. P. Lee, B. K. McMillin, J. L. Palmer and R. K. Hanson, "Two-Dimensional Imaging of Combustion Phenomena in a Shock Tube using Planar Laser-Induced Fluorescence," paper AIAA-91-0460 at AIAA 29th Aerospace Sciences Meeting, Reno, NV, Jan. 1991.

2. P. H. Paul, U. Meier, J. M. Seitzman and R. K. Hanson, "Single-Shot Multiple-Camera Planar Laser-Induced Fluorescence Imaging in Gaseous Flows," paper AIAA-91-0459 at AIAA 29th Aerospace Sciences Meeting, Reno, NV, Jan. 1991.

3. M. D. DiRosa, A. Y. Chang, D. F. Davidson and R. K. Hanson, "CW Dye Laser Techniques for Simultaneous Measurements of Temperature, Pressure, and Velocity in High-Speed Flows using NO and O_2," paper AIAA-91-0359 at AIAA 29th Aerospace Sciences Meeting, Reno, NV, Jan. 1991.

4. J. M. Seitzman, P. H. Paul, B. Patrie and R. K. Hanson, "Instantaneous 3-D and Temporal Evolution Measurements by Rapid Acquisition of Planar Images," paper AIAA 91-0178 at AIAA 29th Aerospace Sciences Meeting, Reno, NV, Jan. 1991.

5. L. C. Philippe and R. K. Hanson, "Tunable Diode Laser Absorption Sensor for Temperature and Velocity Measurements of O_2 in Air Flows," paper AIAA-91-0360 at AIAA 29th Aerospace Sciences Meeting, Reno, NV, Jan. 1991.

6. J. M. Seitzman and R. K. Hanson, "Recent Developments in Laser Diagnostics at Stanford's High Temperature Gasdynamics Lab," invited presentation at ICALEO '90, Boston, Nov. 1990; published in Symposium Proceedings.

7. D. F. Davidson, A. J. Dean, M. D. DiRosa and R. K. Hanson, "Shock Tube Measurements of the Reactions of CN with O and O_2," paper 90-13 at Fall WSS/CI Meeting, La Jolla, CA, October 15-16, 1990.

8. B. K. McMillin, M. P. Lee, J. L. Palmer and R. K. Hanson, "Two-Dimensional Temperature Measurements of Nonequilibrium Supersonic Flows Using Planar Laser-Induced Fluorescence of Nitric Oxide," paper AIAA-91-1670 at AIAA 22nd Fluid Dynamics, Plasma Dynamics and Lasers Conference, Honolulu, Hawaii, June 24-26, 1991.

9. J. L. Palmer, B. K. McMillin and R. K. Hanson, "Planar Laser-Induced Fluorescence Imaging of Underexpanded Free Jet Flow in a Shock Tunnel Facility," paper AIAA-91-1687 at AIAA 22nd Fluid Dynamics, Plasma Dynamics and Lasers Conference, Honolulu, Hawaii, June 24-26, 1991.

10. D. S. Baer, L. Philippe and R. K. Hanson, "Tunable Diode Laser Diagnostics for Atmospheric Pressure Plasmas," paper AIAA-91-1495 at AIAA 22nd Fluid Dynamics, Plasma Dynamics and Lasers Conference, Honolulu, Hawaii, June 24-26, 1991.

11. J. G. Liebeskind, R. K. Hanson and M. A. Cappelli, "Velocity Measurement of a Hydrogen Arcjet Using LIF," paper AIAA-91-2112 at AIAA/SAE/ASME/ASEE 27th Joint Propulsion Conf., Sacramento, CA, July 1991.

12. A. Lozano, I. van Cruyningen, P. Danehy and R. K. Hanson, "Medidas De Concentraciones en un Jet Turbulento Mediante Fluorescencia Planar Inducida Por Laser," presented at 9th Congreso Nacional de Ingeniera Mecanica, 17-19 Dec. 1990, Zaragosa, Spain; published in Congress Proceedings.

13. D. F. Davidson, A. Y. Chang, M. D. DiRosa and R. K. Hanson, "Development of a cw Laser Absorption Diagnostics for CH_3," paper WSS/CI 91-20 at WSS/CI Spring Meeting, Boulder, CO, March 18-19, 1991.

14. N. Clemens, P. H. Paul, M. G. Mungal and R. K. Hanson, "Scalar Mixing in the Supersonic Mixing Layer," paper AIAA-91-1720, 22nd Fluid Dynamics, Plasma Dynamics and Lasers Conference, Honolulu, June 24-27, 1991.

15. D. S. Baer, H. J. Chang and R. K. Hanson, "Fluorescence Diagnostics for Atmospheric Pressure Plasmas Using Semiconductor Lasers," paper AIAA 92-0679, AIAA 30th Aerospace Sciences Meeting, Reno, Jan. 1992.

16. D. S. Baer, H. A. Chang and R.K. Hanson, "Semiconductor Laser-Based Measurements of Quench Rates in an Atmospheric Pressure Plasma using Saturated-Fluorescence Spectroscopy, paper AIAA-92-2961 at 20th AIAA/SAE/ASME/ASAE Joint Propulsion Conference, Nashville, July 6-8, 1992.

17. L. C. Philippe and R. K. Hanson, "Sensitive Diode Laser Absorption Technique for Aerodynamic Measurements," paper AIAA 92-0139, AIAA 30th Aerospace Sciences Meeting, Reno, Jan. 1992.

18. M. D. DiRosa and R. K. Hanson, "CW Dye Laser Technique for Simultaneous, Spatially-Resolved Measurements of Temperature, Pressure and Velocity of NO in an Underexpanded Jet," paper AIAA 92-0006, AIAA 30th Aerospace Sciences Meeting, Reno, Jan. 1992.

19. M. P. Arroyo and R. K. Hanson, "Tunable Diode Laser Absorption Technique for Detection of Water Vapor in Aerodynamic Flows," paper AIAA 92-0510, AIAA 30th Aerospace Sciences Meeting, Reno, Jan. 1992.

20. B. J. Patrie, J. M. Seitzman and R. K. Hanson, "Planar Imaging at High Framing Rates: System Characterization and Measurements," paper AIAA 92-0584, AIAA 30th Aerospace Sciences Meeting, Reno, Jan. 1992.

21. James D. Trolinger, Cecil F. Hess, Brandon Yip, Brett Battles and Ronald K. Hanson, "Hydroxyl Density Measurements in a Flame with Resonant Holographic Interferometry," paper AIAA 92-0582, AIAA 30th Aerospace Sciences Meeting, Reno, Jan. 1992.

22. J. L. Palmer, B. K. McMillin and R. K. Hanson, "Planar Laser-Induced Fluorescence Measurements of High-Enthalpy Free Jet Flow with Nitric Oxide," NASA Conference Publication 3161, pp. 375-386 (1992); presented at 1992 NASA Measurement Technology Conf., NASA Langley Res. Ctr., April 22-23, 1992.

23. J. M. Seitzman and R. K. Hanson, "Quantitative Fluorescence Imaging: A Comparison of Linear, Predissociative and Saturated Pumping Techniques," paper AIAA-92-0879 at 30th Aerospace Sciences Meeting, Reno, Jan. 6-9, 1992.

24. J. L. Palmer, B. K. McMillin and R. K. Hanson, "Planar Laser-Induced Fluorescence Imaging of Velocity and Temperature in Shock Tunnel Flows," paper AIAA 92-0762, AIAA 30th Aerospace Sciences Meeting, Reno, Jan. 1992.

25. R. K. Hanson, "Laser-Photolysis Shock Tube Studies of Radical Reactions," invited paper at ACS Nat. Meeting, Symp. on Physical Chemistry in Atmospheric Science and Combustion, San Francisco, April 5-12, 1992.

26. M. D. DiRosa, L. C. Philippe, P. Arroyo and R. K. Hanson, "CW Laser Strategies for Simultaneous Multi-Parameter Measurements in High-Speed Flows," paper AIAA-92-3955 at 17th Aerospace Ground Testing Conference, Nashville, July 6-8, 1992.

27. B. K. McMillin, J. L. Palmer and R. K. Hanson, "Instantaneous 2-D Temperature Measurements of a Tranverse Jet in a Shock-Heated Supersonic Crossflow," paper AIAA-92-3347 at 20th AIAA/SAE/ASME/ASAE Joint Propulsion Conference, Nashville, July 6-8, 1992.

28. M. P. Arroyo and R. K. Hanson, "Tunable Diode Laser Absorption Technique for Multi-Parameter Measurements of Combustion Flows," 6th Int. Symp. on Applications of Laser Techniques to Fluid Mechanics, Lisbon, Portugal, July 1992.

29. B. J. Patrie, J. M. Seitzman and R. K. Hanson, "Planar Imaging for 3-D Flow Visualization," presented at 20th International Congress on High Speed Photography and Photonics, Victoria, B.C., Sept. 1992.

30. R. K. Hanson and L. C. Philippe, "Diode Laser Absorption Technique for Monitoring Mass Flux in High Speed Airflows," invited presentation at NASP Mid-Term Technology Review, Monterey, April 22, 1992; published in NASP Technology Proceedings.

31. L. C. Philippe and R. K. Hanson, "Tunable Diode Laser Sensor for Temperature and Velocity Measurements of Oxygen," paper at Optcon '91, Santa Clara, Nov. 1991

32. M. D. DiRosa and R. K. Hanson, "CW Laser Strategy of Probing NO at 220 nm for Flow Measurements," paper at Optcon '91, Santa Clara, Nov. 1991.

33. R. K. Hanson, "Laser Diagnostics for Combustion and Propulsion," presented at OE/LASE '93, Jan. 18, 1993.

34. S. H. Smith, A. Lozano, M. G. Mungal and R. K. Hanson, "Scalar Mixing in the Subsonic Jet in Crossflow," paper at AGARD 72nd Fluid Dynamics Meeting, April 19-23, 1993, Winchester, United Kingdom.

35. B. K. McMillin, J. L. Palmer, A. L. Antonio and R. K. Hanson, "Comparison of Two SCRAMJET Model Flowfields Using Instantaneous Two-Line PLIF Temperature Imaging," presented as AIAA Paper 93-0044, 31st Aerospace Sciences Meeting, Reno, NV, January 11-14, 1993

36. R. K. Hanson, "Multi-Parameter and Multi-Point Measurements," invited presentation at Rank Prize Symposium on Laser Techniques for Combustion Diagnostics, Lake District, Great Britain, April 19-22, 1993

37. R. K. Hanson, "Quantitative LIF and PLIF Diagnostics," invited paper at Third Int. Symp. on Special Topics in Chemical Propulsion: Nonintrusive Diagnostics," Scheveningen, The Netherlands, May 10-13, 1993.

38. D. S. Baer, H. A. Chang and R. K. Hanson, "Semiconductor Laser Diagnostics of Atomic Oxygen in Atmospheric Pressure Plasmas," paper AIAA-93-0822, AIAA 31st Aerospace Sciences Meeting, Reno, Jan. 1993.

39. H. A. Chang, D. S. Baer and R. K. Hanson, "Semiconductor Laser Diagnostics of Atomic Oxygen for Hypersonic Flowfield Measurements," paper AIAA-93-0628, AIAA 31st Aerospace Sciences Meeting, Reno, Jan. 1993.

40. G. W. Butler, D. Q. King, J. G. Liebeskind, R. K. Hanson and M. A. Cappelli, "A Comparison of Arcjet Plume Properties to Model Predictions," paper AIAA-93-0820, AIAA 31st Aerospace Sciences Meeting, Reno, Jan. 1993.

41. B. J. Patrie, J. M. Seitzman and R. K. Hanson, "Planar Imaging at High Framing Rates: System Characterization and Measurements, Part II," paper AIAA-93-0364, AIAA 31st Aerospace Sciences Meeting, Reno, Jan. 1993.

42. J. L. Palmer, B. K. McMillin, and R. K. Hanson, "Planar Laser-Induced Fluorescence Temperature Measurements in Free Jet Flow with Vibrational Nonequilibrium," paper AIAA-93-0046, AIAA 31st Aerospace Sciences Meeting, Reno, Jan. 1993.

43. B. Yip, A. Lozano and R. K. Hanson, "Gas Phase Molecular Mixing Imaging Measurements Using the Acetone-Biacetyl System," paper AIAA-93-0221, AIAA 31st Aerospace Sciences Meeting, Reno, Jan. 1993.

44. B. K. McMillin, J. M. Seitzman and R. K. Hanson, "Comparison of NO and OH PLIF Temperature Measurements in a Scramjet Model Flowfield," paper AIAA-93-2035 at 29th AIAA/SAE/ASME/ASEE Joint Propulsion Conf., Monterey, CA, June 1993.

45. J. L. Palmer, M. Thurber, and R. K. Hanson, "Single-Shot Velocimetry Using Planar Laser-Induced Fluorescence Imaging of Nitric Oxide," paper AIAA-93-2020 at AIAA/SAE/ASME 29th Joint Propulsion Conf., Monterey, CA, June 1993.

46. J. M. Seitzman, J. L. Palmer, A. L. Antonio, R. K. Hanson, P. A. DeBarber and C. F. Hess, "Instantaneous Planar Thermometry of Shock-Heated Flows using PLIF of OH," paper AIAA-93-0802, AIAA 31st Aerospace Sciences Meeting, Reno, Jan. 1993.

47. H. A. Chang, D. S. Baer and R. K. Hanson, "Semiconductor Laser Diagnostics for Simultaneous Determination of Kinetic and Population Temperatures in High-Enthalpy Flows," 19th Int. Symp. on Shock Waves (ISSW 19), Marseille, July 26-30, 1993.

48. R. K. Hanson, "The Role of Lasers in Shock Tube Studies of Chemical Kinetics," 19th Int. Symp. on Shock Waves (ISSW 19), Marseille, July 26-30, 1993.

49. B. K. McMillin, J. M. Seitzman, J. L. Palmer and R. K. Hanson, "Dual-Laser PLIF Imaging Techniques for Shock Tube Studies of Mixing and Combustion," 19th Int. Symp. on Shock Waves (ISSW 19), Marseille, July 26-30, 1993.

50. A. Lozano, B. Yip and R. K. Hanson, "Simultaneous OH and Acetone Fluorescence Imaging in Diffusion Flames," presented at Joint Meeting of Italian and Spanish Sections of the Combustion Instituto, Stresa, Italy, July 1, 1993.

51. R. K. Hanson, D. S. Baer, B. J. McMillin and P. Arroyo, "Multi-Parameter and Multi-Point Measurements," invited paper at Symposium on Laser Diagnostics for Industrial Processes, Heidelberg, June 28, 1993; Ber. Bunsenges. Phys. Chem. **97**, 1548-1555 (1993).

52. J. M. Seitzman, M. F. Miller, R. K. Hanson, P. DeBarber and C. Hess, "Multiple-Scalar Planar Fluorescence Imaging for Reacting Flows, paper AIAA-94-0228 at 32nd AIAA Aerospace Sciences Meeting, Reno, Jan. 10-13, 1994.

53. H. A. Chang, D. S. Baer and R. K. Hanson, "Semiconductor Diode Laser Absorption Diagnostics of Atomic Nitrogen for Hypersonic Flowfield Measurements," paper AIAA-94-0385 at 32nd AIAA Aerospace Sciences Meeting, Reno, Jan. 10-13, 1994.

54. J. Palmer and R. K. Hanson, "PLIF Measurements of Temperature and Velocity in a Reacting Supersonic Free Jet with OH, paper AIAA-94-0168 at 32nd AIAA Aerospace Sciences Meeting, Reno, Jan. 10-13, 1994.

55. R. J. Cedolin, R. K. Hanson and M. A. Cappelli, "Semiconductor Laser Diagnostics for Xenon Plasmas," paper AIAA-94-2739 at 30th AIAA/ASME/SAE/ASEE Joint Propulsion Conference, Indianapolis, IN, June 27-29, 1994.

56. D. S. Baer, R. K. Hanson, M. E. Newfield and N. K. J. M. Gopaul, "Multi-Species Diode-Laser Sensor System for H_2O and O_2 Measurements," paper AIAA-94-2643 at AIAA 18th Ground Test Conference, Colorado Springs, CO, June 20-23, 1994.

57. R. L. Farrow, P. M. Danehy, P. H. Paul and E. J. Friedman-Hill, Degenerate Four-Wave Mixing For Quantitative Diagnostic Measurements, *Laser Applications to Chemical Analysis*, Jackson Hole, WY, Optical Society of America, Washington, DC, April, 1994.

58. P. M. Danehy, E. J. Friedman-Hill and R. L. Farrow, Population and Thermal Grating Contributions to Degenerate Four-Wave Mixing Line Shapes, *Laser Applications to Chemical Analysis*, Jackson Hole, WY, Optical Society of America, Washington, DC, April, 1994.

59. P. M. Danehy, P. H. Paul and R. L. Farrow, Temporal Evolution of Thermal Gratings in DFWM, *Conference on Lasers and Electro-Optics*, Anaheim, CA, Optical Society of America, Washington, DC, May, 1994.

60. P. M. Danehy and R. L. Farrow, Gas-Phase Velocimetry by Nearly Degenerate Four-Wave Mixing, *AIAA - 33rd Aerospace Sciences Meeting and Exhibit*, Reno, NV, American Institute of Aeronautics and Astronautics, Washington, DC, (to be presented), Jan. 1995.

3.2 Refereed Publications (10/90 - 10/94)

1. B. Hiller and R. K. Hanson, "Properties of the Iodine Molecule Relevant to Absorption/Fluorescence Experiments in Gas Flows," Experiments in Fluids **10**, 1-11 (1990).

2. A. J. Dean, D. F. Davidson and R. K. Hanson, "A Shock Tube Study of Reactions of C-atoms with H_2 and O_2 using Excimer Photolysis of C_3O_2 and C-Atom ARAS," J. Phys. Chemistry **95**, 183-191 (1991).

3. I. van Cruyningen, A. Lozano, M. G. Mungal, and R. K. Hanson, "3D Visualization of Temporal Flow Sequences," AIAA J. **29**, 479-482 (1991).

4. A. J. Dean and R. K. Hanson, "CH and C-Atom Time Histories in Dilute Hydrocarbon Pyrolysis: Measurements and Kinetics Calculations," Int. J. Chem. Kinetics **24**, 517-532 (1992).

5. I van Cruyningen, A. Lozano and R. K. Hanson, "Quantitative Imaging of Concentration by Planar Laser-Induced Fluorescence," Experiments in Fluids **10**, 41-49 (1990).

6. A. J. Dean, R. K. Hanson and C. T. Bowman, "A Shock Tube Study of Reactions of C-atoms and CH with NO including Product Channel Measurements," J. Phys. Chem. **95**, 3180-3189 (1991).

7. D. F. Davidson, A. J. Dean, M. D. DiRosa and R. K. Hanson, "Shock Tube Measurements of the Reactions of CN with O and O_2," Int. J. of Chem. Kinetics **23**, 1035-1050 (1991).

8. D. F. Davidson, A. Y. Chang, M. D. DiRosa and R. K. Hanson, "Continuous Wave Laser Absorption Techniques for Gasdynamic Measurements in Supersonic Flows," Applied Optics **30**, 2598-2608 (1991).

9. A. Y. Chang, M. D. DiRosa, D. F. Davidson and R. K. Hanson, "Rapid-Tuning CW Laser Technique for Measurements of Gas Velocity, Temperature, Pressure, Density and Mass Flux Using NO," Applied Optics **30**, 3011-3022 (1991).

10. J. D. Mertens, K. Kohse-Höinghaus, R. K. Hanson and C. T. Bowman, "A Shock Tube Study of H + HNCO $\rightarrow$ NH_2 + CO," Int. J. of Chem. Kinet. **23**, 655-668 (1991).

11. D. L. Hofeldt and R. K. Hanson, "Instantaneous Imaging of Particle Size and Spatial Distribution in Two-Phase Flows," Applied Optics **30**, 4936-4948 (1992).

12. J. D. Mertens, A. Y. Chang, D. A. Masten, R. K. Hanson and C. T. Bowman, "A Shock Tube Study of the Reactions of NH with NO, O and O_2," Int. J. of Chemical Kinetics **23**, 173-196 (1991).

13. M. P. Lee, B. K. McMillin, J. L. Palmer and R. K. Hanson, "Two-Dimensional Imaging of a Transverse Jet in Supersonic Crossflow," J. Prop. and Power **8**, 729-735 (1992).

14. A. J. Dean, R. K. Hanson and C. T. Bowman, "High Temperature Shock Tube Study of Reactions of CH and C-Atoms with N_2," *Twenty-Third Symposium (International) on Combustion*, The Combustion Institute, 259-265 (1990).

15. B. K. McMillin, M. P. Lee, P. H. Paul and R. K. Hanson, "Planar Laser-Induced Fluorescence Imaging of Shock-Induced Ignition," *Twenty-Third Symposium (International) on Combustion*, The Combustion Institute, 1909-1913 (1990).

16. D. F. Davidson and R. K. Hanson, "Shock Tube Measurements of the Rate Coefficient for N + CH$_3$ → H$_2$CN + H using N-Atom ARAS and Excimer Photolysis of NO," *Twenty-Third Symposium (International) on Combustion*, The Combustion Institute, 267-273 (1990).

17. J. M. Seitzman, A. Ungut, P. H. Paul and R. K. Hanson, "Imaging and Characterization of OH Structures in a Turbulent Nonpremixed Flame," *Twenty-Third Symposium (International) on Combustion*, The Combustion Institute, 637-644 (1990).

18. J. M. Seitzman and R. K. Hanson, "Planar Fluorescence Imaging: Basic Concepts for Scalar and Velocity Measurements," chapter 14 in *Combusting-Flow Diagnostics*, eds. D. Durao, M. Heitor, J. Whitelaw and P. Witze, Kluwer Academic Publishers, NATO/ASI Series E, 1991.

19. D. S. Baer and R. K. Hanson, "Tunable Diode Laser Absorption Diagnostics for Atmospheric Pressure Plasmas," Jour. of Quant. Spectrosc. and Radiative Transfer **47**, 455-475 (1992).

20. L. C. Cohen and R. K. Hanson, "Emission and Laser-Induced Fluorescence Measurements in a Supersonic Jet of Plasma-Heated Nitrogen," J. Phys. D: Applied Phys. **25**, 339-351 (1992).

21. B. Yip, P. M. Danehy and R. K. Hanson, "Degenerate Four-Wave Mixing Temperature Measurements in a Flame," Optics Letters **17**, 751-753 (1992).

22. L. C. Philippe and R. K. Hanson, "Laser-Absorption Mass Flux Sensor for High-Speed Air Flows," Opt. Letters **16**, 2002-2004 (1992).

23. D. S. Baer and R. K. Hanson, "Semiconductor Laser-Based Measurements of Quench Rates in an Atmospheric Pressure Plasma Using Saturated-Fluorescence Spectroscopy," Applied Optics **32**, 948-955 (1993).

24. D. S. Baer, H. J. Chang and R. K. Hanson, "Fluorescence Diagnostics for Atmospheric Pressure Plasmas Using Semiconductor Lasers," J. Opt. Soc. Am. B, Vol. 9, 1968-1978 (1992).

25. A. Lozano, B. Yip and R. K. Hanson, "Acetone: A Tracer for Concentration Measurements in Gaseous Flows by Planar Laser-Induced Fluorescence," Experiments in Fluids **13**, 369-376 (1992).

26. J. M. Seitzman and R. K. Hanson, "Comparison of Excitation Techniques for Quantitative Fluorescence Imaging of Reacting Flows," AIAA J. **31**, 513-519 (1993).

27. M. D. DiRosa, A. Y. Chang and R. K. Hanson, "CW Dye Laser Technique for Simultaneous, Spatially-Resolved Measurements of Temperature, Pressure and Velocity of NO in an Underexpanded Free Jet," Applied Optics **32**, 4074-4087 (1993).

28. M. P. Lee, B. K. McMillin and R. K. Hanson, "Temperature Measurements in Gases Using Planar Laser-Induced Fluorescence Imaging of NO," App. Optics **32**, 5379-5396 (1993).

29. M. P. Arroyo and R. K. Hanson, "Absorption Measurements of Water Vapor Concentration, Temperature and Lineshape Parameters Using a Tunable InGaAsP Diode Laser," Applied Optics **32**, 6104-6116 (1993).

30. B. K. McMillin, J. M. Seitzman and R. K. Hanson, "Comparison of NO and OH PLIF Temperature Measurements in a Scramjet Model Flowfield," AIAA J. **32**, 1945-1952 (1994).

31. J. M. Seitzman and R. K. Hanson, "Planar Fluorescence Imaging in Gases," Chapter 6, (pp. 405-466) in <u>Experimental Methods for Flows with Combustion</u>, ed. A. Taylor, Academic Press, London, 1993.

32. P. M. Danehyt, E. J. Friedman-Hill, R. P. Lucht and R. L. Farrow, "Effects of Collisional Quenching on Degenerate Four-Wave Mixing," App. Phys. **57**, 243-248 (1993).

33. J. M. Seitzman and R. K. Hanson, "Two-Line Planar Fluorescence for Temporally Resolved Temperature Imaging in Reacting Supersonic Flow over a Body," App. Phys. B **57**, 385-391 (1994).

34. B. K. McMillin, J. L. Palmer and R. K. Hanson, "Temporally Resolved, Two-Line Fluorescence Imaging of NO Temperature in a Transverse Jet in a Supersonic Cross Flow," Applied Optics 32, 7532-7545 (1993).

35. D. S. Baer, H. A. Chang and R. K. Hanson, "Semiconductor Laser Diagnostics of Atomic Oxygen in Atmospheric Pressure Plasmas," J. Quant. Spectrosc. Radiat. Transfer 50, 621-633 (1993).

36. M. P. Arroyo, S. Langlois, and R. K. Hanson, "Diode Laser Absorption Technique for Simultaneous Measurements of Multiple Gasdynamic Parameters in High-Speed Flows Containing Water Vapor," Applied Optics 33, 3296-3307 (1994).

37. B. J. Patrie, J. M. Seitzman and R. K. Hanson, "Instantaneous 3-D Flow Visualization by Rapid Acquisition of Multiple Planar Flow Images," Opt. Engineering 33, 975-980 (1994).

38. B. Yip, A. Lozano and R. K. Hanson, "Sensitized Phosphorescence: A Gas-Phase Molecular Mixing Diagnostic," Experiments in Fluids 17, 16-23 (1994).

39. S. Langlois, T. B. Birbeck and R. K. Hanson, "Diode Laser Measurements of H_2O Line Intensities and Self-Broadening Coefficients in the 1.4 mm Region," J. Molec. Spectroscopy 163, 27-42 (1994).

40. R. K. Hanson, D. S. Baer, B. J. McMillin and P. Arroyo, "Multi-Parameter and Multi-Point Measurements," Ber. Bunsenges. Phys. Chem. 97, 1548-1555 (1993).

41. M. P. Arroyo, T. P. Birbeck, D. S. Baer and R. K. Hanson, "Dual Diode-Laser Fiber-Optic Diagnostic for Water Vapor Measurements," Optics Letters 19, 1091-1093 (1994).

42. J. M. Seitzman, R. K. Hanson, P. A. DeBarber, and C. F. Hess, "Application of Quantitative Two-Line OH PLIF for Temporally Resolved Planar Thermometry in Reacting Flows," Applied Optics 33, 4000-4012 (1994).

43. L. C. Philippe and R. K. Hanson, "Laser Diode Wavelength-Modulation Spectroscopy for Simultaneous Measurement of Temperature, Pressure and Velocity in Shock-Heated Oxygen Flows," Applied Optics 32, 6090-6103 (1993).

44. A. Lozano, S. H. Smith, M. G. Mungal and R. K. Hanson, "Concentration Measurements in a Transverse Jet by Planar Laser-Induced Fluorescence of Acetone," AIAA J. 32, 218-221 (1994).

45. P. M. Danehy, P. H. Paul and R. L. Farrow, Thermal-Grating Contributions to Degenerate Four-Wave Mixing in Nitric Oxide, J. Opt. Soc. Am. B (submitted).

46. P. H. Paul, R. L. Farrow and P. M. Danehy, The Characteristics of Thermal Gratings Produced in a DFWM Scattering Geometry, J. Opt. Soc. Am. B (submitted).

47. B. J. Patrie, J. M. Seitzman and R. K. Hanson, "Modeling of Spatial Distortions in a High-Speed Image Converter Camera," Rev. of Sci. Inst. **64** (10), 2901-2904 (1993).

48. B. Yip, M. F. Miller, A. Lozano and R. K. Hanson, "A Combined OH/Acetone Planar Laser-Induced Fluorescence Imaging Technique for Visualizing Combustion Flows," Expts. In Fluids **17**, 330-336 (1994).

4.0 PERSONNEL

Individual researchers partially or fully supported by the program during one or more of the past 4 years are listed below. All the work has been carried out in the High Temperature Gasdynamic Laboratory, in the Department of Mechanical Engineering, under the supervision of Professor R. K. Hanson.

4.1 Postdoctoral Research Associates

Dr. D. Davidson (1990-94)   Dr. B. Yip (1990-93)

Dr. K. Klavuhn (1994 only)   Dr. P. Arroyo (1990-93)

Dr. J. Seitzman (1990-93)   Dr. S. Langlois (1991-92)

Dr. D. Baer (1990-94)

4.2 Graduate Research Assistants

Renato Cedolin   Mike Lee

Andrew Chang   Dave Hofeldt

Paul Danehy   Antonio Lozano

Ted Furlong   Brian McMillin

Venu Nagali   Doug Baer

Jennifer Palmer   Larry Cohen

Bryan Patrie   Jerry Seitzman

4.3 Ph.D. Degrees Awarded (1990-1994)

Dr. David Hofeldt, 11/90, "Instantaneous Imaging Diagnostics for Measuring Particle Sizes and Spatial Distributions over Extended Regions in Two-Phase Flows,"

Dr. Larry Cohen, 11/90, "Emission and Laser-Induced Fluorescence Diagnostics of a Supersonic Jet of Plasma-Heated Nitrogen,"

Dr. Jerry Seitzman, 6/91, "Quantitative Applications of Fluorescence Imaging in Combustion,"

Dr. Michael Lee, 11/91, "Temperature Measurements in Gases Using Planar Laser-Induced Fluorescence Imaging of NO and O_2,"

Dr. Antonio Lozano, 8/92, "Laser-Excited Luminescent Tracers for Planar Concentration Measurements in Gaseous Jets,"

Dr. Douglas Baer, 3/93, "Plasma Diagnostics with Semiconductor Lasers using Fluorescence and Absorption Spectroscopy,"

Dr. Brian McMillin, 5/93, "Instantaneous Two-Line PLIF Temperature Imaging of Nitric Oxide in Supersonic Mixing and Combustion Flowfields,"

Dr. Bryan Patrie, 4/94, "Instantaneous 3-D Flow Visualization by Rapid Acquisition of Multiple Planar Images."

5.0 SIGNIFICANT INTERACTIONS/TRANSITIONS

In addition to the interactions associated with the presentations and publications listed in Section 3, we have had numerous visitors to our laboratory during these past four years. Foreign visitors have come from Germany, France, Great Britain, Canada, Spain, Finland, Holland, Korea, South Africa, Belgium and Japan; industrial and national laboratory visitors have included representatives from Rocketdyne, Aerometrics, Physical Sciences, Inc., GASL, Boeing, Metrolaser, AEDC, AF Wright Labs, AF Philips Labs, NASA Ames, NASA Lewis, NASA Langley, Sandia, Lawrence Livermore, General Motors, Nissan, Hitachi, Kao Corporation and Toyota. Professor Hanson has given invited presentations on AFOSR-sponsored diagnostics research to several industrial laboratories, universities, and government groups in the U.S., Japan and Europe. Members of our group have provided technical information and advice, by telephone and mail, to several external researchers interested in duplicating or extending our diagnostics concepts.

Interest in the application of laser diagnostics techniques developed at Stanford to various practical problems continues at a high level, and several notable transitions have been accomplished. During the past four years, we have collaborated with researchers at NASA-Ames to implement three of our diagnostics schemes (ring dye laser absorption of OH, diode laser absorption of O_2, and diode laser absorption of H_2O) in their 16-inch shock tunnel test program on advanced scramjet combustors; and we have engaged in a series of collaborative projects with Metrolaser to apply and transfer Stanford's expertise with PLIF imaging. In addition, Metrolaser now markets a dual-camera PLIF system developed at Stanford. Another company, PSI, has hired three recent Ph.D. graduates of our High Temperature Gasdynamics Lab as part of their growing effort to develop and apply laser diagnostics, much of which is based on techniques pioneered at Stanford. The use of acetone as a flow tracer for PLIF imaging, a concept developed at Stanford, has quickly been adopted by at least 20 research groups in the U.S. and Europe, including researchers at AF Wright Labs.
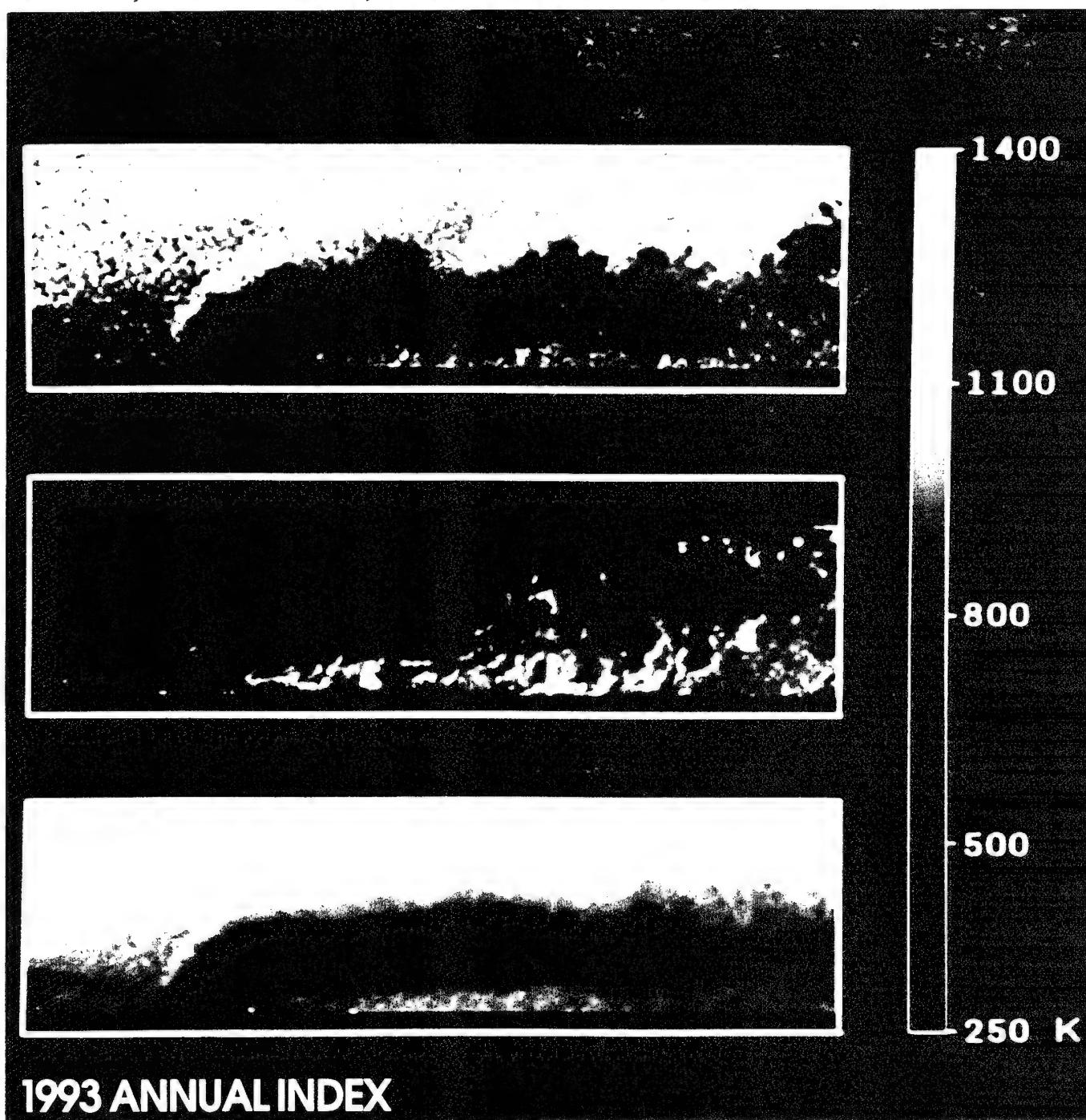
6.0 INVENTIONS

None.

7.0 COPIES OF KEY PUBLICATIONS

Reprints of most of our refereed papers have been submitted previously. Copies of our most recent papers, not submitted previously, are attached. These include papers 34 through 42 listed in Sec. 3.2.

Applied Optics

LASERS, PHOTONICS, AND ENVIRONMENTAL OPTICS

1400

1100

800

500

250 K

1993 ANNUAL INDEX

a reprint from Applied Optics

Temporally resolved, two-line fluorescence imaging of NO temperature in a transverse jet in a supersonic cross flow

Brian K. McMillin, Jennifer L. Palmer, and Ronald K. Hanson

Temporally resolved temperature imaging of a fuel jet in a hot, nonoxidizing supersonic cross flow is described. The temperature measurements are obtained with two lasers and two intensified cameras, with a two-line ratio of planar laser-induced fluorescence from nitric oxide, seeded either in the jet or in both the jet and the cross flow. Diagnostic issues related to the application of the two-line technique in high-speed combustion flows are addressed and include temperature sensitivity, transition selection, measurement resolution, fluorescence lifetime, temporal resolution, and intensifier and camera dynamic-range limitations. Single-shot and frame-averaged side-view temperature images of the flow field are presented, and the measurement uncertainties, which are dominated by photon statistical noise and pulse-to-pulse laser fluctuations, are discussed.

Key words: Planar laser-induced fluorescence, PLIF, temperature imaging, instantaneous temperature measurements, nitric oxide fluorescence, transverse jet in supersonic cross flow, SCRAMJET, jet mixing.

1. Introduction

The value of planar laser-induced fluorescence (PLIF) imaging as a diagnostic technique in fluid mechanics and combustion studies is now widely recognized.[1,2] While most of the previous PLIF applications have been used for flow visualization or for qualitative measurements, current PLIF research is directed toward making more quantitative measurements on both a time-averaged and a temporally resolved basis. Generally, time-averaged measurements are useful for validation of existing computational flow models, but there is a clear need for temporally resolved or instantaneous imaging measurements in realistic mixing and combustion flow fields. For example, temporally resolved measurements are needed to increase the understanding and to improve the modeling of turbulent mixing mechanisms in nonreacting flows and of the interaction between turbulence and combustion in reacting flows.

One of the most promising applications for quantitative, instantaneous PLIF measurements in combustion flows is temperature imaging. Temperature measurements are generally useful in combustion applications for examining fuel and air mixing, when the streams are at different temperatures; for monitoring the heat release and its influence on the fluid mechanics; for locating reaction zones and burned and unburned gases; and for studying the convective heat transfer to combustor walls. PLIF thermometry techniques are well established and have been demonstrated in a variety of flows by use of the hydroxyl radical (OH),[3–7] molecular oxygen,[8] iodine,[9,10] and nitric oxide (NO)[11–15] as the temperature tracer. However, instantaneous data and detailed two-dimensional measurements in complex mixing and combustion flows have been limited.

In this paper, we describe what is to our knowledge the first detailed example of *temporally resolved,* two-line NO temperature imaging in a complex, combustion-related flow field. The two-line strategy used here was originally devised by Cattolica[16] for OH temperature measurements, and it was later applied to NO for single-point measurements in a low-temperature, wind-tunnel boundary layer.[17] The measurements described here are based on the ratio of fluorescence signals obtained following sequential laser excitation of two rovibronic transitions originating from different rotational states in the $A\,^2\Sigma^+ \leftarrow X\,^2\Pi$ (0, 0) band of NO. Although rather equipment

intensive, the two laser–two camera technique employed here is particularly useful in flows that are compressible or that vary in composition, because in taking the ratio of fluorescence signals, the signal dependence on number density, absorbing-species mole fraction, and collisional quenching is removed. Thus, unlike previous NO temperature-imaging experiments,[11–15] the two laser–two camera technique is not limited to steady flows or to flows with a constant mole fraction of NO.

To illustrate the application of instantaneous temperature imaging, we discuss measurements obtained in a supersonic combustion ramjet (SCRAMJET) model flow field, i.e., a combustion system in which a cold hydrogen jet is injected into a hot supersonic cross flow. The flow field was generated in a shock tube by sonic injection of fuel (seeded with NO) through a pulsed valve, into the high-temperature supersonic cross flow generated by the passage of an incident shock wave. Although the flow examined is nonreacting, it is a challenging environment for instantaneous temperature measurements because of the wide variation in pressure, temperature, composition, and velocity throughout the flow. As a result, this study serves to demonstrate the feasibility of the technique in other practical combustion environments.

NO is an attractive probe species for this application, because it is present naturally in the free-stream region of many high-enthalpy air facilities and can be easily seeded into the hydrogen fuel jet. In reacting flows, the use of NO as a fuel tracer is also attractive because it provides the opportunity for making temperature measurements throughout the flow field, in contrast to measurements with combustion radicals such as OH that are feasible in the reaction zones or burned-gas regions. In reacting flows, however, the NO may sensitize ignition[18] and may be partially consumed by the combustion process; but, assuming the surviving NO is sufficient for fluorescence detection, accurate two-line temperature measurements are still possible because the NO-mole-fraction dependence cancels in the signal ratio.

NO is also an attractive tracer from a diagnostic standpoint for several reasons: First, it provides a relatively strong absorption cross section and good fluorescence efficiency, which is crucial for imaging applications. Second, it exhibits strong nonresonant fluorescence signals, which, when combined with spectral filtering, can alleviate potential problems with radiative trapping and laser scattering. Third, it does not exhibit J-dependent radiative lifetimes or quenching rates that can lead to systematic measurement errors. Finally, its spectroscopy is well characterized, which facilitates modeling and interpretation of the fluorescence signal. It should be noted, however, that although NO offers these advantages from a diagnostic standpoint, it is toxic, and this may limit its practical use in large-scale flow facilities.

In the following sections we discuss the application of instantaneous, two-line NO temperature imaging in a nonreacting hydrogen jet in supersonic cross flow. The two-line temperature-imaging strategy is briefly reviewed, and various diagnostic issues related to applying the technique in these flows are addressed, including temperature sensitivity, transition selection, measurement resolution, fluoresence lifetime, and signal dynamic-range limitations. The experimental setup and data-reduction procedure are then described, and temporally resolved and frame-averaged, sideview temperature images are presented. Finally, the relative temperature uncertainties are estimated, including those due to photon statistical noise and fluctuations in the laser mode structure.

2. Measurement Technique

A. Two-Line Temperature-Imaging Strategy

For weak (i.e., nonperturbing) pulsed laser excitation, the temporally integrated, broadband fluorescence signal, S_f, can be modeled by[2]

$$S_f = BEg(N, T)f_B(T)N_{abs}V\phi(\chi_i, N, T)\eta \frac{\Omega}{4\pi}, \quad (1)$$

where B is the Einstein coefficient for stimulated absorption; E is the laser pulse energy; $g(N, T)$ is the overlap integral between the absorption and laser line shapes; $f_B(T)$ is the Boltzmann population fraction of the absorbing state; N_{abs} is the absorbing-species number density; V is the measurement volume; $\phi(\chi_i, N, T)$ is the fluorescence yield, which depends on the species mole fractions χ_i, the spontaneous-emission (A) and collisional quenching-rate coefficients (Q), and is given by $\phi = A/[A + Q(\chi_i, N, T)]$; η is the optical-collection efficiency; and $\Omega/4\pi$ is the optical-collection solid angle. As indicated in Eq. (1), laser-induced fluorescence is a complicated function of the chemical composition, number density, absorption linewidth, Boltzmann fraction of the absorbing state, and the local collisional transfer rates. However, several strategies including both one- and two-wavelength techniques have been developed to isolate the temperature dependence of the signal in various situations.[19]

For imaging measurements, the two-wavelength technique is usually the most versatile approach, and it can be applied in a wide range of applications, including flows that are compressible and that vary in composition. The essence of the two-line technique is to use the fluorescence ratio, obtained by sequentially exciting two different initial states, to isolate the temperature dependence of the absorbing-state populations. By taking the ratio of fluorescence signals, the dependencies on the number density, absorbing-species mole fraction, overlap integral, and collisional quenching may be minimized. Provided the resolution is sufficient (see discussion below), the temperature can be determined from the fluorescence ratio, on a pixel-by-pixel basis, from the relative Boltzmann fractions in the ground electronic state.

The two-line method generally requires the use of two lasers and two cameras for temporally resolved

measurements. The lasers are tuned to different transitions and are fired sequentially, with a delay that is sufficient to temporally separate the respective fluorescence-signal decays. The cameras are gated so that each camera integrates the fluorescence signal induced from only one of the lasers. The temporal resolution is therefore limited by twice the maximum fluorescence lifetime within the flow field of interest, i.e., one lifetime for each laser pulse.

In this application, the rotational temperature is obtained by selecting transitions that originate from different rotational states within the same vibrational level of the electronic ground state. In the limit of weak excitation, the fluorescence ratio R_{12} can be written as

$$R_{12} \equiv \frac{S_{f1}}{S_{f2}} = C_{12}' \frac{B_1 E_1 f_{B1}(T) g_1(N,T) \phi_1(\chi_i, N, T)}{B_2 E_2 f_{B2}(T) g_2(N,T) \phi_2(\chi_i, N, T)}, \quad (2)$$

where C_{12}' is a constant that depends on the detection systems, and the subscripts 1 and 2 refer to the values associated with the respective fluorescence images. In this form, the temperature dependence is implicit in the Boltzmann fractions, overlap integrals, and fluorescence yields. If we assume the primary temperature dependence results from the Boltzmann fractions and incorporate the various spectroscopic terms and laser-pulse energies into C_{12}, the fluorescence ratio can be written as an explicit function of temperature given by

$$R_{12} = C_{12} \exp\left(-\frac{\Delta\varepsilon_{12}}{kT}\right), \quad (3)$$

where $\Delta\varepsilon_{12}$ is the energy difference between the initial absorbing states; k is the Boltzmann constant; and T is the rotational (and, effectively, the gas-kinetic) temperature. The constant C_{12} can be determined by independent calibration or from the signal ratio directly (*in situ*), if the temperature is accurately known at some location within the image.

In writing Eq. (3), we have implicitly assumed that the number-density and temperature dependencies of the fluorescence yields cancel in the ratio. This is a reasonable assumption here because the quenching cross sections, fluorescence lifetimes,[20,21] and fluorescence-branching ratios[22] for the $A\,^2\Sigma^+$, $v' = 0$ state of NO are known to be insensitive to rotational quantum number. Hence, despite any potential collisional transfer within the upper state, the broadband fluorescence efficiencies will cancel in the fluorescence ratio in this application. In other cases, e.g., OH, where the collisional-transfer and spontaneous-emission-rate coefficients vary with rotational quantum number, calibration may be necessary, because the fluorescence yields strictly cancel in the signal ratio only if the excited transitions have the same laser-coupled upper state (see, for example, Ref. 16).

Also in writing Eq. (3), we have assumed that the number-density and temperature dependencies of the overlap integrals cancel in the ratio. The validity of this assumption is dependent on the characteristics of both the laser and the absorption line shapes. In general, this assumption is valid for broadband excitation because the entire absorption line shape sees a relatively uniform spectral laser intensity. This assumption is also valid here, where the laser linewidths are comparable to the absorption linewidths, assuming the lasers have identical spectral profiles and are accurately tuned to each transition. In practice, however, the combination of pulse-to-pulse laser fluctuations and variations in the absorption linewidths throughout the flow field can lead to systematic errors in temperatures determined with the use of Eq. (3). These effects are discussed in detail in Section 3 below.

Finally, it should be noted that the effects of radiative trapping have been neglected in Eq. (3). In the experiments considered here, this is a valid assumption because the signal is spectrally filtered so that only fluorescence that is emitted to vibrational levels with $v'' > 0$ is detected. As a result, the self-absorption of the spectrally filtered fluorescence is minimal, because, at typical combustion conditions, the vibrationally excited states are not significantly populated.

B. Temperature Sensitivity

Obtaining good sensitivity to temperature in the fluorescence ratio requires that the energy difference of the two absorbing states be comparable to (or preferably greater than) the characteristic flow temperature, i.e., $\Delta\varepsilon_{12} \geq kT$. This requirement can be deduced from the differentiated form of Eq. (3), which can be written as

$$\frac{\delta T}{T} = \frac{1}{(\Delta\varepsilon_{12}/kT)} \frac{\delta R_{12}}{R_{12}}, \quad (4)$$

where δT is the uncertainty in the inferred temperature and δR_{12} is the uncertainty in the measured fluorescence ratio. Eq. (4) shows that, by selecting transitions with absorbing states such that $\Delta\varepsilon_{12} \geq kT$, the uncertainty in temperature is always less than the uncertainty in the fluorescence ratio. Note that although maximizing $\Delta\varepsilon_{12}$ appears desirable, a practical limit exists because the high-energy rotational states will have correspondingly less population and will yield lower signal-to-noise ratios (SNR's). Eventually the increased temperature sensitivity for large energy separations may be overwhelmed by the temperature uncertainty because of shot noise; hence, balancing the trade-off between the temperature sensitivity and the uncertainty that is due to shot noise will ultimately limit the largest useful energy difference.

In most cases, a reasonable starting point for PLIF temperature-imaging experiments is to choose candidate transitions with an energy difference comparable to the maximum temperature of interest. It should also be noted though that, based on Boltzmann fractions alone, it is generally advantageous to choose transitions with absorbing states that are well

populated at high rather than low temperatures. The motivation for this is to maximize the SNR, and thus minimize the random uncertainty, at high temperatures, to compensate for the reduced temperature sensitivity ($\Delta\varepsilon_{12} \sim kT$). At lower temperatures a loss in the SNR because of decreased population can be better tolerated because of the increased temperature sensitivity ($\Delta\varepsilon_{12} > kT$).

C. Resolution Requirements

As with any technique, the experimental resolution in fluorescence experiments can have a significant impact on the accuracy of the temperature measurements. Temperature errors can result in measurements based on laser-induced fluorescence (LIF) if the spatial and temporal resolution is not sufficient to adequately resolve the temperature gradients within the flow of interest. As an example, consider a case where the flow motion is frozen, but several fluid elements exist at different temperatures within the measurement volume of an individual pixel. The signal indicated by the pixel represents the averaged fluorescence signal of the fluid elements within the probe volume; however, because the temperature is a nonlinear function of the fluorescence signal, the linearly averaged fluorescence signal will not necessarily reflect the linearly averaged temperature.

The significance of this effect depends upon the magnitude of temperature fluctuations within the probe volume. Small temperature differences within the probe volume generally will not be significant, but large temperature fluctuations can potentially lead to considerable temperature-measurement errors. Note that in the two-line technique, each of the fluorescence signals may be biased if the spatial resolution is inadequate. As a result, the inferred temperature may be high or low, depending on the flow conditions and the transitions used.

As an illustration, consider an NO temperature measurement within a volume defined by the (static) spatial resolution and consisting of two uniform pockets of fluid at temperatures T_1 and T_2, respectively. For simplicity, assume that the two pockets of fluid are identical in all respects except for a 500 K temperature difference, i.e., $T_2 = T_1 + 500$ K; the fluorescence can be modeled by $S_f \propto f_B/\sqrt{T}$, and the two transitions used for the measurement are the $R_1 + Q_{21}(13.5)$ and $Q_1 + P_{21}(28.5)$ lines. We now consider the potential temperature-measurement errors that occur for various values of T_1, i.e., $T_1 = 300$ K and $T_2 = 800$ K, $T_1 = 400$ K and $T_2 = 900$ K, and so forth. Based on these assumptions, as T_1 varies from 300 to 1500 K, the error in the measured temperature (i.e., the difference between the average temperature of the two fluid elements and the temperature inferred from the average fluorescence signal of the two elements) ranges from approximately -5% to -12%. In this example, the error peaks for the case with fluid elements at 600 and 1100 K, respectively, where the average temperature is 850 K, but the measured temperature is 749 K (12% low).

Similarly, the temperature measurement error is -5.3% when $T_1 = 300$ K and -4.7% when $T_1 = 1500$ K. Although this example yields negative temperature errors, positive temperature errors are also possible. For example, if the fluid-element temperatures were 300 and 500 K, respectively, the measured temperature would be 407 K, 2% higher than the actual average temperature of 400 K.

Similar to the static spatial resolution considered above, the temporal or dynamic resolution must also be sufficient to ensure that the thermodynamic state of the fluid does not change significantly during the measurement. Temporal changes in the gas within the measurement volume can generally occur due to convection, diffusion, or chemical reaction. Because the local temperature measurement depends on the fluorescence ratio of an *individual* fluid element, the ability to freeze the motion of the flow is critical in the present supersonic flows, as the characteristic flow times are less than diffusion or chemical-reaction times. If the flow moves significantly during the measurement, the local fluorescence ratio obtained will, in general, represent the ratio of some combination of fluid elements. Here again the accuracy of the local inferred temperature will be degraded if the flow properties vary significantly over the scale of the flow motion.

3. Application Considerations

In principle, accurate two-line temperature measurements of NO can be achieved in a wide range of combustion-related flows. In practice, however, many details must be carefully considered to minimize potential systematic errors. For example, the choice of transitions is critical in preventing laser attenuation owing to optical thickness and in providing good temperature sensitivity with acceptable signal levels and dynamic range. In addition, the laser energy one uses should be sufficient to lead to good signal levels, but low enough to avoid perturbing the population distributions of either initial state. Also, in high-speed flows in particular, fluorescence lifetime and temporal resolution must be considered, because the combination of high flow velocities and the relatively long fluorescence lifetime of NO can lead to blurring in the images. Finally, instrumentation limitations need to be considered, such as shot-to-shot laser fluctuations, and camera linearity and dynamic range. As these issues are all interrelated and often in conflict, compromises must generally be made in designing the diagnostic strategy for a given application. For the measurements presented here, these issues have been examined in detail elsewhere.[23] Here, we briefly summarize the results of this analysis and discuss the effects of shot-to-shot laser mode fluctuations for the flow field investigated.

A. Flow Field Deseld Description and Spectroscopic and Resolution Issues

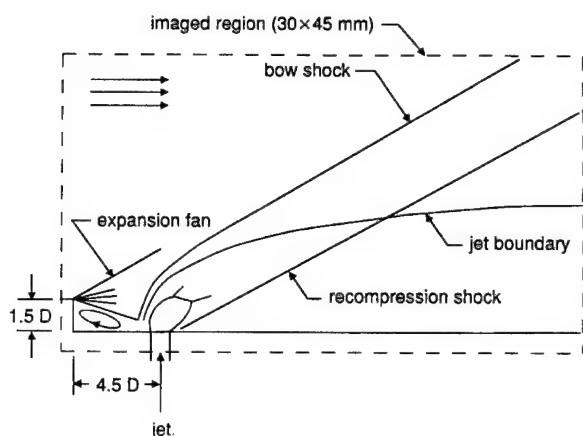The SCRAMJET-model flow field we examined is shown schematically in Fig. 1, where the cross flow is

Fig. 1. Schematic diagram of the flow field showing the nominal flow conditions: Jet: 1% NO/19% CO/80% H_2 at 300 K and 3.0 atm; $M = 1$, and $D = 2$. Cross flow: 0.1% NO/10% CO/N_2 at 1260 K and 0.4 atm; $M = 1.64$.

supersonic and flows from left to right. As the cross flow passes over the step, it expands through a Prandtl–Meyer expansion fan and separates, leading to a recirculation zone jet downstream of the step. Fuel is injected sonically through a circular orifice (diameter $= D$) located $4.5D$ downstream of a rearward-facing step (height $= 1.5D$). The fuel jet is underexpanded and results in the characteristic barrel-shock structure, which is swept over because of the momentum of the oncoming cross flow. A bow shock is formed upstream of the fuel jet because the jet acts as an obstruction to the cross flow. Downstream of the fuel jet, the cross flow is turned parallel to the wall by a recompression shock wave.

The nominal flow field conditions for this experiment, noted in Fig. 1, are representative of the inlet conditions for a SCRAMJET combustor. The temperatures and pressures indicated in the figure caption are the static values of the free stream and the stagnation values of the jet gas, respectively. A free stream composed predominantly of nitrogen was used to simulate air in these noncombusting measurements. However, because both nitrogen and hydrogen are weak quenchers of NO $A(v' = 0)$ fluorescence,[24] carbon monoxide (CO) was added to the free stream and the fuel jet to reduce the fluorescence lifetime of NO. The added CO limited the fluorescence lifetime to less than 200 ns (including 30 ns of laser pulse duration) to help maintain acceptable spatial resolution. The CO in the jet also served to reduce the peak signals within the cold, fuel-rich regions, thereby ensuring a linear detector response.

Experiments were conducted with NO seeded in the jet to mark the mixed-fuel temperature, as well as in both the jet and free stream to mark the entire temperature field. For cases with free-stream seeding, the free-stream NO was limited to 1000 ppm to minimize optical thickness over the relatively long path length ($< 10\%$ laser absorption over 6–7 cm). A higher seeding fraction was used in the jet (1% NO) to increase signal levels within the jet plume (the

primary region of interest). Although the jet-seeding fraction led to as much as 20–30% attenuation in the cold, fuel-rich regions, the resulting temperature errors were less significant because the regions with the highest absorption also had the most favorable temperature sensitivity (see below) and the shortest optical path lengths (~ 1 cm or less).

The absorption lines used in these measurements were the $Q_1 + P_{21}$ (28.5) and the $R_1 + Q_{21}$ (13.5) transition pairs in the $A \leftarrow X$ (0, 0) band of NO near 226 nm. These transitions were chosen for a number of reasons. First, as recently noted by Lee et al.,[15] this NO band is attractive for temperature measurements because it is easily accessible with tunable dye lasers and has a fairly complete spectroscopic data base. In addition, these particular rovibronic transitions are well isolated from neighboring transitions (> 3-cm^{-1} separation) and provide good temperature sensitivity for this application (~ 1040 cm^{-1} or ~ 1531 K), where the primary region of interest (the jet plume) is at the free-stream temperature or less. Finally, the initial states for these transitions provide relatively high population densities at high temperatures (without an excessive population loss for the high-J'' transition at low temperatures), which enhances the SNR's where the temperature sensitivity is reduced (i.e., where $\Delta \varepsilon_{12} \sim kT$).

With interest in relatively large-scale features, we chose a reasonable compromise between signal level and resolution. Here, we limited the fluorescence lifetimes so that the plume motion during the measurement interval (< 350 ns) was about the same as the static spatial resolution (~ 230 μm in the flow or 3 CCD pixels; see Ref. 23). Including the flow motion and the finite spatial resolution of the imaging system, the overall measurement resolution is better than ~ 0.5 mm. Hence the measurement resolution here is many times larger than the smallest temperature scale (100 times or more larger than the Batchelor scale), and the sharpest temperature gradients and fine-scale temperature fluctuations within the flow are not resolved. It is expected, however, that the large-scale features of the temperature field are adequately resolved. Indeed, no significant temperature errors within the plume owing to flow motion were observable, as determined during image processing by shifting the second image by one- and two-binned pixels upstream to account for the flow motion between the laser pulses. Some noticeable temperature errors were observed in the shear layer owing to the flow motion (usually as hot spots) because of the higher velocities there, but they are ignored here because the shear layer represents a relatively small area of the total plume.

B. Laser Mode Fluctuations and Overlap Integral Effects

As noted above, the accuracy of two-line temperature measurements also depends on the degree to which the temperature and number-density dependence of the respective overlap integrals cancel in the fluores-

cence ratio. In this and many other PLIF applications, the laser linewidths are of the same order as the absorption linewidths, and overlap integral effects need to be examined. This is particularly true in light of the fact that most pulsed dye lasers used in PLIF experiments generally operate with multiple axial modes, and the intensity of the individual modes fluctuates from pulse to pulse.

The significance of these mode fluctuations in LIF measurements depends in large part on the relative number, width, and spacing of the axial modes that fall within the absorption linewidth. One can argue that the ideal multimode spectral laser profile for LIF measurements should have a small axial mode spacing with a broad gain envelope, so that a large number of modes fall within the absorption linewidth. This type of spectral profile will tend to reduce the influence of any given mode on the absorption and will also tend to reduce the peak spectral intensity of the individual modes. Although the presence of multiple discrete modes can lead to hole-burning or inhomogeneous-saturation effects, as long as a number of modes fall within the absorption width and the mode spacing is much less than the homogeneous linewidth, the molecular response to the irradiation should be relatively homogeneous.

To examine the impact that pulse-to-pulse mode fluctuations have on the accuracy of the temperature measurements (through the overlap integrals), we developed a simple computer model to simulate the statistical fluctuations of the multimode spectral profiles of the lasers used in these experiments. The average and standard deviation of the overlap integral were calculated as a function of mixture temperature using 100 simulated laser spectral profiles. The calculations and results are briefly described here; further details of the laser spectral profile model and overlap integral calculations are described elsewhere.[23]

The mode structure of the visible output of the dye lasers (~ 450 nm) was modeled as a series of Gaussian modes (0.003 cm^{-1} FWHM and 0.017-cm^{-1} spacing) within an ~ 0.2-cm^{-1} Gaussian gain envelope. These characteristics were based on single-shot measurements of the lasers' spectral profiles. The individual modes were assumed to be uncorrelated and to exhibit intensities described by exponential statistics. The frequency-doubled mode structure was modeled as the self-convolution of the visible mode structure.

The absorption line shape, including both collisional and Doppler broadening, was modeled as a function of mixture temperature throughout the flow field using a Voigt line-shape function. The pressure was assumed constant at the free-stream value (0.4 atm) throughout most of the flow ($T > 500$ K). The pressure just downstream of the Mach disk ($T = 300$ K) was assumed to be 0.8 atm, which corresponds to that of a simple underexpanded jet at the same pressure ratio. A linear pressure variation was assumed between these (temperature) regions.

Collisional shifts of the NO-absorption line shapes were included in the overlap integral calculations to account for the relative laser detuning throughout the flow field. The collisional shift is always toward lower frequencies and the shift-to-width ratio is nominally independent of both temperature and pressure. Doppler shifts are generally negligible throughout most of the flow field because the bulk flow velocity is essentially normal to the laser sheet propagation. Some Doppler shift is expected near the jet exit, but it is offset by the relatively large, opposing collisional shift and is not significant. The laser was assumed to be tuned to absorption line center at the 1260 K, 0.4 atm free-stream condition.

Figure 2(a) shows the estimated Voigt width and calculated (nominal) overlap integral as a function of the temperature (from 300 to 1500 K) of the mixture. The variation of the collisional width and shift, and the Doppler width are also shown. As indicated in the figure, the Voigt width is nearly constant throughout most of the flow field, owing to the counterbalancing effects of the collisional and Doppler widths. At mixture temperatures below 500 K, which occur near the jet exit, the Voigt width is somewhat higher, primarily because of the higher pressure. The magnitude of the overlap integral shows a variation with
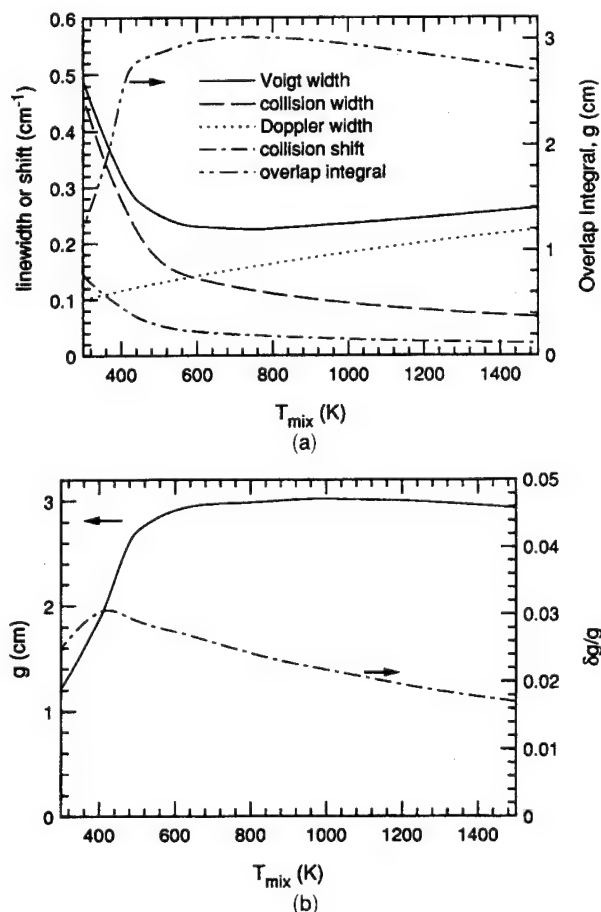

Fig. 2. (a) Variation of absorption width, collisional shift, and nominal overlap integral as a function of the mixture temperature; and (b) nominal overlap integral and its shot-to-shot standard deviation as a function of the mixture temperature.

temperature that is essentially the inverse of the Voigt absorption-width variation. The value of the overlap integral is lowest at the jet-exit condition and increases with the mixture temperature until it levels off near 600 K. This behavior is expected based on a nominal laser spectral envelope of ~ 0.3 cm^{-1}, because regions that have an absorption width larger than the laser spectral width will exhibit less response to the laser radiation.

In Fig. 2(b), the model results for the standard deviation and the nominal overlap integral values are shown as a function of temperature, based on 100 simulated laser spectral profiles. The calculated fluctuation in the individual overlap integrals, is relatively small, deviating only 2–3% from the nominal value over the entire temperature range of these measurements. This corresponds to ~ 3–4% uncertainty in the fluorescence ratio based on the combined uncorrelated fluctuations in the individual overlap integrals of each laser.

The relative insignificance of the axial mode fluctuations here is due to the comparatively large number of modes that fall within the absorption linewidth throughout the flow. This is true even in the low-temperature regions where the laser is significantly detuned from line center, because the absorption width in the low-temperature regions is larger than the laser spectral width. Based on a laser spectral envelope of ~ 0.3 cm^{-1} and a mode spacing of ~ 0.017 cm^{-1} for the dye lasers used here, approximately 15–20 modes are expected to fall within the absorption linewidth throughout the flow field. The significance of the mode fluctuations would generally increase for cases where fewer modes fall within the absorption linewidth.

4. Experimental Setup and Procedure

A. Shock-Tube and Jet-Injection System

A schematic of the experimental facility is shown in Fig. 3. The flows studied were generated in a 6-m-long shock tube with a 4.5-m-long driven section of square 7.62 cm $\times$ 7.62 cm cross section. UV-grade
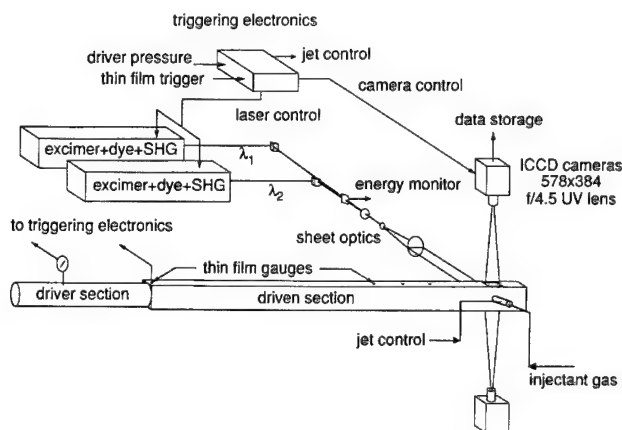
Fig. 3. Schematic diagram of the shock tube and PLIF-imaging facility.

fused-silica windows were mounted flush with the shock-tube walls to provide optical access with minimal flow disturbance. Two of the windows allow optical access to the wall of the shock tube and permit imaging up to the nozzle exit.

The driven section was instrumented with four platinum thin-film gauges along its length. The thin films were used in conjunction with electronic counters to measure the shock velocity over two intervals just upstream of the test section. These velocity measurements were used in the standard shock relations along with the measured initial pressure to determine the temperature, pressure, and gas velocity behind the incident shock wave. A thin film located just downstream of the diaphragm station was used to initiate the electronic-delay sequence used for triggering the jet, laser, and camera systems. Because neither pump laser had a fire-on-demand capability, the pump lasers were operated continuously at 1 Hz and synchronized to the firing of the shock tube just prior to diaphragm rupture. This was accomplished with a custom-made laser-triggering circuit that used the driver-pressure monitor as an interrupt for the 1-Hz oscillator. Operating the lasers in this manner eliminated potential misfirings and large shot-to-shot laser fluctuations.

A pulsed molecular-beam valve (General Valve Series 9 with Iota One controller) was used to inject fuel normal to the cross flow. The valve had a 2-mm-diameter orifice and was mounted flush with the shock-tube wall. Flow-visualization measurements showed that flow through the valve reached steady state in ~ 1.2 msec and that the effective jet-stagnation pressure decreased by $< 5\%$ during the valve-open time (5 msec). The valve was triggered to open ~ 1.8 msec before the image acquisition, and images were typically acquired ~ 200 μsec after the incident shock arrival at the jet location. This timing sequence provided adequate time for the flow to develop, but was short enough to avoid significant jet contamination of the initial shock-tube test-gas mixture.

The shock-tube test-gas mixtures were composed of NO, CO, and N$_2$ and were created by diluting a commercial, unanalyzed mixture of 5% NO in N$_2$ with CO (99% purity) and nitrogen (99.9% purity). The jet mixtures were composed of NO, CO, and H$_2$ and were obtained by diluting NO (99% purity) with CO and H$_2$ (99.99% purity). The test gases were mixed in separate stainless-steel cylinders, each of which was mechanically stirred.

B. Lasers and Sheet Optics

The lasers used in these experiments were Xe–Cl excimer-pumped dye lasers (Lambda Physik FL2002 and FL3002). The pump beams at 308 nm had pulse energies of more than 100 mJ with pulse widths of ~ 20 nsec. Coumarin 450 dye mixtures were used and the fundamental dye laser beams were frequency-doubled to ~ 226 nm using barium borate (BBO) crystals. The lasers were tuned to different transi-

tions (noted above) in the $A\,^2\Sigma^+ \leftarrow X\,^2\Pi$ (0, 0) band of NO and were fired sequentially with a delay of 250 nsec to temporally separate the fluorescence signals. To minimize potential systematic errors associated with the ratio of overlap integrals, we tuned the lasers before each shock-tube run using static fluorescence measurements of a subatmospheric, 300 K NO–CO–N_2 mixture within the shock tube. The pressure in the shock tube was adjusted so that the collisional width and shift matched the corresponding values in the free-stream supersonic flow. Including transmission losses through the optics, the pulse energy of each laser sheet (in the test section) was ~ 0.25 mJ in a spectral bandwidth of ~ 0.3 cm^{-1}.

The UV dye laser beams were expanded into sheets by a cylindrical telescope (-12.5- and 500-mm focal lengths) and focused using a 1-mm spherical lens. As shown in Fig. 3, the λ_2 beam was directed horizontally along the optical axis, while the λ_1 beam was propagated at a slight vertical angle ($\sim 0.25°$) to the optical axis. The λ_1 beam height and angle were adjusted so that the sheets crossed near the center of the imaged region, with no significant differences in the combined sheet thickness and position. The resulting horizontal sheet measured ~ 300 μm $\times$ 75 mm with a nearly Gaussian spatial distribution of energy. Beam splitters were placed in the optical train to permit monitoring of the laser pulse energy on a shot-to-shot basis, using photodiodes calibrated with a Molectron energy meter.

C. Imaging System

The broadband fluorescence in the spectral range from 225–335 nm was collected at right angles to the plane of illumination with f/4.5 UV Nikkor lenses (105-mm focal length). UG-5 Schott Glass filters (2-mm thick) were used to block elastic laser scattering. The UG-5 filters also blocked the resonant fluorescence from the $A \leftarrow X$ (0, 0) band, while transmitting $\sim 45\%$ of the total fluorescence signal.

The fluorescence signals were imaged onto two intensified, cooled CCD cameras (Princeton Instruments, each using an EEV 578 $\times$ 384 array of 23 μm $\times$ 23 μm pixels). The 30 mm $\times$ 45 mm images were acquired and processed using two IBM-compatible 486 personal computers equipped with Princeton Instruments' CSMA software. The intensifier-gate widths were set to 250 nsec. The rise and fall times of the intensifier gates were ~ 20 nsec which resulted in ~ 210 nsec of uniform gating. The laser pulses were carefully positioned temporally to occur just after the respective intensifier gates were fully on. This ensured uniform amplification of the fluorescence decay, and was verified by monitoring the laser-induced-fluorescence signal within a static cell.

D. Image Corrections and Data Reduction

A number of image corrections[4,25] were necessary to quantitatively determine the temperature from the raw fluorescence images. Each raw fluorescence image was corrected for camera dark noise, flat-field nonuniformity of the array and collection lens, relative pixel-to-pixel spectral response, and laser energy, spatial distribution, and scattering.

If necessary, prior to dividing the corrected images to determine the fluorescence ratio, one image was warped or remapped pixel by pixel using a registration function (including translation, rotation, and magnification) to correct for the misalignment of the respective cameras. This correction was generally minor here, because great care was taken during the experiments to align the fields of view to within 1–2 pixels throughout the images. In general, however, this warping may be necessary because it is difficult in practice to align the cameras so that each pixel images *exactly* the same region. The registration function used here was created by comparing images of a rectangular-grid target positioned in the object plane.

The scattering and sheet corrections used here were 25-frame averages to reduce random noise. Average sheet corrections were sufficient, because the instantaneous laser sheet profiles were found to fluctuate about the average by less than $\sim 5\%$. The sheet corrections were obtained by imaging NO fluorescence within the shock tube; hence the sheet corrections also provided a simultaneous flat-field and relative-spectral-response correction. After performing these corrections, but prior to determing the ratio, the pixels in the images were software-binned 2 $\times$ 2 to improve the SNR. The resulting nominal pixel resolution was approximately 300 μm $\times$ 160 μm $\times$ 160 μm. As discussed above, however, the effective spatial resolution is somewhat worse because of both the finite resolution of the imaging system and the flow motion between laser pulses.

The sheet corrections were obtained by imaging a subatmospheric, 300 K, optically thin, static NO–CO–N_2 mixture within the shock tube. The sheet-correction mixtures were customized for each transition to ensure that no significant laser attenuation was observed. In addition, the mixtures were chosen to permit the use of the same intensifier gain in both the sheet-correction and flow field images, to eliminate any gain dependencies in the corrected images. The linearity of the sheet-correction fluorescence with respect to laser pulse energy was verified using various UV neutral-density filters.

5. Temperature-Imaging Results and Discussion

In this section, representative instantaneous and frame-averaged temperature images of a nonreacting SCRAMJET-model flow field are presented, along with a discussion of the measurement uncertainties. Additional results with a flush-wall geometry and with oxidizing free streams are described in Ref. 23, and will be available in a future publication of ours. In general, the sample results shown here illustrate the strikingly different characteristics of the instantaneous and time-averaged flow fields, and thus demonstrate the importance of temporally resolved measurements for elucidating complex mixing phenomena. Measurements both with and without free-stream

NO are presented, as these alternative-seeding strategies provide different temperature information, i.e., NO seeded in both streams provides a means of measuring the (instantaneous or average) temperature throughout the entire flow field, whereas NO seeded only in the fuel yields the temperature and location of the fuel. As will be illustrated below, the latter strategy is more useful for inferring the time-averaged mixedness of the two streams.

A. Verification Measurements

Prior to examining the jet in cross flow, temperature-verification measurements were performed by imaging the uniform region behind incident shocks for several temperatures, and within a static cell at 300 K. The measurements were conducted using the same respective intensifier gains and were normalized for laser energy variations to ensure a nominally constant value for C_{12}. Figure 4 shows a plot of the measured fluorescence ratio versus the shock-tube test-gas temperature. The fluorescence-ratio data were obtained by spatially averaging each image to minimize the uncertainty due to random noise. The solid line shows a least squares fit to the data with the slope fixed by the energy separation of the absorbing states.

The scatter in these data represents the shot-to-shot uncertainties in the fluorescence ratio owing to the combined fluctuations of the respective lasers' spectral line shapes, detunings, and spatial-energy distributions. The maximum deviation of the measured fluorescence ratio from the best fit is $\sim 17\%$, with a standard deviation of $\sim 8\%$. Most of this scatter is likely caused by spectral line-shape fluctuations, because the spatial averaging of the images tends to reduce the effect of laser spatial energy fluctuations. These results verify that accurate instantaneous temperatures can be determined throughout the entire temperature range of the jet measurements discussed below. In addition, these results give an indication of the expected measurement precision without accounting for laser line-shape fluctuations.
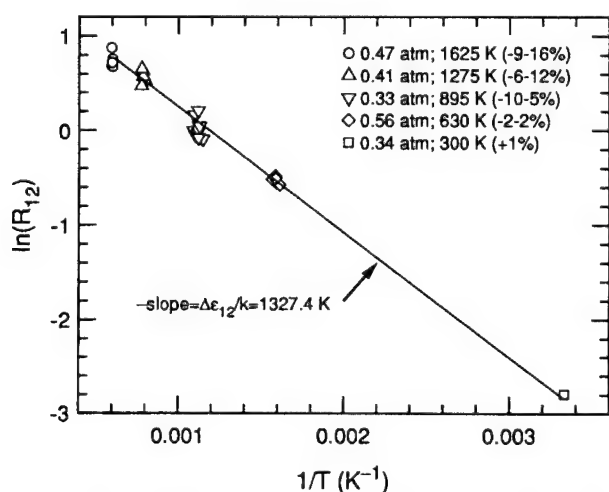
B. Jet-in-Cross Flow Measow Measurements

The temperature measurements discussed below are generally valid throughout the flow field except in three small regions: within the barrel-shock structure; in the recirculation zone downstream of the back step; and in the low-pressure region just downstream of the barrel-shock structure (approximately bounded by $0 < x/D < 1.5$, $0 < y/D < 1.5$). The temperatures are suspect in these regions because the fluorescence lifetimes were sufficiently long to cause a portion of the signal from the first laser pulse to appear on the second camera. Outside of these regions, the temperature measurements are reliable, although the SNR is generally much higher in the jet plume than in the free stream, because of the higher NO-seeding fraction in the jet.

For the cases with NO seeded in the freestream, C_{12} was evaluated by averaging the signal over a large area within the uniform free-stream region. For cases without free-stream NO, *in situ* evaluation of C_{12} was not feasible because of the lack of a suitable calibration point. Hence for the experiments without free-stream NO, the average value of C_{12} from the former cases was used. In image processing the cases without free-stream NO, the images were conditioned on the presence of jet fluid. This conditioning was accomplished by thresholding the images just above the ghost-background signal in the free stream. The ghost background noted here refers to the relatively specular, partial reflectance of the NO fluorescence from the window behind the object plane of each camera. The ghost-background signal is relatively small, generally a few percent of the local maximum signal. As discussed in Ref. 23, the systematic temperature error introduced by the ghost background is expected to be relatively minor ($<5\%$), except in the free-stream region along the plume boundary.

Figure 5 shows instantaneous temperature images for cases with and without NO seeded in the free stream. These images clearly show the complexity of the instantaneous flow field structure. In particular, the instantaneous images highlight the turbulent nature of the plume, which is characterized by pockets of undiluted free-stream fluid penetrating deep into the jet plume and vice versa. The jet boundary is easily identified in the temperature field, even for the case with NO seeded in the free stream, and is indicative of a sharp scalar gradient in the shear layer. Within the plume, the temperature increases with increasing x/D because of the warmer free stream mixing with the cooler jet. Although pockets of relatively cool gas persist within the plume for several jet diameters, the plume reaches a relatively uniform temperature for $x/D \geq 12$.

Fig. 4. Measured fluorescence ratio as a function of free stream temperature. The nominal pressure and temperature are noted in the legend, along with the range of scatter in the inferred temperature. The transitions used in these measurements were $R_1 + Q_{21}(16.5)$ and $Q_l + P_{21}(28.5)$, and the point at 300 K represents an average of 25 measurements.
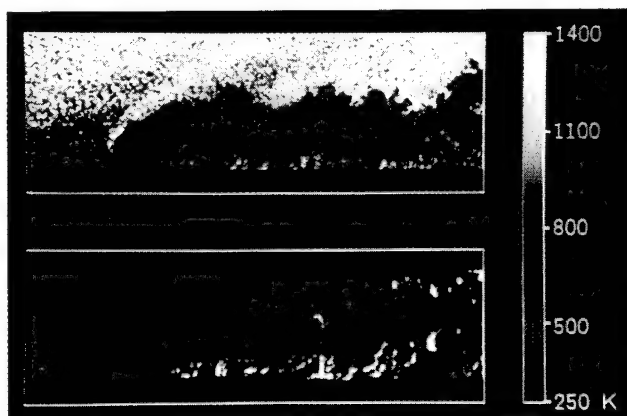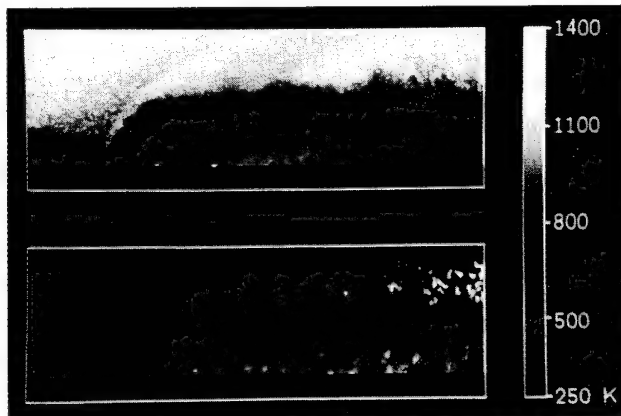
Fig. 5. Instantaneous temperature images of the jet in cross flow (a) with 0.1% NO and (b) without NO seeded in the free stream. Each image has been trimmed to 15 × 45 mm and shows approximately 18 jet diameters of the plume. Note that in (b), as no measurements were obtained in the free stream, the image was thresholded to remove the extraneous noise.

Fig. 6. Fifteen-frame average-temperature images of the jet in cross flow (a) with 0.1% NO and (b) without NO seeded in the free stream. The images were trimmed to 15 × 45 mm and show approximately 18 jet diameters of the plume. Image (b) is a thresholded, conditioned average, which was conditioned on the presence of jet fluid. Again, no measurements were obtained in the free stream of (b).

In both images, the lower plume region near the wall is seen to be the warmest mixing region, reaching 700–1000 K in just a few jet diameters. Note that the fuel generally permeates the entire lower plume region [evidenced by the absence of major pockets of free-stream fluid in Fig. 5(b)] and that similar temperatures are measured in the lower plume region for both seeding strategies. These observations, combined with the rapid temperature increase, suggest that the two streams are efficiently mixed in the lower portion of the plume. The efficient mixing and relatively high temperatures in this region are likely to make it the most favorable for autoignition and efficient combustion in a reacting flow, which is consistent with previous OH-imaging measurements[5,26] in similar combusting flows.

In comparing Figs. 5(a) and 5(b) note that some of the fine detail of the plume–cross-flow shear layer is not well resolved in Fig. 5(b), i.e., the case without NO in the free stream. This is primarily because of the increased noise and loss of detection sensitivity that results from the dilution of fuel NO when free-stream NO is not present. The raggedness of the plume boundary for the unseeded case results from the thresholding applied to remove the noise in the free stream.

Fig. 6(a) shows a 15-frame average-temperature image for the case with NO seeded in the free stream. The average image is generally less noisy, which makes the expansion fan, bow shock, and reattachment shock easier to identify. Note that although the signal-to-noise ratio is increased in the average image, the details of the large-scale turbulent structures in the plume–cross-flow shear layer are lost. In addition, note that while the same general trends observed in the instantaneous images are apparent in the average image, there is a significant difference: the average-temperature image shows a deceivingly thick thermal shear layer at the jet boundary, which is in direct contrast to the sharp temperature gradi-

ent observed in the instantaneous images. This important difference between the instantaneous and mean scalar fields is well established and has been observed in a number of subsonic gaseous and liquid shear flows.[27]

This difference is shown quite clearly in Fig. 7, which shows instantaneous and average cross-sectional temperature profiles at an axial location of $x/D = 12$. In the figure, the instantaneous profile shows a relatively uniform temperature distribution across the jet plume with a very steep gradient at the plume–cross flow interface. The average profile (which here is not sufficiently converged) shows a smoother character within the plume, and a much weaker temperature gradient in the shear layer. The smoother temperature distribution in the shear layer of the mean image results from the averaging of intermittent tongues of hot, undiluted free-stream fluid with the otherwise cooler, mixed jet fluid.

Fig. 6(b) shows a 15-frame, conditioned-average temperature image for the case without NO seeded in the free stream. In this case the average temperature at a given pixel in this image is conditioned on the presence of jet fluid; that is, the temperature at a given pixel is included in the average only if the raw fluorescence signal was above a threshold value, set just above the noise background of the image. Hence, Fig. 6(b) shows the mean temperature of the *mixed* jet fluid, i.e., the mixed-mean temperature.

We should note here that, although we believe the general trends in the mean-temperature distributions are correct, the number of images included in Figs. 6(a) and 6(b) is not sufficient for convergence. This is evidenced by the remnants of turbulent structure that persist in the shear layer of both average-temperature images, but to a larger extent in the conditionally averaged temperature images, due to the relatively low intermittency of the jet fluid (and thus temperature measurements). Nevertheless, a
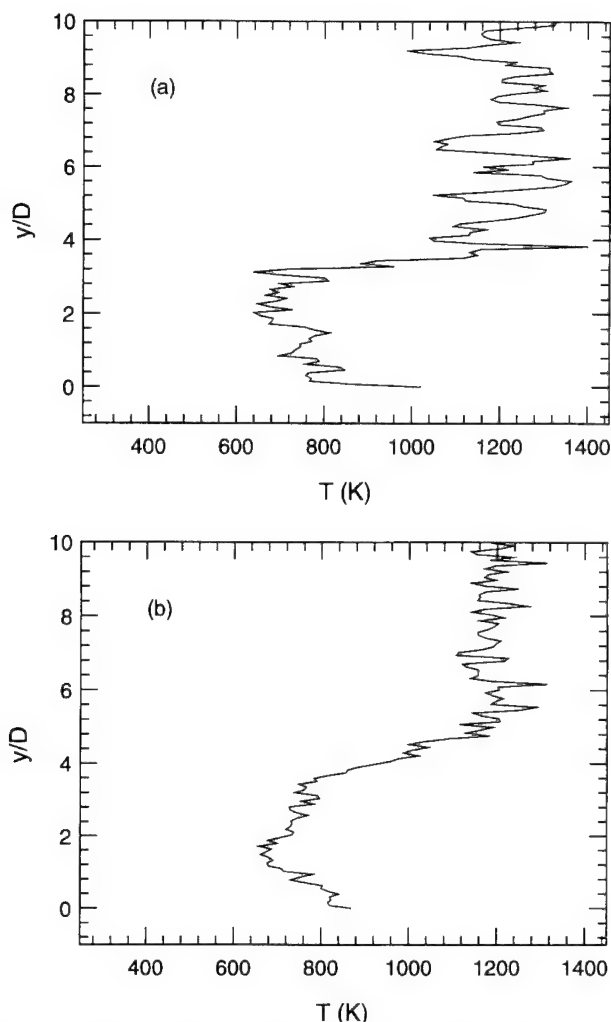
Fig. 7. Temperature cross sections at axial station $x/D = 12$. (a) Taken from the instantaneous temperature field shown in Fig. 5(a). (b) Taken from the 15-frame average-temperature field shown in Fig. 6(a). The profiles are relatively noisy in the free stream because of the low NO-seeding fraction, but they are much less noisy in the plume region because of a higher NO-seeding fraction. Hence the apparent temperature fluctuations in the free stream owe to noise, but the temperature fluctuations within the plume are primarily due to flow variations.

comparison of these images is useful because they provide different temperature information, i.e., Fig. 6(a) shows the overall temperature (fuel plus free-stream fluid), while Fig. 6(b) shows the mean temperature of the fuel.

It is precisely this distinction that accounts for the markedly different temperatures indicated in the plume–cross flow shear layer. Figure 6(a) shows a generally higher temperature in the shear layer, which, as noted above, results from the averaging of intermittent tongues of undiluted, hot free-stream fluid with the otherwise cooler, mixed jet fluid. (Similar differences in the average and conditioned-average concentration profiles have been observed in the shear layer of simple round jets.[27]) The significance of the cooler *fuel temperature* in the shear layer of Fig. 6(b) is that the mixing there is not as efficient

as implied by the *overall* average-temperature field. With the exception of the shear layer, however, Figs. 6(a) and 6(b) show essentially the same temperature field. This suggests that the lower and central plume-core regions are reasonably well mixed, which is consistent with the fact that large pockets of pure free-stream fluid within the plume are generally only observed in the shear layer.

These sample results illustrate the usefulness of instantaneous temperature imaging in clarifying the mixing and the role of large-scale structures in this flow field. For example, examining only the frame-or time-averaged flow field can lead to misinterpretations in the scalar fields. Furthermore, because of the important differences in the mean and mixed-mean properties, instantaneous measurements are necessary to permit the conditional averaging that is required to evaluate the mixed-mean properties.

C. SNR and Estimation of Uncertainties

The potential sources of uncertainty in these measurements include resolution effects, fluorescence scattering or ghosting, photon statistical noise, shot-to-shot laser sheet and line-shape fluctuations, and laser attenuation caused by optical thickness. Errors resulting from resolution effects and ghosting, however, are not expected to be significant in these measurements (with the possible exception of the plume–free stream shear-layer region, as discussed above and in Ref. 23). In the following paragraphs, we estimate the relative magnitudes of the other major sources of uncertainty.

The uncertainty that is due to photon statistics can be estimated from the SNR based on shot-noise limited detection. The SNR in the fluorescence images ($1/\text{SNR} \equiv \delta S_f/S_f$) can be related to the uncertainty in the ratio through

$$\frac{\delta R_{12}}{R_{12}} = \left(\frac{\delta S_{f1}}{S_{f1}} + \frac{\delta S_{f2}}{S_{f2}}\right)^{1/2}, \qquad (5)$$

and to the uncertainty in temperature through Eqs. (3) and (4). To estimate the temperature uncertainty attributable to shot noise, we calculated the fluorescence SNR as a function of mixture temperature by scaling the minimum SNR measured in the free stream. After using Eq. (1) in conjunction with a simple molar-enthalpy balance between the two streams to calculate the fluorescence signal as a function of temperature,[23] we scaled the SNR using the relation $SNR \propto \sqrt{S_f}$. The minimum free-stream SNR's were obtained from typical sheet-corrected images, using the standard deviation of the average signal over a large area in the low-energy region of the sheet. (The SNR, and hence the temperature uncertainty that is due to shot noise, varies throughout the respective images because of variations in the flow field properties as well as variations in the laser sheet-energy distribution. For example, even in the free stream where the properties are uniform, the SNR varies by as much as a factor of 2 because of variations in laser energy.)

Figure 8 shows the estimated signal, ratio, and temperature uncertainties caused by shot noise as a function of mixture temperature. These uncertainties were calculated based on minimum free-stream SNR's, which were measured to be ~5 and ~7, respectively. The signal uncertainties show the variation of the SNR for each transition, with the SNR ranging from ~7–30 for the low-J'' line and from ~4–10 for the high-J'' line. Note that, by design, the temperature uncertainty is lower than the uncertainty in the fluorescence ratio for all temperatures. The temperature uncertainty is noticeably suppressed at low temperatures, due to the low temperature sensitivity of the fluorescence ratio at low temperatures. Based on these calculations, the instantaneous temperature uncertainty (due to shot noise) ranges from ~5–20% over 300–1260 K. Within the plume, though, the temperature is generally less than ~1000 K and the shot-noise temperature uncertainties are less than ~9%. (For the cases without free-stream seeding, the uncertainties are slightly higher within the plume because of the increased NO dilution by the free-stream fluid.)

Shot-to-shot fluctuations in the laser spectral profile, laser detuning from the absorption-line center, and laser spatial energy distribution also add to the temperature uncertainty. For the cases with NO in the freestream, the line-shape-based errors were minimized by the *in situ* determination of C_{12}. (Although differences in the absorption linewidth and pressure shift throughout the flow can result in some residual line-shape-based error, this error is expected to be much smaller than the other sources and will be neglected here.) For these cases, the uncertainty owing to laser fluctuations primarily results from using average rather than instantaneous sheet-correction measurements. (Fluctuations of ~±5% were observed in the normalized, instantaneous sheet profiles when compared to the average.) Including the combined sheet corrections of both images, the uncertainty in the fluorescence ratio is ~±7% and
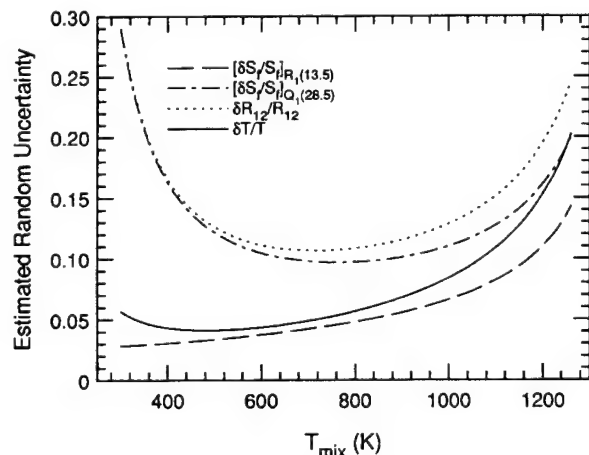
the resulting uncertainty in temperature ranges from 1.5–6%.

For the cases without NO in the free stream, the fluctuations in the laser spectral profile were not accounted for. In these cases, we used the average value of C_{12} determined from an ensemble of 24 measurements with NO in the free stream. In these measurements, we observed ~±10% fluctuation in C_{12}, which is higher than, although on the order of, that predicted by the laser model described above. Here, we attribute the primary uncertainty in C_{12} to shot-to-shot fluctuations in the laser mode structures (and thus overlap integrals), because the laser energies were normalized and the sheet fluctuations were minimized by averaging across the entire free stream. (Other possible sources include imperfect absolute-energy corrections and shot-to-shot fluctuations in the intensifier gains.) Combining the uncertainty in C_{12} with that of the instantaneous sheet corrections leads to a temperature uncertainty of ~2–8%, over 300–1000 K, because of laser fluctuations alone.

Some systematic error in these instantaneous measurements also arises from laser attenuation. These errors are mixture and temperature dependent and are therefore difficult to correct. The estimated (worst case) systematic errors due to laser attenuation are listed in Table 1 as a function of mixture temperature. The values of laser attenuation shown in the table were calculated assuming a uniform mixture over the noted path length and assuming a Gaussian laser line shape (0.30 cm^{-1}). The results show that attenuation is always more severe for the low-J'' line, and combining both measurements results in measured temperatures that are systematically high by 2–14%.

In comparing the sources of uncertainty in these measurements, we note that the shot-to-shot laser mode fluctuations and the photon statistical noise are the most dominant. Combining the random sources (assuming they are uncorrelated) leads to temperature uncertainties that range from ~5–10% within the plume (<1000 K), and up to ~21% in the free stream for cases with free-stream NO. For cases without free-stream NO, the shot-to-shot uncertainties in the plume are slightly higher (~5–13%) because of the uncertainty in C_{12} and the dilution of fuel NO. The estimated worst-case systematic errors

Fig. 8. Estimated uncertainties due to shot noise in the instantaneous jet in cross-flow-temperature images: $\Delta\varepsilon_{12}/k = 1531\ K$; $T_\infty = 1260$ K, nonoxidizing free stream with 0.1% NO.

Table 1. Estimated Worst-Case Systematic Errors Owing to Laser Absorption within the Jet Plume

| T (K) | path (mm) | P (atm) | % Attenuation | | $\delta R_{12}/R_{12}$ | $\delta T/T$ |
			$R_1(13.5)$	$Q_1(28.5)$		
300	5	0.8	32	0.6	+0.46	+0.09
400	7.5	0.6	35	2.3	+0.50	+0.13
500	7.5	0.4	24	3.5	+0.27	+0.09
600	10	0.4	24	5.7	+0.24	+0.09
700	10	0.4	18	5.4	+0.15	+0.07
800	10	0.4	13	5.5	+0.09	+0.05
900	10	0.4	9	4.5	+0.05	+0.03
1000	10	0.4	6	3.7	+0.03	+0.02

due to optical thickness are somewhat less than the random errors, but are of comparable magnitude.

6. Summary and Conclusions

In this paper, we have described one of the first detailed applications of two-line instantaneous temperature *imaging* in a supersonic mixing flow field. The measurements were based on laser-induced fluorescence from NO $A\,^2\Sigma^+ \leftarrow X\,^2\Pi$ (0, 0) transitions near 226 nm, with two sequentially pulsed dye lasers and two intensified, cooled CCD cameras used for temporally resolved measurements. Several aspects of the technique have been discussed in the context of measurements in a SCRAMJET-model flow field, including temperature sensitivity, random uncertainties, spatial and temporal resolution, and systematic errors such as laser attenuation and overlap integral effects.

Both instantaneous and frame-averaged temperature measurements of the nonreacting flow field were obtained with NO seeded in the fuel, for cases with and without free-stream-seeded NO. While the former seeding strategy permits temperature measurements throughout the flow field, the latter strategy unambiguously marks the fuel and may be more useful in examining the mixing phenomena. In both cases, the dominant sources of temperature uncertainty were generally shot-noise and laser spectral fluctuations. The temperature errors that are due to laser attenuation generally dominated the random uncertainties only in the coldest regions of the jet plume.

For cases with free-stream NO, random temperature uncertainties ranged from approximately 5% at 300 K to approximately 10% in the warmest regions of the plume at ~ 1000 K, and up to ~ 21% in the free stream at 1260 K. The random temperature uncertainties in the plume were slightly higher (5–13%) for the cases without NO in the free stream, primarily because of the shot-to-shot laser fluctuations and the lack of *in situ* calibration. At worst, the systematic temperature errors that were due to laser attenuation were ~ 10% and resulted in measured temperatures that were systematically high. The measurement uncertainties owing to laser fluctuations could be reduced in future experiments by using lasers with a broader linewidth, real-time laser monitors,[7] and *in situ* calibration. Shot-noise uncertainties may also be reduced (by perhaps 5 times) by using higher laser pulse energies and faster collection optics (e.g., $f/2.5$).

Overall, these measurements demonstrate the ability to make high-quality, instantaneous temperature measurements in complex combustion flow fields. As recently reported,[28] these NO measurements can be easily extended to the reacting case and offer several advantages over OH measurements, including the following: the ability to seed NO in both streams, not just in combustion regions, to obtain measurements at all points; the absence of J''-dependent quenching rates or radiative lifetimes that can lead to systematic errors; and the opportunity to collect strong nonresonant fluorescence to spectrally isolated, high-lying vibrational states, which reduces potential errors associated with radiative trapping.

References

1. R. K. Hanson, "Combustion diagnostics: planar imaging techniques," in *Twenty-first Symposium (International) on Combustion* (Combustion Institute, Pittsburgh, Pa., 1986), pp. 1677–1691.
2. R. K. Hanson, J. M. Seitzman, and P. H. Paul, "Planar laser-fluorescence imaging of combustion gases," Appl. Phys. B **50,** 441–454 (1990).
3. R. J. Cattolica and D. A. Stephenson, "Two-dimensional imaging of flame temperature using laser-induced fluorescence," in *Dynamics of Flames and Reactive Systems,* J. R. Bowen, N. Manson, A. K. Oppenheim, and R. I. Soloukhin, eds., Vol. 95 of Progress in Aeronautics and Astronautics Series (American Institute of Aeronautics and Astronautics, Washington, D.C., 1984), pp. 714–721.
4. P. H. Paul and R. K. Hanson, "Applications of planar laser-induced fluorescence imaging diagnostics to reacting flows," in *Technical Digest of the 26th Joint Propulsion Conference* (American Institute of Aeronautics and Astronautics, Washington, D.C., 1990), paper 90–1844.
5. M. G. Allen, S. J. Davis, and K. Donohue, "Planar measurements of instantaneous species and temperature distributions in reacting flows: a novel approach to ground testing instrumentation," in *Technical Digest of the 26th Joint Propulsion Conference* (American Institute of Aeronautics and Astronautics, Washington, D.C., 1990), paper 90–2383.
6. P. H. Paul, U. E. Meier, and R. K. Hanson, "Single-shot, multiple-camera planar laser-induced fluorescence imaging in gaseous flows," in *Technical Digest of the 29th Aerospace Sciences Meeting* (American Institute of Aeronautics and Astronautics, Washington, D.C., 1991), paper 90–0459.
7. J. M. Seitzman, J. L. Palmer, A. L. Antonio, R. K. Hanson, P. A. DeBarber, and C. F. Hess, "Instantaneous planar thermometry of shock heated flows using PLIF of OH," in *Technical Digest of the 31st Aerospace Sciences Meeting* (American Institute of Aeronautics and Astronautics, Washington, D.C., 1993), paper 93–0802.
8. M. P. Lee, P. H. Paul, and R. K. Hanson, "Quantitative imaging of temperature fields in air using planar laser-induced fluorescence of O_2," Opt. Lett. **12,** 75–77 (1987).
9. R. J. Hartfield, Jr., S. D. Hollo, and J. C. McDaniel, "Planar temperature measurement in compressible flows using laser-induced iodine fluorescence," Opt. Lett. **16,** 106–108 (1991).
10. T. Ni-Imi, T. Fujimoto, and N. Shimizu, "Method for planar measurement of temperature in compressible flow using two-line laser-induced iodine fluorescence," Opt. Lett. **15,** 918–921 (1990).
11. J. M. Seitzman, G. Kychakoff, and R. K. Hanson, "Instantaneous temperature field measurements using planar laser-induced fluorescence," Opt. Lett. **10,** 439–441 (1985).
12. B. K. McMillin, J. L. Palmer, and R. K. Hanson, "Two-dimensional temperature measurements of shock tube flows using planar laser-induced fluorescence imaging of nitric oxide," in *Technical Digest of the 22nd Fluid Dynamics, Plasma Dynamics & Lasers Conference* (American Institute of

13. M. G. Allen, T. E. Parker, W. G. Reinecke, H. H. Legner, R. R. Foutter, W. T. Rawlins, and S. J. Davis, "Instantaneous temperature and concentration imaging in supersonic air flow behind a rear-facing step with hydrogen injection," in *Technical Digest of the 30th Aerospace Sciences Meeting* (American Aeronautics and Astronautics, Washington, D.C., 1992), paper 92–0137.

14. J. L. Palmer, B. K. McMillin, and R. K. Hanson, "Planar laser-induced fluorescence imaging of velocity and temperature in shock-tunnel free-jet flow," in *Technical Digest of the 30th Aerospace Sciences Meeting* (American Institute of Aeronautics and Astronautics, Washington, D.C., 1992), paper 92–0762.

15. M. P. Lee, B. K. McMillin, and R. K. Hanson, "Temperature measurements in gases using planar laser-induced fluorescence imaging of NO," Appl. Opt. (to be published).

16. R. Cattolica, "OH rotational temperature from two-line laser-excited fluorescence," Appl. Opt. **20,** 1156–1166 (1981).

17. K. P. Gross and R. L. McKenzie, "Measurements of fluctuating temperatures in a supersonic turbulent flow using laser-induced fluorescence," AIAA J. **23,** 1932–1936 (1985).

18. M. Slack and A. Grillo, "Investigation of hydrogen–air ignition sensitized by nitric oxide and nitrogen dioxide," NASA Rep. CR-2896 (Grumman Aerospace Corporation, Bethpage, N.Y., October 1977).

19. N. M. Laurendeau, "Temperature measurements by light-scattering methods," Prog. in Energy Combust. Sci. **14,** 147–170 (1988).

20. I. S. McDermid and J. B. Laudenslager, "Radiative lifetimes and electronic quenching rate constants for single-photon-excited rotational levels of NO ($A\,^2\Sigma^+$, $v' = 0$)," J. Quant. Spectrosc. Radiat. Transfer **27,** 483–492 (1982).

21. G. F. Nutt, S. C. Haydon, and A. I. McIntosh, "Measurement of electronic quenching rates in nitric oxide using two-photon spectroscopy," Chem. Phys. Let. **62,** 402–404 (1979).

22. T. J. McGee, G. E. Miller, J. Burris, Jr., and T. J. McIlrath, "Fluorescence branching ratios from the $A\,^2\Sigma^+$ ($v' = 0$) state of NO," J. Quant. Spectrosc. Radiat. Transfer **29,** 333–338 (1983).

23. B. K. McMillin, "Instantaneous two-line PLIF temperature imaging of nitric oxide in supersonic mixing and combustion flow fields," Ph. D. dissertation (Department of Mechanical Engineering, Stanford University, Stanford, Calif., 1993).

24. J. A. Gray, P. H. Paul, J. L. Durant, Jr., and J. W. Thoman, Jr., "Collisional electronic quenching of NO ($A\,^2\Sigma^+$) measured at high temperatures," in *Technical Digest of the 31st Aerospace Sciences Meeting* (American Institute of Aeronautics and Astronautics, Washington, D.C., 1993), paper 93–0924.

25. I. van Cruyningen, A. Lozano, and R. K. Hanson, "Quantitative imaging of concentration by planar laser-induced fluorescence," Exp. Fluids **10,** 41–49 (1990).

26. M. P. Lee, B. K. McMillin, J. L. Palmer, and R. K. Hanson, "Planar fluorescence imaging of a transverse jet in a supersonic cross flow," J. Propul. Power **8,** 729–735 (1992).

27. J. E. Broadwell and M. G. Mungal, "Large-scale structures and molecular mixing," Phys. Fluids A **3,** 1193–1206 (1991).

28. B. K. McMillin, J. L. Palmer, J. M. Seitzman, and R. K. Hanson, "Two-line instantaneous temperature imaging of NO in a SCRAMJET model flow field," in *Technical Digest of the 31st Aerospace Sciences Meeting* (American Institute of Aeronautics and Astronautics, Washington, D.C., 1993), paper 93–0044.

SEMICONDUCTOR LASER ABSORPTION DIAGNOSTICS OF ATOMIC OXYGEN IN AN ATMOSPHERIC-PRESSURE PLASMA

D. S. Baer,† H. A. Chang, and R. K. Hanson

High Temperature Gasdynamics Laboratory, Department of Mechanical Engineering,
Stanford University, Stanford, CA 94305, U.S.A.

Abstract—Narrow-bandwidth semiconductor (GaAlAs) lasers have been used to record spectrally resolved atomic oxygen (7772 Å) and argon (8425 Å) lineshapes, corresponding to the $3s^5S_2^0 \to 3p^5P_3$ and $4s^3P_1 \to 4p^3D_2$ transitions, in an atmospheric pressure, 1.4-kW, 27-MHz inductively coupled argon–oxygen (12% O_2/argon) plasma. Electron number density and kinetic temperature values were inferred from the Stark- and Doppler-broadening components of the absorption lineshapes, respectively. The ionization temperature was calculated from the measured electron number density assuming ionization (Saha) equilibrium. Values of excited-state species number density and population temperature were determined from the frequency-integrated absorption coefficient for each transition. The difference between the ionization and population temperatures reflects the presence of a suprathermal electron number density in the flowfield. In addition, the excellent agreement between the kinetic and population temperatures suggests that the population in the oxygen and argon lowest excited states may be described by a Boltzmann distribution at the kinetic temperature. The methods presented extend effectively the range of semiconductor-laser diagnostics to mixed-gas plasmas and flowfields containing atomic oxygen.

INTRODUCTION

Semiconductor-laser diagnostics have recently been developed to determine important plasma parameters in atmospheric-pressure argon plasmas from Stark-affected absorption and fluorescence lineshape measurements.[1-3] Values of electron number density (n_e), electron temperature (T_e), kinetic temperature (T), ionization temperature (T_i), and population temperature (T_{pop}) have been inferred directly from lineshape analyses of measured Stark-broadened and -shifted profiles. In addition, spatially resolved values of saturation intensity (I_{sat}) and nonradiative collisional transfer (quench) rate have been determined from analyses of partially saturated lineshapes.[3]

In the present investigation, a pair of narrow-bandwidth semiconductor (GaAlAs) lasers were operated independently and used to record highly resolved atomic oxygen (7772 Å) and argon (8425 Å) absorption lineshapes, corresponding to the transitions $3s^5S_2^0 \to 3p^5P_3$ and $4s^3P_1 \to 4p^3D_2$, in an atmospheric-pressure, 27-MHz, inductively coupled argon–oxygen plasma (ICP). The measurements were made 6 mm above the induction coil ($z = 6$ mm). The gas mixture supplied to the torch which was used to maintain the plasma flowfield was 12% O_2 in argon. Values of n_e, T, T_i, and T_{pop} were determined from line-broadening analyses and frequency-integrated line intensities. The extent of local thermodynamic equilibrium (LTE) in the probed region was assessed from the parameters inferred from each probed transition.

Partially ionized atmospheric-pressure plasmas which include appreciable quantities of inexpensive gases such as N_2 and/or O_2 have significant practical advantages over the relatively common pure argon flowfields. For example, the mixed-gas plasma can reduce the overall operating cost, expand the analytical capability, and provide additional variables for operational optimization compared with the conventional argon flowfield.[4-6] In addition, atomic oxygen is an important constituent in many high temperature environments (e.g., hypersonic air flows). Hence diagnostic techniques capable of probing atomic oxygen at high temperatures are of broad interest.

†To whom all correspondence should be addressed.

THEORY

Figures 1 and 2 show atomic oxygen and argon energy-level diagrams which include the relevant states and wavelengths for the transitions investigated. The large energy spacing between the ground and first excited states in both atomic energy-level structures effectively prohibits single-photon excitation from the atomic ground states and monitoring of emission from the resonance levels. Absorption-based techniques, however, can provide effective methods for probing the oxygen-3p and the argon-4s levels, the lowest excited levels of each atom. Since a description of absorption lineshape theory for argon has been described previously,[1,2] only the fundamental issues and details pertinent to atomic oxygen spectroscopy will be discussed.

The spectral transmission, $T(v)$, of a probe beam of light of frequency v through a linearly absorbing medium may be expressed[1]

$$T(v) = I(v)/I_0 = \exp(-k(v)\,\mathrm{d}x), \tag{1}$$

where $T(v)$ is the spectral transmittance, $I(v)$ is the transmitted intensity at frequency v, I_0 is the incident beam intensity, and $k(v)$ is the spectral absorption coefficient, which may be expressed[1]

$$k(v) = hvn_1(B_{lu}/c)(1 - \exp(-hv/kT_{ex}))\phi(v), \tag{2}$$

where n_1 is the lower state number density, B_{lu} is the Einstein coefficient for absorption between levels l and u, T_{ex} is the excitation temperature which describes the ratio of populations in the laser-coupled excited states l and u, and $\phi(v)$ is the lineshape function. The frequency integral of the lineshape function is normalized to unity, $\int \phi(v)\,\mathrm{d}v \equiv 1$. The lower state number density, n_1 may be related to the population temperature, T_{pop}, for a system in Boltzmann equilibrium with the ground state, through the relation

$$n_1/n_a = g_1/Z_a \exp(-E_1/kT_{pop}), \tag{3}$$

where g_1 and E_1 are the lower state degeneracy and excitation energy; Z_a and n_a are the atomic partition function and total species number density, respectively.

The lineshape function, $\phi(v)$, reflects the thermodynamic state of the plasma and is a result of the various broadening mechanisms acting on the absorbing particle. Hence an accurate determination of plasma state parameters from spectral profile analyses requires proper consideration of all significant broadening mechanisms. In general, collisional interactions and radiative decay give rise to Lorentzian lineshapes and relative motional (Doppler) effects yield Gaussian profiles. If the
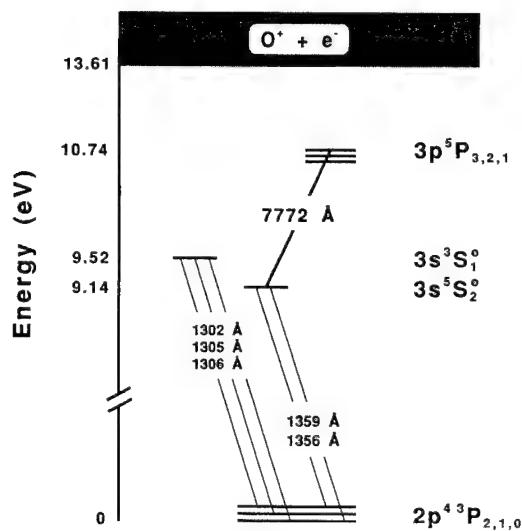
Fig. 1. Energy-level diagram of atomic oxygen illustrating the relevant transitions for the present investigation.
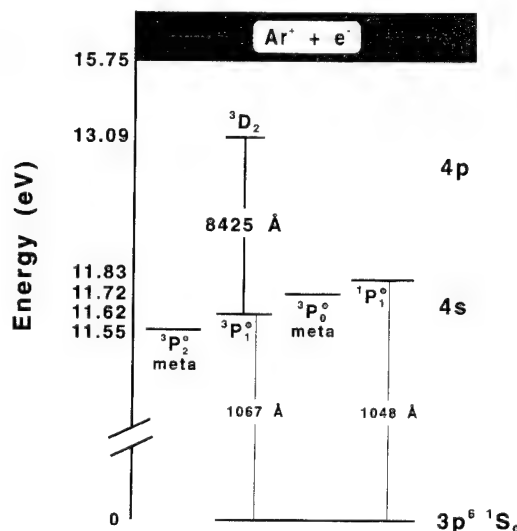
Fig. 2. Energy-level diagram of argon illustrating the relevant transitions for the present investigation.

individual broadening mechanisms are uncorrelated, the measured lineshape may be accurately described by a Voigt profile in terms of the kinetic temperature and the Voigt a parameter, which is given by

$$a \equiv (\ln 2)^{1/2} \Delta v_c / \Delta v_D, \tag{4}$$

where Δv_c and Δv_D are the Lorentzian and Doppler widths (FWHM) of the lineshape, respectively.[1]

For partially ionized atmospheric-pressure plasmas, the radiative and collisional interactions which reduce the level lifetimes include natural, resonance, van der Waals, and Stark-broadening mechanisms. For the probed argon and oxygen transitions, natural broadening (Δv_N), due to the finite lifetimes of the upper and lower states in the transition, contributes 245 and 5.4 MHz to the total Lorentzian lineshape components, respectively.[7] Resonance broadening is proportional to the oscillator strength of a radiative transition connecting a probed level to the ground state. Since the lower state ($3s^5 S_2^0$) of the probed oxygen transition is optically connected to the closely spaced "ground" states through a pair of weak (quintet–triplet) transitions[7] (Fig. 1), the resonance broadening contribution to the total Lorentzian width is relatively insignificant and may be neglected. [Note that resonance (triplet–triplet) transitions ($\lambda \approx 130$ nm) from the nearby $3s^3 S_1^0$ state (76795 cm^{-1}) to the ground states have significantly stronger oscillator strengths.][7] Conversely, resonance broadening must be considered in the argon lineshape analysis since the oscillator strength of the radiative transition which connects the probed argon lower level to the ground state is non-negligible.[3,7]

Van der Waals (pressure) broadening, due to non-radiative interactions with other neutral species, may be significant in mixed-gas flowfields. The theoretical relation which describes the Lorentzian width (FWHM) due to van der Waals broadening, $\Delta\lambda_{vdw}$, is given in MKS units by[8]

$$\Delta\lambda_{vdw}(\text{GHz}) = N \left(\frac{9\pi\hbar^5 \overline{R}_\alpha^2}{16 m_e^3 E_p^2} \right)^{2/5} \bar{v}^{3/5} 10^{-9}, \tag{5a}$$

where N is the perturber number density, m_e is the electron mass, E_p is the perturber resonance-level excitation energy (e.g., $E_p = 1.86 \times 10^{-18}$ J, 1.52×10^{-18} J for argon and oxygen perturbers, respectively),[7] $\bar{v}$ (m/sec) is the mean relative velocity between the perturber and absorber, and $\overline{R}_\alpha^2$ is the square of the coordinate vector of the radiating electron. For the oxygen transition, the nominal value of the square of the coordinate vector is $\overline{R}_\alpha^2 \approx 44$. Furthermore, for atmospheric-pressure flowfields consisting of atomic oxygen and argon, the van der Waals contribution to the total Lorentzian width for the oxygen transition may be expressed

$$\Delta\lambda_{vdw}(\text{GHz}) \approx 760 \, T^{-0.7} (1.3\chi_O + \chi_{Ar}), \tag{5b}$$

where χ_O and χ_{Ar} are the mole fractions of atomic oxygen and argon in the flowfield, respectively.

For non-hydrogenic species, the total theoretical Stark width (FWHM), $w_{th}(\text{Å})$, and shift, $d_{th}(\text{Å})$, due to Coulombic interactions with charged particles, may be described in terms of state-specific parameters, n_e and T, by the relations[9]

$$w_{th} \approx 2[1 + 1.75 \times 10^{-4} n_e^{1/4} \alpha (1 - 0.068 n_e^{1/6} T_e^{-1/2})] \, n_e w \, 10^{-16} \tag{6}$$

$$d_{th} \approx 2\left[\frac{d}{w} \pm 2.0 \times 10^{-4} n_e^{1/4} \alpha (1 - 0.068 n_e^{1/6} T_e^{-1/2}) \right] n_e w \, 10^{-16}, \tag{7}$$

where w (Å) is the electron impact parameter, α is the ion broadening parameter, and the ratio d/w is the relative electron impact shift.[8,9] The parametric variations of the tabulated parameters[9] with n_e and T_e are included in Eqs. (6, 7). The Stark shift is generally towards longer wavelengths except for negative values of d/w.

For typical conditions encountered in the present investigation (i.e., $T = 8300$ K and $n_e = 3.4 \times 10^{15}$ cm^{-3}), the effective Stark parameters for the probed oxygen transition were $\alpha \approx 0.013$, $w \approx 0.036$, and $d \approx 0.014$, whereas for the probed argon transition, the values were $\alpha \approx 0.011$, $w \approx 0.047$, and $d \approx 0.015$.[10] For a system of particles with a Maxwellian velocity distribution, the relation between the Doppler-broadening linewidth, Δv_D (FWHM), and the kinetic temperature is given by[11]

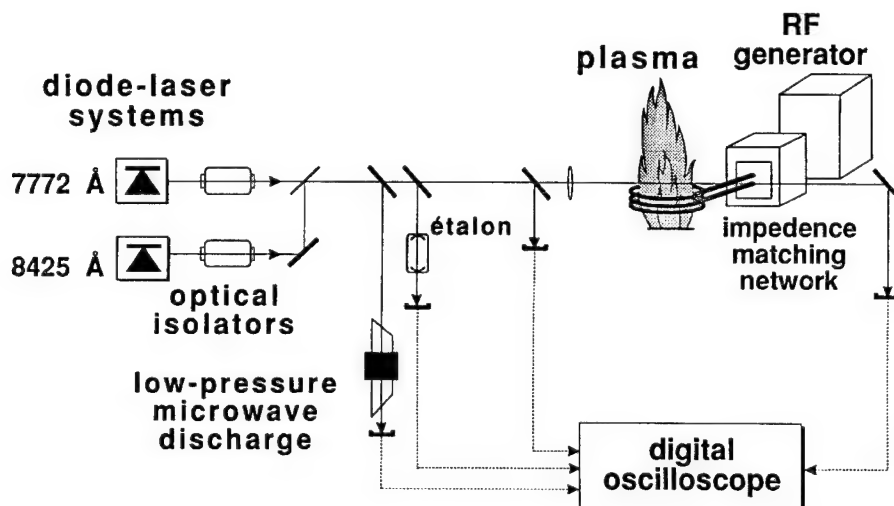$$\Delta v_D / v_0 = (8 \ln 2 \, kT/Mc^2)^{1/2}, \tag{8}$$

Fig. 3. Schematic diagram of the experimental setup.

where M is the absorber mass and v_0 is the transition linecenter frequency. Thus, the Voigt parameters a and T, which accurately describe a measured lineshape, may be used to determine the total Lorentzian width and kinetic temperature in the probed region.

The frequency integral of the spectral absorption coefficient yields the integrated absorption coefficient, K, given by[1]

$$K = hvn_1(B_{lu}/c)\,[1 - \exp(-hv/kT_{ex})],\tag{9}$$

Since the exponential term in Eq. (9) is relatively insensitive to changes in T_{ex}, the population temperature, T_{pop}, is the parameter which essentially describes the lower state number density and thus may be determined from the measured integrated absorption coefficient, Eqs. (3, 9).[1]

The ionization temperature, T_i, may be determined for a system in ionization equilibrium from the measured electron number density and the Saha equation, given by[11]

$$n_e n_i/n_a = (2Z_i/Z_a)(2\pi m_e kT_e)^{3/2}/h^3 \exp(-E_i/kT_i),\tag{10}$$

where n_i is the ion number density, E_i is the effective ionization energy of the probed species, and Z_i is the ion partition function. Since the Saha equation is relatively insensitive to the electron temperature in the pre-exponential term (i.e., $T_e^{3/2}$), the ionization temperature is the parameter which essentially describes the charged particle number density. Moreover, since results from previous investigations suggest that the electrons and heavy particles are in kinetic equilibrium, the ionization temperature, T_i, may be determined from measured values of n_e and T from Eq. (10).[1]

EXPERIMENTAL STUDIES

Figure 3 is a schematic diagram of the experimental setup which was used for simultaneous measurements of oxygen and argon absorption lineshapes in an ICP flowfield and a low-pressure microwave discharge. A detailed description of the basic setup for a single laser experiment has been described previously.[1] In the present experiment, a pair of semiconductor lasers [Laser #1: Sharp LT021MD (7772 Å); Laser #2: Spectra Diode Labs 5410 (8425 Å)] were operated independently and tuned across the desired transitions by modulating the individual injection currents at a rate of 500 Hz while maintaining constant case temperatures. The output beams were directed through separate tunable optical isolators (Optics for Research NIR-5) to minimize retroreflections from disturbing the single-mode operation of the lasers.

The operating conditions for Laser #1 (case temperature = 9.0°C, bias current = 65 mA, current modulation amplitude = 120 mA) provided a 54-GHz spectral scan centered about the oxygen absorption line (7772 Å), the strongest of three closely spaced transitions.[7] The neighboring oxygen transition $3s^5S_2^0 \rightarrow 3p^5P_2$ (7774 Å) could also be probed by appropriately varying the

injection current and increasing the case temperature to about 11°C. Since the signal-to-noise ratio for the lineshape recorded from the 7772 Å transition was about twice that of the 7774 Å transition due to the larger oscillator strength (f_{lu}) (i.e., for 7772 A, $f_{lu} = 0.431$; 7774 Å, $f_{lu} = 0.307$),[7] only the stronger transition was probed in the present investigation.

The operating conditions for Laser #2 (case temperature = 10.5°C, bias current = 85 mA, current modulation amplitude = 7.5 mA) yielded a 52-GHz spectral scan over the argon transition (8425 Å). Each output beam was split before entering the flowfield and directed through a fixed étalon (2.00-GHz free spectral range), low-pressure microwave (2.45-GHz) discharge, and onto the face of a silicon photodetector to monitor the incident laser power to the flowfield. The absolute laser wavelength was monitored by a wavemeter (Burleigh WA-10). The incident laser powers into the flowfields for Lasers #1 and #2, measured by a (Lexel) power meter, were approx. 5 and 10 mW, respectively. The beams were focused loosely through the flowfield by a 40-cm lens. The dimensions of each beam [480 μm (horizontal) $\times$ 275 μm (vertical)] at the waist were similar and stayed relatively constant over the 1-cm pathlength through the plasma. The transmitted intensity was directed through a series of spatial filters and focused onto the face of a silicon photodetector. The measured frequency response of all detectors was > 500 kHz at the -3 dB point.

All measured lineshapes were independent of laser intensity and thus essentially free from laser-saturation (power-broadening) effects. The addition of oxygen to the flowfield will increase the effective collision rate and the saturation intensity for the probed argon and the weaker oxygen transition compared with the pure argon flowfield, since the atomic oxygen collision cross-section with electrons is almost twice the value for argon.[13] The nominal values of the laser intensities ($I_{laser} \approx 7.6$ W/cm^2) which were used to probe the transitions were substantially less than the measured I_{sat} value for the argon transition (8425 Å) in a pure argon atmospheric-pressure plasma, where $I_{sat} \approx 140$ W/cm^2.[3] Hence the observation of essentially unsaturated lineshapes for the present conditions is consistent with the results from a previous investigation.[3]

The ICP plasma was sustained at atmospheric pressure by inductively coupling 1.4 kW (< 10 W reflected) of electrical power out of a radio-frequency (r.f.) generator into gas flowing through a quartz torch with a three-turn copper induction coil. The plasma was initially ignited in a pure argon environment. Molecular oxygen was slowly introduced to the gas flow prior to entering the torch gas injection ports while the matching network impedance was adjusted to compensate for the changing plasma impedance and minimize reflected power to the generator. The volumetric gas flow rates (40 standard l/min argon, 6 standard l/min O$_2$) were metered by calibrated rotameter tubes and adjusted to achieve maximum absorption for the atomic oxygen transition at the given input r.f. power. The maximum atomic oxygen absorption for the probed transition was obtained by maximizing the product of the lower state number density and the effective pathlength (l) through the flowfield. For the given input r.f. power, variations in the relative proportions of the constituent gases resulted in a decrease in the product ($n_l l$) and consequently the effective total absorption.

The plasma volume decreased considerably as oxygen was added to the pure argon flowfield. The smaller size of mixed-gas plasmas relative to pure argon flowfields has been attributed to the thermal pinch effect that results from the dissociation of molecular gases.[12] The addition of a molecular species increases the thermal conductivity and the heat transfer rate through the flowfield which, in turn, cools the outer edges and reduces the extent of the plasma. Specifically, the thermal conductivity of oxygen at 8000 K is approx. 33% higher than that for argon.[13] Consequently, despite the slightly higher input r.f. power for the present case, the flowfield dimensions parallel and perpendicular to the direction of gas flow were approx. 20 and 50% smaller, respectively, than those for pure argon plasmas.[1-3] The origin of the coordinates is along the torch axis at the top of the induction coil, 2 mm below the nozzle exit.[1]

A low-pressure discharge, which contained nominally 2 torr of oxygen and was sustained with 80 W net electrical power from a microwave generator, provided a stable source of excited oxygen atoms and served as an absolute wavelength reference as the laser wavelength was tuned near the probed transition. The flat ends of the cylindrical discharge tube were oriented at a non-90° angle to minimize étalon effects and specular retroreflections.
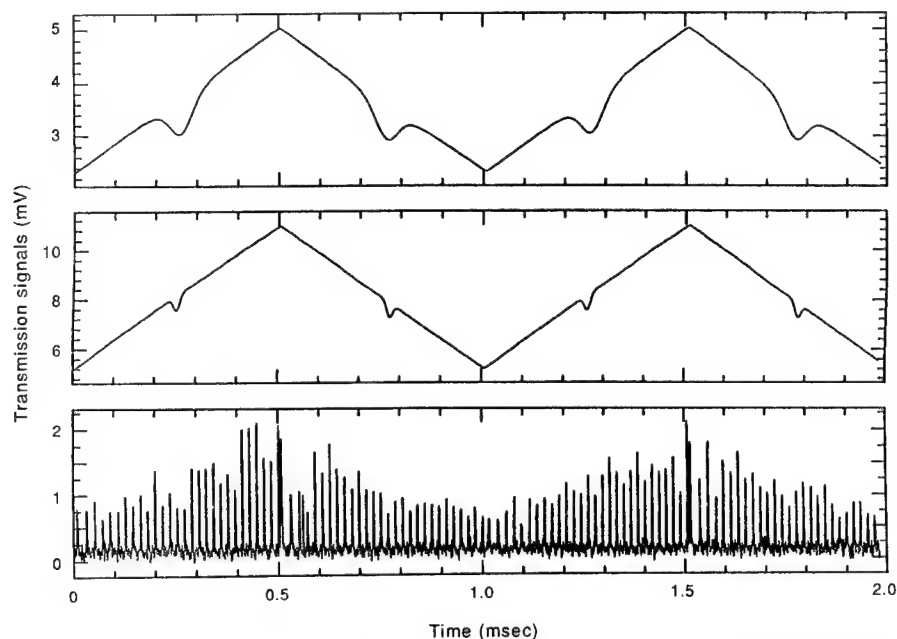
Fig. 4. Example raw data set which consists of repeated scans as the laser is tuned over the oxygen absorption line $3s^5S_2^0 \to 3p^5P_3$ (7772 Å) recorded through (top) the ICP flowfield ($z = 6$ mm), (center) the positive column of a low-pressure microwave discharge, (bottom) the fixed (2.00-GHz) étalon.

DATA ANALYSIS

Figure 4 shows a set of single-sweep data traces of spectrally resolved transmission profiles of the oxygen transition $3s^5S_2^0 \to 3p^5P_3$(7772 Å) simultaneously recorded through the ICP and the low-pressure microwave discharge, and through the fixed étalon over a 2-msec measurement interval. Spectral lineshapes were normalized by dividing the transmitted signal by the unattenuated incident laser intensity and subsequently analyzed by standard data-reduction techniques.[1] All measurements were recorded through paths which were 6 mm above the induction coil.
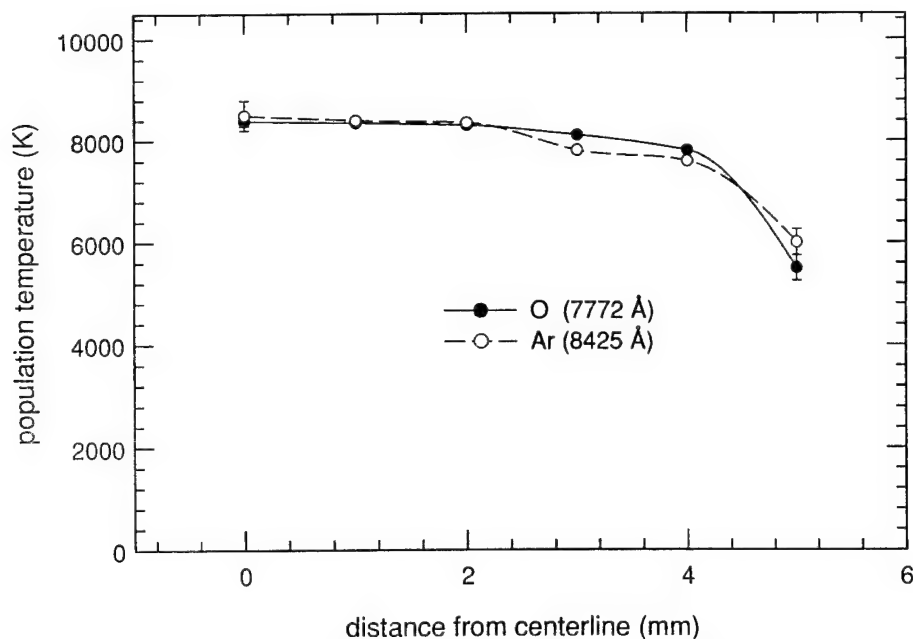
Fig. 5. Radial population-temperature distributions for the oxygen $3s^5S_2^0$ and argon $4s^3P_1$ levels in the ICP ($z = 6$ mm).
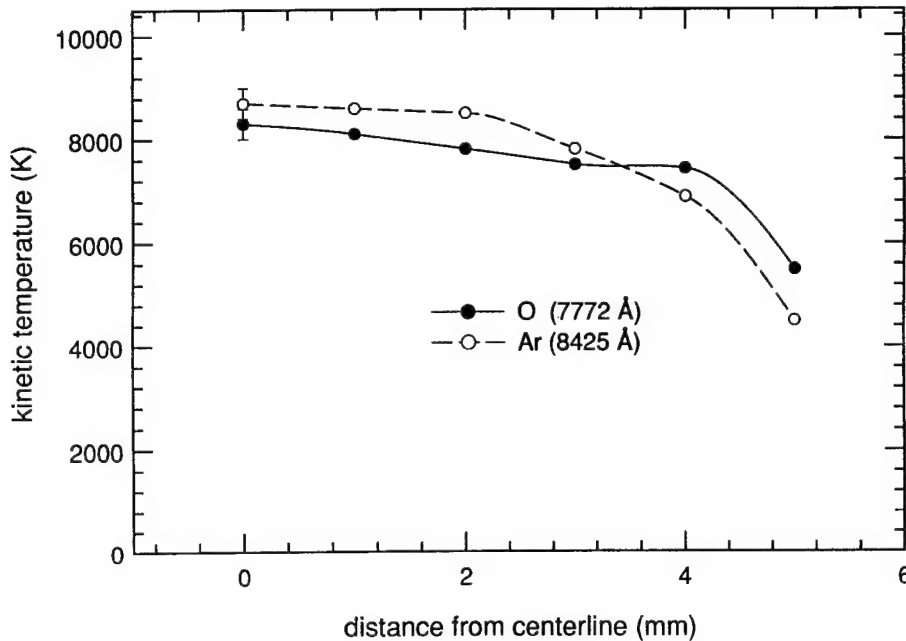
Fig. 6. Kinetic temperature distributions in the ICP ($z = 6$ mm) determined from Voigt fits of the oxygen (7772 Å) and argon (8425 Å) absorption lineshapes.

Figure 5 compares the radial population-temperature distributions for the probed oxygen ($3s^5S_2^0$) and argon ($4s^3P_1$) levels calculated from integrated absorption coefficients. The radial variation of integrated absorption coefficients was determined by performing an Abel-inversion of a measured optical-depth (product of the integrated absorption coefficient and the effective pathlength through the flowfield) lateral distribution.[1] Figures 6 and 7 show comparisons of kinetic temperature and electron number-density values, respectively, recorded over a set of paths through the flowfield. Vertical error bars were determined from the range of n_e and T values which could be calculated given the range of a and T values which result from a combination of noise within individual scans and the variation in the mean value of best-fit parameters observed during a sequence of several scans recorded at each location. The excellent agreement between the measured population and kinetic temperature values over the measured flowfield suggests that the populations in the lower-state energy levels for the probed transitions are in Boltzmann equilibrium with the ground state at the kinetic temperature.

Electron number-density values were determined from the Stark-broadening component of the measured oxygen and argon lineshapes after subtracting van der Waals and resonance broadening contributions. For example, the total Lorentzian width inferred from the best-fit Voigt profile for the oxygen absorption lineshape recorded through the diameter of the flowfield [Fig. 8(a)] was $\Delta v_c \approx 2.71$ GHz. The individual contributions to the total Lorentzian width from van der Waals and Stark broadening mechanisms, calculated from Eqs. (5, 6) and the appropriate Stark parameters, were 1.47 and 1.24 GHz, respectively. The resonance broadening contribution was negligible. Similarly, the Lorentzian width inferred from the best-fit Voigt profile for the argon absorption lineshape recorded through the same region [Fig. 8(b)] was $\Delta v_c \approx 2.48$ GHz. The Stark-broadening contribution ($\Delta v_{Stark} \approx 1.41$ GHz) to the total Lorentzian width was determined after subtracting the resonance and van der Waals broadening contributions ($\Delta v_{res} \approx 0.77$ GHz, $\Delta v_{vdw} \approx 0.30$ GHz).[1,2] The accuracy in the determination of the resonance and van der Waals broadening contributions, 20–30%, was limited by the uncertainties in broadening theory,[8,9] absorption oscillator strengths,[7] and the kinetic temperature. As a result, since approx. 40% of the 8425-A Lorentzian component is due to non-Stark broadening mechanisms, a 30% uncertainty corresponds to a 12% uncertainty in the value of n_e inferred from a lineshape analysis. Similarly, since approx. 46% of the oxygen Lorentzian component is due to non-Stark broadening mechanisms, a 30% uncertainty corresponds to a 14% uncertainty in the inferred n_e value. The

analysis implicitly assumes that the atomic and ionic constituents are relatively well mixed and that the mole fractions of the probed species remain essentially constant throughout the measured region. The agreement between the electron number-density distributions inferred from each of the transitions suggest that the measuements, theoretical Stark parameters, and respective broadening calculations are mutually consistent and that demixing effects are insignificant.

The accuracy and reliability of the fit procedure was assessed by measuring the relative sensitivity to independent changes in the Voigt-fit parameters. In order to illustrate the accuracy of the fitting procedure and verify the uniqueness of a set of best-fit Voigt parameters for a particular measured lineshape, values of Δ, the frequency-integrated squared difference between the data and the fit,[1] were determined for appropriate a and T values by optimizing a for each value of T. The procedure was repeated over a range of temperatures until the minimum Δ value, Δ_{min}, which corresponded to the best-fit Voigt parameters was determined. Voigt-fit sensitivity analyses for each of the transitions probed were determined by a method described previously,[1,3] where % variation is defined $(\Delta - \Delta_{min})/\Delta_{min} \times 100\%$. The sets of a and T values which yielded a Δ value 5% greater than Δ_{min} (i.e., $\Delta/\Delta_{min} = 1.05$) were used to describe the relative accuracy of the best-fit parameters for a particular lineshape.

The total measurement uncertainty, the vertical error bars in the parameter distributions (Figs. 5–7), was based on a combination of the uncertainty in Voigt-fit parameters for a single lineshape and the mean variation of plasma parameters over several successive measurements at a particular location. For example, for % variation = 5%, the measurement uncertainties in the Voigt-fit parameters for the oxygen absorption line where $\Delta a \approx \pm 0.03$ and $\Delta T \approx \pm 280$ K. Variations in n_e and T values from scan to scan, combined with the uncertainty associated with a particular lineshape yielded a total measurement uncertainty of $\Delta n_e \approx \pm 0.3 \times 10^{15}$ cm^{-3} and $\Delta T \approx \pm 400$ K. Similarly, for the argon absorption line, the uncertainty estimates for an individual lineshape, for % variation = 5%, were $\Delta a \approx \pm 0.06$ and $\Delta T \approx \pm 300$ K, and the corresponding total measurement uncertainty estimates were $\Delta n_e \approx \pm 0.3 \times 10^{15}$ cm^{-3} and $\Delta T \approx \pm 500$ K.

Figure 9 compares the measured kinetic and population temperature distributions with the ionization temperatures calculated from measured values of electron number density and Eq. (10), and assuming all species are in translational equilibrium. Since Stark broadening theory is independent of LTE considerations,[8,9] the significant difference between T_i and the kinetic
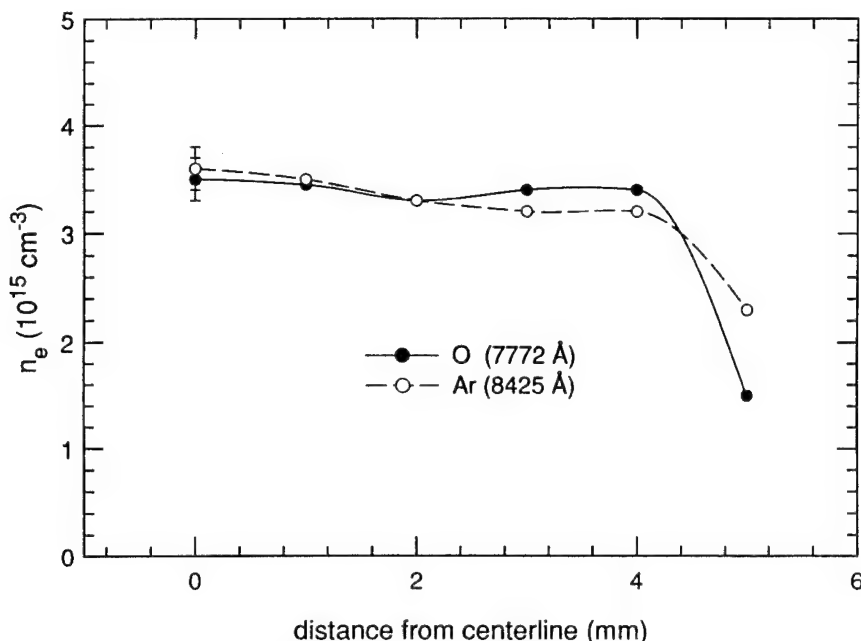

Fig. 7. Electron number density distributions in the ICP ($z = 6$ mm) determined from the Stark-broadening contribution to the oxygen (7772 Å) and argon (8425 Å) absorption lineshapes.
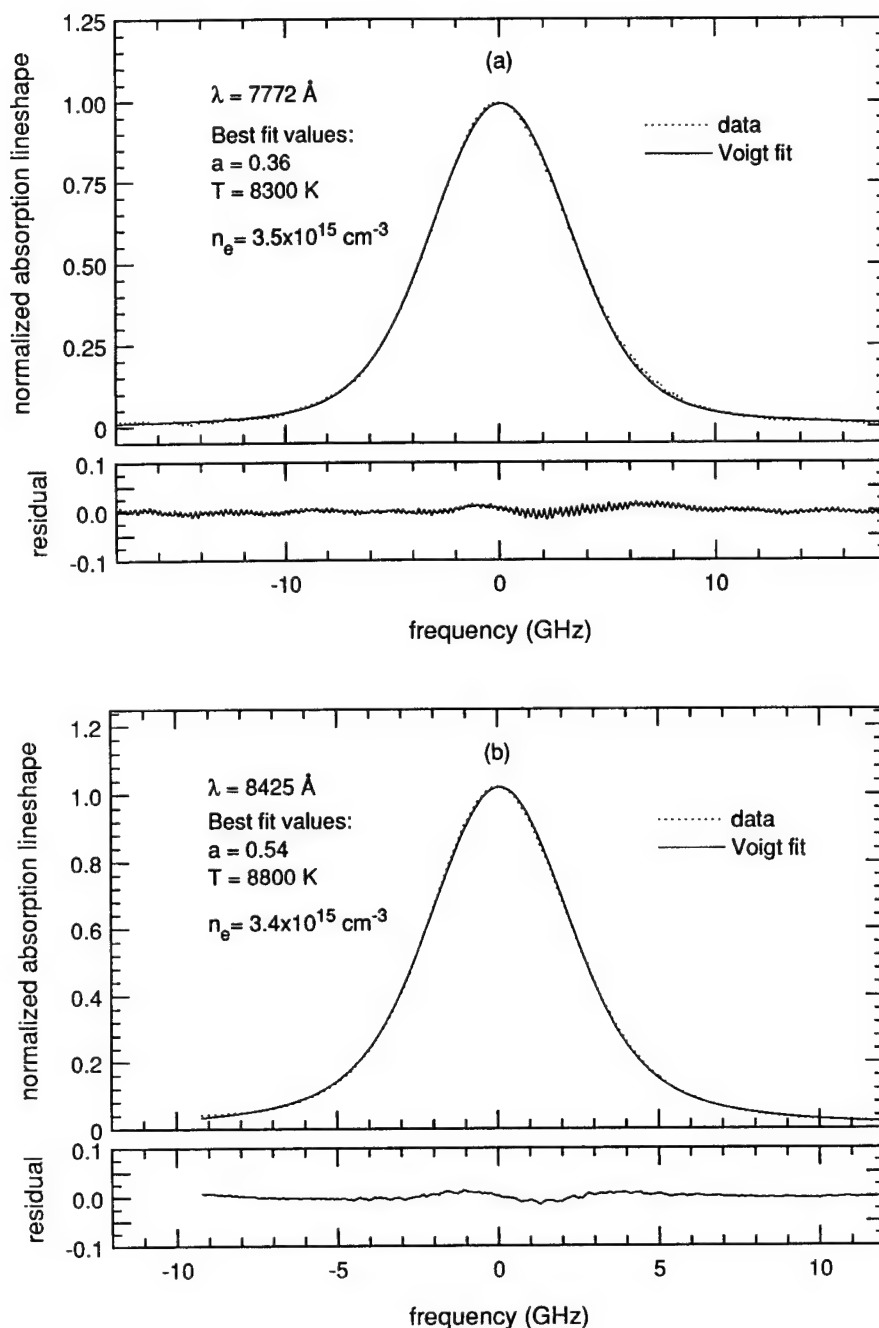
Fig. 8. Example of reduced absorption lineshapes recorded in the ICP from single scans of the (a) oxygen $3s^5S_2^0 \rightarrow 3p^5P_3$ and (b) argon $4s^3P_1 \rightarrow 4p^3D_2$ transitions. The residual is the difference between the data and the best-fit Voigt profile.

temperature (e.g., at the centerline, $T_i - T \approx 740$ K) strongly suggests the presence of a suprathermal electron number density. The present results are consistent with previous absorption and fluorescence measurements in pure argon plasmas.[1-3] The elevated electron population in the ICP is probably due to an incomplete equilibration between atoms and electrons which results from the relatively slow recombination rate compared with the characteristic flow rate to the observation region and the relatively inefficient energy transfer process.

Equilibrium calculations indicate that O_2 is almost totally dissociated at the temperatures encountered (e.g., $n_{O_2}/n_O < 0.003$ for $T > 6000$ K) and thus does not significantly contribute to the flowfield kinetics in the probed region. Moreover, since the oxygen ion–electron recombination rate

is not appreciably greater than that for argon,[14] the effective electron–ion recombination rate in the argon–oxygen plasma will not change significantly compared with the pure argon case. As a result, the addition of 12% O_2 to the pure argon flowfield will not alter the recombining nature of the plasma. The observation of an elevated electron number density is consistent with previous emission-based measurements in argon–oxygen[6] and air plasmas.[15]

Figure 10 shows a reduced oxygen absorption lineshape, normalized by the linecenter value [where $k(v_0)l \approx 0.12$, $l \approx 4$ cm)], recorded along the axis of the low-pressure microwave discharge. The Voigt parameters which were determined from a best-fit analysis ($a = 0.02$, $T = 820$ K) suggest that Doppler broadening is the predominant broadening mechanism for the probed transition. The nominal Lorentzian width which corresponded to the measured a parameter was 47 MHz ($a \approx 0.02$). Hence, for the given discharge conditions, the inferred collision width ($\Delta v_c \approx 42$ MHz), determined after accounting for natural broadening, was presumably due to collisional interactions between atomic and molecular oxygen. Since nonradiative collisional interactions which induce a finite broadening and shift are often correlated,[8] the relatively insignificant Lorentzian width suggests that effects which induce a line shift are small. Thus the low-pressure microwave discharge provides a reliable absolute wavelength reference for the present investigation. Figure 11 shows the reduced absorption profiles of the atomic oxygen transition recorded simultaneously through the diameter of the ICP and along the axis of the low-pressure discharge. The total shift ($\Delta v_0 \approx 0.46$ GHz) was determined from the spectral separation between Voigt fits through each absorption lineshape.

As demonstrated previously in a pure argon plasma, a value for the electron number density may be inferred from an accurate measurement of the Stark shift of a spectral line.[1,2,8,10] For the oxygen transition studied here, however, the contribution to the total shift from charged-particle (Stark) interactions was difficult to ascertain due to a relatively large uncertainty in the non-negligible van der Waals contribution. Although Lorentzian width due to van der Waals broadening effects may be determined from Eq. (5), the theoretical relation for the corresponding shift is only approximate.[8,16] In fact, the width-to-shift ratio is extremely transition-sensitive and can vary from about 2.8, in the ideal case for a pure van der Waals interaction, to greater than 5, for some atomic
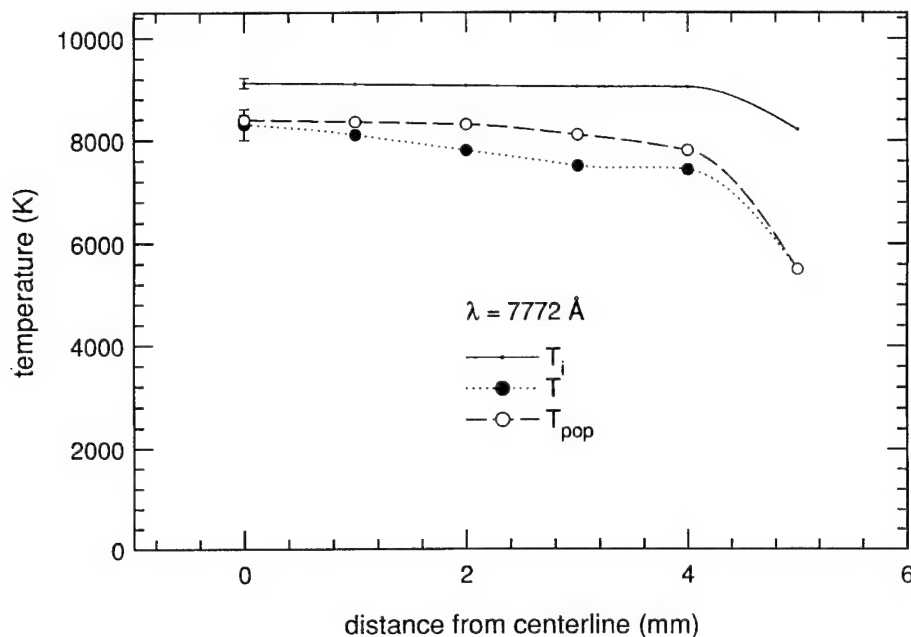

Fig. 9. Temperature distributions in the ICP ($z = 6$ mm) determined from analyses of oxygen absorption lineshapes ($3s^5S_2^0 \rightarrow 3p^5P_3$). T_i is the ionization temperature calculated from n_e values determined from a Stark-broadening analysis assuming Saha equilibrium. T is the kinetic temperature determined from the Gaussian component of the Voigt lineshape. T_{pop} is the population temperature determined from the frequency-integrated lineshape.
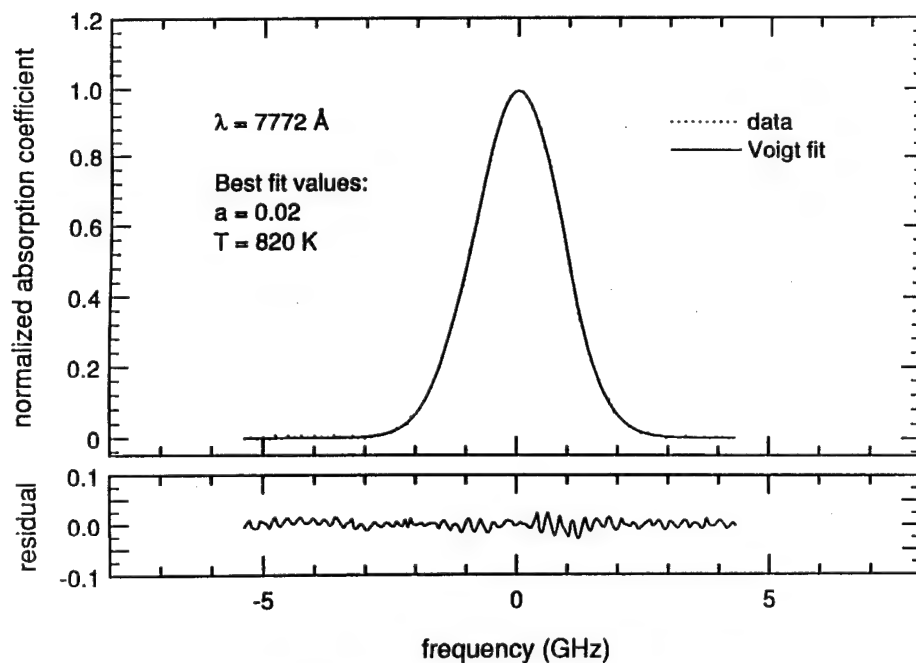
Fig. 10. Example absorption lineshape of the oxygen transition $3s^5S_2^0 \rightarrow 3p^5P_3$ recorded along the axis of a low-pressure oxygen (2-torr) microwave (2.45-GHz) discharge (net input power 80 W).

transitions.[16] Nevertheless, the magnitude of the van der Waals contribution to the total shift may be estimated from the difference between the total measured shift and the calculated Stark shift from Eq. (7) and n_e and T values inferred from lineshape analyses. For example, the theoretical Stark-shift contribution to the measured total shift ($\Delta \nu_0 \approx 0.46$ GHz), calculated for the conditions present in Fig. 11 ($n_e = 3.4 \times 10^{15}\,\mathrm{cm}^{-3}$, $T = 8300$ K) from Eq. (7) and the appropriate Stark
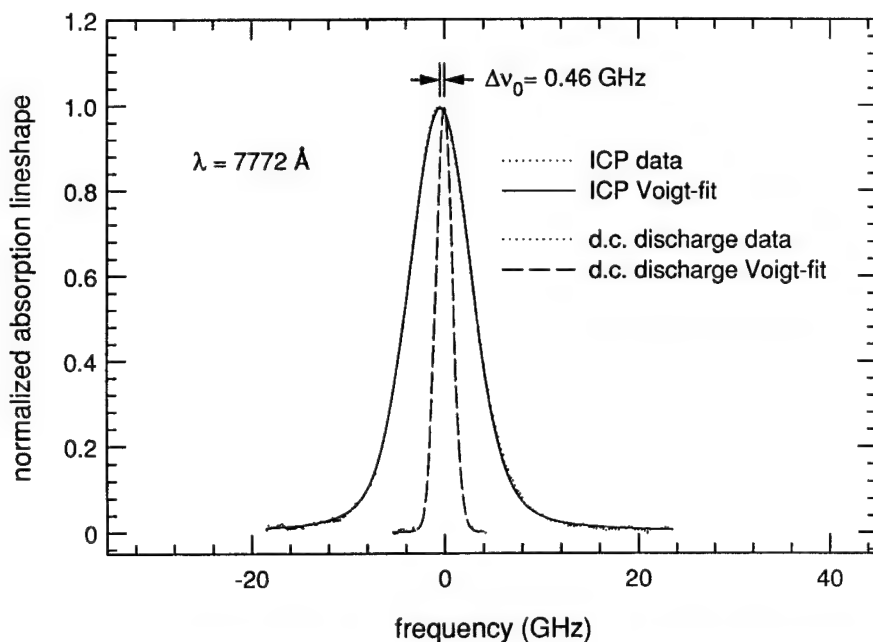
Fig. 11. Reduced absorption lineshapes and best-fit Voigt profiles of the oxygen transition $3s^5S_2^0 \rightarrow 3p^5P_3$ (7772 A) recorded simultaneously through the ICP ($z = 6$ mm) and the low-pressure microwave discharge reference cell.

parameters[9] is ≈ 0.26 GHz. Consequently, the inferred van der Waals shift is 0.20 GHz and the van der Waals width/shift ratio for the oxygen transition is $3s^5S_2^0 \rightarrow 3p^5P_3$ is approx. 7.

The Stark-shift parameter for the atomic oxygen multiplet $3p^5P \rightarrow 5d^5D^0$ (5330 Å), which includes the upper level of the probed oxygen transition (i.e., $3p^5P_3$), has been estimated experimentally from emission lineshapes recorded in an atmospheric-pressure wall-stabilized d.c. arc and shown to vary from the theoretical value by approx. 52%.[17] The relatively large variation of the Stark-shift parameter for the 5330-Å multiplet may be due to unspecified effects involving the probed state in the $3p^5P$ manifold which are not adequately included in the theoretical Stark calculations. Thus, since the Stark shift is nearly proportional to the state-specific shift parameter in Eq. (7), for the present investigation, the uncertainty in the calculated Stark shift may be $\pm 50\%$ and the uncertainty in the inferred van der Waals shift and in the corresponding van der Waals width/shift ratio may be $\pm 65\%$. An accurate determination of the individual contributions to the total shift of the oxygen line from the various collisional interactions requires a series of independent measurements under controlled conditions to establish the sensitivity of the shift to variations in the number density of neutral and charged species.

CONCLUSIONS

Semiconductor-laser absorption diagnostics have been applied to atomic oxygen and argon transitions in an argon–oxygen atmospheric-pressure plasma (12% O_2/argon) generated by a 27-MHz inductively coupled plasma torch. The electron number density, kinetic temperature, ionization temperature, and population temperature of the plasma were determined from analyses of measured spectrally resolved oxygen $3s^5S_2^0 \rightarrow 3p^5P_3$ (7772 Å) and argon $4s^3P_1 \rightarrow 4p^3D_2$ (8425 Å) absorption lineshapes which were recorded 6 mm above the induction coil. The measured electron number-density values determined from both transitions are in excellent agreement throughout the measured region and thus suggests that the measurements and broadening calculations are consistent. In addition, the agreement between measured values of kinetic and population temperature suggests that the lower states of the probed transitions are in Boltzmann equilibrium with the ground state at the kinetic temperature. Finally, a comparison of the measured kinetic, population, and ionization temperatures illustrates the extent of the suprathermal electron number density throughout the measured region. Hence, for the present flowfield conditions, the relationships between the measured temperature distributions may be expressed $T_i > T_{pop} \approx T$.

The presence of an elevated electron number density in the argon–oxygen flowfield is qualitatively similar to the case of pure argon atmospheric-pressure plasma. However, in contrast with the pure argon case, the difference between the population and atomic kinetic temperatures becomes insignificant with the addition of 12% O_2 to the total gas flow.

Atomic oxygen lineshapes were also recorded in a microwave (2.45-GHz) discharge filled with 2 torr of oxygen and sustained with a net input power of 80 W. The atomic kinetic temperature inferred from the predominantly Doppler-broadened profile was 820 K.

Measurements of atomic oxygen absorption lineshapes simultaneously recorded through the atmospheric-pressure plasma and the low-pressure discharge allowed an accurate determination of the net shift of the probed transition in the plasma. An approximate value of the van der Waals shift and width-to-shift ratio for the probed oxygen transition was inferred from the difference between the net shift and the calculated Stark-shift contribution determined from measured electron number-density and kinetic temperature values, tabulated state-specific parameters, and the theoretical Stark-shift relation. The techniques and results presented illustrate the effectiveness of semiconductor laser absorption diagnostics for the determination of state parameters for the important cases of mixed-gas plasmas and flowfields containing atomic oxygen.

REFERENCES

1. D. S. Baer and R. K. Hanson, *JQSRT* **47**, 455 (1992).
2. D. S. Baer, H. A. Chang, and R. K. Hanson, *JOSA B* **9**, 1968 (1992).
3. D. S. Baer and R. K. Hanson, *Appl. Opt.* **31**, 948 (1993).

4. H. A. Chang, D. S. Baer, and R. K. Hanson, AIAA-92-0628 31st Aerospace Sciences Meeting, Reno, NV (January 1993).
5. E. H. Choot and G. Horlick, *Spectrochim. Acta* **41B,** 889 (1986).
6. E. H. Choot and G. Horlick, *Spectrochim. Acta* **41B,** 907 (1986).
7. W. L. Wiese, M. W. Smith, and B. M. Glenon, "Atomic Transition Probabilties," NBS, U.S. National Bureau of Standard Reference Series-4, Vol. 1, U.S. Government Printing Office, Washington, DC (1966).
8. H. Griem, *Plasma Spectroscopy*, McGraw–Hill, New York, NY (1964).
9. W. L. Wiese, "Line broadening," in *Plasma Diagnostic Techniques*, R. H. Huddlestone and S. L. Leonard eds., p. 227, Academic Press, New York, NY (1974).
10. H. Griem, *Spectral Line Broadening by Plasmas*, Academic Press, New York, NY (1974).
11. M. Mitchner and C. H. Kruger, *Partially Ionized Gases*, Chap. 2, Wiley–Interscience, New York, NY (1973).
12. S. Greenfield, I. L. Jones, H. McGreachin, and P. B. Smith, *Anal. Chim. Acta* **74,** 225 (1975).
13. S. V. Dresvin, *Physics and Technology of Low-temperature Plasmas*, Chap. 2, Iowa State University Press, Ames, IA (1977).
14. I. I. Sobelman, L. A. Vainshtein, and E. A. Yukov, *Excitation of Atoms and Broadening of Spectral Lines*, Chap. 5, Springer, Berlin (1981).
15. H. U. Eckert, *J. Appl. Phys.* **41,** 1529 (1970).
16. W. Demtröder, *Laser Spectroscopy, p.* 99, Springer, Berlin (1982).
17. A. Goly and S. Weniger, *JQSRT* **38,** 225 (1987).

Diode-laser absorption technique for simultaneous measurements of multiple gasdynamic parameters in high-speed flows containing water vapor

M. P. Arroyo, S. Langlois, and R. K. Hanson

A distributed-feedback InGaAsP diode laser, emitting near 1.38 μm, was used to acquire spectrally resolved absorption profiles of H_2O lines in the $\nu_1 + \nu_3$ band at a repetition rate of 10 kHz. The profiles were used for simultaneous measurements of flow parameters in high-speed, one-dimensional (1-D) transient flows generated in a shock tube. Velocity was determined from the Doppler shift, which was measured with a pair of profiles simultaneously acquired at different angles with respect to the flow direction. Temperature was determined from the intensity ratio of two adjacent lines. Pressure and density were found from the fractional absorption. From these primary gasdynamic variables, the mass and momentum fluxes were determined. Experiments were conducted with three different gas mixtures in the shock tube: pure H_2O at initial pressures lower than 3 Torr, up to 6% of H_2O in O_2 at initial pressures below 120 Torr, and up to 8% of H_2 in O_2 at initial pressures below 35 Torr. In the third case, pyrolysis of H_2/O_2 behind incident shocks produced known yields of H_2O. With all three mixtures, results compare well with 1-D shock calculations. This H_2O diagnostic strategy shows promise for applications in both ground and flight testing.

Key words: Velocimetry, flow, temperature, water vapor, diode laser, spectroscopy, mass flux, momentum flux.

Introduction

Renewed interest in supersonic combustion and hypersonic flows has increased the need for nonintrusive optical diagnostics for measuring flow parameters in high-speed gases. High-resolution spectroscopy techniques have recently been developed to provide fast, sensitive, and nonintrusive means of measuring multiple quantities such as temperature, pressure, velocity, and density.[1–3] In these methods one of the species that is present in the flow is monitored by spectrally resolved absorption spectroscopy. The species H_2O is of special interest because it naturally occurs in flows involving air, and it is also a primary combustion product. Furthermore, measurements of water vapor are generally relevant to combustion,

propulsion, and aerodynamic facilities, because water vapor can be related to performance parameters such as extent and efficiency of combustion, propulsion efficiency, and heat release.

The use of tunable semiconductor diode lasers for application of this spectroscopic technique is attractive as these lasers are compact, rugged, cost effective, compatible with optical fiber transmission, and simple to operate. These lasers are narrow-linewidth light sources whose wavelength can be tuned easily by changing the laser temperature and injection current. The fact that the laser diodes may be tuned over a range of wavelengths by varying the injection current is of special interest in high-speed flows, because fast tuning rates are obtained, and hence measurements at high temporal resolution can be made. Water vapor has many absorption bands in the emission wavelength range of these lasers (between 0.7 and 1.6 μm). The strongest absorption lines occur between 1.34 and 1.46 μm. In earlier papers[4,5] we demonstrated the application of such a spectroscopy technique by using a diode laser emitting near 1.38 μm to measure simultaneously the concentration and temperature of the water vapor present in the labora-

tory room air and in the postflame gases above a methane–air flat flame burner, both at atmospheric pressure. The laser tuning rate in these initial experiments was only 80 Hz, because the gas velocities were low. Here we present the extension of this technique to transient high-velocity and high-temperature flows, which requires an extension of the tuning rate to 5 kHz (measurement repetition rate of 10 kHz), and to a wider range of flow parameters, including pressure, density, mass flux, and momentum flux (related to thrust).

Measurement Technique

The measurement technique is based on spectrally resolved absorption of water vapor and uses a tunable near-infrared laser source; an earlier description of the method is given in Ref. 4.

The strategy for measuring the temperature of the gas is based on the ratio of two absorption line intensities, which is given by[4]

$$R = S(T_0, v_1)/S(T_0, v_2)$$
$$\times \exp[-(hc/k)(E_1'' - E_2'')(1/T - 1/T_0)], \quad (1)$$

where $S(T_0, v)$ is the line intensity of the transition centered at v (in inverse centimeters squared per inverse atmosphere), for a certain reference temperature T_0, with v_1 and v_2 referring to the two lines; h is Planck's constant (in erg seconds); k is Boltzmann's constant (in ergs per kelvin); c is the speed of light (in centimeters per second); E'' (in inverse centimeters) is the energy of the lower state of the transition, and T (in degrees Kelvin) is the gas temperature to be measured.

Thus, for a given pair of lines, the intensity ratio is a function of temperature only. In practice, it is convenient to select line 1 as the weaker of the two, so as to keep the intensity ratio between 0 and 1.[2] The sensitivity of this ratio to temperature can be obtained by differentiating Eq. (1):

$$dR/dT = (hc/k)(E_1'' - E_2'')R/T^2. \quad (2)$$

This quantity is of interest in selecting line pairs with suitable sensitivity for temperature determination.

The partial pressure of water vapor, P_{abs}, can be obtained from the Beer–Lambert relation[4] if the temperature, line intensity, and path length are known. If the mole fraction of water vapor, X, is also known we can obtain the total pressure, P, because

$$P = P_{abs}/X. \quad (3)$$

The total pressure can be alternatively inferred from the collision width of the absorption profile if sufficient information about its dependence with pressure and temperature is available. In that case the mole fraction can be inferred from Eq. (3).

The strategy to measure velocity usually consists of simultaneously recording the absorption profiles through two directions at different angles with the flow velocity, with one direction chosen to be orthogo-

nal to the expected flow direction. The profiles will be shifted in frequency, because of collision-induced shifts, which affect both profiles equally, and because of the Doppler effect, by an amount Δv_D given by

$$\Delta v_D = (v_0/c)V \cos \phi, \quad (4)$$

where v_0 is the line-center frequency, V is the flow velocity, and ϕ is the angle between the flow and the laser beam directions. The difference between the peaks of the two profiles is used to infer the velocity.

The density ρ can be obtained from the measured pressure and temperature through

$$\rho = P/(TR/M), \quad (5)$$

where R/M is the specific gas constant. Finally, the mass flux $\dot{m}$ and momentum flux $\dot{m}V$, which are of critical interest in many practical applications, can be determined from the measured density and velocity; i.e.,

$$\dot{m} = \rho V, \qquad \dot{m}V = \rho V^2. \quad (6)$$

Selection of Line Intensity Pairs

Although the Voigt profile itself can be resolved to determine both temperature and pressure, the use of a pair of lines with a temperature-dependent intensity ratio offers the potential for increased sensitivity to temperature. The two lines should have similar enough absorption coefficients that both lines are well resolved, with sufficiently different energy E'' to yield an intensity ratio that is sensitive to temperature. The lines should be close enough in frequency to be covered in a single laser scan but separated enough to be isolated one from the other. If the lines are too close, the broadening blurs the lines into a single feature, making it difficult to unambiguously determine the individual line intensities.

In the present experiments, a distributed-feedback InGaAsP diode laser from Anritsu Corporation was used as a source of monochromatic radiation.[4] Given that the maximum range of tuning of this laser is approximately 25 GHz, when its driving current is modulated at 5 kHz, the optimal separation of the lines is between 3 and 7 GHz. Previously,[4,5] we showed that there are only a few line pairs ($4_{40} \leftarrow 4_{41} + 4_{41} \leftarrow 4_{40}$ and $6_{42} \leftarrow 6_{43} + 3_{13} \leftarrow 3_{12}$, using a J_{kakc} notation) with spacing near the optimum in the limited range of wavelength available with our diode laser. The $4_{40} \leftarrow 4_{41} + 4_{41} \leftarrow 4_{40}$ pair is not good for thermometry because both transitions have the same energy E'', and so we have used for the present experiments the line pair $6_{42} \leftarrow 6_{43} + 3_{13} \leftarrow 3_{12}$. Line positions have been taken from Ref. 6 that also agree with Ref. 7; line intensities have been taken from our previous paper[4]; lower state energies have been taken from the HITRAN data base,[8] and broadening parameters have been calculated following the theoretical research of Delaye.[9] The line pair is centered around 7212.9 cm^{-1} and has a spacing of 2 GHz. Because this spacing is smaller than optimum, some blending

of the lines occurs. This will limit the accuracy of the temperature and collision-broadening measurements. The intensity ratio for this line pair and its sensitivity to temperature as a function of temperature are plotted in Fig. 1. It can be seen that the sensitivity of this line pair is maximum at around 400 K. At higher temperatures, the sensitivity decreases quite quickly to less than 10^{-4} above 1350 K. If R is determined within 0.01, the accuracy in the temperature measurements will be better than 100 K only for temperatures below 1350 K; however, at 400 K, a measurement error in R of 0.01 corresponds to an error of 1.8 K in temperature.

The line pair was accessed by operating the laser at a temperature of 46 °C and with a mean driving current of 80 mA. A triangular modulation of 35 mA amplitude at 5 kHz frequency superposed on the mean current produced a tuning range of 22 GHz. The measurement rate is twice the modulation frequency, or 10 kHz, because data are obtained from both scan directions.

Shock Tube

Flow fields in this experiment were generated behind pressure-driven incident shocks passing through a shock tube. The shock tube has a 6-m-long, 14.3-cm-diameter driven section and a 2-m-long, 5-cm-diameter driver section that expands smoothly to the full driven tube diameter immediately after the diaphragm station. The test section is located 45 cm from the end wall; it is bounded by two sets of windows permitting optical access to the flow at 90° and 60° of incidence, respectively. Three types of gas mixtures were used to fill the driven section: pure H_2O, H_2O with O_2, and H_2 with O_2. Shocks were produced using high-pressure helium to burst polycarbonate diaphragms into the gas mixtures at 296 K. Two different diaphragm thicknesses (1 or 0.25 mm) were used to increase the range of postshock conditions obtained (see Table 1).

The shock speed was measured with a series of thin-film gauges regularly spaced on the shock-tube walls. With the additional knowledge of the initial pressure P_1 of the mixture in the driven section, one can predict the gas conditions of pressure P_2, tempera-
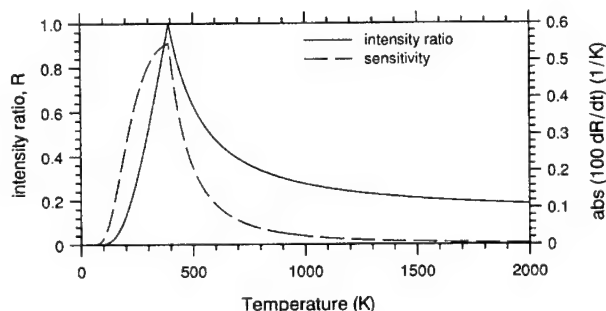
Table 1. Range of Initial Conditions, Postshock Gas Conditions, and Absorption Levels in the Incident Shock Experiments

Gas Mixture	Initial Pressure (Torr)	Postshock Conditions			Absorption Level (%)
		T (K)	P (atm)	V (m/s)	
H_2O	1–3	950–1200	0.02–0.08	1350–1700	10–30
H_2O/O_2 (0.25-mm-thick dia.)	10–100	460–950	0.1–0.5	300–900	5–15
H_2O/O_2 (1.0-mm-thick dia.)	20–120	600–1100	0.4–1.1	550–1100	7–25
H_2/O_2	15–30	950–1250^a	0.4–0.7	950–1200	3–6

^{a}Without pyrolysis.

ture T_2, and velocity V behind the incident shock by the use of the Rankine–Hugoniot relations.[10] A code similar to that described by Gardiner et al.[11] was used for the calculation. In the case of the H_2/O_2 mixtures, the mole fraction and temperature of the H_2O produced by combustion were calculated with the reaction mechanism described in Ref. 12 using the Chemkin computer codes[13] and the Sandia National Laboratories thermodynamic data base.[14] The postshock temperatures and pressures calculated from the one-dimensional (1-D) shock theory (see Table 1) were used as the initial conditions in the Chemkin calculations. These calculations indicated an increase of approximately 500 K in the temperature of the gas, because of the reaction, with a maximum mole fraction of 8.3% of H_2O being produced approximately 200 μs after passage of the shock wave, for mixtures of 8.1% H_2 in O_2. Pressure was monitored independently with a fast piezoelectric transducer for verification of postshock conditions determined by normal shock calculations.

The absorption levels obtained in the incident shock zone for the present experiments (see Table 1) range from 10% to 30% for the pure water vapor shocks, from 5% to 25% for the shocks in mixtures of 1–6% of H_2O in O_2, and from 3% to 6% for the H_2/O_2 shocks.

Experimental Procedure

The experimental arrangement used for the direct absorption detection is shown in Fig. 2. The collimated diode-laser output was split into four components: the first component passed through a low-finesse solid étalon (free spectral range, 2.00 GHz) and onto detector 2 to provide a calibration of the actual rate of wavelength tuning, the second component passed directly onto detector 1 to record the incident laser intensity as a function of time (I_0), the third component passed through the shock tube at 90° and onto detector 4 to provide the perpendicular transmission signal (I_{90}), and the fourth component passed through the shock tube at 60° and onto detector 3 to provide the oblique transmission signal (I_{60}). The last three beams were roughly balanced by varying the beam-splitter angles. The fine balance

Fig. 1. Intensity ratio and its sensitivity to temperature versus temperature for the line pair $6_{43} \leftarrow 6_{42}$, $3_{13} \leftarrow 3_{12}$ ($\nu \approx 7212.9$ cm^{-1}). The intensity ratio is defined so that it is always less than unity.
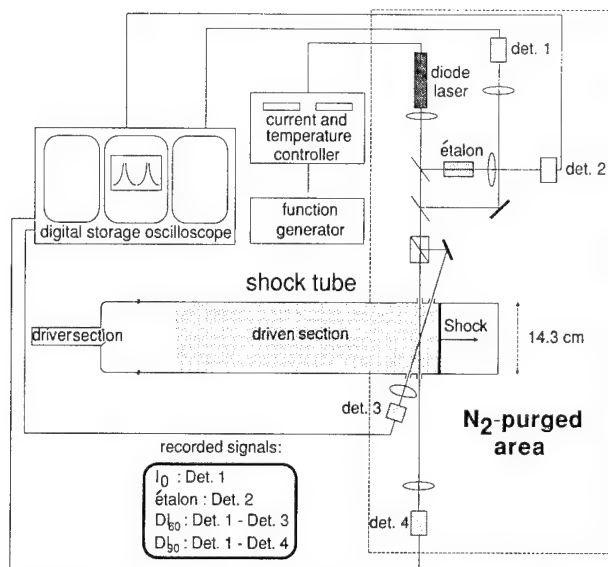
Fig. 2. Experimental schematic. High-temperature, high-speed gases are produced in a shock tube. The diode-laser output is passed through the shock tube at 90° and 60° angles relative to the flow. The laser is tuned over an absorption feature at a rate of 10 kHz, and spectral profiles are recorded in absorption.
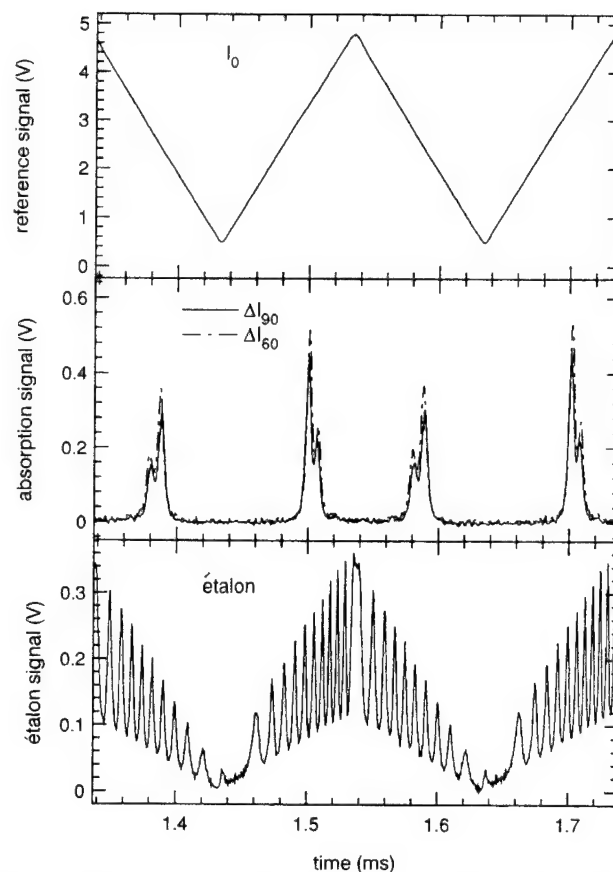

Fig. 3. Experimental absorption traces in the flow generated behind an incident shock in the shock tube. The shock wave reached the test section at 1.1 ms. Note on the middle trace the difference of the line-center positions for the absorption scans acquired at 90° and 60° to the flow direction. Calculated post-shock conditions: $T = 598$ K, $P = 0.317$ atm, $V_{gas} = 571$ m/s, 5.9% H_2O in O_2. Diaphragm thickness, 0.25 mm.

was done electronically by varying the gain of the amplifying circuits of detectors 3 and 4. Laser, detectors, and optics were enclosed in a nitrogen-purged area to prevent absorption by room air. Furthermore, the path length in room air for all the detectors was matched to minimize errors resulting from any residual absorption in the purged area. The two absorption signals ($\Delta I_{90} = I_0 - I_{90}$ and $\Delta I_{60} = I_0 - I_{60}$), the incident signal ($I_0$), and the signal from the étalon were recorded with digital oscilloscopes sampling at 0.5 μs/point. The detectors used were germanium photodiodes (EG&G J16-18A-R01M-HS) mounted in amplifier–filter packages giving a low-pass cutoff frequency (-3 dB) of 1 MHz.

The oscilloscopes were triggered by the passage of the shock upstream of the optical ports by the use of a thin-film gauge. The oscilloscopes were triggered shortly before (0.5 to 1 ms) the shock wave reached the test section and continued for 4 ms until their memory was full. Thus 40 absorption profiles were accumulated for each of the four signals. During the recording, the laser beams saw three consecutive stages of the flow: (1) room-temperature gas at initial pressure P_1, (2) gas accelerated to V behind the incident shock at P_2 and T_2 because of the incident shock, and (3) gas further heated and compressed to P_5 and T_5 because of the reflection of the shock at the end wall of the shock tube. The duration of the second period was between 0.3 and 2.1 ms, depending on the shock speed.

Sample Data

Sample data showing four repeated scans of the line intensity pair during a shock-tube experiment are shown in Fig. 3. Figure 3 shows a window of 400 μs extracted from the total 4-ms recording; the window

corresponds to a shock produced by bursting a 0.25-mm-thick diaphragm into a mixture of 5.9% H_2O in O_2 at a pressure of 35 Torr. The shock wave reached the test section 1.1 ms after the oscilloscopes were triggered. The top curve shows the laser intensity reference signal I_0; the middle curves show both absorption signals, ΔI_{60} and ΔI_{90}; and the bottom curve shows the étalon trace. Variations in I_0 are due to the dependence of the power output of the diode laser with the injection current. There is an apparent lack of symmetry between the ramp up and the ramp down on the étalon trace, which is another typical characteristic of the diode laser. This implies a discrepancy in the maximum value of the absorption signals between the ramp up and the ramp down of the tuning, because the reference intensity for a certain wavelength is different in both ramps. The two lines of the line intensity pair are not fully isolated because of the small spacing between them, as we have remarked above. The ordering of the two lines can be seen to alternate as the laser wavelength is tuned back and forth in time. Because both absorption signals were obtained with the same flow conditions of temperature and pressure, the fre-

quency shift $\Delta\nu_s$ apparent in the traces is due solely to the Doppler effect.

Figure 4 shows a reduced pair of experimental profiles corresponding to the absorption features at 1.38 ms. The quantity plotted in the absorbance, $-\ln(1 - \Delta I/I_0)$, normalized to unity at the larger peak. The time base has been converted to relative frequency by using the information in the étalon trace.[4] The location corresponding to zero frequency is set near the peak of the larger of the lines of the perpendicular (90°) data, and the identical zero is used for the oblique profile.

The experimental profiles (of normalized absorbance) are best fit using Voigt profiles, with the ratio of line intensities as an additional variable; the temperature dependence of this intensity ratio is given in Eq. (1). The separation of the lines is also determined from fits to the data. The fitting procedure minimizes the integrated squared difference between the experimental profile and a calculated profile with the same area. The fit is first optimized with respect to the shift in frequency of each profile from zero, using an assumed temperature and a given Voigt a parameter. The fit is then optimized with respect to temperature (through the intensity ratio) with the best-fit Voigt a parameter determined at each temperature. Once the best-fit a parameter and temperature are determined, the fit of the shift is reoptimized. If there is appreciable change in this fit the iteration procedure is repeated.

Because the perpendicular beam experiences no Doppler shift, the velocity is determined from the relative shift between the 90° and 60° profiles, $\Delta\nu_s$, using Eq. (4) in the form

$$V\,(\mathrm{m/s}) = 2765\Delta\nu_s\,(\mathrm{GHz}). \tag{7}$$

Because both profiles are acquired at the same gas conditions, the effects of any collision-induced line
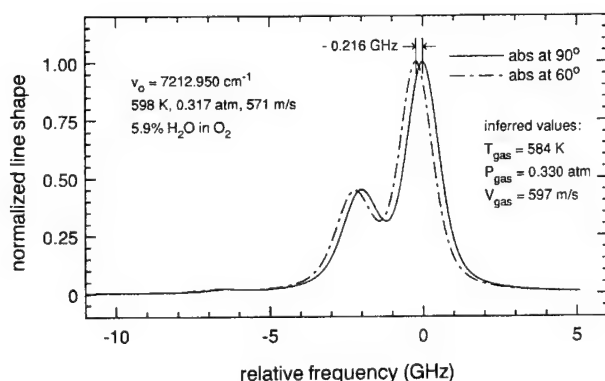
Fig. 4. Pair of reduced profiles from the data of Fig. 3, corresponding to the absorption features at 1.38 ms. The line shapes are $-\ln(1 - \Delta I/I_0)$, normalized to unity at the line center. The $3_{13} \leftarrow 3_{12}$ line is located -2.04 GHz from the larger $6_{43} \leftarrow 6_{42}$ line ($\nu = 7212.950$ cm^{-1}). A third line, much weaker than the other two lines and centered at -6.5 GHz from the $6_{43} \leftarrow 6_{42}$ line, is also apparent in the reduced profiles. The inferred gas velocity, temperatures, and pressures are 597 m/s, 588 K (60°), 580 K (90°), 0.332 atm (60°), and 0.328 atm (90°), respectively.

shift of the profiles automatically cancel in the subtraction. Temperature is determined from the intensity ratio that gives the best fit. The pressure is obtained using the value of $-\ln(1 - \Delta I/I_0)$ measured at the larger peak, the line intensity at the measured temperature, the known mole fraction, and the measured Voigt a parameters.

At present, pressure has not been determined from the measured temperature and Voigt a parameters because of the lack of reliable information about the temperature dependence of pressure-broadening coefficients. We have seen discrepancies as high as 30% between the Voigt a parameters that were experimentally found over the range of postshock conditions studied here and the values expected from theoretical calculations[9] at our shock conditions. Because the agreement at the initial conditions is much better, this suggests that more reliable information on temperature dependence of collision broadening for this line pair of water vapor is needed. Note, however, that this uncertainty in the pressure-broadening temperature dependence does not affect the measurement of temperature because the intensity ratio is related not to the broadening of the line but to the integrated area under the line.

In Fig. 4 the shift between the two profiles is 0.216 GHz; the intensity ratios are 0.49 and 0.50 for the oblique and the perpendicular profiles, respectively; and the Voigt a parameters for the two primary lines are 0.593, 0.819 and 0.583, 0.818, respectively (see Table 2). The shift corresponds to an axial velocity of 597 m/s, and the intensity ratios correspond to temperatures of 588 and 580 K. The 0.154 and 0.133 peak absorbances (14.3% and 12.5% absorption, respectively) of the same data give pressures of 0.332 and 0.328 atm, respectively. These values compare reasonably with the calculated conditions of 571 m/s, 598 K, and 0.317 atm.

Figure 5 shows additional examples of pairs of reduced profiles for each of the three types of shock studied. The calculated conditions (P, T, V) and the measured parameters from each profile (together with the P, T, V values inferred from them) are listed in Table 2. Figure 5(a) corresponds to a shock produced by bursting a 1.0-mm-thick diaphragm into a mixture of 3% of H_2O in O_2 at a pressure of 115 Torr. This shock has a temperature and velocity similar to the example in Fig. 4 but with a pressure more than 3 times greater. This is reflected in the broadening of the lines, which is remarkably larger in Fig. 5(a) than in Fig. 4, making the lines less isolated. As we stated above, this inhibits separation of the effects of intensity ratio and collision broadening, which explains the high intensity ratio obtained from the perpendicular profile. The Voigt a parameters are approximately 15% smaller than the values we would expect if the only difference between both shocks was the pressure. This result can be explained by the fact that there is also a difference in the mole fraction of water vapor, and the self-broadening of water vapor is large. Considering that there is

Table 2. Calculated Conditions (*P*, *T*, *V*) and Measured Parameters for the Profiles Shown in Figs. 4 and 5

Parameter	Fig. 4 Calculated	Fig. 4 Measured Oblique	Fig. 4 Measured Perpendicular	Fig. 5(a) Calculated	Fig. 5(a) Measured Oblique	Fig. 5(a) Measured Perpendicular	Fig. 5(b) Calculated	Fig. 5(b) Measured Oblique	Fig. 5(b) Measured Perpendicular	Fig. 5(c) Calculated	Fig. 5(c) Measured Oblique	Fig. 5(c) Measured Perpendicular
$\Delta\nu_s$ (GHz)		0.216			0.212			0.554			0.411	
V (m/s)	571	597		564	586		1429	1532		1193	1136	
R		0.49	0.50		0.49	0.54		0.260	0.266		—	—
a_1		0.593	0.583		1.677	1.676		0.177	0.188		0.208	0.216
a_2		0.819	0.818		2.496	2.450		0.186	0.224		0.199	0.140
Peak absorbance		0.154	0.133		0.135	0.116		0.137	0.118		0.039	0.032
P (atm)	0.317	0.332	0.328	1.030	1.018	1.005	0.026	0.031	0.031	0.440	0.454	0.443
T (K)	598	588	580	597	588	551	1005	1070	1040	1700	—	—

approximately a 4% decrease in the broadening coefficient per each 1% decrease in the mole fraction of water vapor at the conditions of our shocks, the Voigt *a* parameters match to better than 2% in both examples.

Figure 5(b) corresponds to a shock produced in pure water vapor at a pressure of 1 Torr. The calculated conditions in this instance are smaller than the measured values. Much better agreement is found if the shock speed used in the 1-D calculations is approximately 5% bigger than the value inferred from the tin-film gauges. This result may be explained by the fact that the shock was accelerating en route to our observation port, and the last thin-film sensor used in measuring shock speed was 0.6 m upstream.

Figure 5(c) corresponds to a shock produced in a mixture of 8.1% of H_2 in O_2 at a pressure of 15 Torr. The postshock calculated conditions in this instance are 1193 m/s, 1235 K, and 0.440 atm. Pyrolysis of H_2/O_2 increases the temperature to 1700 K and produces 8% of H_2O. No temperature measurement has been inferred from the intensity ratio, because this ratio is too insensitive to temperature in this case. The theoretical temperature has been used in the fitting of the experimental profiles.

In all the reduced profiles, there is a third line centered at -6.5 GHz from the $6_{43} \leftarrow 6_{42}$ line whose intensity increases with temperature. From the temperature dependence of the line intensity we have estimated that $E'' \approx 2500$ cm^{-1} and $S(296$ K$) \approx 8 \times 10^{-6}$ cm^{-2} atm^{-1}. However, we could not identify this line with any of the lines reported in the literature.

Results and Discussion

The evolution of temperature, pressure, and velocity can be followed during the experiment shown in Fig. 3 by reducing the 40 individual absorption profiles. The results are presented in Fig. 6. Average temperatures of 295 and 601 K in the first two stages of the flow (initial and incident shock conditions, respectively) are very close to the measured room temperature of 296 K and the 598 K predicted by theory. The accuracy of the measured temperature in the first stage is 2 K, corresponding to a ± 0.01 variation

in the intensity ratio. In the second stage, the intensity ratio can be measured with a smaller accuracy (± 0.02) because of the overlapping of the two line shapes, giving an error in the temperature measurements of ± 18 K. No reliable measurement of temperature in the reflected shock regime can be made because the lines are so broad that the line pair is blended.

The average pressures of the gas inferred from the measured partial pressure of water vapor in the three flow regimes are 0.046, 0.375, and 1.476 atm. The agreement between the values inferred from the I_{90} and I_{60} signals is well within 4%. In the first stage of the flow there are random deviations from the mean value of $\pm 4\%$. In the second stage there is a systematic increase with time of the measured pressure, giving a difference of 25% between the two extreme values. This pressure has been inferred from the measured partial pressure of water vapor, assuming the mole fraction is constant (and known). This may not be a correct assumption, as the evolution of the Voigt *a* parameters indicates. Theoretical calculations following Ref. 9 show that these parameters increase with an increase in the mole fraction of water vapor, even if the total pressure and temperature are constant, because of the high value of the self-broadening coefficients compared with the H_2O–O_2 coefficient. Therefore the mole fraction can be inferred from the ratio a/P_{H_2O} because this ratio is independent of pressure. In this way the mole fraction has been shown to increase linearly up to 7.7%, right before the reflected shock. The evolution of the pressure corrected by the mole fraction inferred in such a way is nearly constant. Using this approach, the average pressure is 0.318 atm, which is in much better agreement with the calculated value of 0.317 and with the value of 0.311 measured from the pressure gauge.

We think the increase in the mole fraction of water vapor as the shock progresses is due to a gradient in the concentration of water in the mixture that fills the driven section. This gradient exists before firing of the shock tube. The gradient is set when the driven section is being filled with the H_2O/O_2 mixture from a reservoir, which is located at the diaphragm
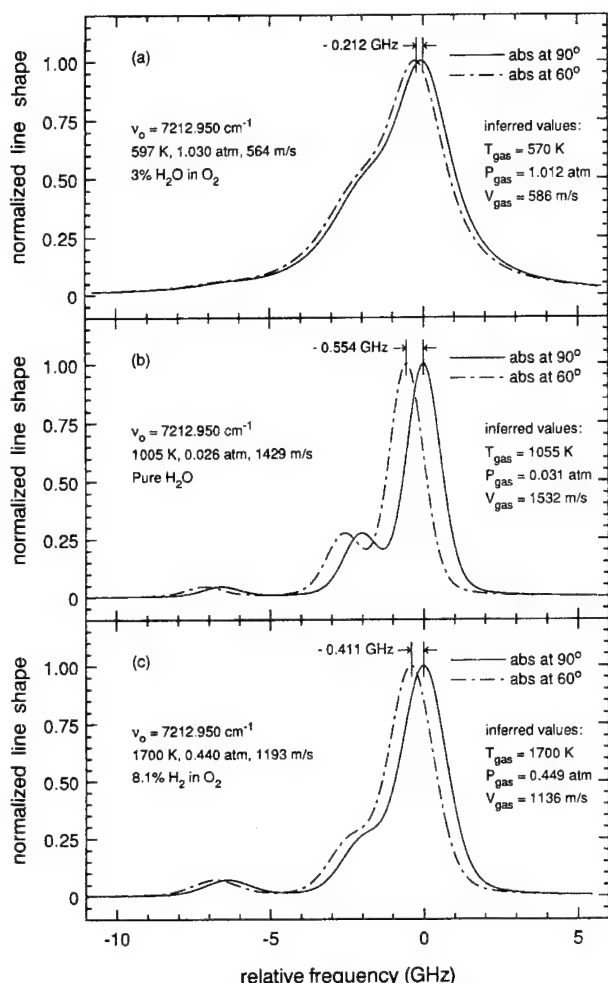
Fig. 5. Pair of reduced profiles for three different types of shocks. The line shapes are $-\ln(1 - \Delta I/I_0)$, normalized to unity at line center. The $3_{13} \leftarrow 3_{12}$ line is located -2.02 GHz from the larger $6_{43} \leftarrow 6_{42}$ line ($\nu = 7212.950$ cm^{-1}). A third line, weaker than the other two lines and centered at -6.5 GHz from the $6_{43} \leftarrow 6_{42}$ line, is also apparent in the reduced profiles. (a) Shock in a mixture of 3% of H_2O in O_2 for a diaphragm thickness of 1 mm. The inferred gas velocity, temperatures, and pressures are 586 m/s, 588 K (90°), 551 K (90°), 1.018 atm (60°), and 1.005 atm (90°), respectively. (b) Shock in pure H_2O. The inferred gas velocity, temperatures, and pressures are 1532 m/s, 1070 K (60°), 1040 K (90°), 0.031 atm (60°), and 0.031 atm (90°), respectively. (c) Shock in a mixture of 8.1% of H_2 in O_2. The inferred gas velocity and pressures are 1136 m/s, 0.454 atm (60°), and 0.443 atm (90°), respectively. The temperature has not been inferred because the sensitivity of the line pair is too low above 1350 K.

end of the driven section. Water is being adsorbed by the shock-tube walls as the mixture fills the driven section. Thus the amount of water left in the mixture decreases with increasing distances to the inlet from the reservoir. This means that mixtures with higher concentrations of water vapor pass by the test section with increasing time after passage of the incident shock wave.

In the third (reflected shock) stage, the pressure obtained is remarkably constant, although the average is higher than the calculated value of 1.342 atm.
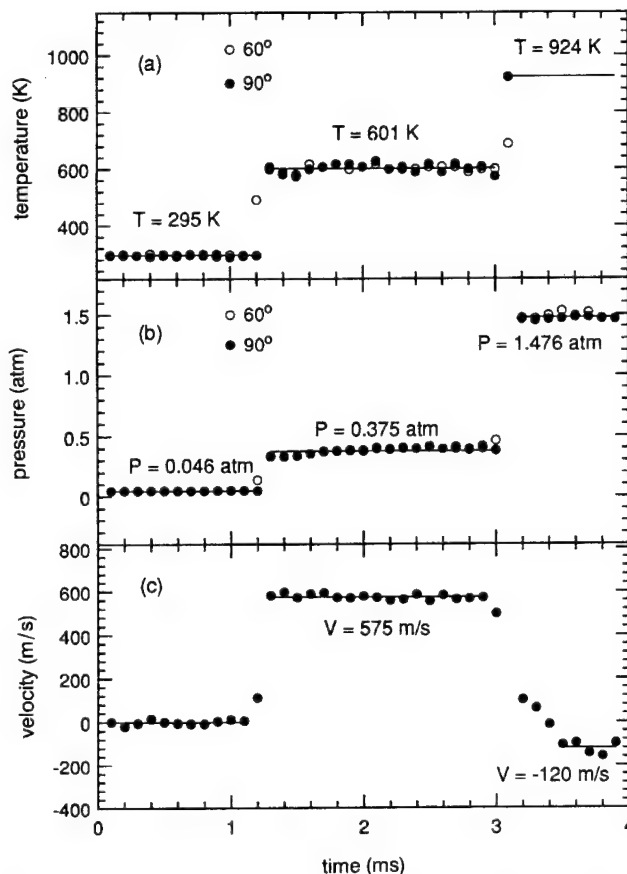
Fig. 6. Variation of (a) gas temperature, (b) pressure, and (c) velocity as a function of time at our measurement location, 45 cm from the end wall of the shock tube. The initial pressure is 0.046 atm for a mixture of 5.9% H_2O in O_2. Calculated postshock conditions: $T = 598$ K, $P = 0.317$ atm, $V_{gas} = 571$ m/s.

Assuming the mole fraction in this stage is 7.7%, we would obtain a value of 1.131 atm, which is lower than the calculated value but in perfect agreement with the value of 1.133 atm measured with the pressure gauge. Recall, however, that the mole fraction cannot be inferred accurately at present because of the lack of accurate data for the broadening coefficients. At room temperature, the calculated a parameters agree reasonably well with the measured a parameters, but in the postshock conditions the measured a parameters are approximately 20% smaller than the calculated ones. Thus the evolution of the mole fraction in the postshock regions has been obtained assuming an empirical proportionality factor of 0.79 between the calculated and the measured a/P_{H_2O}.

The average velocity of 575 m/s observed in the postshock conditions agrees very well with the 571 m/s predicted by shock-wave theory. The accuracy of the velocity measurements is ± 25 m/s, corresponding to an error in the shift measurement of 0.009 GHz. Behind the reflected shock the flow has a nonzero velocity, in accordance with similar measurements made by Philippe and Hanson in O_2 flows.[3]

The use of two probing directions for the velocity

measurement is necessary to account for the collision-induced shifts that affect the absorption lines. This remark is illustrated in Fig. 7, in which the evolution in time of the line-center positions (for the $6_{43} \leftarrow 6_{42}$ transition) for the two absorption signals is plotted for the same conditions as in Fig. 6. The quantity reported on the vertical axis is the line-center position of the absorbance signal after the time scale has been converted to a frequency scale with the étalon signal. Each of the 40 absorbance signals is converted with its corresponding étalon signal, and for all the absorbance signals the zero frequency has been taken as the peak near the absolute maximum of the étalon signal. We have also considered that the frequency decreases with time in the ramp up of the reference signal and increases with time in the ramp down. The deviations of the data from the lines through the experimental data are due mostly to the asymmetry in the frequency dependence on time between the ramp up and the ramp down; this is confirmed by the alternating change in sign of these deviations. The absorption signal does not experience a Doppler shift when the beam is perpendicular to the flow, yet the break in the solid lines of Fig. 7 at 1.3 ms gives evidence of a displacement of the line-center position when the shock passes in front of the laser. This collision-induced shift Δv_c is due to the difference in pressure and temperature before and behind the shock. An experimental shift of -5.2×10^{-2} GHz has been measured, which represents 25% of the Doppler shift. To our knowledge no reliable data on the shift coefficient measurements are available, in the literature for comparison at present. The shift is even more obvious at the reflected shock (time, 3.1 ms) because the pressure is higher, although the data points are more scattered. This scattering is due to the difficulty in accurately measuring the line-center position when the absorption lines are much broader than the shifts.

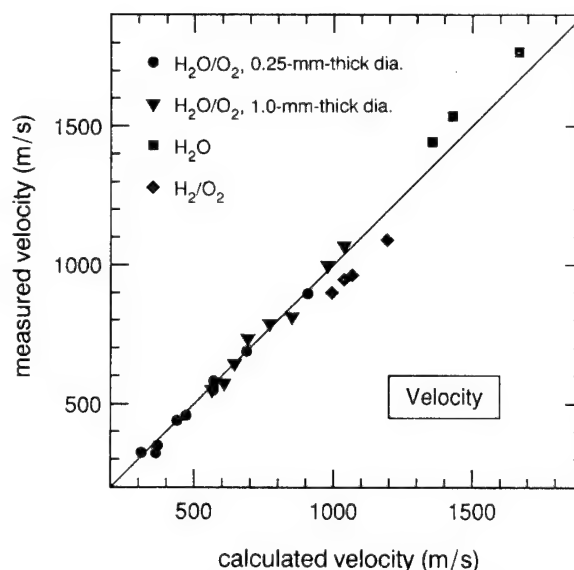Figure 8 shows the comparison between the measured and the calculated axial velocities for 24 shock

Fig. 8. Measured axial gas velocity versus calculated velocity. The symbols represent the data from the experiments; the solid line represents the 1-D shock calculation.

experiments, classified according to the gas mixture and the thickness of the diaphragm. Because the peak absorptions in these experiments were low (see Table 1), an average of several absorption signals would be desirable to reduce the noise of the signals and facilitate the fitting. However, for all the data presented here only the results for the first (reducible) pair of profiles are shown for each shock experiment, because the absorption profiles were not uniform enough to calculate an accurate average. In the experiments on the H_2O/O_2 mixture, the nonuniformity arises from an increase in the partial pressure of water vapor with time, mainly because of an increase in the mole fraction of water vapor as the shock progresses. In the experiments on pure H_2O, a decrease in the temperature of the gas shortly after the passage of the shock has been found, resulting from the nonideal shock-tube behavior of these conditions. Finally, in the experiments on the H_2/O_2 mixture, the mole fraction of water vapor increases with time because of the combustion process. In this case we have analyzed the absorption signals that were recorded approximately 0.7 ms after the passage of the shock, when the combustion process has been finished.

Doppler shifts in the experiment ranged from -0.10 to -0.65 GHz, with the corresponding shift-to-width (FWHM) ratios being between 0.07 and 0.45. The agreement with the calculated velocities is better than 10%. However, the experiments in pure H_2O and in H_2/O_2 show discrepancies of approximately 100 m/s with the calculated values. We believe this is attributable in part to errors in the measured shock velocity on which the calculated gas velocities are based, because errors in the shift measurement itself cannot account for errors greater than ± 30 m/s for the narrower line shapes and ± 60 m/s for the broader line shapes obtained in these experiments.

Fig. 7. Evolution of the relative line-center positions for the absorption signals measured along the two probe directions of the flow; evidence of a collision-induced frequency shift is given by the discontinuity of the curve corresponding to 90° (solid circles) occurring at 1.3 ms; the absorption signal at 60° (hollow circles) experiences a collision-induced shift and a Doppler shift in the same direction.

Thus the shocks in pure water vapor undergo significant acceleration along the shock tube. Because the shock speed was measured 40 diameters upstream from our observation port, we may have calculated the gas velocities with a shock speed lower than the speed that was actually present in our measurement section. In fact we have checked that the error between the measured and calculated gas velocities is reduced to zero if we use a 5% higher value for the shock speed. The agreement in the measured temperature and pressure with the calculated values is also improved in this way.

Figure 9 shows the comparison between measured and calculated temperature for each shock experiment. The measured temperatures are on average 3% lower than calculated for the H_2O/O_2 mixtures for the 0.25-mm-thick diaphragm experiments, 5% lower for the 1.0-mm-thick diaphragm experiments, and 3% higher for the pure H_2O experiments. The scatter in temperature is ±5% over the whole range. No attempt at measuring the temperature for the H_2/O_2 experiments has been made, because the sensitivity to temperature of the line pair is too low at this high temperature. Nevertheless, the calculated temperatures of these shocks are included in Fig. 9, because they are used to infer all the other magnitudes that depend on the temperature. The discrepancies in measured temperature in the experiments with pure H_2O are mainly due to an incorrect value in the measured shock velocity on which the calculated gas conditions are based, as pointed out above. The measured temperature presented here corresponds to the first (reducible) pair of profiles for each shock experiment. The results from reducing the following pairs of profiles show a dramatic decrease in temperature (and also in pressure). This suggests that nonideal shock-tube effects, such as boundary-layer growth, are not negligible here.
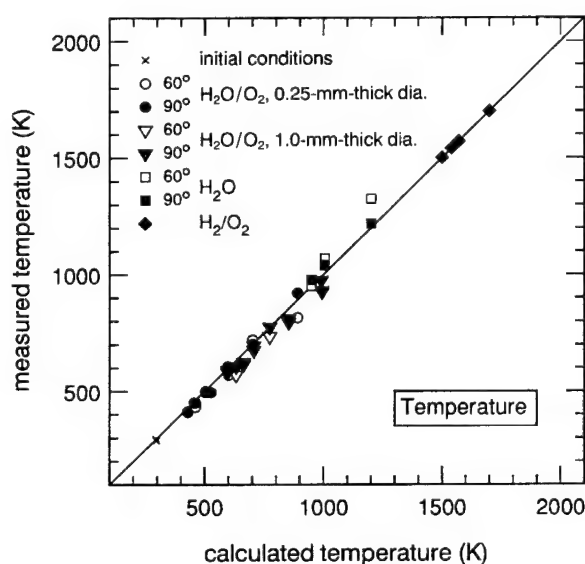
Concerning the experiments with H_2O/O_2, there are several possible explanations for the observed discrepancies in measured temperature. One possibility is a systematic error in the calculated temperatures, because of the neglect in the model of nonideal shock-tube effects. However, the results from reducing several pairs of lines in each shock indicate that the temperature behind the shocks is uniform with time. This suggests that boundary-layer growth is a negligible effect in this case. Another possibility is the use of incorrect line intensities in the intensity ratio formula of Eq. (1). We took care of this by an experimental calibration of both lines at room temperature.[4] An additional factor that cannot be dismissed is the presence of small, thermal boundary layers that would have affected the line-of-sight absorption measurement. The maximum absorption coefficient occurs at a temperature of 100 K for the $3_{13} \leftarrow 3_{12}$ line and 430 K for the line $6_{43} \leftarrow 6_{42}$. Thus the small fraction of cold H_2O molecules in the boundary layer causes a disproportionate effect on the perceived temperature. Other effects that would have contributed to errors in the measurement are those resulting from beam misalignment. Although care was taken to ensure that the beams passing through the tube were balanced to the reference I_0 beam before each experiment, the alignment following the shock was often perturbed because of displacement of the shock tube, vibration, and distortion of the windows. This perturbation will displace and tilt the baseline of the absorption signals obtained. The baseline was corrected afterwards, looking at the residuals of the Voigt fitting in the wings of the signal. This correction works better for narrow signals (i.e., the experiments with the 0.25-mm-thick diaphragms) than for the signals in the experiments with the 1.0-mm-thick diaphragm. In this latter case the lines are so broad that the signal does not reach zero on the wings.

Figure 10 shows the comparison of calculated and measured pressures determined from the absorption method. These values compare well with those derived from the 1-D shock calculations. There is a small systematic deviation in the pressures, which correlates with the underestimation of the temperatures. This is because the inferred pressure would compensate for an error in temperature and because the absorption coefficient increases with decreasing temperature. Thus, in the experiments in H_2O/O_2 with a 1.0-mm-thick diaphragm, the measured pressures are on average 4% too low. Here the ability to measure pressure obviously depends on knowlege of the H_2O mole fractions. In the H_2O/O_2 experiments, the H_2O mole fraction was known to approximately 100 parts in 10^6 in the mixture tank. However, these mole fractions may change by as much as 100% when filling the shock tube, as confirmed by the partial pressure in the initial conditions. The uncertainty as to the amount of water vapor on the shock tube may be because of nonuniformities in the mixing tank and absorption and deabsorption on

Fig. 9. Measured temperature versus calculated temperature: solid symbols, data from 90° beam; open symbols, data from 60° beam; solid line, 1-D shock calculation.
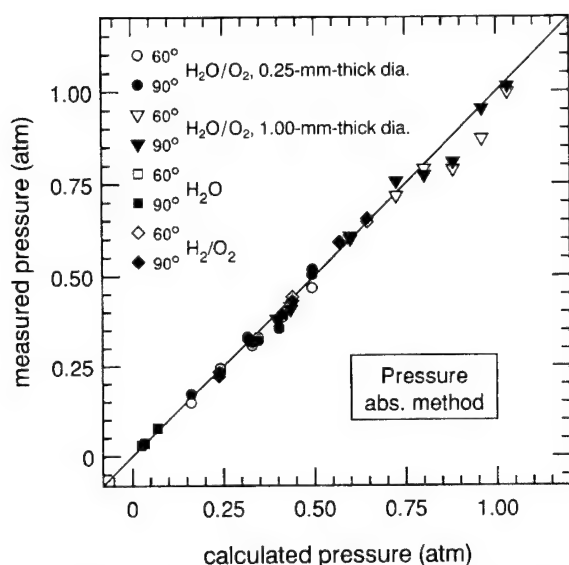
Fig. 10. Measured total pressure from the fractional absorption versus calculated pressure: solid symbols, data from 90° beam; hollow symbols, data from 60° beam; solid line, 1-D shock calculation.
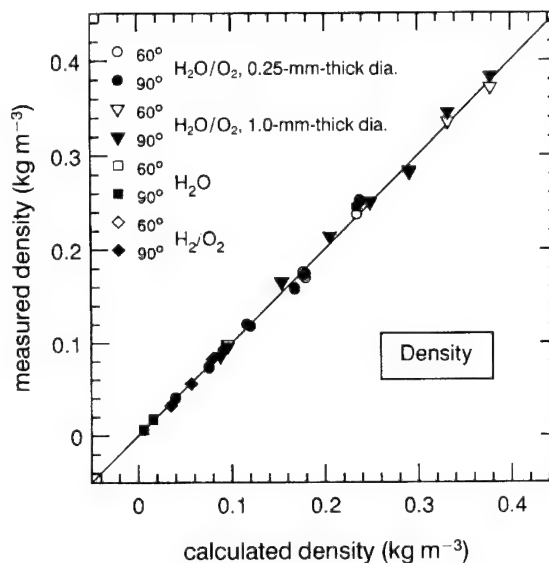

Fig. 11. Measured density from the fractional absorption versus calculated density: solid symbols, data from 90° beam; open symbols, data from 60° beam; solid line, 1-D shock calculation.

the tube walls. In general the first shock with a certain mixture tends to have low mole fractions. Afterwards, higher mole fractions are obtained, although no consistent relationship was found between the actual mole fraction and either the number of shocks created with the same mixture or the initial conditions of the shock. Thus the actual mole fraction for each experiment is measured in the initial conditions with an estimated accuracy of 5%.

As we have pointed out above (see Fig. 6), the mole fraction seems to change as the shock progresses. Thus the pressures presented here have been obtained from the first (reducible) pair of profiles for each shock. In the H_2/O_2 experiments, the mole fraction increases with time as the combustion process is taking place. The data presented here have been inferred from the pair of profiles obtained 0.7 ms after the passage of the shock by our observation port, using the mole fraction predicted by the Chemkin codes.[13] Measured pressures agree within 5% with calculated pressures. In the pure H_2O, the pressure inferred agrees within 0.1 Torr with the measured pressure at the initial conditions. The measured pressures in the postshock conditions (from the first reducible pair) agree within 2% with the value given by a pressure gauge but differ by as much as 0.09 atm (15% error) with the calculated condition. As noted above, the agreement with the calculated pressure is much better if the shock speed used to calculate the gas conditions is 5% higher than the shock speed measured at the thin-film sensor 0.6 m upstream.

Figure 11 shows the comparison between measured and the calculated densities. The scatter exhibits trends similar to those of the pressures, but the agreement is remarkably better; this suggests that the underestimation of both pressure and temperature cancels to first order in Eq. (5).

Figure 12 shows the measured and calculated mass flux. The mass flux generated in these experiments ranged from 10 to 200 kg m^{-2} s^{-1}. The agreement is better than 10% for all the experiments in H_2O/O_2. Higher discrepancies are found in the pure water vapor and in the H_2/O_2 shocks because of errors in the velocity measurements.

Finally, Fig. 13 shows the measured and calculated momentum flux. The scatter exhibits trends similar to those of the mass flux. The momentum flux generated in these experiments ranged from 1.0×10^4 to 1.5×10^5 kg m^{-1} s^{-2}. The agreement is better than 12% for all the experiments in H_2O/O_2, whereas the discrepancies in the pure water vapor and in the
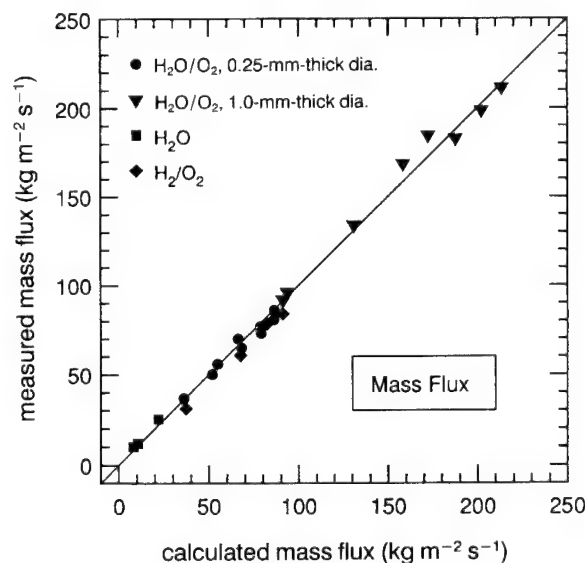

Fig. 12. Measured mass flux versus calculated mass flux: solid symbols, experimental data; solid line, 1-D shock calculation.
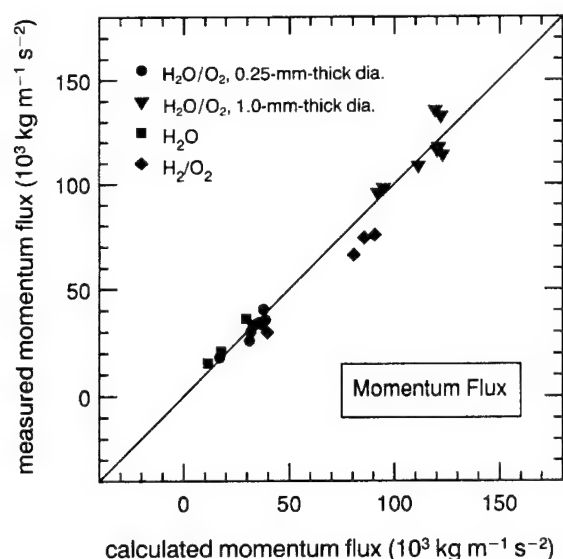
Fig. 13. Measured momentum flux versus calculated mass flux: solid symbols, experimental data; solid line, 1-D shock calculation.

H_2/O_2 shocks are aggravated because of the errors in the velocity measurements.

Conclusions

Simultaneous measurements of velocity, temperature, pressure, density, mass flux, and momentum flux in transient flows were demonstrated by recording absorption profiles of the H_2O line pair $6_{43} \leftarrow 6_{42}$, $3_{13} \leftarrow 3_{12}$ in the $\nu_1 + \nu_3$ band at 1.386 µm. The tunable radiation was provided by a distributed feedback InGaAsP diode laser. The unique current-tuning capabilities of laser diodes were exploited to achieve high measurement-repetition rates (10 kHz). Experiments were performed in a shock tube for three different gas mixtures: pure H_2O at initial pressures lower than 3 Torr, up to 6% of H_2O in O_2 at initial pressures below 120 Torr, and up to 8% of H_2 in O_2 at initial pressures below 35 Torr. The test conditions generated in the shock tube ranged from 300 to 1700 m/s, 460 to 1700 K, 0.02 to 1.1 atm, 0.006 to 0.4 kg m^{-3}, 10 to 200 kg m^{-2} s^{-1}, and 1.0 × 10^4 to 1.5 × 10^5 kg m^{-1} s^{-2}. The fractional absorptions were between 3% and 30%.

The measured velocities agreed well with calculated values, even though the Doppler shifts were much smaller than the linewidths. The method would work even better at higher velocities. Because the identical flow was used to provide the unshifted reference feature, any effects of collision-induced line shifts (which are of the same order as the Doppler shifts) were eliminated. The temperature-sensitive spectral feature that was investigated for measuring temperature was suitable in the range from 180 to 1350 K. The pressures determined from the fractional absorption were accurate over the entire pressure range. This method requires accurate knowledge of the H_2O mole fraction. Pressures could be alternatively obtained from measured line shapes if the collision-broadening coefficients are

known. In this case only gross knowledge of the gas composition is needed to specify the overall collision-broadening coefficient. This suggests the desirability of obtaining accurate broadening coefficients for H_2O at elevated temperature. This method has not been used to infer pressures here because the available broadening data[9] are not accurate enough at temperatures other than ambient temperature. Finally, the accuracy of the density and mass and momentum fluxes reflects that of the velocity, temperature, and pressure measurement.

References

1. E. C. Rea and R. K. Hanson, "Rapid laser-wavelength modulation spectroscopy used as a fast temperature measurement technique in hydrocarbon combustion," Appl. Opt. **27**, 4454–4464 (1988).
2. A. Y. Chang, M. D. DiRosa, D. F. Davidson, and R. K. Hanson, "Rapid tuning cw laser technique for measurements of gas velocity, temperature, pressure, density, and mass flux using NO," Appl. Opt. **30**, 3011–3022 (1991).
3. L. C. Philippe and R. K. Hanson, "Laser diode wavelength-modulation spectroscopy for simultaneous measurement of temperature, pressure, and velocity in shock-heated oxygen flows," Appl. Opt. **32**, 6090–6103 (1993).
4. M. P. Arroyo and R. K. Hanson, "Absorption measurements of water vapor concentration, temperature and line-shape parameters using a tunable InGaAsP diode laser," Appl. Opt. **32**, 6104–6116 (1993).
5. M. P. Arroyo and R. K. Hanson, "Tunable diode laser absorption technique for multiparameter measurements of combustion flows," presented at the Sixth International Symposium on Applications of Laser Techniques to Fluid Mechanics, Lisbon, Spain, 20–23 July 1992.
6. R. A. Toth, Jet Propulsion Laboratory, 4800 Oak Grove Drive, Pasadena, Calif. 91109 (personal communication, 1992).
7. J. M. Flaud, C. Camy-Peyret, and J. P. Maillard, "Higher Ro-vibrational levels of H_2O deduced from high resolution oxygen–hydrogen flame spectra between 2800–6200 cm^{-1}," Mol. Phys. **32**, 499–521 (1976); C. Camy-Peyret, J. M. Flaud, and J. P. Maillard, "Higher ro-vibrational levels of H_2O deduced from high resolution oxygen–hydrogen flame spectra between 6200 and 9100 cm^{-1}," Mol. Phys. **33**, 1641–1650 (1977).
8. HITRAN Database, 1991 ed. (Digital Product Section, National Climatic Center, National Oceanic and Atmospheric Administration, Federal Building, Asheville, N.C. 28801).
9. C. Delaye, J.-M. Hartmann, and J. Taine, "Calculated tabulations of H_2O line broadening by H_2O, N_2, O_2, and CO_2 at high temperature," Appl. Opt. **28**, 5080–5087 (1989).
10. A. G. Gaydon and I. R. Hurle, *The Shock Tube in High-Temperature Chemical Physics* (Reinhold, New York, 1963).
11. W. C. Gardiner, Jr., B. F. Walker, and C. B. Wakefield, "Mathematical methods for modeling chemical reactions in

shock waves," in *Shock Waves in Chemistry,* A. Lifshitz, ed. (Dekker, New York, 1981), Chap. 7, pp. 319–372.

12. D. A. Masten, R. K. Hanson, and C. T. Bowman, "Shock tube study of the reaction $H + O_2 \rightarrow OH + O$ using OH laser absorption," J. Phys. Chem. **94,** 7119–7128 (1990).

13. R. J. Kee, J. A. Miller, and T. H. Jefferson, "Chemkin: a general-purpose problem-independent, transportable, FORTRAN chemical kinetics code package," Rep. SAND80-8003 (Sandia National Laboratory, Livermore, Calif., 1980).

14. R. J. Kee, F. M. Rupley, and J. A. Miller, "The Chemkin thermodynamic database," Rep. SAND87-8215 (Sandia National Laboratory, Livermore, Calif., 1987).

Sensitized phosphorescence: a gas phase molecular mixing diagnostic

B. Yip, A. Lozano, R. K. Hanson

Abstract The use of sensitized phosphorescence for visualization of gas phase fluid mixing and the requirements for quantitative imaging measurements are discussed. A model for estimating the molecular-mixing signal's dependence on fluid composition is developed and candidate molecular reactants are considered within the framework of the model. Experiments based on sensitized phosphorescence from both an acetone-biacetyl system and a toluene-biacetyl system show good qualitative agreement with modeled results. It is concluded that quantitative measurements using sensitized phosphorescence are feasible.

1
Introduction

The mixing of two different fluid streams is of great practical interest, since it can limit the overall rate of progress of a particular process. As an example, for nonpremixed combustion in the limit of fast chemistry, the total heat release rate is governed by the rate at which fuel and oxidizer streams mix. Since true mixing at a molecular level is a prerequisite to chemical reaction, an understanding of how molecularly-mixed fluid is generated in the flowfield is essential for predictive modeling of such a process.

Typically the mixing field is studied using passive scalar dilution measurements, where inert particles or molecules are uniformly seeded into one stream and dilution of the marker concentration through fluid mixing is used to infer the local mixture fraction. However, the size of the smallest mixing scales is of the order of the Batchelor scale diffusion thickness $\lambda \sim \delta$ $Sc^{-1/2} Re^{-3/4}$, where δ is the local integral length scale, Sc the Schmidt number and Re the Reynolds number. For laboratory-scale liquid flows (where molecular diffusion is slow and the Schmidt number high) or in high Reynolds number gas flows, the Batchelor scale is typically very small and often cannot be resolved by physical probes or optical sampling. Passive scalar measurements then overestimate the amount of mixing in the flow.

Reaction or product marker techniques (Breidenthal 1981, Mungal and Dimotakis 1984, Dimotakis 1989) have been

designed to circumvent problems associated with insufficient spatial resolution in mixing measurements. In these measurements, each of the two fluids is seeded with a different reactant. When molecularly mixed, a chemical reaction between the reactants of the two streams produces a product, which therefore directly tags mixed fluid. The product concentration is measured in order to determine the degree of mixing. Such a methodology avoids some of the ambiguities associated with inadequate resolution – even if the smallest fluid scales are not resolved, the actual amount of molecularly-mixed fluid in the measurement volume is recorded correctly via the product concentration. Mixing experiments performed in turbulent liquid shear layers have successfully exploited reaction marker techniques and shown that experimental bias in passive scalar measurements is indeed significant (Breidenthal 1981, Koochesfahani and Dimotakis 1986). Single-point measurements in incompressible (Mungal and Dimotakis 1984) and compressible (Hall et al. 1991) gas mixing layers have also been made.

A worthwhile extension of the chemical reaction technique is the development of a non-intrusive optical measurement scheme which would enable quantitative two-dimensional imaging of gas phase mixing, similar to the liquid phase diagnostic of Koochesfahani and Dimotakis. Quantitative imaging provides information on the instantaneous spatial structure of the flow that cannot be obtained from single point measurements. Clemens and Mungal (1991) developed a technique for visualizing mixing in a supersonic shear layer, but quantitative interpretation of their product signal is difficult due to the complexity of the vapor condensation process upon which they base their diagnostic. Another imaging method based on oxygen quenching of NO fluorescence can be used to indirectly determine the mean volume occupied by mixed fluid, by measuring the volume occupied by unmixed fluid (Clemens and Paul 1993).

A promising reaction-marker-type diagnostic for visualizing gas phase mixing was introduced by Bates (1977); a similar technique was later used by Winter (1992). These techniques are based on a process known as sensitized phosphorescence. The goal of the current work is to take a closer look at these techniques, in order to evaluate their applicability for quantitative mixing measurements within the framework of the chemical reaction methodology. This paper first describes sensitized phosphorescence and how it can be used to visualize molecular mixing. In order to exploit the process for quantitative mixing measurements, the variation of phosphorescence intensity with local mixture composition must be well understood, and in order to predict this variation,

B. Yip, A. Lozano, R. K. Hanson
High Temperature Gasdynamics Laboratory, Department of Mechanical Engineering, Stanford University,
Stanford CA 94305, USA

Correspondence to: B. Yip

a generalized photophysical model is developed. Candidate molecular reactants for the diagnostic are considered, and their behavior is modeled. Experiments designed to verify the model predictions are presented, and good qualitative agreement is obtained.

2
Sensitized phosphorescence

Sensitized phosphorescence is the luminous emission generated when, through molecular collisions, excited state molecules of one species (the donor) transfer energy to another species (the acceptor), which then phosphoresces. The utility of sensitized phosphorescence for mixing visualizations is immediately apparent. By seeding donor molecules in one stream and acceptor molecules in another, donors can be excited in a two-dimensional cross section of the flow by illumination with a laser sheet. Phosphorescence will then be emitted where fluid mixing allows donors to sensitize acceptors through molecular collisions. The system behaves somewhat like a diffusion flame which does not release heat and which has its own particular chemistry. No real chemical reaction actually occurs (only collisional energy transfer takes place), making the system a potential candidate for mixing studies without the complications of heat release and the subsequent density and velocity changes normally associated with exothermic reactions.

Such radiationless electronic energy transfer between molecules has useful photochemical applications and has been studied extensively (Lamola and Turro 1969). A typical energy level diagram is shown in Fig. 1, with bold arrows denoting the most important transitions for this discussion. Both donor and acceptor molecules will typically possess singlet ground states, D_0 and A_0. An allowed radiative transition does not change spin, so that laser excitation raises the donor to its first excited singlet electronic state D_1. Corresponding to the excited singlet is the first excited triplet state D_3, of lower energy (Jaffé and Orchin 1962). Intersystem crossing, a nonradiative spin-changing transition which can occur in polyatomic molecules, rapidly transfers the donor from the excited singlet to excited triplet state. Energy transfer can occur when the excited

donor undergoes a collision with an acceptor, and is most favored when the acceptor A_0 can be excited to a triplet state A_3 of lower energy than that of the donor's, i.e.

$$D_3 + A_0 \rightarrow D_0 + A_3. \tag{1}$$

This mechanism is referred to as triplet-triplet electronic energy transfer and the emission from the excited acceptor A_3, which is analogous to the product of a chemical reaction (Eq. (1)) is the sensitized phosphorescence.

To develop a good mixing diagnostic based on the triplet-triplet energy transfer of Eq. (1), the ideal donor molecule would be easily excited to its excited singlet state D_1, have rapid intersystem crossing to the triplet state D_3 and a low triplet relaxation rate (so that the donor would have time to transfer energy to the acceptor). The acceptor would ideally exhibit a high visible phosphorescence yield from the triplet state A_3 (for strong mixing signals) and would only be excited by molecular collisions with donor molecules, not by direct laser absorption. For efficient intermolecular energy transfer and to reduce unsensitized acceptor excitation, the donor excited states would be much higher in energy than those of the acceptor.

Biacetyl is an attractive acceptor molecule which has been used extensively in photochemical studies. Its triplet state is low in energy with an exceptionally high phosphorescence yield (15%). Direct absorption of UV photons produces little emission because of photodissociation (Richard et al. 1978). Gas phase donor molecules which can be excited in the near UV spectrum include aromatics, ketones and aldehydes. In order to compare different donor molecules for use in a quantitative, sensitized phosphorescence mixing diagnostic, a generalized photophysical model was developed, as described below.

3
Modeling

Although the bold arrows in Fig. 1 summarize the most important transitions involved in sensitized phosphorescence, some secondary processes must be included if a real system is to be adequately modeled. Additional processes are represented in Fig. 1 by lightly-shaded arrows. Photodissociation of excited
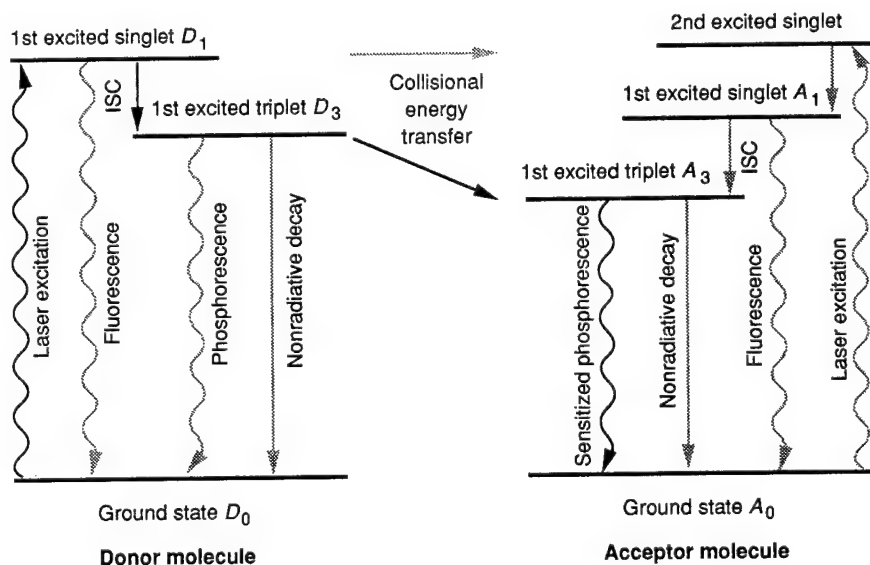
Fig. 1. Energy level diagram for sensitized phosphorescence

states, normally observed at low overall pressures when excess vibrational energy is not quickly dissipated by intermolecular collisions, have been neglected. Vibrational relaxation is assumed to be rapid and complete. The objective here is only to construct a simple framework upon which to build a qualitative understanding of the system.

After laser excitation, aside from intersystem crossing to the excited triplet state D_3, excited donor singlets can decay radiatively by spin-allowed fluorescence emission. For aromatics in particular, another possibility is energy transfer to the acceptor through a singlet-energy-transfer mechanism. For those excited donor molecules which do attain the excited triplet state D_3, not all will produce the desired acceptor triplets. Some donor triplets will radiatively decay before they collide with an acceptor molecule A_0. Others relax nonradiatively, either internally or by collisions, with molecules other than the acceptor.

Acceptor triplets A_3 do not all result as a product of collisions with excited donors (Eq. (1)). Some are created directly by the UV laser pumping, while others may be produced after collisions with aromatic donor excited singlets. In either case, the acceptor is typically promoted to its second excited singlet state, which can relax to the first excited singlet state under the aid of molecular collisions (Richard et al. 1978). These acceptor singlets can emit fluorescence or enter the triplet state A_3 by intersystem crossing. Only a fraction of the excited acceptor triplets actually emit phosphorescence (the signal of interest), the rest undergoing nonradiative relaxation either internally or after collisions with neighboring molecules. Oxygen in particular is extremely efficient in quenching triplet phosphorescence, and must be excluded from the flow in order to obtain good signal levels. It will be assumed that nitrogen (or an equivalent inefficient quencher species) is the buffer gas.

The following coupled rate equations describe the system:

$$\frac{dD_0}{dt} = -k^D_{abs} I_{laser} D_0 + [k^D_{flu} + k^{DA}_{11} A_0] D_1$$

$$+ [k^D_{pho} + k^D_{nr} + k^{DA}_{33} A_0 + \sum_M k^D_{qM} M] D_3 ,$$

$$\frac{dD_1}{dt} = k^D_{abs} I_{laser} D_0 - [k^D_{flu} + k^D_{isc} + k^{DA}_{11} A_0] D_1 ,$$

$$\frac{dD_3}{dt} = k^D_{isc} D_1 - [k^D_{pho} + k^D_{nr} + k^{DA}_{33} A_0 + \sum_M k^D_{qM} M] D_3 ,$$

$$\frac{dA_0}{dt} = -[k^A_{abs} I_{laser} + k^{DA}_{11} D_1 + k^{DA}_{33} D_3] A_0 + k^A_{flu} A_1$$

$$+ [k^A_{pho} + k^A_{nr} + \sum_M k^A_{qM} M] A_3 ,$$

$$\frac{dA_1}{dt} = \phi^A_{21} [k^A_{abs} I_{laser} + k^{DA}_{11} D_1] A_0 - [k^A_{flu} + k^A_{isc}] A_1 ,$$

$$\frac{dA_3}{dt} = k^{DA}_{33} D_3 A_0 + k^A_{isc} A_1 - [k^A_{pho} + k^A_{nr} + \sum_M k^A_{qM} M] A_3 , \qquad (2)$$

where D_i, and A_i denote the concentrations of donor and acceptor molecules in the electronic energy levels denoted by i, M denotes molecular species which collisionally quench triplets and the rate constants k are defined in Tables 1 and 2. I_{laser} is the intensity of the pump laser and k^{DA}_{11} and k^{DA}_{33} denote the intermolecular energy transfer processes by which acceptors from one stream are sensitized by laser-excited donors from the other stream.

As mentioned above, biacetyl is an attractive acceptor molecule; its rate constants are listed in Table 1. Since molecules within a chemical group show similar electronic structure which is largely determined by the active bonds, acetone will be considered as an example of ketones and aldehydes as donor molecules. The aromatic donor molecules benzene and toluene were used by Bates (1977) and Winter et al. (1992) in their visualization experiments. Since it has the practical advantage of being amenable to efficient excitation by a quadrupled Nd:YAG laser, toluene will be considered here as an example of an aromatic donor. The rate constants for acetone and toluene are listed in Table 2.

While the donor-acceptor photophysical rates are described by Eq. (2), the fluid mechanics determines the initial conditions. In a mixing experiment, one free stream will be seeded with a partial pressure p^A_0 of acceptor molecules and the other with a partial pressure p^D_0 of donor molecules. An arbitrary fluid element in the mixing interface will have a mixture fraction ξ of

Table 1. Acceptor rate constants for the biacetyl molecule.

	Acceptor rate		Value	Reference
k^A_{abs}	Absorption at 308 nm (XeCl)		$1.2 \times 10^1 \text{ s}^{-1}/(\text{MW/cm}^2)$	Lozano 1992
		266 nm (4 × Nd:YAG)	$5.1 \times 10^1 \text{ s}^{-1}/(\text{MW/cm}^2)$	Lozano 1992
ϕ^A_{21}	2nd to 1st singlet yield at 308 nm		0.5	fit, cf Richard et al. 1978
		266 nm	0	observed
k^A_{flu}	Singlet fluorescence		$9.8(\pm 2.8) \times 10^4 \text{ s}^{-1}$	Sidebottom et al. 1972
k^A_{isc}	Intersystem crossing		$4.3(\pm 0.8) \times 10^7 \text{ s}^{-1}$	Sidebottom et al. 1972
k^A_{pho}	Triplet phosphorescence		$100(\pm 20) \text{ s}^{-1}$	Sidebottom et al. 1972
k^A_{nr}	Triplet internal nonradiative decay		$560(\pm 130) \text{ s}^{-1}$	Sidebottom et al. 1972
k^A_{qM}	Triplet quenching by $M = A_0$		$4.2 \text{ s}^{-1}/\text{Torr}$	Garabedian and Dows 1968
		A_3	$2 \times 5.7 \times 10^5 \text{ s}^{-1}/\text{Torr}$	fit, cf. Lozano 1992
		acetone	$2.5 \text{ s}^{-1}/\text{Torr}$	Garabedian and Dows 1968
		N_2	$0 \text{ s}^{-1}/\text{Torr}$	observed
		toluene	$0 \text{ s}^{-1}/\text{Torr}$	Winter et al. 1992

Table 2. Comparison of donor molecules for electronic energy transfer to a biacetyl acceptor

	Donor rate	Acetone	Toluene
p_{vap}	Vapor pressure (25°C)	233 Torr	29 Torr
λ	Excitation wavelength	308 nm	266 nm
σ_{abs}^D	Absorption cross section	1.6×10^{-20} cm^2 Lozano 1992	$2.9 (\pm 0.2) \times 10^{-19}$ cm^2 measured here
$\phi_{21}^A \dfrac{\sigma_{abs}^A}{\sigma_{abs}^D}$	Relative acceptor absorption	0.5×0.5	0
l_{abs}	Optical depth	18 cm (@ 100 Torr)	33 cm (@ 3 Torr)
k_{abs}^D	Absorption	2.5×10^4 s^{-1}/(MW/cm^2)	$3.9 (\pm 0.3) \times 10^5$ s^{-1}/(MW/cm^2)
k_{flu}^D	Singlet fluorescence	$8.0 (\pm 0.2) \times 10^5$ s^{-1} Hansen and Lee 1975	7.1×10^6 s^{-1} Burton and Noyes 1968
k_{11}^{DA}	Singlet energy transfer to A	~ 0 s^{-1}/Torr	1.7×10^7 s^{-1}/Torr Brown et al. 1974
k_{isc}^D	Intersystem crossing	$3.8 (\pm 0.5) \times 10^8$ s^{-1} Hansen and Lee 1975	2.0×10^7 s^{-1} Burton and Noyes 1968
k_{pho}^D	Triplet phosphorescence	100 s^{-1} using Heicklen 1959	~ 0 s^{-1}
k_{nr}^D	Triplet internal nonradiative decay	5.6×10^3 s^{-1} Borge et al. 1990	$3.8 (\pm 1.0) \times 10^3$ s^{-1} Holtzclaw and Schuh 1981
k_{qM}^D	Triplet quenching, $M = D_0$	$650 (\pm 50)$ s^{-1}/Torr Borge et al. 1990	$3.9 (\pm 0.5) \times 10^3$ s^{-1}/Torr Holtzclaw and Schuh 1981
	$M = D_3$	$2 \times 3.6 \times 10^5$ s^{-1}/Torr fit	
	$M = N_2$	$500 (\pm 300)$ s^{-1}/Torr Borge et al. 1990	~ 0 s^{-1}
k_{33}^{DA}	Triplet energy transfer to A	1.9×10^5 s^{-1}/Torr fit, cf. Cundall and Davies 1966	$1.4 (\pm 0.2) \times 10^6$ s^{-1}/Torr Holtzclaw and Schuh 1981

(say) the stream seeded with the acceptor. The initial conditions in the fluid element are then $A_0 = \xi p_0^A$, $D_0 = (1 - \xi) p_0^D$, $A_1 = A_3 = D_1 = D_3 = 0$.

The temporal response when the fluid element is subjected to pulsed laser excitation at time $t = 0$ can then be modeled by numerical integration of Eq. (2). Typical results are as shown in Fig. 2 for a mixture of fluids from an acetone-seeded stream and a biacetyl-seeded stream in equal proportions. Donor singlets D_1 (not seen in the figure due to the long time scale) exist essentially only during the 20 ns laser pulse. However, laser-generated donor triplets D_3 persist considerably longer. These molecules act as a source for generating acceptor triplets A_3, through the efficient collisional energy transfer mechanism. The long-lived acceptor triplets emit sensitized phosphorescence.

The phosphorescence measured in an actual experiment will depend on the characteristics of the detection system, and may be written as

$$P(\xi) = C^A \int k_{pho}^A A_3(\xi, t)\, dt\, dV \left(+ C^D \int k_{pho}^D D_3(\xi, t)\, dt\, dV \right), \qquad (3)$$

where the domain of integration corresponds to the detector's integration time and the volume of the fluid element considered. The constant C^A accounts for the overall optical collection efficiency and detector gain for acceptor phosphorescence. The term in brackets is a potential contribution from donor phosphorescence, which is undesirable because it is not sensitized by fluid mixing.
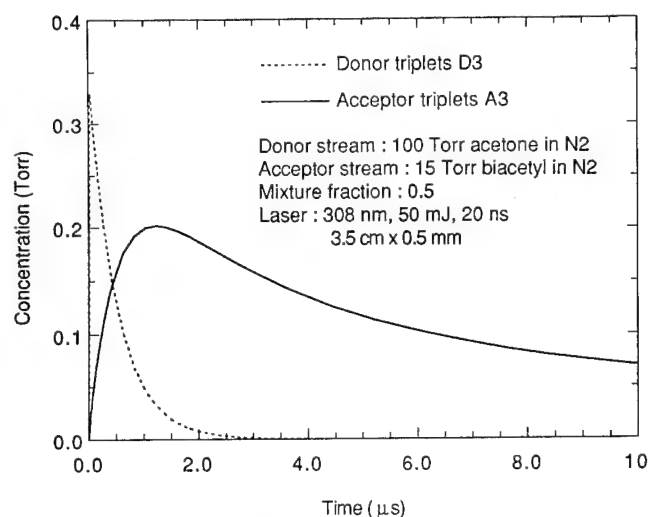

Fig. 2. Temporal response of a donor-acceptor mixture (acetone-biacetyl) after pulsed laser excitation at time $t = 0$

4
Requirements for quantitative measurements

The motivation for modeling the sensitized phosphorescence yields for different donors is to be able to assess the feasibility of using this diagnostic as a pseudo-chemical reaction for quantitative mixing measurements. For such measurements, the donor and acceptor molecules seeded in the two streams would play the role of chemical reactants, producing a detectable "product", the sensitized phosphorescence, by Eq. (1) when

brought together by fluid mixing. As explained in Koochesfahani and Dimotakis (1986), even though the smallest fluid scales are not resolved, measurements of the mean volume occupied by mixed fluid and its mean composition can be made using chemical reaction techniques if the product yield approximates that from a rapid, irreversible chemical reaction with one reactant in short supply, i.e. if $P(\xi)$ is almost linear. To satisfy this requirement using sensitized phosphorescence, the signal $P(\xi)$ would approximate a straight line over most of the mixture fraction domain, but take zero values in the free streams $\xi = 0$ and $\xi = 1$. The maximum mixing signal would occur for an effective "stoichiometric" mixture fraction $\xi_s \approx 0$ or $\xi_s \approx 1$. In keeping with the application for fluid mechanical mixing experiments, the sensitized phosphorescence will often be referred to as the product, or chemical reaction, or molecular mixing signal in the following.

First we consider the case where acetone is used as the donor to a biacetyl acceptor. Figure 3a shows the modeled sensitized phosphorescence yield $P(\xi)$ from mixing in an acetone-biacetyl system, using a 10 μs detector integration time and collection efficiencies corresponding to parameters in experiments to be presented later. In particular, an optical filter has been included to reduce the contribution of spurious donor phosphorescence. Pumping at 308 nm by a XeCl laser forming a 50 mJ, 20 ns laser sheet of 3.5 cm × 0.5 mm cross section is assumed. The free stream endpoint $P(\xi = 0)$ is non-zero due to this acetone phosphorescence (the spurious term in Eq. (3)), and $P(\xi = 1)$ is non-zero due to phosphorescence from acceptors excited directly by the laser and not by collisions with donor triplets from the other stream. A mixture of $\xi = \xi_s \sim 0.25$ gives maximum product yield. Clearly the product yield curve is inappropriate for quantitative measurements.

However, the excited donor D_3 appears to be the reactant in short supply, and if the free stream donor seeding were reduced, the desired donor-lean limit of $\xi_s = 0$ might be expected to be approached (and the spurious donor phosphorescence $P(\xi = 0)$

to be reduced). Unfortunately, this is not the case. Calculations at reduced acetone seeding or laser energy still show a peak product yield for $\xi_s \sim 0.25$. This initially surprising result can be explained as follows. To first order, most of the secondary processes in Fig. 1 can be ignored. After laser excitation, the number of donor triplets is just proportional to the initial amount of fluid from the donor stream, $(1 - \xi)$. These donor triplets can either react by Eq. (1) to form biacetyl triplets or relax by other paths (primarily by collisions with nitrogen for acetone donors). Assuming D_3 is the reactant in short supply, the total number of biacetyl triplets formed (and hence the product yield) is then just the initial number of donor triplets multiplied by the probability of reacting with biacetyl,

$$P(\xi) \propto p_0^D (1 - \xi) \frac{k_{33}^{DA} p_0^A \xi}{k_{33}^{DA} p_0^A \xi + k_{\text{nontransfer}}^D}, \tag{4}$$

where p_0^D and p_0^A are the free stream acetone and biacetyl seeding partial pressures (100 and 15 Torr in Fig. 3a) and $k_{\text{nontransfer}}^D$ is the rate for donor triplet relaxation by paths other than energy transfer to biacetyl. The maximum yield then occurs for

$$\xi_s \sim \frac{\sqrt{1 + \frac{k_{33}^{DA} p_0^A}{k_{\text{nontransfer}}^D}} - 1}{\frac{k_{33}^{DA} p_0^A}{k_{\text{nontransfer}}^D}}, \tag{5}$$

which reduces to $\xi_s \sim 0.26$ for $p_0^A = 15$ Torr and $k_{\text{nontransfer}}^D \sim k_{qN2}^D \times 760$ Torr. The effective stoichiometry is then independent of the free stream donor seeding p_0^D, as observed. This curious behavior stems from the fact that the rate of the triplet-triplet energy transfer reaction (Eq. (1)), characterized by the rate constant k_{33}^{DA}, is not infinitely fast compared to other decay paths for donor triplets.

It is clear that using acetone as a donor, the lean donor seeding limit of $\xi_s \approx 0$ cannot be attained. The lean acceptor seeding limit of $\xi_s \approx 1$ is not practical either, because interference from donor phosphorescence (Eq. (3)) would overcome the mixing-sensitive sensitized phosphorescence if the acceptor was made the lean reactant. If the modeling of Sect. 3 is adequate, acetone would not appear to be a suitable donor for use in quantitative chemical reaction measurements.

Now consider toluene as a donor. From the comparison of Table 2, some advantages of toluene compared to acetone are immediately apparent. There is no gas phase toluene phosphorescence or direct 266 nm laser excitation of biacetyl triplets, so that the sensitized phosphorescence resulting from excited toluene collisions with biacetyl will not have interference from non-mixing-related emission. Because collisions with nitrogen do not deactivate toluene triplets, the triplet lifetime is longer than that of acetone, and coupled with the larger energy transfer rate constant k_{33}^{DA}, collisional excitation of biacetyl is more efficient with toluene than with acetone. As indicated in Fig. 3b, sensitized phosphorescence using toluene as a donor shows stronger signals than with acetone, no spurious signal from the unmixed streams, and a value of ξ_s much closer to zero. Pumping at 266 nm by a frequency-quadrupled Nd:YAG laser forming a 50 mJ, 10 ns laser sheet of 7 cm × 0.5 mm cross section is assumed, along with a detection system identical to that used for the calculation of Fig. 3a, with
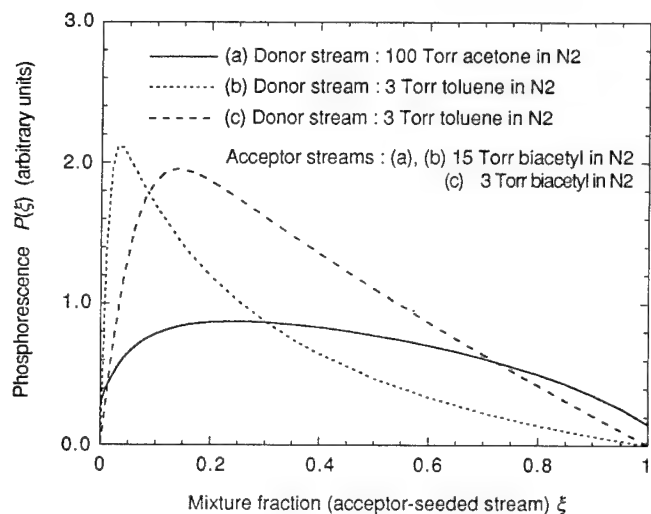

Fig. 3a–c. Calculated phosphorescence yields. **a** Acetone donor at 100 Torr free stream seeding, pumped at 308 nm with a 50 mJ, 20 ns, 3.5 cm × 0.5 mm laser sheet; **b** Toluene donor at 3 Torr free stream seeding, pumped at 266 nm with a 50 mJ, 10 ns, 7 cm × 0.5 mm laser sheet. In each case the acceptor stream is seeded with biacetyl at 15 Torr. **c** Same as case (**b**) but with 3 Torr biacetyl seeding in the acceptor stream

the exception that an optical filter for discriminating against donor phosphorescence is not required.

A complication is that in addition to the triplet-triplet energy transfer reaction (Eq. 1), energy transfer to biacetyl from toluene singlets also occurs (see Fig. 1), and this additional mechanism is responsible for the qualitative difference between the curves of Fig. 3a and 3b. However, if the acceptor seeding is reduced, the effect of singlet energy transfer is lessened. The product yield curve of Fig. 3c which is linear with mixture fraction for most ξ and which shows zero contribution in the unmixed free streams, is the result. The shift of maximum product yield to higher acceptor mixture fractions (than in Fig. 3b) can be rationalized using the chemical reaction analogy. When the acceptor seeding is reduced, more acceptor-stream fluid is required to obtain a stoichiometric mixture.

In summary, sensitized phosphorescence from the toluene-biacetyl system is more complicated than that from acetone and biacetyl. However, using appropriate donor and acceptor seeding densities, the system appears promising for quantitative mixing measurements.

5
Experimental

Experiments are required to assess the validity of the conclusions based on modeling. The objective then is to measure the product yield as a function of mixture composition, when one nitrogen stream seeded with a given concentration of donor molecules mixes with a second stream seeded with biacetyl acceptors. The most obvious methodology is to take a static cell, choose a hypothetical mixture of streams one and two, add donors, acceptors and nitrogen at partial pressures corresponding to the chosen mixture fraction ξ, and then measure the product signal $P(\xi)$ from the mixture. Indeed this approach was undertaken initially to evaluate an acetone-biacetyl system, but proved to be slow and inefficient, because each data point required evacuation of the static cell and careful introduction of the gases at the correct partial pressures before a measurement $P(\xi)$ could be made. If the product response for different seeding in the two streams was desired, the whole measuring sequence would have to be repeated for the different gas mixtures required.

Since there is no interaction of excited acetone singlets with biacetyl molecules, it was realized that in an acetone-biacetyl system, if all mixing scales in a real mixing layer were resolved, the product yield function could be measured in situ. Blue fluorescence from excited acetone singlets would provide a passive scalar dilution measurement of the local mixture fraction ξ (Lozano et al. 1992) and the green sensitized biacetyl phosphorescence would give the corresponding reaction product signal $P(\xi)$. A slow, laminar flow in which diffusion had time to thicken the mixing layer to a fully-resolvable scale was chosen to perform the product yield measurement.

Figure 4 shows a schematic of the experimental setup. The flow configuration consisted of a 6 mm diameter axisymmetric jet of nitrogen seeded with biacetyl vapor at a partial pressure of 15 Torr exiting into a coflowing stream of nitrogen, seeded with acetone vapor at between 12 and 100 Torr. Seeding of the two streams was achieved by bubbling the nitrogen through baths of liquid biacetyl and acetone respectively, then passing the seeded gases through 40 μm micropore filters to remove liquid
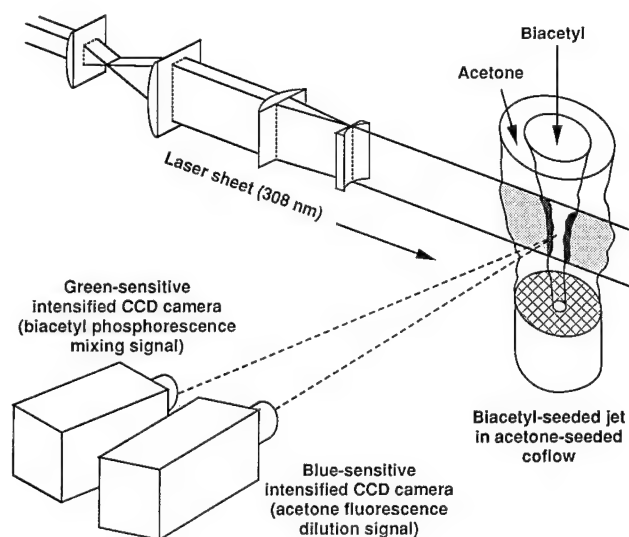

Fig. 4. Experimental apparatus for molecular mixing measurements using the acetone-biacetyl system

droplets. Nitrogen rather than air was used as the carrier gas, because as has been mentioned, oxygen severely quenches phosphorescence and must be avoided in order to obtain strong signal levels. The seeding levels were measured using Rayleigh scattering. While biacetyl and acetone have relatively low toxicity, their odor is unpleasant, so ventilation was required.

A XeCl excimer laser (Lambda Physik Model EMG 160) delivered 50 mJ of 308 nm radiation in a 20 ns pulse, which was formed into a collimated sheet 3.5 cm tall and ~0.5 mm thick with cylindrical optics. The laser sheet illuminated a cross section of the flow along the central axis of the jet.

Blue acetone fluorescence (the passive scalar dilution signal) generated by the laser excitation was detected with a gated, intensified, CCD video camera equipped with a glass, "$f/2$", 50 mm photographic lens. A shortwave-pass interference filter with 500 nm cutoff was used to reject green phosphorescence, and the intensifier was gated on for a duration of 2 μs overlapping the laser pulse.

Green biacetyl phosphorescence (the chemical reaction product signal) was measured simultaneously with a second intensified camera. This camera's intensifier was gated for a 10 μs exposure, but delayed by ~0.1 μs with respect to the laser pulse in order not to be sensitive to short-lived fluorescence. A long-wave-pass filter (cutoff 550 nm) placed in front of this second camera reduced spurious contributions from acetone phosphorescence (Eq. (3)), which is bluer than that from biacetyl. The product of filter transmission, detector sensitivity and intensifier gain gave an overall camera gain for phosphorescence approximately 8 times greater than that of the other camera, which was necessary in order to detect the weaker signals.

Post-processing of the digital images (which included background subtraction and normalization for spatially non-uniform laser sheet intensity and camera response), was applied to correct for rotation, displacement and differing magnification between the images from the two cameras. After this, comparison of the passive scalar and corresponding product signals from identical locations in the flow could be made.
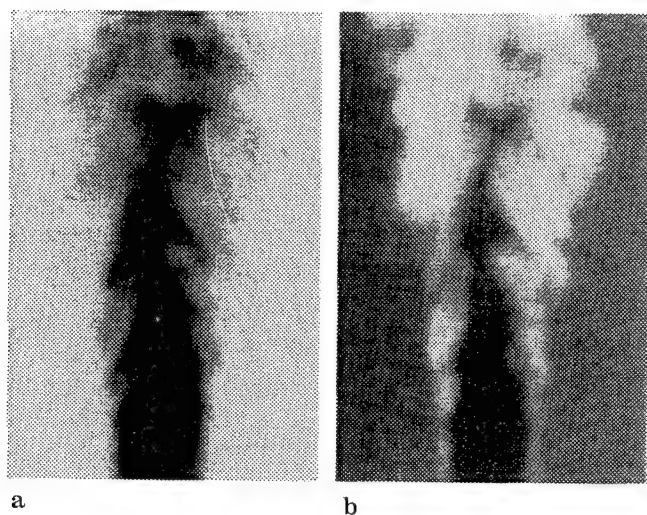
Fig. 5a,b. Simultaneous a fluorescence image and b phosphorescence image of a transitional biacetyl-seeded nitrogen jet exiting into a coflow of acetone-seeded nitrogen
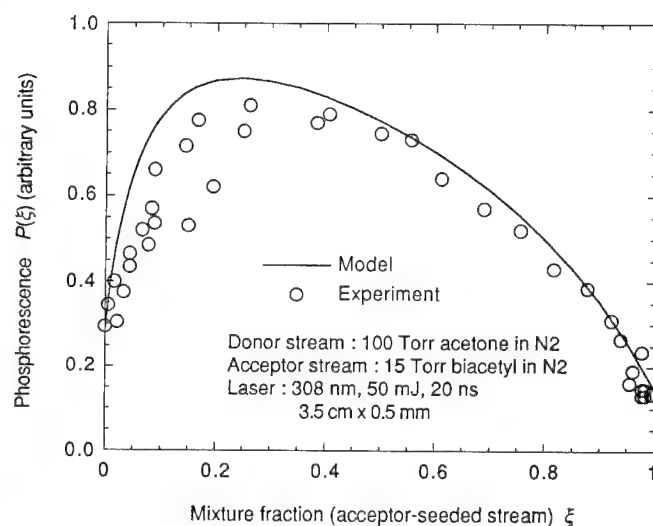

Fig. 6. Comparison of measured and calculated product yield versus mixture fraction for the case of 15 Torr biacetyl and 100 Torr acetone seeding in the two streams.

Firstly, to demonstrate molecular mixing visualization using sensitized phosphorescence, Fig. 5 shows a pair of simultaneous time-resolved (10 μs) passive scalar-reaction marker images taken in a transitional jet ($Re = 3150$). The jet is 15 Torr of biacetyl in nitrogen and the coflow is 60 Torr of acetone in nitrogen. The images cover 3.9 d × 5.5 d, starting 0.2 d downstream of the $d = 6$ mm inner diameter nozzle. Blurring in the phosphorescence image due to movement of the flow during the 10 μs image intensifier gating time is too small to be resolved and hence negligible. Brighter shading indicates higher fluorescence and phosphorescence signals in Figs. 5a and 5b respectively (the peak signal-to-noise ratio in both images is approximately 15 to 20), and the flow direction is from bottom to top. In Fig. 5a the passive scalar signal (acetone fluorescence) is seen to be at a maximum in the pure acetone-seeded coflow and minimum in the biacetyl-seeded jet. The mixing layer, where the passive scalar is diluted by mixing of the jet and coflow streams, is not well visualized. Figure 5b in contrast, shows product signals (biacetyl phosphorescence) strongly peaked in the shear layer where mixing between the two streams occurs.

A thick laminar mixing layer was imaged in order to measure the variation of product yield with mixture composition. Figure 6 shows the product yield variation with mixture fraction for the case of 15 Torr biacetyl and 100 Torr acetone seeding in the two streams. The experimental data points come from a radial traverse of the mixing layer images, with the value of the product signal $P(\xi)$ obtained from the biacetyl phosphorescence image and the local mixture fraction ξ derived from the corresponding value in the acetone fluorescence image. Plotted in the same figure is the calculated product yield from Fig. 3a, and good qualitative agreement is seen. Furthermore, reduction of the acetone free stream seeding was observed not to change the stoichiometric mixture fraction, as discussed in Sect. 4.

To verify the toluene-biacetyl modeling, static cell measurements had to be performed. (Due to the singlet energy transfer mechanism, toluene singlet fluorescence could not be used to determine the local mixture fraction in a mixing layer at
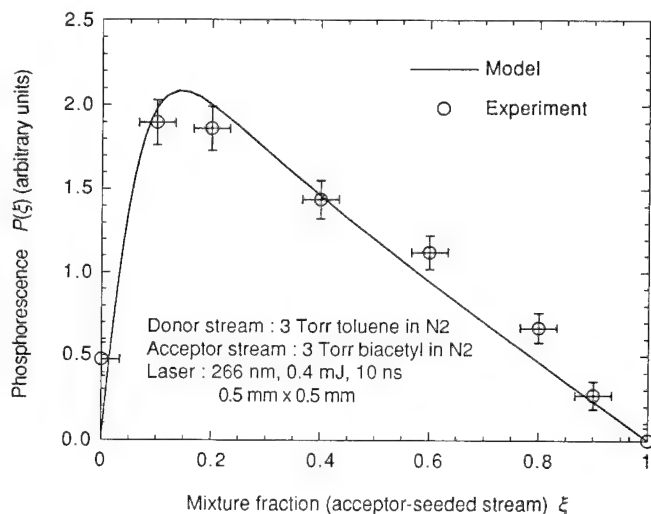
Fig. 7. Comparison of measured and calculated product yield versus mixture fraction for the case of 3 Torr biacetyl and 3 Torr toluene seedling in the two streams

the same time as the corresponding product signal was measured, as was done in the acetone-biacetyl experiments.) Toluene, although not carcinogenic, is considered to be mildly toxic. Dilution in a laboratory exhaust system is necessary to reduce concentrations to safe levels (200 ppm in air). A frequency-quadrupled Nd:YAG laser (Quanta Ray Model DCR-2) was used to obtain 0.4 mJ of 266 nm radiation in a collimated beam of ∼0.5 mm diameter. The sensitized phosphorescence excited by this beam in a static cell filled with appropriate toluene-biacetyl-nitrogen mixtures was measured with a photomultiplier and a boxcar averager set to integrate over a 10 μs window delayed ∼0.1 μs after the laser pulse. Figure 7 shows the experimental results along with the corresponding model predictions, which again show good qualitative agreement. Corrections for measured laser beam attenuation (here 15% at most) have been included. The non-zero product signal measured from "pure" toluene ($\xi = 0$)

arises from low-level biacetyl contamination in the static cell and should be ignored. The product yield curve corresponds to excited donor molecules acting as the deficient reactant and is appropriate for quantitative mixing measurements.

6
Conclusions

Sensitized phosphorescence has previously been used for qualitative visualization of gas phase fluid mixing (Bates 1977, Winter et al. 1992). The goal of this work has been to explore the possibility of performing quantitative mixing measurements using sensitized phosphorescence, within the framework of the chemical reaction methodology (Dimotakis 1989). A generalized photophysical model was developed in order to predict the dependence of sensitized phosphorescence on fluid composition in mixing experiments, and both acetone and toluene were considered as donor species for sensitizing biacetyl phosphorescence. Experiments performed in acetone-biacetyl and toluene-biacetyl systems showed strong signal levels and good qualitative agreement with the model results. Sensitized phosphorescence from the toluene-biacetyl system in particular is suitable for quantitative mixing measurements.

References

Bates SC (1977) Luminescent visualization of molecular and turbulent transport in a plane shear layer. Ph.D. Thesis, Dept. of Aero. and Astro., Massachusetts Institute of Technology. Also MIT Gas Lab Report 134

Borge MJG; Figuera JM; Luque J (1990) Study of the emission of the excited acetone vapor at intermediate pressures. Spectrochim Acta 46A (4): 617–621

Breidenthal R (1981) Structure in turbulent mixing layers and wakes using a chemical reaction. J Fluid Mech 109: 1–24

Brown RG; Phillips D; Das Gupta G (1974) Mechanisms of electronic energy transfer in the gas phase. J Phys Chem 78 (23): 2407–2414

Burton CS; Noyes WA Jr (1968) Electronic energy relaxation in toluene vapor. J Chem Phys 49 (4): 1705–1714

Clemens NT; Mungal MG (1991) A planar Mie scattering technique for visualizing supersonic mixing flows. Exp Fluids 11: 175–185

Clemens NT; Paul PH (1993) Scalar measurements in compressible axisymmetric mixing layers. AIAA 31st Aerospace Sciences Meeting, 11–14 January 1993 (Reno, Nevada), AIAA 93-0220

Cundall RB; Davies AS (1966) The mechanism of the gas phase photolysis of acetone. Proc R Soc London, Ser A, 290: 563–582

Dimotakis PE (1989) Turbulent free shear layer mixing. AIAA 27th Aerospace Sciences Meeting, 9–12 January 1989 (Reno, Nevada), AIAA 89–0262

Garabedian ME; Dows DA (1968) Vapor-phase bimolecular quenching of the triplet state of biacetyl. J Am Chem Soc 90 (10): 2468–2470

Hall JL; Dimotakis PE; Rosemann H (1991) Some measurements of molecular mixing in compressible turbulent shear layers. AIAA 22nd Fluid Dynamics, Plasma Dynamics and Lasers Conference, 24–26 June 1991 (Honolulu, Hawaii), AIAA 91-1719

Hansen DA; Lee EKC (1975) Radiative and nonradiative transitions in the first excited singlet state of symmetrical methyl-substituted acetones. J Chem Phys 62 (1): 183–189

Heicklen J (1959) The fluorescence and phosphorescence of biacetyl vapor and acetone vapor. J Am Chem Soc 81: 3863–3866

Holtzclaw KW; Schuh D (1981) Lifetimes of triplet state alkylbenzenes in the vapor phase. Chem Phys 56: 219–229

Jaffé HH; Orchin M (1962) Theory and applications of ultraviolet spectroscopy. pp 545–552. New York: Wiley

Koochesfahani MM; Dimotakis PE (1986) Mixing and chemical reactions in a turbulent liquid mixing layer. J Fluid Mech 170: 83–112

Lamola AA; Turro NJ (1969) Energy transfer and organic photochemistry. Volume XIV of Technique of Organic Photochemistry. (ed. Weissberger, A.) New York: Interscience Publishers

Lozano A (1992) Laser-excited luminescent tracers for planar concentration measurements in gaseous jets. Ph.D. Thesis, Dept. of Mechanical Engineering, Stanford University. Also HTGL Report T-284

Lozano A; Yip B; Hanson RK (1992) Acetone: a tracer for concentration measurements in gaseous flows by planar laser-induced fluorescence. Exp Fluids 13: 369–376

Mungal MG; Dimotakis PE (1984) Mixing and combustion with low heat release in a turbulent mixing layer. J Fluid Mech 148: 349–382

Richard C; Bouchy M; André J-C; Niclausse M (1978) Radiationless transitions between excited singlet states of biacetyl. Int J Chem Kin 10: 213–226

Sidebottom HW; Badcock CC; Calvert JG; Rabe BR; Damon EK (1972) Lifetime studies of the biacetyl excited singlet and triplet states in the gas phase at 25°. J Am Chem Soc 94: 13–19

Winter M; Hermanson JC; Dobbs GM (1992) Imaging of molecular mixing in a gas-phase turbulent jet by collisional energy-transfer fluorescence. AIAA 30th Aerospace Sciences Meeting, 6–9 January 1992 (Reno, Nevada), AIAA 92-0381

INSTANTANEOUS THREE-DIMENSIONAL FLOW VISUALIZATION BY RAPID ACQUISITION OF MULTIPLE PLANAR FLOW IMAGES

Bryan J. Patrie
Jerry M. Seitzman
Ronald K. Hanson

Stanford University
High Temperature Gasdynamics Laboratory
Department of Mechanical Engineering
Stanford, California 94305

Instantaneous three-dimensional flow visualization by rapid acquisition of multiple planar flow images

Bryan J. Patrie
Jerry M. Seitzman
Ronald K. Hanson, MEMBER SPIE
Stanford University
High Temperature Gasdynamics Laboratory
Department of Mechanical Engineering
Stanford, California 94305

Abstract. A flow visualization system is described that provides 3-D snapshots of instantaneous flow structures by rapidly acquiring successive image planes from within the flow. For each 3-D snapshot, up to 20 planar images are collected at the rate of 10,000,000 images/s. Flow visualization at successive planes is by planar particulate scattering or planar laser-induced fluorescence using a laser sheet rapidly swept once across the flow by a 30,000-rpm polygon scanner. Variations in the laser sheet intensity are monitored by placing an on-edge image of the sheet on the periphery of every planar flow image. The camera is a high-speed image converter coupled by fiber optics to a slow-scan CCD camera. The fiber optics provide 2.5 times better light gathering efficiency than lens coupling without reducing the available spatial resolution. The overall measurement technique shows excellent potential as demonstrated with a selection of 3-D measurements.

Subject terms: three-dimensional flow visualization; high-speed imaging; turbulence measurement.

Optical Engineering 33(3), 975–980 (March 1994).

1 Introduction

Turbulent flames and flows require 3-D measurement techniques to comprehensively investigate their highly nonisotropic mixing characteristics. The measurement technique described herein provides 3-D snapshots of turbulent mixing characteristics in cold-flow or combustion settings. More specifically, the technique provides instantaneous full-field 3-D measurements of particle or species concentrations within a volume of the flow. These measurements can be studied for properties such as flame connectedness, surface-to-volume ratios, absolute mixing gradients, and mixing topology. A better understanding of these 3-D matters will impact a broad range of turbulent-flow devices.

Normally, a 2-D measurement technique, planar flow imaging provides visualization of a specific flow plane by scattering a laser sheet from molecules or particles within the flow.[1] We have applied the technique in three dimensions by sweeping the laser sheet across the flow while a high-speed camera acquires a set of images, as shown in Fig. 1. Each image set is comprised of up to 20 planar flow images recorded at 10^7 images/s for a total recording time of under 2 μs. This recording time is instantaneous with respect to most flows of interest. After acquisition of an image set, the individual planar flow images are digitally processed and stacked to form an instantaneous 3-D measurement.

Previously, 2-D planar flow imaging at lower image rates ($\sim 10^3$ images/s) has been used for noninstantaneous 3-D measurement of flows with periodic structure.[2] Higher imaging rates ($\sim 10^5$ images/s) suitable for instantaneous 3-D measurement of slow nonperiodic flows have been achieved with a frame-transfer CCD (Ref. 3) and a scanned-input vidicon device.[4] A high-speed system suitable for instantaneous 3-D measurement of fast flows, similar to the system described herein, has been demonstrated by Yip et al.[5] and Long and Yip.[6] We have improved on this work by providing (1) faster laser sheet scan rates and therefore larger measurement volumes, (2) instantaneous monitoring of the laser sheet energy for more accurate laser sheet corrections, and (3) improved camera hardware for higher image resolution and better sensitivity to low-light flow visualizations. In this paper, we describe the improved measurement technique, assess the performance of the camera system, and present a selection of 3-D measurements.
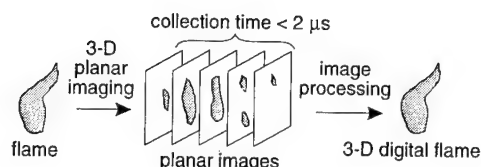
2 Measurement Technique

Shown in an exploded format in Fig. 2, the camera is based on an image converter coupled by a series of coherent fiber optics bundles to a CCD array. The image converter is a Hadland Imacon 790 internally triggered at 10^7 images/s. As the image converter is triggered, an image set of up to 20 images is briefly displayed on the 40- × 70-mm P-20 phosphor in a two-row, side-by-side format. The exposure time for each image is about ⅕ the interframe time, or about 20 ns. The dynamic range of the image converter at that speed, as specified by the manufacturer, is approximately 50:1. To re-
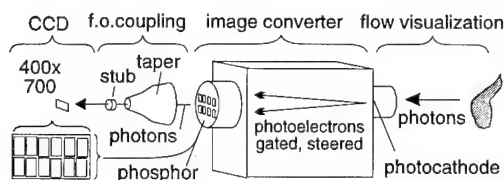
Fig. 1 Multiple planar images are rapidly acquired by the 3-D planar imaging technique. Digital image processing converts the planar images into a 3-D flow visualization measurement.
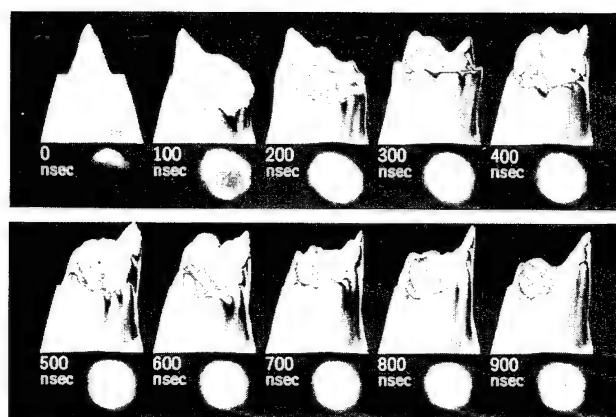

Fig. 2 Exploded schematic of camera hardware. Capability to frame at 10^7 images/s is provided by image converter. Output images are displayed on phosphor screen and then recorded by CCD camera.


Fig. 3 History of a single laser pulse from a flashlamp-pumped dye laser collected at 10^7 images/s by directing the beam onto a diffuse surface. Images and renderings show rapid energy variations.

Fig. 4 Plan view of 3-D measurement configuration. For sheet monitoring, a beam split is made prior to the scanner and directed onto a card in the field of view of the camera. Registration marks are provided by fiber optic cables fed by a coordinated flashbulb.

cord the image converter output, most use Polaroid film placed directly against the output phosphor, or a video-grade CCD camera lens-coupled to the phosphor. In contrast, we are using a 400×700 Reticon slow-scan CCD camera sealed in a cooled camera head by a 1:1 fiber optic stub and coupled to the phosphor by a 3.75:1 (diameter ratio) fiber optic taper. The fiber optics substantially improve the performance of the camera, which is detailed in the following section.

Planar flow images collected with exposure times of 20 ns require intense laser power, which precludes the use of a continuous-beam laser. The repetition rate of available pulsed lasers precludes pulsed operation synchronized with framing of the camera. For these reasons, planar illumination for an entire image set is provided by a single long-duration pulse from a Candela SLL8000 flashlamp-pumped dye laser. The pulse duration is 2 µs full width at half maximum (FWHM), which is sufficient for up to 20 images when collected at 10^7 images/s. The pulse energy is as high as 10 J at 590 nm using Rhodamine 590 dye. The output wavelength can be tuned within the limits of the Rhodamine 590 gain curve (about ± 30 nm) using an intracavity triple-prism tuner, and frequency doubling into the ultraviolet is possible with about 6% conversion efficiency using an external angle-tuned doubling crystal. A transient record of the first microsecond of a typical laser pulse at 590 nm is illustrated in Fig. 3, which includes surface rendering of the beam intensity. The data was collected at 10^7 images/s and illustrates the duration and the rapid energy variations of the beam.

For 3-D flow visualization, the beam is formed into sheet and swept once across flow, as shown in Fig. 4. To sweep the sheet, we use a 12-sided aluminum polygon scanner driven by an asynchronous ac motor rotating at 30,000 rpm. A stationary mirror adjacent to the scanner doubles the speed imparted to the laser by causing a second strike of the scanner. Additional stationary mirrors will further increase the sheet speed according to $\omega_{sheet} = 2n\omega_{scanner}$, where ω refers to angular speed and n is the total number of scanner strikes. With the flow located 1 m from the scanner and with one stationary mirror, the lateral speed of the sheet through the flame gives
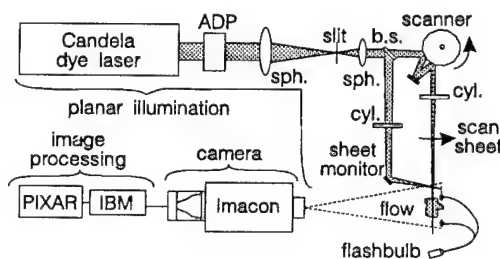
1.1 mm of sheet travel between images collected at 10^7 images/s, allowing a sheet sweep of several centimeters during a 3-D measurement.

As with most quantitative planar flow imaging, laser sheet monitoring is necessary because the flow visualization depends on the laser energy at the instant each planar flow image is collected. As previously shown in Fig. 3, the flashlamp-pumped dye laser exhibits rapid energy variations over the course of a single pulse. These variations necessitate temporally resolved sheet monitoring. For this purpose, as illustrated in the plan view of Fig. 4, a split of the main beam prior to the scanner is directed onto a card in the camera's field of view. A stationary on-edge sheet thus appears within every frame, giving an instantaneous record of the sheet profile at the time each planar flow image is collected.

With the Hadland image converter, fluctuations in the placement of the individual images on the output phosphor necessitate registration marks within every image so the flow visualizations can be accurately located from within the image set and then stacked to form a 3-D array. As shown in bottom-right of Fig. 4, fiber optic cables fed by a coordinated flashbulb create registration marks within the field of view of the camera. A single 5-µs flash provides illumination for registering all the images of the image set.

After an image set is captured as single 400×700 CCD image, the data is downloaded to a 80486-based computer through an IEEE-488 interface. The format of the output is

illustrated in Fig. 5. After manually identifying the registration marks, custom Windows-based software performs laser sheet corrections, image enhancements, and image stacking to generate the 3-D data array. The measurement can then be applied to volume rendering routines and other 3-D engineering analyses.

3 Camera System Characterization

The performance characteristics of the camera system have been evaluated to assist in the design of meaningful experiments and to identify critical areas for future camera improvements. The characterization presented here includes the fiber optic coupling efficiency, the system resolution, and the overall sensitivity.

3.1 Fiber Optic Coupling Efficiency

The sensitivity of the camera system is directly proportional to the efficiency of the fiber optics coupling the image converter phosphor to the CCD array. The coupling efficiency is defined as the fraction of the image converter output photons that are collected and delivered to the CCD array. The coupling efficiency is $\eta = \eta_{taper}\eta_{stub}$, i.e., the product of the efficiencies of the two coupling components (c.f., Fig. 3). The coupling efficiency of the taper can be computed from

$$\eta_{taper} = \frac{coupled}{available} = \int_{2\pi} \beta_{taper}I_{Imacon}\ d\omega / \int_{2\pi} I_{Imacon}d\omega \ , \qquad (1)$$

where I_{Imacon} is the directional optical energy output per solid angle delivered out the phosphor and β_{taper} is the directional transmission of the taper, which depends on the direction of the applied input. The data for β_{taper} was measured using a distant point source of light from a P-20 phosphor unidirectionally applied to the input face of the taper with the stub and CCD attached. The resulting pixel values, scaled by the taper area ratio, were divided by the pixel values obtained with the taper removed. The resulting β_{taper} distribution and I_{Imacon} are plotted in Fig. 6. The data shows that the image converter exhibits a fairly Lambertian output distribution, whereas the taper provides only a very narrow transmission cone. When applied to Eq. (1), the data yield $\eta_{taper} = 5.3\%$, which compares well with related measurements by Coleman.[7] Similarly, the efficiency of the stub can be computed from

$$\eta_{stub} = \frac{coupled}{available} = \int_{2\pi} \beta_{stub}I_{taper}\ d\omega / \int_{2\pi} I_{taper}\ d\omega \ , \qquad (2)$$
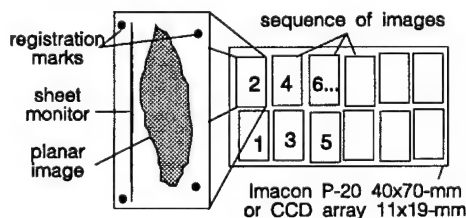

Fig. 5 Format of system output. High-speed images appear side by side on the CCD array. Each high-speed image contains a planar flow image, a sheet monitor record, and registration marks.
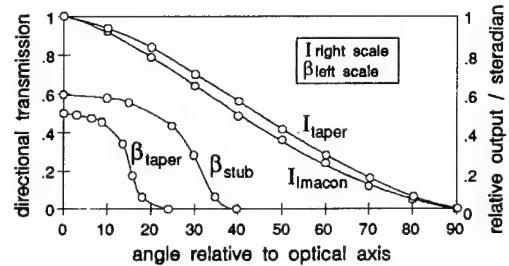

Fig. 6 Directional properties of camera components. The properties determine the efficiency of the fiber optics coupling the image converter to the CCD array. Based on these curves, the taper passes 5.3% of the Imacon output, while the stub, in turn, passes 18% of the taper output.
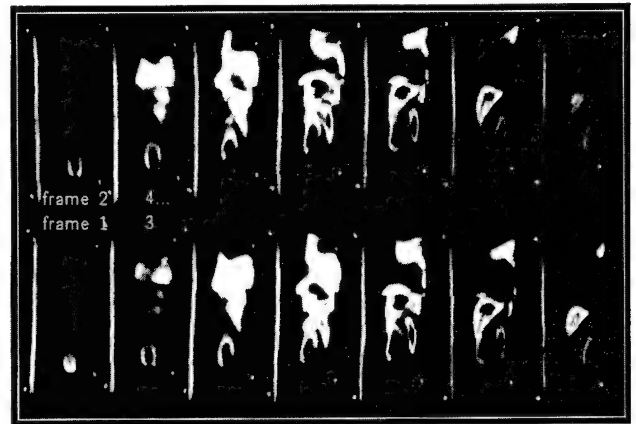

Fig. 7 Unprocessed image set showing the top 10 cm of a 15-cm-tall swirling ethylene diffusion flame. Flow visualization is by planar particulate scattering from naturally occurring soot particles. Total image set recording time is 1.4 μs.

where I_{taper} is the directional distribution of the taper output and β_{stub} is the directional transmission of the stub. These data are also plotted in Fig. 7 and give $\eta_{stub} = 18\%$. Thus the combined coupling efficiency of the taper and stub is 5.3 $\times$ 18%, or approximately 1.0%.

At 1% coupling efficiency, the fiber optic system provides substantially better performance than most lens-coupled CCD recording systems. Considering commercially available complex lenses and specified resolution limits, an $f/2$ lens is approximately the fastest that can maintain the spatial resolution available at the image converter output. The coupling efficiency of an $f/2$ lens for the I_{Imacon} distribution is only 0.4%, assuming no lens reflection or absorption losses, and assuming 3.75:1 image minification as is achieved with the fiber optics. Thus, the fiber optics are 2.5 times more efficient than a $f/2$ lens-coupled design.

3.2 Resolution

The resolution of the system indicates the potential quality of the flow visualization results. For comparison purposes, the line-pair (lp) resolutions reported here have been projected to the input of the system, i.e., the 9- $\times$ 8-mm photocathode. To measure the resolution, images were collected of a standard U.S. Air Force (USAF) 1951 resolution test target. The resolution was measured for the image converter

alone using images of the test target recorded from the phosphor directly onto Polaroid film. On the developed film, 9 lp/mm could not be resolved by the human eye, whereas 10 lp/mm was resolved. Thus the image converter provides approximately 9 to 10 lp/mm. In comparison, for the digital output of the complete system (i.e., including the fiber optic coupling and the CCD), the resolution was again measured between 9 and 10 lp/mm. In other words, the resolution of the system is limited by the image converter, not by Nyquist sampling restrictions on the fiber optics or the CCD array.

3.3 Sensitivity

The sensitivity of the camera system depends on the overall noise and signal gain. The gain is defined as the number of electrons generated at the CCD per photon input at the image converter photocathode and can be computed from

$$G_{system} = G_{Imacon}\eta_{taper}\eta_{stub}QE_{CCD} \ . \tag{3}$$

In this expression, G_{Imacon} is the photon gain of the Imacon, defined as the number of phosphor photons exiting from the image converter per photon applied to the photocathode. The Imacon gain includes the quantum efficiency (QE) of the photocathode and is therefore spectrally dependent. For input at 442 and 632 nm, G_{Imacon} has been measured at 25 and 10, respectively, using diffused and metered HeCd and HeNe laser light. Averaged over the P-20 spectrum, the quantum efficiency of the CCD, QE_{CCD}, was measured at 24%. These values give $G_{system} = 0.06$ and 0.02 CCD electrons per photocathode photon for the HeCd and HeNe wavelengths, respectively.

The noise of the system is comprised of photon shot noise and electronic noise. At the level of the minimum detectable signal, the shot noise is small compared to the electronic noise of the system, which is dominated by the CCD dark noise of approximately 30 CCD electrons/pixel rms. Based on the previously computed values of G_{system}, the camera thus requires 500 and 1500 photons/pixel at the photocathode to generate an SNR of 1 at the HeCd and HeNe wavelengths, respectively. Considering that a CCD pixel projected onto the photocathode is 26×10^{-4} mm^2, the minimum detectable signal at the 9- $\times$ 8-mm photocathode is thus 19×10^4 and 58×10^4 photons/mm^2 at 442 and 632 nm, respectively. Such quantities of photons must be deposited on the photocathode within the exposure time of each image.

4 3-D Results

We have demonstrated the potential of the system for making instantaneous 3-D measurements using planar particulate scattering (PPS) from naturally occurring soot particles and planar laser-induced fluorescence (PLIF) from seeded acetone. Other visualization approaches are planned for the future. The intent here is to illustrate the potential quality of the imaging results.

4.1 Instantaneous 3-D PPS: Ethylene Flame

Figure 7 is an unprocessed 14-frame 3-D PPS image set showing the top 10 cm of a 15-cm-tall swirling ethylene diffusion flame with $Re_D = 3000$. The scan distance between successive frames was set to 1.1 mm to enable a full traverse across the flame with 14 frames. The sheet thickness was approximately 1 mm, the total sheet energy was 3 J and was

centered at 590 nm. The image converter was equipped with a 50-mm AF Nikkor lens set to $f/5.6$. The recording time for the entire image set was less than 1.4 µs, whereas characteristic flow times for the smallest resolved length scales were of the order of tens of milliseconds. For our exposure times, the natural orange-yellow soot emissions fall far below the detection threshold, so only the PPS was imaged. Signal levels are as high as 14,000 CCD electrons/pixel.

The images of Fig. 7 also illustrate the electrodynamic image distortions that are inherent with high-speed operation of the image converter camera. These distortions are most evident in the vertical lines comprising the laser sheet monitor, which should be straight, yet they are mildly curved. Notice each vertical line is attracted toward the bright portions of the flame image. This is due to an electrodynamic attractive force arising from high photoelectric currents within the image converter. A digital image post processor is under development to correct this distortion.

Figure 8 shows volume renderings of the same image set after correcting for laser sheet variations and after stacking the images. The purpose of the renderings is to reveal surface topology and characteristic lengths of a variety of flame features that are not apparent in the unrendered data. The flame was produced with a rifled nozzle; note the swirling character is only vaguely evident in any single 2-D image, however, the swirling character is plainly evident across the unrendered image set, and vividly evident as the braided legs of the volume rendering.

4.2 Instantaneous 3-D PPS: Acetylene Flame

A second demonstration of 3-D PPS examined soot formation in a 20-cm-tall acetylene jet diffusion flame with $Re_D = 5000$. The flame was scanned with 0.7 mm between successive frames, enabling a full traverse of the flame. The photocathode was equipped with a 50-mm AF Nikkor lens set to $f/5.6$, and the laser pulse energy was set to approximately 5 J. Figure 9 shows a typical image set on the left and volume renderings on the right. Signal levels are as high as 12,000 CCD electrons/pixel. Note that almost any of the 2-D images taken alone suggest an axisymmetric jet mode with periodic burnout. Yet the complete image set and especially the volume renderings show the axial mode is not axisymmetric, and in fact, the 3-D data shows no periodic burnout.

4.3 Instantaneous 3-D PLIF: Acetone-Seeded Jet

To demonstrate the potential of the system for 3-D PLIF, we have examined a nonreacting flow of air seeded with acetone. The flow was a jet from a straight nozzle 1.7 mm in diameter at conditions ranging from laminar to fully turbulent with
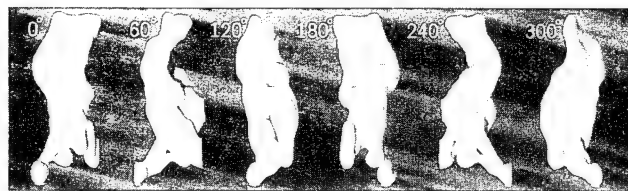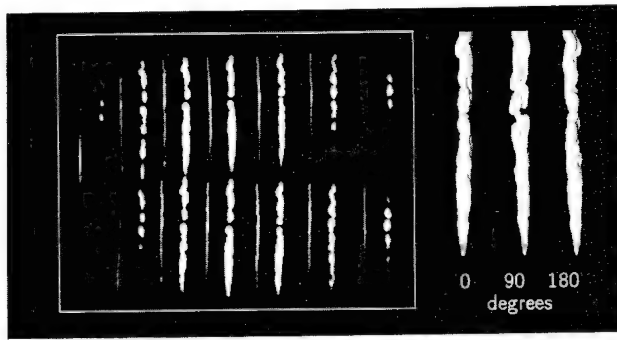

Fig. 8 Volume rendering of the instantaneous 3-D data shown in Fig. 7. Volume rendering is based on an isosignal surface from the 3-D measurement and is progressively rotated to illustrate the 3-D character of the data.

Fig. 9 Unprocessed image set and rendered images of an acetylene diffusion flame. Flow visualization is by planar particulate scattering from naturally occurring soot particles. Total image set recording time is 1.4 µs.
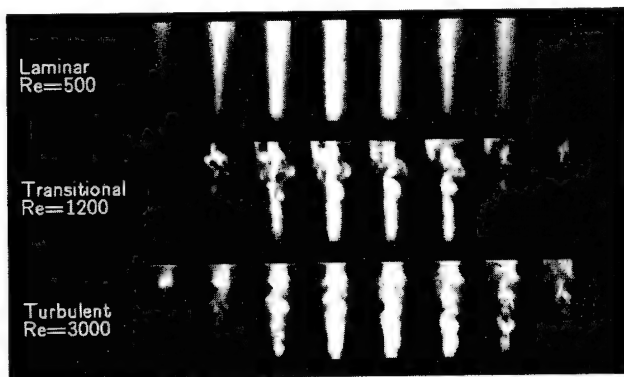
Fig. 10 Instantaneous 3-D data of an acetone-seeded nonreacting jet at various flow conditions from laminar to turbulent. Visualization is by planar laser-induced fluorescence of acetone pumped by ultraviolet illumination at 285 nm.
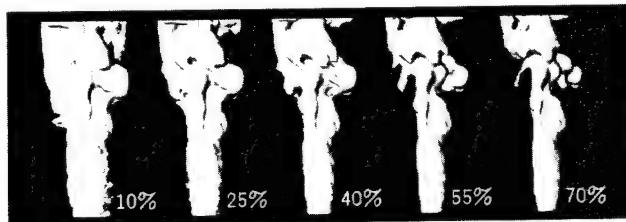
Fig. 11 Volume renderings of the transitional flow shown in Fig. 10. Renderings are based on isosignal surfaces, the isosignal value progressively raised as a percentage of the maximum signal.

seeding accomplished by first bubbling the flow through an acetone liquid reservoir. The acetone concentration corresponds to the saturation pressure at room temperature. To optically pump the acetone, the dye laser was tuned to 570 nm and then frequency doubled to 285 nm, which is near the peak of the acetone absorption curve.[8] The UV pulse energy was approximately 300 mJ, and the scan distance between frames was set to 0.7 mm. The photocathode was equipped with a 50-mm AF Nikkor lens set of $f/1.2$, and the imaged region was 2.5-cm tall beginning 0.5 cm downstream from the nozzle exit. Figure 10 shows partially processed 3-D image sets for three flow conditions. Signal levels are as high

as 7000 CCD photoelectrons/pixel. Figure 11 shows the transitional flow data after volume rendering of various isosignal surfaces, which vividly illustrate the topology of the mixing and the characteristic lengths of a variety of structures at successive depths within the flow.

5 Summary

This work has demonstrated several advances in rapid acquisition of multiple planar flow images for flow visualization in three dimensions. Specifically, this work has demonstrated that an image converter coupled to a CCD by fiber optics is an effective means for rapid planar flow image acquisition. The fiber optics provide 2.5 times the coupling efficiency of an ideal lens-coupled CCD system without reducing the system resolution. This work has also demonstrated a means for temporally resolved laser sheet monitoring by recording instantaneous sheet profiles along with each flow visualization image. This allows corrections to the planar flow images using the sheet intensity at the exact moment each planar flow image was collected. For 3-D flow visualization, the laser sheet must be rapidly swept across the flow. This work has demonstrated a 30,000 rpm polygon scanner with an adjacent stationary mirror can provide sweep distances of over 1 mm between frames collected at 10^7 images/s. This allows a measurement volume of several centimeters in depth. Through measurements gathered with this system, potential signal levels and image quality have been demonstrated via 3-D soot scattering and 3-D planar laser-induced fluorescence in several flows. The merits of 3-D flow information were apparent as even simple 3-D volume rendering of the measurements provided insights into these flows.

References

1. R. K. Hanson, "Combustion diagnostics: planar flowfield imaging," in *Proc. 21st Symp. (Int.) on Combustion*, pp. 1677–1691, the Combustion Institute, Pittsburgh (1987).
2. G. Kychakoff, P. H. Paul, I. van Cruyningen, and R. K. Hanson, "Movies and three-dimensional images of flowfields using planar laser-induced fluorescence," *Appl. Opt.* **26**, 2498–2500 (1987).
3. W. J. Hiller and T. A. Kowalewski, "Application of the frame-transfer charge-coupled device for high speed imaging," *Opt. Eng.* **28**, 197–200 (1989).
4. B. Yip, J. K. Lam, M. Winter, and M. B. Long, "Time-resolved 3-D concentration measurements in gas jets," *Science* **235**, 1209–1211 (1987).
5. B. Yip, R. L. Schmitt, and M. B. Long, "Instantaneous three-dimensional concentration measurements in turbulent jets and flames," *Opt. Lett.* **13**, 96–98 (1987).
6. M. B. Long and B. Yip, "Measurement of three-dimensional concentrations in turbulent jets and flames," in *Proc. 21st Symp. (Int.) on Combustion*, pp. 701–709, the Combustion Institute, Pittsburgh (1988).
7. C. I. Coleman, "Imaging characteristics of rigid coherent fiber optic tapers," *Adv. Elec. Elec. Phys.* **64B**, 649–661 (1985).
8. A. Lozano, B. Yip, and R. K. Hanson, "Acetone: a tracer for concentration measurements in gaseous flows by planar laser-induced fluorescence," *Exper. Fluids* **13**, 369–376 (1992).
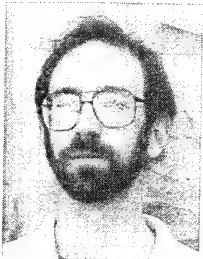
Bryan J. Patrie received his BSME from South Dakota State University in 1981 and his MSME from the University of Wisconsin at Madison in 1987 with a focus on computer-assisted flow visualization. He worked for 2 years at General Dynamics Corporation on measurement of infrared signatures from fighter aircraft. He is currently completing his PhD in the High Temperature Gasdynamics Laboratory at Stanford University. His research interests include flow diagnostics, image processing, and instrumentation electronics.

Jerry M. Seitzman received his BSME from the University of Texas, Austin. During his undergraduate years, he also studied public policy as an ASME/WISE intern in Washington, D.C. He subsequently earned an MSME in 1983 and a PhDME in 1992 both from Stanford University as an IBM Graduate Fellow. Currently he is a research associate at Stanford University in the High Temperature Gasdynamics Laboratory. His research interests are in the fields of flow imaging, combustion, and laser spectroscopy.

Ronald K. Hanson received his BSME from Oregon State University, his master's degree at Arizona State University, and a PhD from Stanford University in aeronautics and astronautics in 1968. His research has been in the fields of reactive gas dynamics, laser spectroscopy, combustion, and gas-phase chemistry. He presently directs the High Temperature Gasdynamics Laboratory and chairs the Thermoscience Division of Mechanical Engineering at Stanford University.

Temperature-Dependent Collision-Broadening Parameters of H_2O Lines in the 1.4-μm Region Using Diode Laser Absorption Spectroscopy

S. Langlois, T. P. Birbeck, and R. K. Hanson

*High Temperature Gasdynamics Laboratory, Department of Mechanical Engineering,
Stanford University, Stanford, California 94305-3032*

Spectrally resolved measurements of water vapor absorption spectra near 1.4 μm have been performed with a tunable, distributed-feedback InGaAsP diode laser. A lineshape analysis was used to infer the collision-broadening coefficient of 11 rovibrational transitions in the $\nu_1 + \nu_3$ and $2\nu_1$ vibration bands perturbed separately by N_2, O_2, CO_2, and H_2. The temperature dependence of the broadening coefficients was determined using a temperature-controlled static cell and a pressure-driven shock tube over the range 300–1200 K. The measured coefficients are in good agreement with the previous calculations of Delaye. Also, agreement is found between prior experimental data, obtained for the same rotational transitions but different vibration bands, and our results. © 1994 Academic Press, Inc.

INTRODUCTION

Radiative properties of water vapor in the infrared spectrum are important in a variety of applications, including atmospheric sounding experiments, radiative sensing of combustion processes, and optical diagnostics for gasdynamic and aerodynamic studies. Spectroscopic parameters that determine the radiative properties of molecules include the line intensity, $S(T)$, the line center position, ν_0, and the linewidth, $\delta(T, P)$ (in this paper all linewidths will be considered as the halfwidth at half maximum, HWHM), and its associated shape profile, Φ.

Collision-broadening coefficients of H_2O have been studied in several spectral regions (see Ref. (*1*) and references within). For example, Grossman and Browell (*2, 3*) have measured the collision-broadening coefficient of H_2O, when perturbed by itself, air, O_2, and N_2, near 720 nm. Wilkerson *et al.* (*4*) have measured the N_2-broadening coefficient in the same spectral region. Mandin *et al.* (*5–7*) measured the N_2-broadening coefficient of lines between 500 and 1200 nm. More recently, Arroyo and Hanson (*8*) measured the Voigt "*a*" parameter for several H_2O transitions near 1.4 μm broadened by H_2O and air, and Langlois *et al.* (*9*), measured the self-broadening coefficient for several lines near 1.4 μm. The room-temperature self-broadening coefficients have been measured and calculated for mid-IR transitions (see Ref. (*10*) and references within). Finally, the temperature dependence of the collision-broadening coefficient for H_2O transitions has been investigated in a theoretical study (*11*). Few measurements of the H_2O collision-broadening coefficients near 1.4 μm have been reported (*9, 10, 12*). The values used in the above-mentioned applications, or those listed in current data bases, are the measured or calculated values transferred from other vibration bands to the ones of interest, for equivalent rotational transitions.

EXPERIMENTAL DETAILS

InGaAsP diode lasers emit at wavelengths between 1.3 and 1.6 μm. These semiconductor lasers are attractive light sources for spectroscopy owing to their compactness,

ruggedness, cost-effectiveness, and compatibility with fiberoptics. The present experiment uses a distributed feedback InGaAsP semiconductor laser (Anritsu Corporation) that emits monochromatic radiation in the 1.382–1.384 μm wavelength region.

The laser is driven by an ILX Lightwave LDC-3722 controller. The laser has a nominal output of 5 mW (at 1382 nm) at an injection current of 70 mA and a laser temperature of 25°C. Previous tests performed on this laser (9) have characterized its output. In order to attain the wavelengths of interest in the present study, diode temperatures between 20 and 40°C were used. A mean injection current of 70 mA with a superimposed triangular current profile of amplitude ±35 mA, and repetition frequency of 10 kHz results in the desired tuning range of 60 GHz.

In this work the laser is used in two experimental setups (see Fig. 1); the first incorporates a static cell (9), the second a shock tube (13). The static cell provides an environment whose pressure and temperature are known very accurately, but viton O-rings within the cell limit its maximum temperature to 450 K. The shock tube enables extension of this temperature to much higher values, sufficient to cause dissociation of the H$_2$O; as both the temperature and pressure are calculated from measured shock speeds, their values are known with somewhat lower accuracy. The description of the experimental setup will continue by describing the static cell, the shock tube, the optical components, and the method of data acquisition.

Static Cell

The 15.24-cm-long static cell consists of a 3.17-cm-thick copper sleeve surrounding an aluminum tube which has an outer diameter of 4.45 cm and an inner diameter of 2.54 cm. BK7 windows are attached to the aluminum tube with rubber O-rings forming the gasket. Resistive heating elements raise the temperature in the cell up to 450 K, with a temperature deviation along the cell of less than 1 K. An MKS Baratron gage, with a full-scale deflection of 1 atm, measures the pressure in the cell with an accuracy of ±1% over the experimental pressure range. A mechanical pump evacuates the cell to 0.01 Torr. At this pressure no absorption due to residual gas can be detected. Distilled water contained in a flask connected to the cell provides a source of water
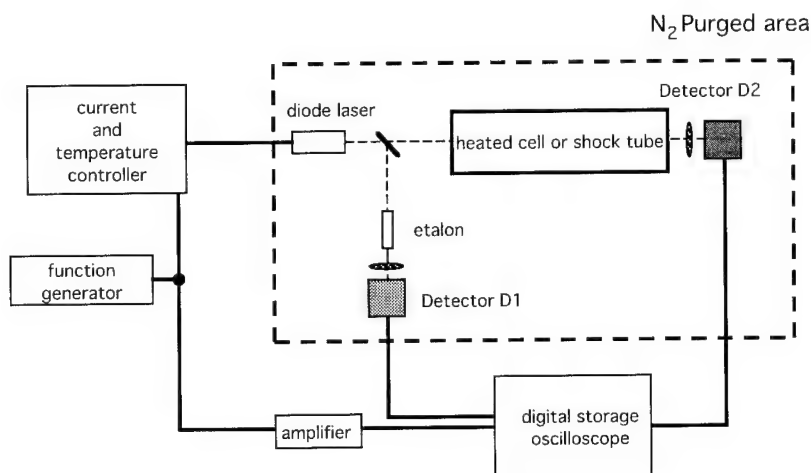

FIG. 1. Experimental schematic for the present work.

vapor. The flask is pumped down for 1 hr prior to measurements to remove all gaseous impurities. Static cell experiments were conducted at temperatures between 290 and 400 K and pressures between 0.007 and 1 atm. Several different concentration ratios of H_2O to its perturber species were used.

Shock Tube

The 15.24-cm-diameter shock tube has a 2.3-m-long driver section and a 10.5-m driven section. CaF_2 windows permit optical access to the flow at an angle of 90° to the tube axis. Gas absorption was measured behind the pressure-driven incident shock wave. The driver section was filled with high pressure helium, and polycarbonate diaphragms were used to separate the driver from the driven section. Four gas mixtures were used to fill the driven section: H_2O with O_2, H_2O with CO_2, H_2O with H_2, and H_2O with N_2. Diaphragm thicknesses varied between 0.1 and 0.4 mm, as needed to generate the required post-shock conditions in the test section. A series of thin film gauges located on the shock tube walls measures the shock speed. Temperatures behind the shock were between 600 and 1200 K, with pressures ranging between 0.1 and 0.4 atm. The post-shock conditions were determined using the Rankine–Hugoniot relations (*14*); a code similar to that described by Gardiner *et al.* (*15*) was used for this calculation.

Optical Components

For clarity, the optical setup will be described by following the optical path of the laser (Fig. 1). Initially the laser beam is collimated by a 6-mm focal-length lens with a broadband antireflection coating. The parallel beam is converted to two beams by a BK7 beam splitter. The first beam passes through a low finesse solid étalon of 2 GHz spectral range and is then focused onto a detector, D1, providing a measurement of relative wavelength change. Germanium photodiodes (EG&G J-16-18A-R01M) function as detectors for each of the focused laser beams. The second and principal beam passes through the static cell, or the shock tube section, and is then focused on a detector, D2. A nitrogen-purged area (Fig. 1) eliminates absorption due to moisture present in the room air.

Data Acquisition

A Nicolet 4-channel digital oscilloscope acquires detector voltages and a reference signal, (I_1); this reference signal is the output from the function generator driving the laser controller (Fig. 1). The two other recorded signals are (1) the étalon signal (I_2) and (2) the difference between the cell signal (I_3) and the reference signal (I_1), i.e., (ΔI_{3-1}). An amplifier placed between the function generator and the oscilloscope ensures close similarity between I_1 and I_3 in the absence of absorption. The signal ΔI_{3-1} is recorded instead of I_3 in order to increase the resolution of the recorded lineshape on the oscilloscope. Perturbation due to both optical and electronic hardware is accounted for by recording ΔI_{3-1}^0, where ΔI_{3-1}^0 is the signal associated with an evacuated gas section and referred to as the "base line" signal.

The similarity of several base line records, separated by a period of 10 min confirmed stability of the diode laser and detectors. The transmission coefficient, $\tau(\nu)$, is related to the ratio of the cell signal (I_3) to the evacuated one (I_3^0):

$$\tau(\nu) = I_3/I_3^0. \tag{1}$$

I_3^0 is obtained by the sum of the reference signal I_1 and the base line $\Delta I_{3\text{-}1}^0$:

$$I_3^0 = \Delta I_{3\text{-}1}^0 + I_1. \tag{2}$$

I_3 is obtained in similar manner:

$$I_3 = \Delta I_{3\text{-}1} + I_1. \tag{3}$$

The experimental transmission $\tau(\nu)$ can thus be determined with Eq. (1). Note that the reference signal, I_1, by virtue of its stability does not affect the evaluation of $\tau(\nu)$.

Interference fringes recorded from the étalon signal enable the conversion from time to frequency. The spectral distance between two extremes, in wavenumbers, is given by

$$\Delta\sigma = (2nl)^{-1}, \tag{4}$$

where n is the refractive index of the material and l is the thickness (cm). A fifth-order polynomial least-squares fit is used to describe the relationship between time and frequency.

DATA ANALYSIS

A Voigt profile analysis of the measured lineshape was used to determine the absorption coefficient, $k(\nu, T)$. Direct modeling of the absorption coefficient determined the line intensity and the linewidth. The linewidth, $\delta(T, P)$, was then determined using the relationship

$$k(\nu, T) = \sum_{i=1}^{N} S_i(T) X P \Phi(\nu - \nu_{0_i}, \delta(T, P)), \tag{5}$$

where S is the line intensity, T is the temperature, X is the mole fraction, P is the total static pressure, Φ is the Voigt profile, and N is the number of overlapping lines.

Our previous paper (9) describes explicitly how the experimental lines are identified. The measured lines listed in Table I are from the $\nu_1 + \nu_3$ and the $2\nu_1$ vibration bands of H₂O. Also present in Table I are other lines which are close enough (0.2 cm⁻¹) to perturb the lines studied. These lines, as listed in HITRAN (1), possess intensities two orders of magnitude lower than those considered, and hence their contribution to the absorption coefficient is neglected.

In order to extract the linewidth, Eq. (5) is directly modeled by a nonlinear least-squares fit of the experimental data, with S_i, ν_0, and δ as variables. The accuracy of the experimental conversion of time to frequency, using the étalon signal and Eq. (4), has been determined. The uncertainty in the relative spectral separation is less than 10^{-2} cm⁻¹ (9). The collision-broadened linewidth (modeled as a Lorentzian profile), δ_L, is now determined using the relationship

$$a = (\ln 2)^{0.5} \frac{\delta_L}{\delta_D}, \tag{6}$$

where "a" is the "Voigt a" parameter which, combined with frequency, characterizes the Voigt Profile; δ_D is the Doppler width given by

$$\delta_D = 3.58 \times 10^{-7} \nu_0 (T, [\text{K}]/\text{amu})^{0.5}. \tag{7}$$

LANGLOIS, BIRBECK, AND HANSON

TABLE I

Spectroscopic Parameters Extracted from the HITRAN (1) Database
in the Spectral Region of Interest

#	ν (cm^{-1})	S (296 K) (cm^{-1}/mole. cm^{-2})	E" (cm^{-1})	v' v"	J'$_{K'_aK'_c}$ J"$_{K"_aK"_c}$	
1	**7226.023926**	**6.33 10^{-21}**	**23.794**	**101 000**	0_{00}	1_{01}
	7226.324219	9.70 10^{-24}	610.341	101 000	6_{24}	5_{41}
	7226.379883	8.50 10^{-24}	1581.336	101 000	10_{46}	10_{47}
2	**7227.982910**	**2.10 10^{-21}**	**383.843**	**101 000**	4_{32}	4_{31}
	7229.791992	3.20 10^{-23}	95.176	101 000	2_{12}	2_{11}
3	**7230.052246**	**9.27 10^{-22}**	**95.176**	**101 000**	2_{12}	2_{11}
	7230.215820	4.99 10^{-24}	1216.194	200 000	7_{52}	7_{61}
4	**7230.315430**	**4.09 10^{-22}**	**275.497**	**200 000**	4_{22}	4_{13}
	7230.618164	5.70 10^{-24}	446.697	101 000	5_{24}	6_{06}
5	**7320.898398**	**6.40 10^{-21}**	**382.517**	**101 000**	4_{31}	4_{32}
	7230.938965	1.00 10^{-23}	1282.919	101 000	9_{45}	9_{36}
6	**7231.358398**	**5.99 10^{-22}**	**503.968**	**101 000**	5_{32}	5_{33}
7	**7231.828125**	**8.00 10^{-22}**	**173.365**	**200 000**	3_{21}	3_{12}
8	**7232.117118**	**1.40 10^{-20}**	**285.419**	**101 000**	3_{31}	3_{30}
	7232.133789	1.70 10^{-22}	37.137	200 000	2_{02}	1_{11}
	7232.192871	7.90 10^{-23}	782.410	200 000	7_{34}	7_{25}
9	**7232.242188**	**6.50 10^{-22}**	**136.762**	**200 000**	7_{34}	7_{25}
10	**7232.525879**	**3.05 10^{-21}**	**285.219**	**101 000**	3_{30}	3_{31}
	7232.926758	1.20 10^{-24}	1360.236	200 000	10_{38}	9_{45}
11	**7233.188965**	**7.37 10^{-22}**	**399.457**	**200 000**	5_{23}	5_{14}
	7233.291992	2.11 10^{-23}	982.912	200 000	8_{35}	8_{26}
12	**7233.423340**	**5.58 10^{-21}**	**212.156**	**101 000**	3_{22}	3_{21}

Note. Bold entries denote lines probed in the present investigation.

In the case of water vapor mixed with a perturber Z, the temperature and pressure dependence of the collision-broadened linewidth, δ_L in cm^{-1}, is given by (11)

$$\delta_L(T, P) = \gamma_L^{H_2O}(T_0)P^{H_2O}(T_0/T)^{n^{H_2O}} + \gamma_L^Z(T_0)P^Z(T_0/T)^{n^z}, \qquad (8)$$

where T_0 is 300 K, n^{H_2O} and n^Z are the temperature dependent parameters, and $\gamma_L^{H_2O}$ and γ_L^Z are the collision-broadening coefficients for H_2O when perturbed by itself and Z, respectively. From Eq. (8), it can be shown that

TABLE II

Collision-Broadening Coefficients ($cm^{-1}\ atm^{-1}$) for H_2O Perturbed by
(a) N_2, (b) CO_2, (c) O_2, and (d) H_2

#	$\gamma_L^{N_2}(300K)$ this work	$\gamma_L^{N_2}(300K)$ Ref.11	n^{N_2} this work	n^{N_2} Ref.11
1	0.117±0.002	0.113	0.76±0.06	0.72
2	0.101±0.004	0.089	*0.66*	0.66
3	0.116±0.012	0.108	*0.72*	0.72
4	0.129±0.024	0.101	*0.70*	0.70
5	0.088±0.005	0.089	0.75±0.19	0.66
6	0.088±0.010	0.090	*0.66*	0.66
7	0.107±0.009	0.103	1.00±0.24	0.69
8	0.096±0.005	0.085	0.85±0.15	0.63
10	0.089±0.002	0.085	0.77±0.07	0.63
11	0.133±0.016	0.100	0.96±0.40	0.70
12	0.114±0.005	0.100	*0.69*	0.69

(a)

#	$\gamma_L^{O_2}(300K)$ this work	$\gamma_L^{O_2}(300K)$ Ref.11	n^{O_2} this work	n^{O_2} Ref.11
1	0.070±0.001	0.076	1.12±0.05	0.65
2	0.055±0.002	0.054	0.92±0.14	0.62
3	0.061±0.006	0.070	*0.64*	0.64
4	0.053±0.008	0.057	*0.62*	0.62
5	0.044±0.002	0.054	0.70±0.27	0.62
6	0.057±0.009	0.060	*0.62*	0.62
7	0.057±0.001	0.067	0.69±0.08	0.62
8	0.045±0.001	0.054	0.79±0.07	0.64
10	0.045±0.001	0.054	0.56±0.08	0.64
11	0.054±0.002	0.063	0.33±0.11	0.62
12	0.056±0.001	0.063	0.86±0.06	0.63

(c)

#	$\gamma_L^{CO_2}(300K)$ this work	$\gamma_L^{CO_2}(300K)$ Ref.11	n^{CO_2} this work	n^{CO_2} Ref.11
1	0.212±0.001	0.206	0.70±0.03	0.69
2	0.115±0.002	0.104	0.41±0.07	0.46
3	0.168±0.003	0.179	0.20±0.08	0.64
4	0.172±0.047	0.173	*0.65*	0.65
5	0.105±0.002	0.104	0.37±0.04	0.46
6	0.106±0.023	0.112	*0.49*	0.49
7	0.187±0.018	0.180	0.79±0.27	0.68
8	0.101±0.002	0.110	0.43±0.04	0.54
10	0.104±0.001	0.110	0.46±0.03	0.54
11	0.196±0.007	0.156	0.75±0.12	0.59
12	0.149±0.003	0.147	0.51±0.05	0.59

(b)

#	$\gamma_L^{H_2}(300K)$ this work	n^{H_2} this work
1	0.093±0.001	0.87±0.04
2	0.070±0.002	0.26±0.10
3	0.101±0.006	1.02±0.27
4	0.123±0.010	1.50±0.38
5	0.064±0.002	0.39±0.11
6	0.067±0.002	0.25±0.10
7	0.086±0.003	0.40±0.10
8	0.065±0.005	0.76±0.25
10	0.063±0.003	0.35±0.13
11	0.104±0.005	0.72±0.20
12	0.088±0.004	0.62±0.16

(d)

Note. Values of the parameter n^Z, fixed at the value recommended by Delaye, are shown in italics.

$$\gamma_L^Z(T_0)(T_0/T)^{n^z} = \delta_L(T, P)/P^Z - \gamma_L^{H_2O}(T_0)(P^{H_2O}/P^Z)(T_0/T)^{n^{H_2O}}. \qquad (9)$$

All parameters on the right-side of Eq. (9) are known or can be determined: $\delta_L(T, P)$ is found from the Voigt fit of the experimental lineshape and Eq. (6); P, P^Z, P^{H_2O}, and T are measured in the experiment; $\gamma_L^{H_2O}$ is fixed to the measured value of Ref. (9); T_0 is 300 K; and n^{H_2O} is fixed to the value of Delaye *et al.* (11). The two parameters γ_L^Z and n^Z are found, for each transition studied, using a least-squares fit method.

When the linewidth can not be accurately measured in the shock tube experiment, n^Z is fixed at the value given by Delaye *et al.*, and γ_L^Z is then found from the cell data only.

RESULTS AND DISCUSSION

Tables IIa–IId regroup the experimental determination of the collision-broadening coefficient and the temperature-dependence parameter for each perturber. The overall uncertainty in these results is ±6% for γ_L^Z and ±25% for n^Z. Table II also compares the collision-broadening coefficient, at 300 K, and the temperature-dependence coefficient with the calculations of Delaye *et al.* (*11*). Good agreement (within 5%) is found for the collision-broadening coefficient, but not for the temperature dependence parameter. For the experimental temperature range (296–1200 K), an error in n^Z induces a smaller error in the collision-broadening coefficient. For example, at 1000 K, an error of 20% in n^Z produces an error of 10% in γ_L^Z.

Figure 2 shows the experimentally determined collision-broadening coefficients for line 8 as functions of temperature. No systematic error can be inferred from the plot. As expected, the collision-broadening coefficients measured in the shock-tube experiment are less accurate than those in the cell. However, the high temperature data are important in establishing the value of the temperature dependence parameter.

Figures 3a and 3b compare the measured collision-broadening coefficients at 296 K with other results (*3–7, 17–19*). In Fig. 3a the perturber is N_2, in Fig. 3b it is O_2. The comparison is made with data from transitions having the same rotational quantum numbers but from different vibration bands. Two trends in the broadening analyses are observed. First, the measured N_2-broadening coefficients are approximately 10% larger than those reported in previous investigations. Second, the O_2-broadening coefficients are approximately 5% lower than those cited previously (*3–7, 17–19*).
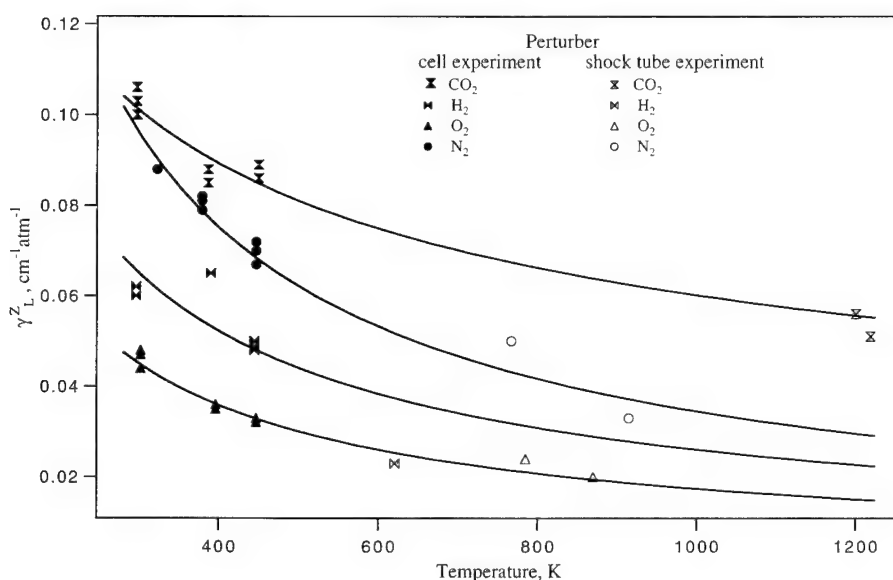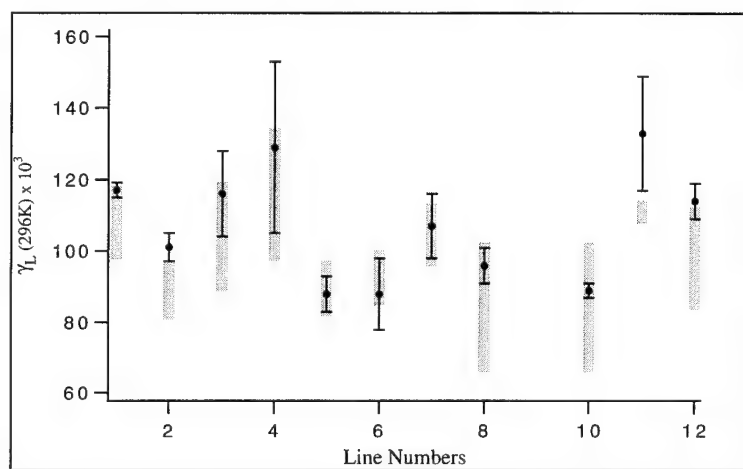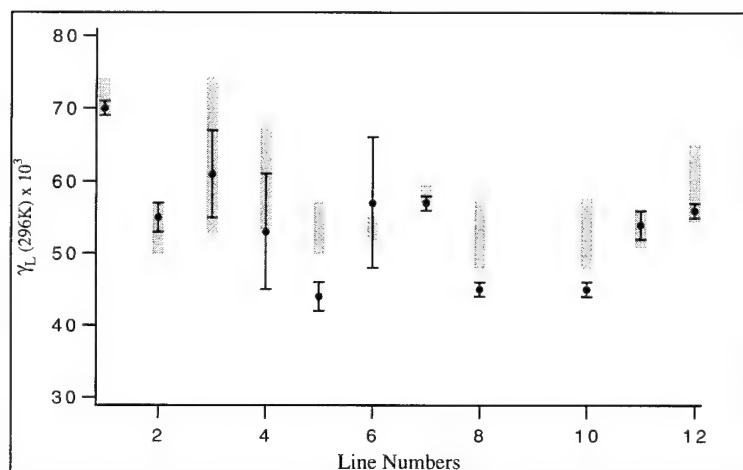

FIG. 2. Measured collision-broadening coefficient for line 8 ($v_0 = 7232.242$ cm^{-1}) as a function of temperature. The solid lines represent least-squares fits through the data recorded for each perturber.

a

b

FIG. 3. Comparison of the collision-broadening coefficient for H_2O (cm^{-1} atm^{-1}) perturbed by (a) N_2 and (b) O_2 with previous measurements. The solid dots, and their error bars, represent values measured in the present work. The shaded regions represent the range of values reported in other studies (*3–7, 16–18*) for transitions having the same rotational quantum numbers in different vibration bands.

Table III compares the calculated air collision-broadening coefficient at 296 K with HITRAN values. The average deviation is less than 12%, but several deviations are larger. Previous measurements of this parameter for the $\nu_1 + \nu_3$ and $2\nu_3$ bands, for different rotational transitions, yielded results in the range 0.068–0.081 cm^{-1} atm^{-1} (*12*). As this paper represents the first experimental measurements of this parameter, for the transitions considered, further work to confirm our findings is called for.

CONCLUSIONS

In this study, the collision-broadening coefficients of 11 rovibrational lines from the $\nu_1 + \nu_3$ and $2\nu_1$ bands of H_2O, when perturbed by N_2, O_2, CO_2, and H_2, have

TABLE III

Comparison between the Experimental Collision-Broadening Coefficients for H_2O Perturbed by Air (cm^{-1} atm^{-1}), and Those Listed in HITRAN (*1*)

#	$\gamma_L^{air}(296K)$ this work	$\gamma_L^{air}(296K)$ Ref. 1	deviation %
1	0.109	0.0778	40.2
2	0.092	0.0810	13.9
3	0.105	0.1003	5.6
4	0.114	0.0924	23.9
5	0.079	0.0843	-5.5
6	0.082	0.0778	5.9
7	0.098	0.0969	1.3
8	0.086	0.0861	0.03
10	0.081	0.0735	9.7
11	0.118	0.0948	24.6
12	0.103	0.0922	11.8

Note. Experimental values are calculated using the parameters listed in Table II, and the relation

$$\gamma_L^{air} = 0.78\gamma_L^{N_2} + 0.21\gamma_L^{O_2} + 0.01\gamma_L^{CO_2}.$$

been determined. Also, the temperature dependence of the majority of these broadening coefficients have been found. The overall scatter of the results is ±6 and ±25% for the broadening coefficients and the temperature dependence, respectively. A comparison of our results has been made with previous calculations (*11*) and experimental work (*3–8, 17–19*). Good agreement (within 5%) is found when the collision-broadening coefficient is compared with these calculations. A larger scatter (up to 18%) is found when the comparison is made with the prior experimental work. However, these prior measurements were for the same rotational transitions but different vibrational bands. These results are apparently the first published measurements of the broadening coefficients, and their temperature dependence, for H_2O lines in the 1.4-μm range.

REFERENCES

1. L. S. ROTHMAN, R. R. GAMACHE, R. H. TIPPING, C. P. RINSLAND, M. A. H. SMITH, B. C. BENNER, V. M. DEVI, J. M. FLAUD, C. CAMY-PEYRET, A. PERRIN, AND A. GOLDMAN, *J. Quant. Spectrosc. Radiat. Transfer* **48**, 449–507 (1992).

2. B. E. GROSSMAN AND E. V. BROWELL, *J. Mol. Spectrosc.* **136,** 264–294 (1989).

3. B. E. GROSSMAN AND E. V. BROWELL, *J. Mol. Spectrosc.* **138,** 562–595 (1989).

4. T. D. WILKERSON, G. SCHWEMMER, B. GENTRY, AND L. P. GIVER, *J. Quant. Spectrosc. Radiat. Transfer.* **22,** 315–331 (1979).

5. J. Y. MANDIN, J. P. CHEVILLARD, J. M. FLAUD, AND C. CAMY-PEYRET, *J. Mol. Spectrosc.* **138,** 430–439 (1989).

6. J. Y. MANDIN, J. P. CHEVILLARD, C. CAMY-PEYRET, AND J. M. FLAUD, *J. Mol. Spectrosc.* **138,** 272–281 (1989).

7. J. Y. MANDIN, J. P. CHEVILLARD, J. M. FLAUD, AND C. CAMY-PEYRET, *J. Mol. Spectrosc.* **132,** 352–360 (1988).

8. M. P. ARROYO AND R. K. HANSON, *Appl. Opt.* **32,** 6104–6116 (1993).

9. S. LANGLOIS, T. P. BIRBECK, AND R. K. HANSON, *J. Mol. Spectrosc.* **163,** 27–42 (1994).

10. J. M. HARTMANN, J. TAINE, J. BONAMY, B. LABANI, AND D. J. ROBERT, *J. Chem. Phys.* **86,** 144–156 (1987).

11. C. DELAYE, J. M. HARTMANN, AND J. TAINE, *Appl. Opt.* **28,** 5080–5087 (1989).

12. S. L. BRAGG AND J. D. KELLEY, *Appl. Opt.* **26,** 506–513 (1987).

13. M. P. ARROYO, S. LANGLOIS, AND R. K. HANSON, *Appl. Opt.* **33,** 3296–3307 (1994).

14. A. G. GAYDON AND I. R. HURLE, "The Shock Tube in High-Temperature Chemical Physics," Reinhold, New York, 1963.

15. W. C. GARDINER, JR., B. F. WALKER, AND C. B. WAKEFIELD, *in* "Shock Waves in Chemistry" (A. Lifshitz, Ed.), Dekker, New York, 1981.

16. S. D. GASSTER, C. H. TOWNES, D. GOORVITCH, AND F. P. J. VALERO, *J. Opt. Soc. Am. B.* **5,** 593–601 (1988).

17. L. P. GIVER, B. GENTRY, G. SCHWEMMER, AND T. D. WILKERSON, *J. Quant. Spectrosc. Radiat. Transfer.* **27,** 423–436 (1982).

18. V. MALATHY DEVI, D. C. BENNER, M. A. H. SMITH, AND C. P. RINSLAND, *J. Mol. Spectrosc.* **155,** 333–342 (1992).

19. J. J. REMEDIOS, "Spectroscopy for Remote Sensing of the Atmosphere," Ph.D. Thesis, University of Oxford, 1990.

Diode Laser Measurements of H_2O Line Intensities and Self-Broadening Coefficients in the 1.4-μm Region

S. LANGLOIS, T. P. BIRBECK, AND R. K. HANSON

*High Temperature Gasdynamics Laboratory, Department of Mechanical Engineering,
Stanford University, Stanford, California 94305-3032*

Spectrally resolved measurements of pure water vapor absorption spectra have been performed with a tunable diode laser. The laser, a distributed feedback InGaAsP diode, emits in the 1.4-μm region. A total of 12 lines were studied corresponding to rovibrational transitions within the $\nu_1 + \nu_3$ and $2\nu_1$ vibrational bands. A Voigt profile analysis of lineshape is used to infer both intensities and self-collision-broadening coefficients of the water vapor. Good agreement is found between the observed line intensities and those recently measured by Toth. These results are apparently the first published measurements of the broadening coefficient within this spectral range. © 1994 Academic Press, Inc.

INTRODUCTION

Precise knowledge of water vapor radiative properties in the infrared spectrum is needed for many applications. Such applications include atmospheric sounding experiments, radiative sensing of combustion processes, and optical diagnostics for gasdynamic and aerodynamic studies. The following spectroscopic parameters are required to quantify radiative properties of molecules: line intensity $S_i(T)$, line position ν_0, and the linewidth $\delta(T, P)$ (in this paper all linewidths are considered as the halfwidth at half maximum) and its associated shape profile Φ. These spectroscopic parameters have received great attention in several spectral regions (see Ref. (*1*) and references within). For example, in the near-IR, line intensity and spectral positions have been experimentally determined recently by Toth (*2*), and by Mandin *et al.* (*3*) for weak intensity lines, near 1.4 μm, and by Grossman and Browell (*4*) in the 720-nm wavelength region; the intensity and spectral position of lines between the microwave and the mid-IR region have been measured by Flaud and Camy-Peyret (*5*).

The collision-broadening coefficient has received equal attention: Grossman and Browell (*4, 6*) have measured the collision-broadening coefficient of H_2O when perturbed by itself, air, O_2, and N_2 in the 720-nm wavelength region. Arroyo and Hanson (*7*) have measured the Voigt "a" parameter for several transitions broadened by H_2O and air, near 1.4 μm, and room temperature self-broadening coefficients have been measured and calculated for mid-IR transitions (see Ref. (*8*) and references within). Finally, the dependence of the collision-broadening coefficient on temperature has also been investigated (*9*). To our knowledge, the only available measurements of the collision-broadening coefficient of water vapor in the 1.4-μm region are those given by Arroyo and Hanson (*7*). The values used in the above-mentioned applications, or those listed in current data bases, are the measured or calculated values transferred from other vibrational bands to the ones of interest, for equivalent rotational transitions.

The purpose of the present experiment is to determine the line intensity and the self-collision-broadening coefficient of water by measuring the absorption coefficient,

$k(v, T)$, in the 1.4-μm wavelength region. These quantities are needed in conjunction with other work in our laboratory to develop absorption diagnostic techniques for applications in combustion and high-speed gas dynamics (7, 10). The parameters of interest are determined using the relationship

$$k(v, T) = \sum_{i=1}^{N} S_i(T)XP\Phi(v - v_{0_i}, \delta(T, P)), \tag{1}$$

where X is the mole fraction, P the total static pressure, and N the number of overlapping lines.

Room temperature GaAlAs and InGaAsP diode lasers emit in the near-IR region, making them candidate sources for absorption measurements. GaAlAs diode lasers emit at wavelengths near 0.7 μm, whereas InGaAsP diode lasers emit at wavelengths between 1.3 and 1.6 μm. These semiconductor lasers have the advantages of being compact, rugged, cost-effective, and compatible with fiberoptics. The present experiment uses an InGaAsP semiconductor laser which emits in the 1.382- to 1.384-μm wavelength region. A 15.24-cm long cell, heatable to 400 K, contains the water vapor. The next section of this paper describes the experimental setup. This apparatus has been used previously in conjunction with flame and shock tube experiments (7, 10) aimed at demonstrating techniques for simultaneous determination of concentration, pressure, temperature, and velocity of gaseous mixtures. The following section, Analysis, briefly discusses several available methods of data analysis which can be used to determine the absorption coefficient, concentrating on the method of choice. In order to extract spectroscopic information on water vapor, Eq. (1) is directly modeled by a nonlinear least-squares fit of the experimental data. An important assumption, verified experimentally, is that the instrumental lineshape function of the diode laser is sufficiently narrow to be neglected. The use of a Voigt profile in describing the spectroscopic lineshape is also justified. The final section, Results, discusses our findings and their relevance.

EXPERIMENTAL DETAILS

Monochromatic radiation is provided by a distributed feedback InGaAsP diode laser (custom fabricated by Anritsu Corp.). The laser is driven by an ILX Lightwave LDC-3722 controller. The laser has a nominal output of 5 mW at 1382 nm at a driving current of 70 mA and a laser temperature of 25°C.

A Jarrell–Ash 0.5-m monochromator is used to characterize the laser diode. Placed before the output slit of this monochromator is a mirror attached to a galvanometer. The galvanometer imposes small angular oscillations upon the mirror at selected frequencies of oscillation between 0 and 100 Hz. This arrangement permits real-time monitoring of laser emission over ±0.5 nm. Recorded spectra for different conditions of laser temperature and driving currents are shown in Fig. 1; these spectra illustrate the single-mode characteristics of the diode. The side mode suppression ratio (SMSR), in decibels, is defined as

$$\text{SMSR} = -10 \log(I_s/I_m), \tag{2}$$

where I_s and I_m correspond to the side and main mode intensities. It is found that the laser diode gives rise to typical SMSR values of 20 dB for the following conditions: diode temperatures between 20 and 40°C and driving currents between 20 and 100 mA.
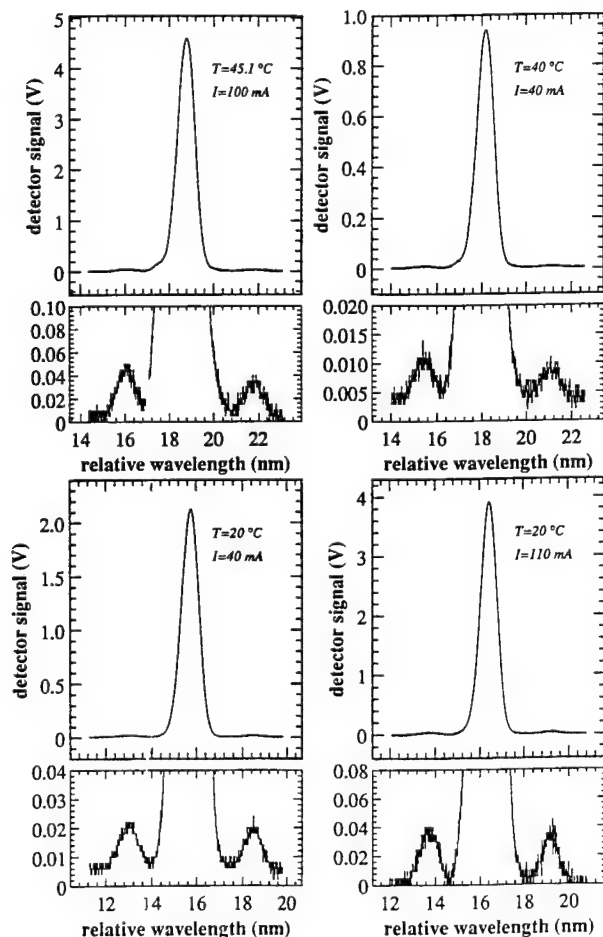
FIG. 1. Diode laser radiation spectra recorded through a monochromator for different diode temperatures and driving currents.

In order to specify the relative wavelength of these signals, the monochromator scanning oscillations must be calibrated. First, the mirror is fixed, the blazed 2.6-μm grating (used in 2nd order) is scanned at 100 nm/sec, and the laser emission is recorded. These data establish the wavelength difference for the two side modes, which is then used to calibrate the relative wavelength scale with an oscillating mirror. Using this calibration, the relationships between the laser emission frequency and both driving current and diode temperature are determined. The emission frequency is linear with respect to both parameters (see Fig. 2), the constants of proportionality being 0.103 nm/°C and 0.0095 nm/mA for diode temperature and driving current, respectively.

For clarity, the experimental setup for the absorption experiments, as shown in Fig. 3, is described by following the optical path of the laser. The laser beam is collimated by a 6-mm focal lens with a broadband antireflection coating. The parallel beam is then split in three by BK7 beam splitters. The first beam passes through a low-finesse solid étalon of 2 GHz spectral range and is then focused onto a detector, D2, providing a measurement of relative wavelength change. Germanium photo diodes (EG&G J-16-18A-R01M) function as detectors for each of the focused laser beams. The second
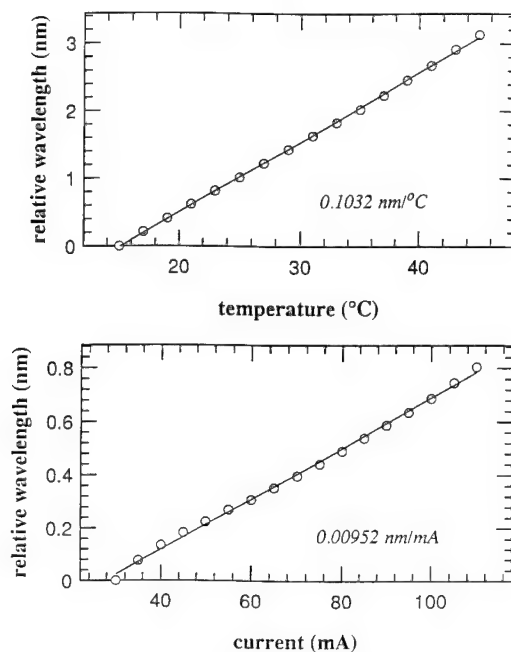
FIG. 2. Wavelength change of the diode laser radiation with both diode temperature and driving current. Open circles, experimental results; solid line, linear fit.

beam is directly focused onto a detector, D1, which serves as a reference intensity monitor. The third and principal beam passes through a 15.24-cm-long heated cell and is then focused on a detector, D3.

The cell consists of a 3.17-cm thick copper tube surrounding an aluminum tube possessing an outer diameter of 4.45 cm and an inner diameter of 2.54 cm. BK7 windows are attached to the aluminum tube. Electrical elements allow heating of the cell to 400 K. The high heat conduction of copper coupled with an insulating blanket dictates a uniform temperature within the cell. Two type-T thermocouples in contact with the aluminum tube measure temperature. Over a separation distance of 10 cm, the thermocouples record less than a 1 K temperature difference in the cell at 400 K. A MKS Baratron gauge, with a full-scale deflection of 1 atm, measures the pressure in the cell with an accuracy of ±1% over the experimental pressure range. A mechanical pump evacuates the cell to 0.01 Torr. At this pressure no absorption due to residual gas can be detected, implying that the vacuum is sufficient. Distilled water contained in a flask connected to the cell provides a source of water vapor. The flask is pumped down for 1 hr prior to measurements to remove all impurities.

A mean driving current of 70 mA with a superimposed triangular current profile of 10 Hz and amplitude ±35 mA results in the desired range of spectral frequency, about 60 GHz, at driving frequency of 10 kHz. However, using the current tuning rate given in Fig. 2, a spectral range of 105 GHz is expected. It is found that the response of the diode to current is dependent on the driving frequency; the tuning rate given in Fig. 2 is calculated from nonmodulating driving currents. Figure 4 shows the change in the diode spectral scan range for different driving currents. The current profiles have the same amplitude (70 mA) but different frequencies. It is found that the diode frequency range decreases with the tuning current frequency.
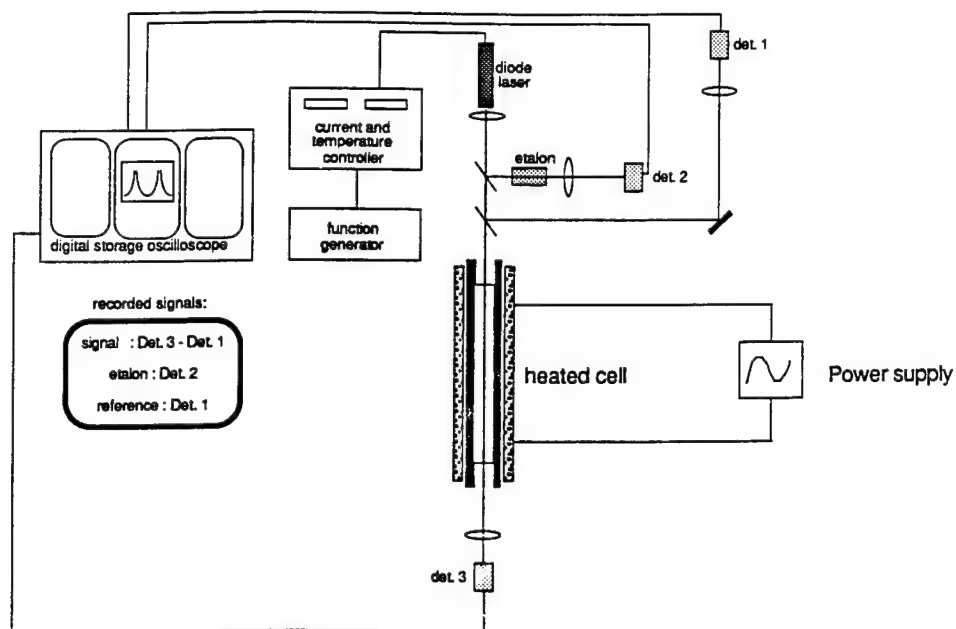
FIG. 3. Experimental schematic for the heated cell absorption experiments.

In order to cover all available wavelengths, data are taken at four diode temperatures between 20 and 40°C. The cell conditions are comprised of four temperatures between 290 and 400 K, and five pressures up to 0.03 atm (23 Torr).

A Nicolet four-channel oscilloscope acquires detector output voltages (Fig. 5). The three recorded signals are (1) the étalon signal (I_2); (2) the reference signal (I_1), and
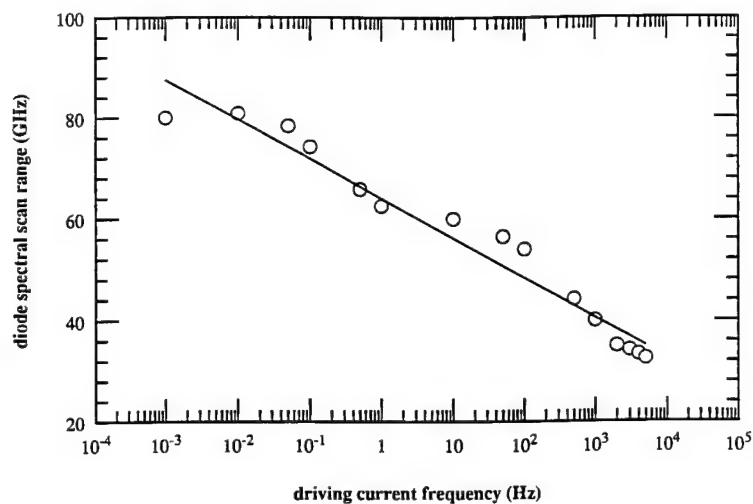

FIG. 4. Change of the diode spectral scan range with the driving current frequency; the current profile is triangular with an amplitude of 70 mA. Open circles, experimental results; solid line, best fit of the relationship $A + B \ln(x)$.
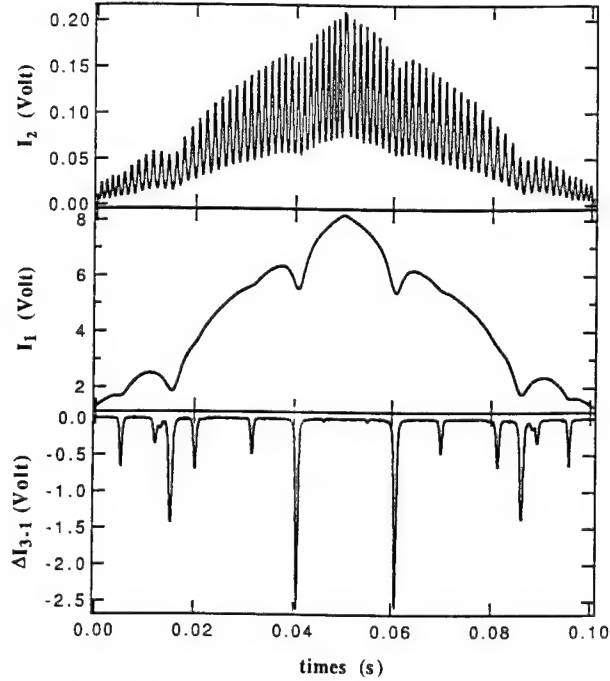
FIG. 5. Raw data as recorded on a single oscilloscope sweep.

(3) the difference between the cell signal (I_3) and the reference signal (I_1), i.e., (ΔI_{3-1}). An amplifier connected to detector D3 ensures similarity between I_1 and I_3. A minimized equal optical path length in air to D1 and D3 reduces signal perturbation from air absorption. The signal ΔI_{3-1} is recorded instead of I_3 in order to increase the resolution of the recorded lineshape on the oscilloscope. Perturbation due to both optical and electronic hardware is accounted for by recording ΔI_{3-1}^0, where ΔI_{3-1}^0 is the signal associated with an evacuated cell and referred to as "baseline."

The similarity of several baseline records, separated by a time period of 10 min, confirmed the stability of the diode radiation. The transmission coefficient, $\tau(\nu)$, of a stable signal is related to the ratio of the cell signal (I_3) to the evacuated cell signal (I_3^0):

$$\tau(\nu) = I_3/I_3^0. \tag{3}$$

I_3^0 is obtained by the sum of the reference signal I_1 and the baseline ΔI_{3-1}^0:

$$I_3^0 = \Delta I_{3-1}^0 + I_1 \tag{4}$$

I_3 is obtained in similar manner:

$$I_3 = \Delta I_{3-1} + I_1 \tag{5}$$

The experimental transmission $\tau(\nu)$ can thus be determined with Eq. (3). Note that the reference signal, I_1, by virtue of its stability does not affect the evaluation of $\tau(\nu)$.

Interference fringes recorded from the étalon signal enable the conversion from time to spectral frequency. The spectral distance between two extremes, in hertz, is given by

$$\Delta\sigma = c/(2\pi nl), \qquad\qquad (6)$$

where n is the refractive index of the material, l is the thickness, and c is the speed of light. A fifth-order polynomial least-squares fit is used to describe the relationship between time and frequency.

DATA ANALYSIS

The nominal laser wavelength is 1383 nm (70 mA, 25°C). The available range of diode temperature and driving current dictate the spectral domain of interest (1381–1385 nm). A line-by-line method, using HITRAN (1) as a data source, is used to calculate a theoretical spectrum within this domain. Graphical comparison of the theoretical spectrum with the experimental spectrum identifies the experimental lines. An example of this process is shown in Fig. 6. The measured lines are listed in Table I; these lines are from the $\nu_1 + \nu_3$ or the $2\nu_1$ vibrational bands of H$_2$O.

Before determining the intensity and the collision-broadening coefficient of the above experimental lines, the accuracy of the experimental conversion from time to frequency, using I_2 and Eq. (6), must be determined. The étalon signal is perturbed by the evolution in amplitude of the diode radiation, causing a shift in spectral position of the fringes. However, the fringe thickness is so small that this shift can be neglected. Comparison between experimental absorption line separations of several line pairs with Toth (2) (see Table II) supports our method of time-to-frequency conversion. We find discrepancies with HITRAN (1) ranging from 0.1 to 1.0 cm^{-1}.

The line intensity can be inferred from transmission data by at least three methods. The first method (Method 1), based on a measurement of the equivalent width, uses direct integration of $\tau(\nu)$ to determine the intensity. The primary advantage of this method is that the result is independent of the instrumental lineshape function. As a consequence, errors are not introduced by neglecting this perturbation. However, this advantage is compromised by introduction of errors associated with the baseline and contributions of adjacent lines.
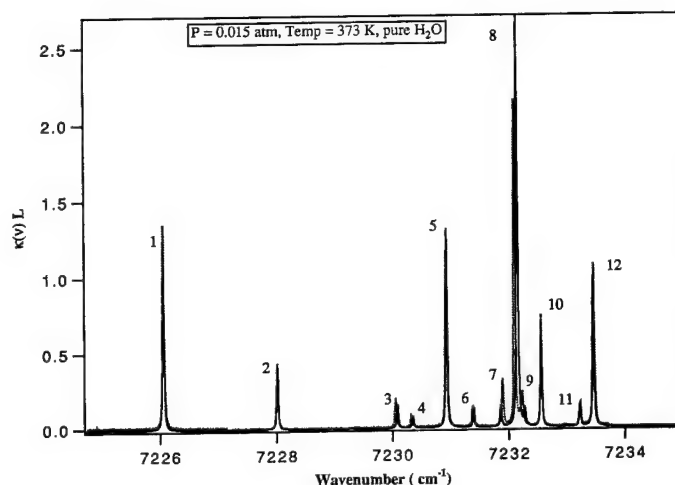

FIG. 6. Graphical comparison between experimental spectra (dotted lines) at a water vapor pressure of 0.015 atm, and a temperature of 373 K, and a line-by-line calculation (solid lines) for the same conditions. Absorption lines are numbered as in Table I.

TABLE I

Spectroscopic Parameters Extracted from HITRAN (*1*) in the Spectral Region of Interest

#	ν (cm^{-1})	S(296 K) (cm^{-1}/mole. cm^{-2})	E" (cm^{-1})	v'	v"	J'$_{K'_aK'_c}$	J"$_{K"_aK"_c}$
1	**7226.023926**	**6.33 10^{-21}**	**23.794**	**101**	**000**	**0$_{00}$**	**1$_{01}$**
	7226.324219	9.70 10^{-24}	610.341	101	000	6$_{24}$	5$_{41}$
	7226.379883	8.50 10^{-24}	1581.336	101	000	10$_{46}$	10$_{47}$
2	**7227.982910**	**2.10 10^{-21}**	**383.843**	**101**	**000**	**4$_{32}$**	**4$_{31}$**
	7229.791992	3.20 10^{-23}	95.176	101	000	2$_{12}$	2$_{11}$
3	**7230.052246**	**9.27 10^{-22}**	**95.176**	**101**	**000**	**2$_{12}$**	**2$_{11}$**
	7230.215820	4.99 10^{-24}	1216.194	200	000	7$_{52}$	7$_{61}$
4	**7230.315430**	**4.09 10^{-22}**	**275.497**	**200**	**000**	**4$_{22}$**	**4$_{13}$**
	7230.618164	5.70 10^{-24}	446.697	101	000	5$_{24}$	6$_{06}$
5	**7320.898398**	**6.40 10^{-21}**	**382.517**	**101**	**000**	**4$_{31}$**	**4$_{32}$**
	7230.938965	1.00 10^{-23}	1282.919	101	000	9$_{45}$	9$_{36}$
6	**7231.358398**	**5.99 10^{-22}**	**503.968**	**101**	**000**	**5$_{32}$**	**5$_{33}$**
7	**7231.828125**	**8.00 10^{-22}**	**173.365**	**200**	**000**	**3$_{21}$**	**3$_{12}$**
8	**7232.117118**	**1.40 10^{-20}**	**285.419**	**101**	**000**	**3$_{31}$**	**3$_{30}$**
	7232.133789	1.70 10^{-22}	37.137	200	000	2$_{02}$	1$_{11}$
	7232.192871	7.90 10^{-23}	782.410	200	000	7$_{34}$	7$_{25}$
9	**7232.242188**	**6.50 10^{-22}**	**136.762**	**200**	**000**	**7$_{34}$**	**7$_{25}$**
10	**7232.525879**	**3.05 10^{-21}**	**285.219**	**101**	**000**	**3$_{30}$**	**3$_{31}$**
	7232.926758	1.20 10^{-24}	1360.236	200	000	10$_{38}$	9$_{45}$
11	**7233.188965**	**7.37 10^{-22}**	**399.457**	**200**	**000**	**5$_{23}$**	**5$_{14}$**
	7233.291992	2.11 10^{-23}	982.912	200	000	8$_{35}$	8$_{26}$
12	**7233.423340**	**5.58 10^{-21}**	**212.156**	**101**	**000**	**3$_{22}$**	**3$_{21}$**

Note. All lines experimentally observed are labeled and written in bold characters.

The two other methods (Methods 2 and 3) considered ignore the perturbation due to the instrumental lineshape function. To verify this approximation, the theoretical transmissions of one of the transitions studied was convolved with different representative instrumental lineshape functions. The instrumental lineshape function can be modeled by a Gaussian profile. The linewidths, of these Gaussian profiles, fall within 3.3×10^{-7} and 6.0×10^{-6} cm^{-1} (extreme value defined by Materson and Webb (*11*) for this type of diode). Upon convolution by the Gaussian profile, the theoretical transmission profile parameters, the intensity and self-broadening coefficient, change by less than 1%. The small changes observed serve to justify the neglect of the instru-

TABLE II

Linecenter Spectral Differences, in cm^{-1}, between Line 7 (See Table I)
and Lines 8–12

LINE	EXP.	HIT. (Ref. 1)	Toth (Ref. 2)
7 – 8	0.205 ± 0.004	0.289	0.2071 ± 0.002
7 – 9	0.343 ± 0.002	0.414	0.2916 ± 0.050
7 – 10	0.659 ± 0.002	0.698	0.653 ± 0.006
7 – 11	1.330 ± 0.002	1.360	1.317 ± 0.013
7 – 12	1.567 ± 0.002	1.595	1.551 ± 0.016

Note. EXP; values deduced from current experiments; HIT; values deduced from HITRAN (*1*); Toth, values deduced from Toth (*2*).

mental lineshape function. The absorption coefficient $k(\nu)L$, where L is the optical length along the cell, can then be correctly approximated from $\tau(\nu)$ by

$$k(\nu)L = -\ln(\tau(\nu)). \qquad (7)$$

Method 2 uses the linecenter absorption coefficient to deduce the intensity from the value of $k(\nu)L$ at the linecenter,

$$S(T) = k(\nu_0)L/XPL\Phi(0, \delta_L, \delta_D), \qquad (8)$$

where P is the pressure, X the mole fraction, δ_L the collision-broadening linewidth, δ_D the Doppler linewidth, and $\Phi(0, \delta_L, \delta_D)$ the profile value at the center of the line position. From Eq. (8) one can see that the collision-broadening linewidth, δ_L, is needed. To our knowledge, experimental values, or accurate calculations of this linewidth within the lines of interest, have yet to be established. The use of transferred values from another vibrational bands introduces unknown errors.

Method 3, direct modeling of the absorption coefficient, accounts for contribution of side lines to the line of interest and determines the collision-broadening linewidth, the line intensity, and the spectral center position. These characteristics make this method superior for our analysis and hence has been adopted for use in our final data analysis. A standard Voigt profile, calculated with the Humlicek algorithm (*12*), models the observed lineshape. In the pressure range of interest a collision-narrowing effect, first observed by Dicke (*13*) and theoretically defined by Galatry (*14*), may be occurring. If this is the case, the use of a Galatry profile is needed. To justify the use of a Voigt profile, synthetic absorption coefficients (representing one of the studied lines) are calculated using both Voigt and Galatry profiles where a typical collision-broadening coefficient of $\gamma_L = 0.4$ cm^{-1} atm^{-1} (*15*) and a narrowing coefficient of $\beta = 0.1$ cm^{-1} atm^{-1} (*16*) are used. The Galatry profile is calculated with a routine developed by Varghese and Hanson (*15*); the routine is based on the numerical approximation of Herbert (*17*). Comparisons between intensity and self-collision-broadening coefficients determined by using a Voigt profile from the two above coefficients show differences of less than 1% for intensity, and less than 2% for the broadening coefficient, regardless of pressure (between 0 and 0.03 atm) and temperature (between 290 and 400 K).

Within the spectral domain of interest, other weak lines may participate in the absorption. These lines, as listed in HITRAN (1), possess intensities two orders of magnitude lower than those considered. Added in Table I are such lines which are close enough (0.2 cm^{-1}) to perturb the lines studied. Their contribution to the absorption coefficient is neglected. An example of the Voigt fit to a studied line is shown in Fig. 7. Residuals of less than 1% are achieved using a nonlinear least-squares fit of the Voigt profile (Fig. 7).

The intensity, at a temperature $T_0 = 296$ K, is related to the intensity at temperature T by

$$S(T_0) = S(T)(Q(T_0)/Q(T)) \times (1 - \exp(-hc\nu_0/kT))/$$

$$(1 - \exp(-hc\nu_0/kT_0)) \times \exp(hcE''/k(1/T_0 - 1/T)), \quad (9)$$

where E'' is the lower level energy, ν_0 is the linecenter position, and $Q(T)$ is the partition function; E'' and ν_0 are read directly from HITRAN (1). A polynomial approximation developed by Gamache et al. (18) gives the value of $Q(T)$.

In the case of pure water vapor, the temperature and pressure dependence of the collision-broadening linewidth, $\delta_L(T, P)$ in cm^{-1}, are given by (9)

$$\delta_L(T, P) = {}^s\gamma_L(T_0)P(T_0/T)^n, \quad (10)$$

where T_0 is the standard temperature (300 K), n is the temperature dependence, and ${}^s\gamma_L(T_0)$ is the standard collision-broadening coefficient. The values of n and ${}^s\gamma_L(T_0)$ completely characterize $\delta_L(T, P)$. The limited temperature range of the experiment prevents an accurate measurement of n. From Eq. (10), one can easily demonstrate
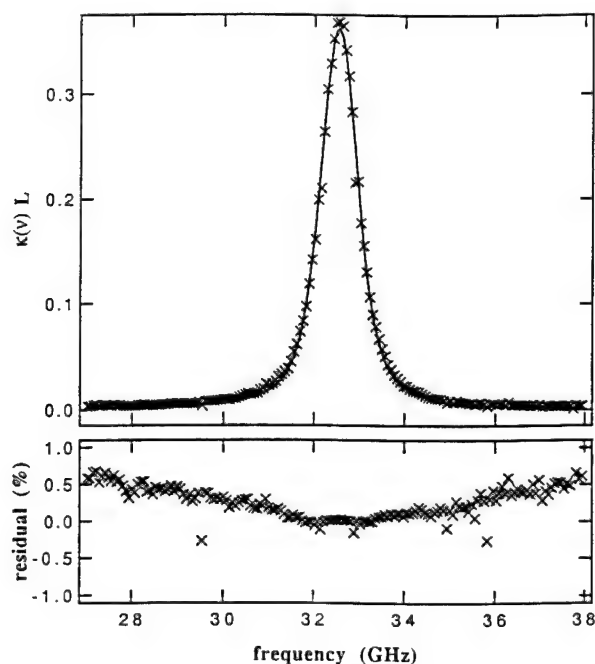

FIG. 7. Experimental absorption coefficient (cross points) (line 2 at 0.246 atm, 320 K) and a nonlinear fit using a Voigt profile (solid line). Residual in percentage between the two above spectra.

that the uncertainty of n is related to the precision of the $\delta_L(T, P)$ measurement, and given by

$$dn/n = 2/(n \ln(T_0/T))d\delta_L(T, P)/\delta_L(T, P). \tag{11}$$

With $n = 0.5$, $T_0 = 300$ K, and $T = 400$ K, the uncertainty of n will be 14 times larger than the precision of $\delta_L(T, P)$. Therefore, two values of $^S\gamma_L(T_0)$ are determined, using Eq. (10) with n fixed at the value given by HITRAN (1) and by Delaye et al. (9).

RESULTS AND DISCUSSION

The consistency of the experimental values of both the intensity and the collision-broadening coefficient can be verified by comparison of these quantities at different temperatures and pressure. Figure 8 shows the experimental intensity, $S(T)$, determined for several lines as a function of temperature. The theoretical intensity shown was calculated using Eq. (9) with $S(T_0)$ as a fitting parameter. Experimental standard intensities, $S(T_0)$, as calculated by Eq. (9), are plotted versus pressure in Fig. 9; the overall scatter of these result is 5%. Due to the uniform scatter, no systematic errors can be inferred from the plot. We define the experimental intensity to be an average of all experimental values and the associated error to be equal to the standard deviation of each experimental line intensity from this average. The lack of systematic error coupled with the small absolute error demonstrates the validity of both the experimental setup and the method of analysis. In particular, this is a test of the accuracy of the determined absorption baseline, the cell pressure and temperature measurements, and the calculated partition function.

Table III compares the averaged intensity results with both the values listed in HITRAN (1) and the experimental results of Toth (2). Close agreement of the results with Toth is achieved; however, there are discrepancies of the results when compared with HITRAN (1). This last fact emphasizes the need for further experiments to improve the existing spectroscopic data base for H₂O in this spectral region.

A similar analysis of the standard collision-broadening coefficient, $^S\gamma_L(T_0)$, was performed. Figure 10 shows the experimental standard collision broadening, $^S\gamma_L(T)$,
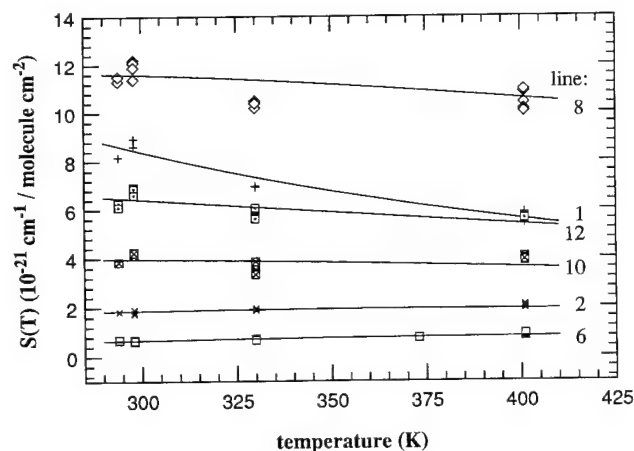

FIG. 8. Measured intensity for six different spectral lines as a function of temperature. The solid lines represent the theoretical temperature evolution of each line, with $S(296$ K$)$ fixed to the best-fit of our experimental data.
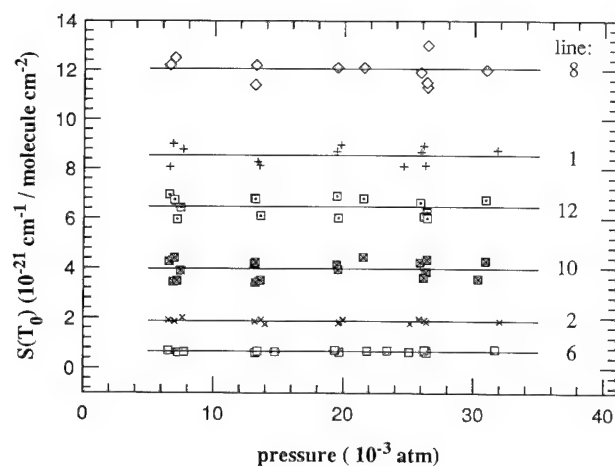
FIG. 9. Measured intensity (converted at 296 K) for six different spectral lines as function of pressure. The solid horizontal lines represent an average value for each data set.

as a function of temperature; also shown are the theoretical values of $^S\gamma_L(T)$, with n set at the Delaye values, and $^S\gamma_L(T_0)$ selected to provide the best fit to the experimental results. In this spectral range, the changes of $^S\gamma_L(T)$ with temperature are in agreement

TABLE III

Comparison of Line Intensities, in 10^{-21} cm^{-1}/Molecule cm^{-2}, Deduced from Experiments and Those Listed in HITRAN (1) and Those Given by Toth (2)

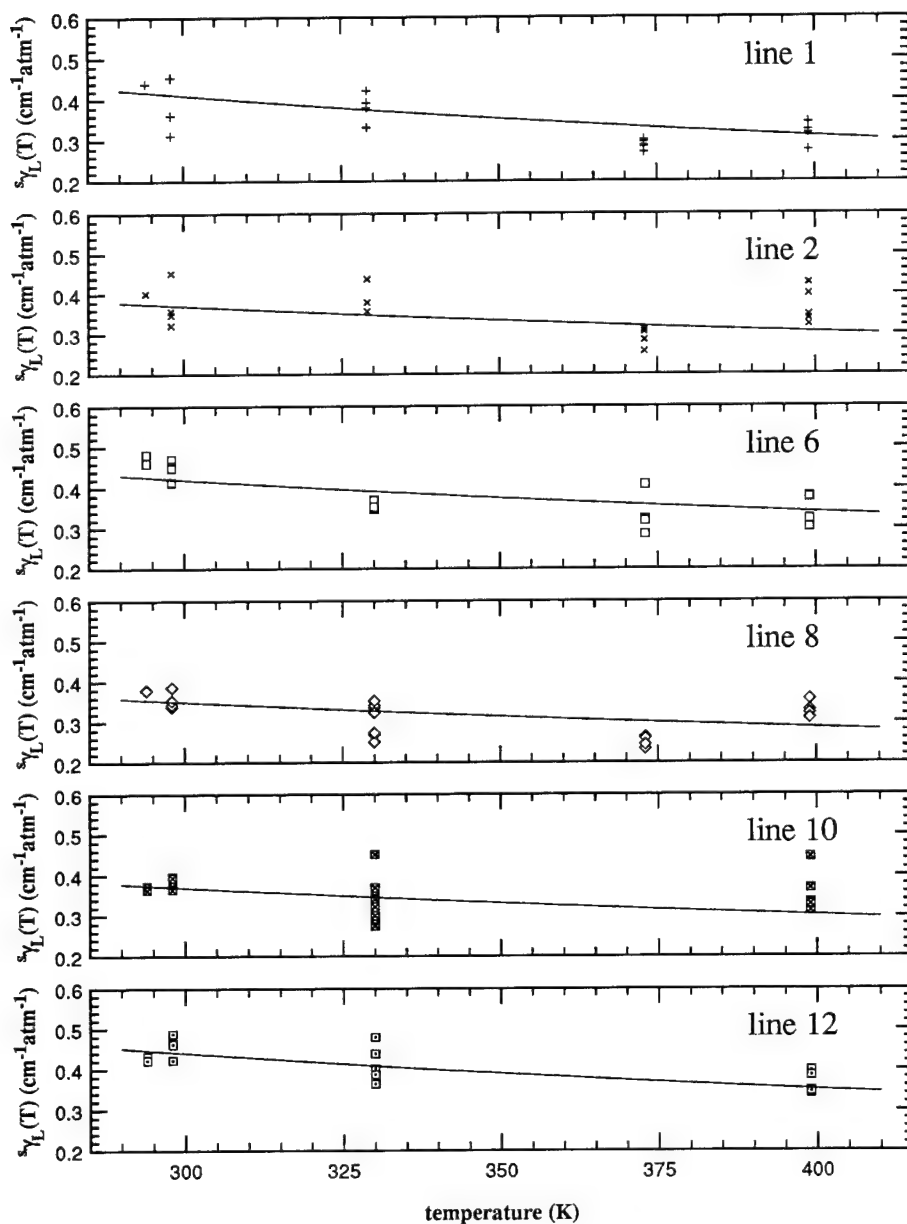| #	S^{exp} (296K)	S(296K) ref. 1	S(296K) ref. 2
1	8.54 ± 0.37	6.33	8.58
2	1.86 ± 0.07	2.10	1.89
3	1.14 ± 0.09	0.927	1.07
4	0.48 ± 0.03	0.409	0.516
5	4.94 ± 0.42	6.40	5.32
6	0.66 ± 0.03	0.599	0.766
7	1.97 ± 0.11	0.800	2.02
8	12.05 ± 0.8	14.0	12.1
9	1.22 ± 0.14	0.650	1.98
10	3.96 ± 0.36	3.05	4.11
11	0.925 ± 0.07	0.737	0.806
12	6.46 ± 0.37	5.58	6.65

FIG. 10. Measured standard self-collision-broadening coefficient for the same line as represented in Fig. 8 as a function of temperature. The solid lines represent theoretical temperature evolution for each data set, determined by using the n parameter recommended by Delaye (9).

with Delaye (9) and HITRAN (1). Two values of $^S\gamma_L(T_0)$ were calculated for each line, one corresponding to n given by HITRAN (1) and one to n given by Delaye (9). The values found with n fixed to Delaye's recommendation are plotted as a function of experimental pressure in Fig. 11. Again, an overall scatter of 5% is determined. Also the fact that no systematic error can be found justifies the use of n given by Delaye (9). Table IV lists the average values of $^S\gamma_L(T_0)$ for each line at the specified
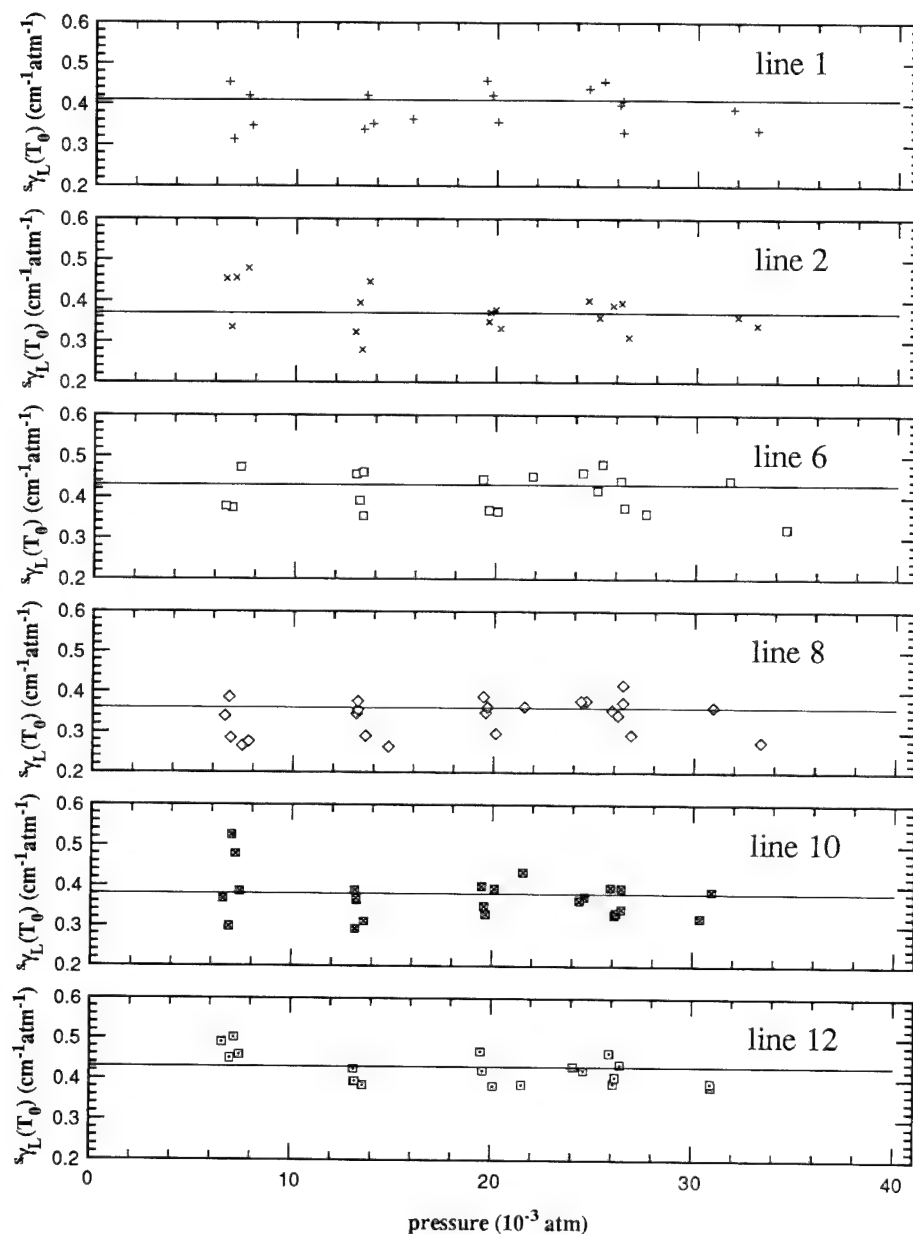
FIG. 11. Measured standard self-collision-broadening coefficient for the same line as represented in Fig. 8. The horizontal lines represent an average for each data set.

n value and the associated $^S\gamma_L(T_0)$ values of Delaye (9) and HITRAN (1). There is good agreement between both sets of comparison, with the exception of Line 11 compared with Delaye (9) (0.52 vs 0.431) and Line 10 compared with HITRAN (1) (0.38 vs 0.466). We recall that in both references, the coefficients were not determined for the vibrational bands of interest in this study. Again, we note the need of further work to improve the spectroscopic database. Our future endeavors will incorporate a larger temperature range allowing quantification of the n parameter.

TABLE IV

Standard Self-Collision-Broadening Coefficients, in $cm^{-1} atm^{-1}$,
Determined by Using the n Parameters Recommended by Delaye (*9*) and
Those in HITRAN (*1*) (Comparison Made with both References)

#	$^s\gamma_L^{exp}$ (300K)	$^s\gamma_L^{the}$ (300K) Ref. 9	n^{the} Ref. 9	$^s\gamma_L^{exp}$ (300K)	$^s\gamma_L$ (300K) Ref. 1	n Ref. 1
1	0.41 ± 0.02	0.398	0.98	0.41 ± 0.02	0.452	0.78
2	0.37 ± 0.01	0.376	0.68	0.37 ± 0.01	0.370	0.71
3	0.45 ± 0.02	0.437	0.90	0.44 ± 0.02	0.458	0.68
4	0.49 ± 0.04	0.437	0.87	0.48 ± 0.04	0.467	0.84
5	0.40 ± 0.03	0.376	0.68	0.39 ± 0.03	0.345	0.62
6	0.43 ± 0.05	0.400	0.74	0.43 ± 0.05	0.429	0.68
7	0.47 ± 0.02	0.440	0.88	0.47 ± 0.02	0.492	0.77
8	0.36 ± 0.02	0.391	0.70	0.36 ± 0.02	0.414	0.68
9	0.43 ± 0.05	0.469	0.95	0.43 ± 0.07	0.514	0.79
10	0.38 ± 0.03	0.391	0.70	0.38 ± 0.04	0.466	0.68
11	0.52 ± 0.09	0.431	0.84	0.50 ± 0.09	0.491	0.70
12	0.43 ± 0.03	0.423	0.79	0.43 ± 0.03	0.486	0.75

CONCLUSION

In this study, the intensity and the standard self-collision-broadening coefficient of 12 rovibrational lines belonging to the $\nu_1 + \nu_3$ and $2\nu_1$ fundamental bands have been determined, both to an average accuracy of 7%. Our results concerning intensity are consistent with recent experimental results of Toth (*2*). Concerning the self-collision-broadening coefficient, the comparison made with experimental (*1*) or calculated (*9*) values belonging to the same rotational transition but to different vibrational band shows discrepancies that may be attributed to vibrational perturbation. Unfortunately, the current range of temperature doesn't allow the determination of the temperature-dependence parameter n. Further work is needed to reach higher temperature and allow a direct determination of this parameter. Moreover, high-temperature experiments will permit us to measure "hot" vibrational transitions (nonzero lower quantum states) and to increase the number of measured lines.

REFERENCES

1. L. S. ROTHMAN, R. R. GAMACHE, R. H. TIPPING, C. P. RINSLAND, M. A. H. SMITH, B. C. BENNER, V. M. DEVI, J. M. FLAUD, C. CAMY-PEYRET, A. PERRIN, AND A. GOLDMAN, *J. Quant. Spectrosc. Radiat. Transfer* **48**, 469–507 (1992).
2. R. A. TOTH, submitted for publication.
3. J. Y. MANDIN, J. P. CHEVILLARD, C. CAMRY-PEYRET, AND J. M. FLAUD, *J. Mol. Spectrosc.* **118**, 96–102 (1986).
4. B. E. GROSSMAN AND E. V. BROWELL, *J. Mol. Spectrosc.* **136**, 264–294 (1989).
5. J. M. FLAUD, C. CAMY-PEYRET, AND R. A. TOTH, "Water Vapour Line Parameters from Microwave to Medium Infrared," Pergamon Press, London, 1981.
6. B. E. GROSSMAN AND E. V. BROWELL, *J. Mol. Spectrosc.* **138**, 562–595 (1989).
7. M. P. ARROYO AND R. K. HANSON, *Appl. Opt.*, in press, 1993.
8. J. M. HARTMANN, J. TAINE, J. BONAMY, B. LABANI, AND D. J. ROBERT, *J. Chem. Phys.* **86**, 144–156 (1987).
9. C. DELAYE, J. M. HARTMANN, AND J. TAINE, *Appl. Opt.* **28**, 5080–5087 (1989).
10. M. P. ARROYO, S. LANGLOIS, AND R. K. HANSON, submitted for publication.
11. B. MATERSON AND J. WEBB, *Photonics Spectra* May, 119–124 (1992).
12. J. HUMLICEK, *J. Quant. Spectrosc. Radiat. Transfer* **21**, 309–313 (1979).
13. R. H. DICKE, *Phys. Rev.* **89**, 472–473 (1953).
14. L. GALATRY, *Phys. Rev.* **122**, 1218–1223 (1961).
15. P. L. VARGHESE AND R. K. HANSON, *Appl. Opt.* **23**, 2376–2385 (1984).
16. R. S. ENG, A. R. CALAWA, T. C. HARMON, P. L. KELLEY, AND A. JAVAN, *Appl. Phys. Lett.* **21**, 303–305 (1972).
17. F. HERBERT, *J. Quant. Spectrosc. Radiat. Transfer* **14**, 943–951 (1974).
18. R. R. GAMACHE, R. L. HAWKINS, AND L. S. ROTHMAN, *J. Mol. Spectrosc.* **142**, 205–219 (1990).

Flow and Particle Diagnostics

Multi-Parameter and Multi-Point Measurements

R. K. Hanson, D. S. Baer, B. K. McMillin, and P. Arroyo

High Temperature Gasdynamics Laboratory, Department of Mechanical Engineering, Stanford University, Stanford, CA USA 94305

Laser-based diagnostic techniques, developed primarily within the combustion community, offer considerable promise for nonintrusive measurements in gaseous flows relevant to industry. In this paper, we review two diagnostic methods under development in our laboratory. The first technique allows simultaneous measurement of multiple parameters through analysis of the shape and shift of fully resolved absorption lineshapes. The light source is a tunable, narrow-linewidth semiconductor diode laser, applied in the present case to either water vapor (1.39 microns) at combustion gas temperatures (to 1700 K) or to argon (800 nm) in an atmospheric pressure plasma (at temperatures to 8000 K). Parameters inferred include, for water: temperature, pressure, velocity and species density; for argon, the parameters are electron density, kinetic temperature and the population temperature for the 4 s levels of argon. The second diagnostic technique is planar laser-induced fluorescence (PLIF), which allows instantaneous measurements of a single parameter at multiple points in the flowfield. The example application to be discussed is single-shot temperature imaging in a model scramjet flowfield using a two laser-two camera imaging scheme.

Introduction

Over the past two decades, several promising laser-based diagnostics have been proposed for nonintrusive measurements in gaseous flows. Interest in combustion, in particular, has driven the development of these advanced measurement techniques. Linear methods, such as absorption and laser-induced fluorescence, are especially attractive owing to their signal strength, species specificity, and relative simplicity of equipment and data interpretation. Equally important is the fact that variations of absorption and fluorescence have been identified for sensing several flowfield parameters of interest including species concentrations, temperature, velocity, pressure and density.

Laser-induced fluorescence (LIF), originally developed as a single-point diagnostic but extended in the early 1980s to simultaneous multi-point measurements in a plane, offers the important attributes of spatial and temporal resolution, assuming use of a pulsed laser source. The planar LIF method (known as PLIF) has been rapidly accepted by the combustion community owing to its value for visualizing complex reacting flowfields. (See Refs. 1 and 2 for an overview.) For example, PLIF images of OH produced in a diffusion flame serve to locate the instantaneous position of flame zones and combustion products; and PLIF images of a tracer compound can be used to quantify the extent of mixing in turbulent jets. During the past few years, as activity in supersonic flow and scramjet combustors has been rekindled, there has also been considerable interest in developing PLIF as a diagnostic for aerodynamic and propulsion research. Applications of PLIF in industry are still limited, although the potential of the method is evident.

The ability of the PLIF method to capture data for many flowfield points simultaneously is particularly relevant to applications in transient or highly three-dimensional flows. It should be noted, however, that LIF and PLIF suffer one particular potential disadvantage, namely that conversion of fluorescence data to absolute species concentrations may be handicapped by various uncertainties, especially in the collisional quenching rate. Much of the current research on PLIF is aimed at developing measurement strategies which avoid these difficulties. Fortunately, good progress has been made for some variables, for example to measure temperature through the ratio of two PLIF images, and to measure velocity through PLIF monitoring of Dopper-shifted absorption. By using signal differences and ratios, many of the problems of unknown quench rates are eliminated. Another limitation of LIF and PLIF, when executed in the usual manner with spectrally broad pulsed lasers, is that an individual measurement typically yields, at best, only one flowfield property. In most cases the fluorescence signal is a combined function of temperature, density and mixture composition, and possibly velocity. Signal interpretation can thus be complex, leading to a requirement for multiple measurements.

Recently, methods based on spectrally resolved absorption lineshapes, using either line-of-sight (LOS) absorption or single-point LIF detection, have emerged as strategies which avoid some of the problems of PLIF and also enable simultaneous determination of multiple flowfield properties [3 – 11]. Spectrally-resolved absorption methods using cw laser sources complement pulsed laser techniques in two important ways: (1) cw absorption can be highly quantitative, easily interpreted, and free of calibration uncertainties; and (2) measurements can be made at high repetition rates or even continuously. Of course absorption is usually a line-of-sight method and thus provides poor spatial resolution, but extension of absorption to multiple paths can relieve this deficiency somewhat. Alternatively, single-point fluorescence detection of spectrally resolved absorption can be used in some cases to provide spatial resolution while retaining most of the advantages of the absorption method [4, 6, 11]. The key limitation to this LIF strategy is that the signal levels may be weak. The concept is therefore limited to cases with sufficiently high absorption and fluorescence yields.

Another significant advantage of cw laser absorption is that the low power levels required are compatible with the use of optical fibers, and hence remote location of laser sources becomes feasible. Semiconductor diode laser sources are particularly attractive, since they are compact, rugged, and economical, and they have low power requirements. We believe that packaged, stand-alone instruments based on these lasers and spectroscopic principles are likely to have substantial impact in future industrial applications.

In the following, we provide brief overviews of current research efforts based on the two methods introduced above, i.e. spectrally resolved absorption and PLIF. More detailed descriptions may be found in the publications cited in the Reference section of this paper.

Spectrally-Resolved Absorption Using Tunable Diode Lasers

Over the past 15 years, our group at Stanford has been active in developing laser absorption diagnostics based on several rapid-scanning narrow-linewidth laser sources, including infrared-emitting lead-salt diode lasers, UV/visible ring dye lasers, and most recently, near-infrared semiconductor diode lasers. The composition of lead-salt diode lasers can be tailored to enable emission in the spectral range $3.3 – 30$ microns, which provides overlaps with the IR-active vibrational bands of many combustion species. Ring dye lasers, on the other hand, emit in the range $200 – 800$ nm, which enables use of the stronger absorption bands associated with electronic transitions. Near-infrared diode lasers, which are still developing rapidly, presently emit in selected spectral windows from about 650 nm to 1.6 microns. These lasers offer high potential for industrial diagnostic applications owing to their compact size, low cost and compatibility with fiberoptic transmission; we have recently reported results for O_2 [7, 8] and H_2O [9, 10] using these lasers at 760 nm and 1.385 microns, respectively, and for O-atoms [12] at very high temperatures using a laser at 777 nm, and for Ar [13, 14] at several wavelengths near 800 nm.

The concepts of high-resolution absorption spectroscopy using laser wavelength modulation are similar for each of the lasers mentioned above. We will focus our discussion here on the use of diode laser sources, owing to the relatively higher potential for industrial applications. These are commercial lasers which allow narrow-linewidth scans over $1 - 2 \, \text{cm}^{-1}$ at repetition rates of 10 kHz and higher; output power is typically several milliwatts, depending on the wavelength of interest. As examples of diode laser-based diagnostics, we will briefly summarize two activities involving detection of H_2O and Ar, respectively; the first topic provides an example of work in combustion gases while the latter serves to illustrate measurement possibilities in plasmas. Further details of this work may be found in Refs. 9, 10, 13 and 14.

Our primary objective with H_2O measurements has been to investigate diagnostic strategies for simultaneously monitoring several gasdynamics parameters in supersonic flows. The central idea is to scan the laser over a spectral region encompassing two (or more) absorption lines, and then to interrogate the line-of-sight data via a Beer's law analysis to infer: (1) temperature, from the ratio of absorption signals for the two lines, assuming a Boltzmann distribution in the absorbing states; (2) pressure, from either the collision-broadened linewidth (found with a Voigt fit to the lineshape data) or the absolute absorption level (if the species mol fraction is known); and (3) velocity, from the Doppler-shifted positions of the absorption lines relative to those of a static sample. Density can be calculated from the ideal gas law once pressure and temperature are known, and derived quantities such as the mass [7] and momentum [10] fluxes (the latter is effectively a thrust measurement) can be calculated from the known density and velocity. Of course, absorption data can also be used for the more limited purpose of determining species concentration, but here our primary goal was to explore the use of spectrally resolved measurements for simultaneous monitoring of multiple parameters.

We have conducted many of our experiments in a shock tube, since this provides a convenient means of generating a controlled, high-speed flow of gases with precisely known conditions that can be varied over a wide range. A schematic of the experimental arrangement is given in Fig. 1. A custom-made distributed feedback InGaAsP diode laser source, emitting narrow-linewidth radiation near 1.385 microns with a power level near 1 mW, is rapidly swept in wavelength across a closely spaced pair of water vapor lines near 7213 cm^{-1} (1.386 microns; the $6_{42} \leftarrow 6_{43}$ and $3_{13} \leftarrow 3_{12}$ lines, using J_{KaKc} notation, with $J = 6$ the stronger of the two lines) which are prominent in the $\nu_1 + \nu_3$ combination band. This is the strongest band of water in the near-IR and thus is particularly attractive for sensitive detection over modest absorption pathlengths. (Information on the strengths of absorption lines in this spectral region may be found in the recent papers by Arroyo et al. of our laboratory; see Refs. 9, 10.) In this experiment, the transmitted laser intensities, measured along two directions in the shock tube (detectors 3 and 4), are converted to frac-
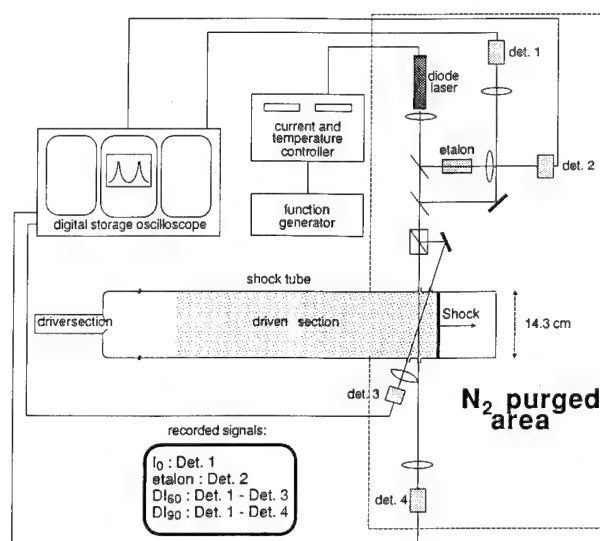

Fig. 1
Experimental arrangement for development of a diode laser diagnostic for line-of-sight absorption measurements of water vapor

tional transmission using the measured reference intensity (detector 1). Measurements are converted from time to laser frequency using a simultaneously recorded etalon trace (detector 2). The spectral transmission data are then analyzed using the Beer-Lambert law to obtain the spectral absorption coefficient versus frequency. Fig. 2 shows a sample data trace, obtained from a single-sweep recording behind an incident shock in a 5.9% H_2O (balance O_2) mixture. The laser was repetitively scanned at 10 kHz, so the duration of the scan was 100 microseconds and several scans were completed during the limited available test time (about 1 millisecond) behind the incident shock wave.

The data analysis involves first obtaining best-fit Voigt profiles to the two lines, with temperature and pressure as the variable parameters (assuming the pressure-broadening coefficient is known). The temperature is determined chiefly from the relative peak heights, with the pressure inferred mostly from the linewidths. Since the data are recorded for
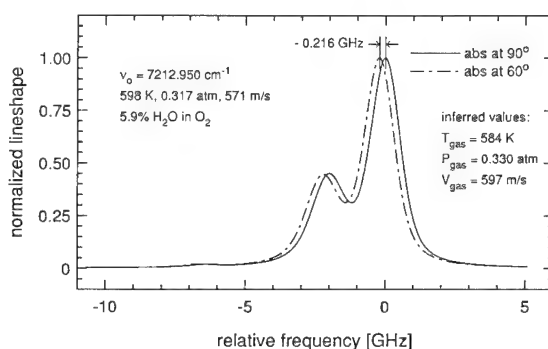

Fig. 2
Reduced shock tube absorption data for single scan of the $6_{42} \leftarrow 6_{43}$ and $3_{13} \leftarrow 3_{12}$ lines in the $\nu_1 + \nu_3$ band of H_2O. The gasdynamic parameters inferred from a Voigt profile analysis are indicated along with the values calculated with shock wave theory. From Ref. 10.
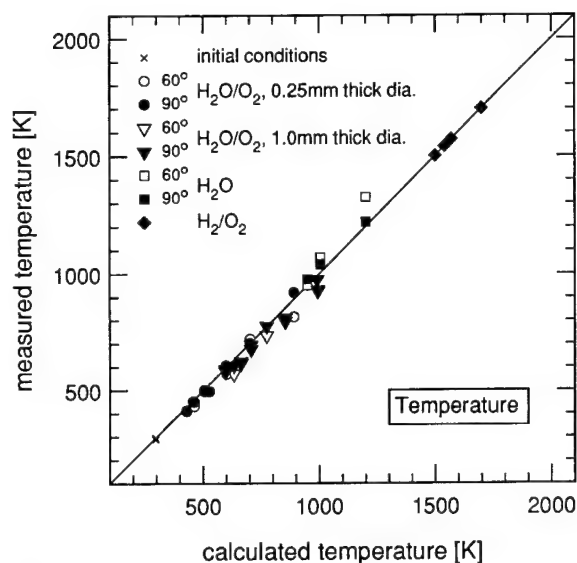
Fig. 3
Comparison of laser-based H_2O temperature measurements with known (calculated) temperatures produced in a shock tube

two flow angles, the separation in frequency between the two data sets can be used to obtain the flow velocity through the standard Doppler-shift relation [10]. As indicated on the figure, the agreement between the known flow conditions (calculated using shock wave relations) and those inferred from the lineshape data is quite good. A sample of results for temperatures up to 1700 K is given in Fig. 3. The accuracy obtained for pressure, velocity, water concentration, and momentum flux is similar.

In addition to applications in combustion gases, diode laser diagnostics based on spectrally-resolved lineshapes also are well-suited for non-intrusive measurements in plasmas. Applications in our laboratory include both low
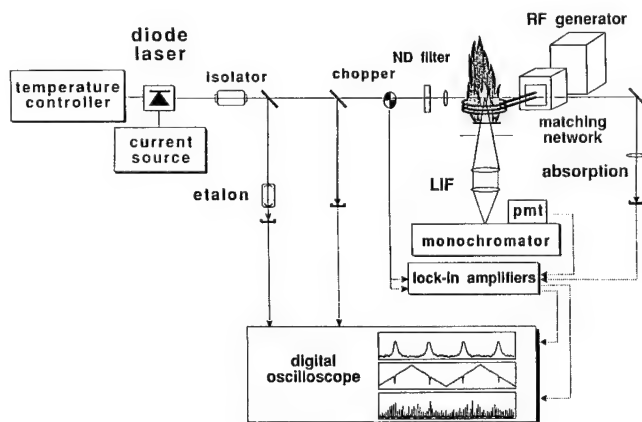
LIF/Absorption Experimental Setup

Fig. 4
Experimental arrangement for combined absorption/LIF measurements in an argon plasma using a wavelength-modulated diode laser source

pressure plasmas and atmospheric pressure (thermal) plasmas. A schematic of the experimental arrangements used to probe a custom-built inductively-coupled plasma torch operating on argon is shown in Fig. 4. The laser beam from a commercial diode laser (Sharp LT016MD0) is current-turned over one of the several allowed $4s \rightarrow 4p$ transitions near 800 nm (see Fig. 5 for an energy level diagram), and data on the fully-resolved lineshape are recorded both in absorption and in fluorescence. The latter has the advantage of providing spatially resolved data, although lower signal levels lead to slower scanning rates and the required use of a lock-in amplifier to separate the weak LIF signal from the strong background plasma emission. Typical laser power levels are 10 mW, and the period of a complete scan ranged up to 500 sec when LIF data were recorded. Much higher scan rates were possible when only line-of-sight absorption recording was employed. Excitation intensities were in the linear regime, well below saturation levels.
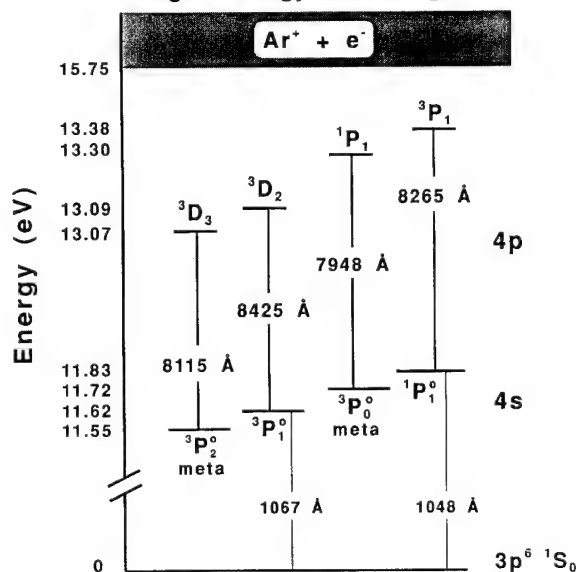
Argon energy level diagram

Fig. 5
Energy level diagram for argon

The plasma was sustained with 1 kW of electrical power from a 27 MHz generator. The plasma torch body and impedance-matching network were fabricated in this laboratory and configured to permit unrestricted optical access to the flowfield. Most measurements were made on the torch centerline at distances of 6 – 13 mm downstream of the torch body exit plane and with submillimeter spatial resolution. The torch body was of a conventional concentric glass tube design. The two outer tubes, with inside diameters of 18 and 13 mm, were made of silica and were used to contain the plasma. The argon flow was injected tangentially into the outer tube and monitored by a calibrated rotometer. Portions of the laser beam were also passed through a low pressure electrical discharge (not shown in Fig. 4), to pro-

vide an unshifted frequency reference, and through a 2 GHz (free spectral range) etalon to measure changes in laser frequency.

A sample of LIF data for a point at $r = 0$, $z = 11$ mm, is shown in Fig. 6. The data were best fit with a Voigt profile, thereby allowing simultaneous determination of both the kinetic temperature (Doppler broadening) and the Voigt parameter (a). The latter quantity specifies a value for the total Lorentzian linewidth, from which one can infer the Stark broadening contribution once the contribution of
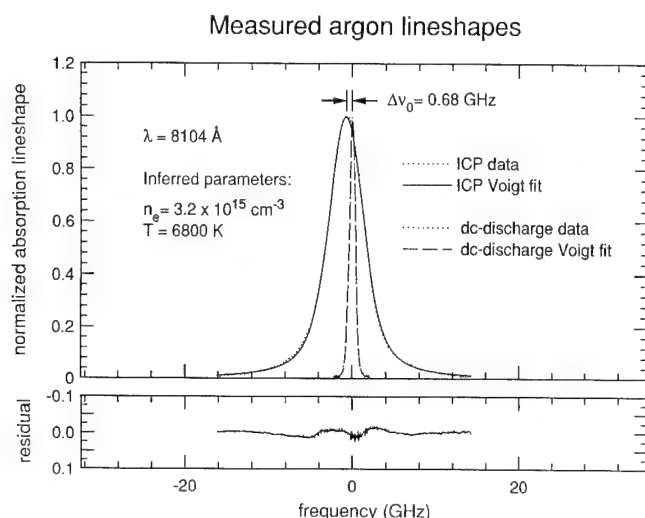
Measured argon lineshapes

Fig. 6
Experimental absorption lineshape and shift data for 810.4 nm excitation of argon in an atmospheric pressure plasma; detection is by LIF

resonance broadening is subtracted [13, 14]. The Stark-broadened linewidth, in turn, leads to a value for the local electron density using known parameters for Stark broadening. The best-fit values of n_e and T_{kin} are indicated on Fig. 6. It should be noted that the measured frequency shift of the line (relative to the low pressure discharge) can also be used to infer the electron density, through known Stark-shift relations, and good agreement is consistently found between the two methods for n_e. Agreement is also found with values of T_{kin} and n_e inferred from Abel-inverted emission data as well as with the laser-based measurements for the other $4s \rightarrow 4p$ transitions studied [13, 14]. Although the maximum temperature observed in this study was about 8000 K, we have measured O-atom temperatures (in absorption) using this same laser system in shock-heated gases up to about 14,000 K [12]. The lower temperature limit in the present study is set by Boltzmann statistics for the fractional population of atoms in the 4s manifold, which of course drops off sharply with temperature since the 4s energy level is about 11.5 eV above the ground state.

The ability to make local measurements of plasma properties is of great practical utility, since most past spectroscopic measurements have been based on spatially-averaged emission data. Thus these LIF data provided an important check on the Abel-inversion procedures previously used in our laboratory and elsewhere. To our knowledge,

this study also represents the first application of diode lasers to measurements in atmospheric pressure plasmas.

The above two examples of laser diagnostics serve to illustrate the power of spectrally-resolved-lineshape strategies. These methods are suitable for use over an extremely broad range of flow conditions and for a large number of species. Eventually these laser sources will be packaged in user-friendly systems for a variety of industrial applications. Most obvious of these are stack and process monitors. Owing to the compatibility of low power lasers with fiberoptics, it is also likely that multiplexing will be utilized to allow several channels of measurements with a common laser source and data processing system.

Planar Laser-Induced Fluorescence Imaging

We turn now to our second diagnostic strategy, planar laser-induced fluorescence, which offers the ability to simultaneously monitor flowfields at a large number of measurement locations. PLIF has developed rapidly from its initial demonstration as a combustion diagnostic in 1982; see Refs. 1 and 2 for reviews of PLIF and a detailed treatment of PLIF theory and experimental considerations. Much of the current research on PLIF is concerned with: rendering image data quantitative; extending the concept to new species and flowfield parameters; improving the performance of the equipment, particularly the lasers and detectors; improving analysis of the images through computer-based image processing; and implementation of PLIF systems in basic and applied research, particularly involving combustion and propulsion.

The experimental arrangement employed in our current PLIF studies of supersonic mixing and combustion is illustrated in Fig. 7. Sheets of laser light, from two pulsed laser sources, are propagated through the shock tube-generated flowfield of interest. If each laser is tuned in wavelength to match an allowed absorption transition of the species to be probed, then a fraction of the light absorbed at each region (point) in the illumination plane is converted to fluorescence which is emitted into all directions.
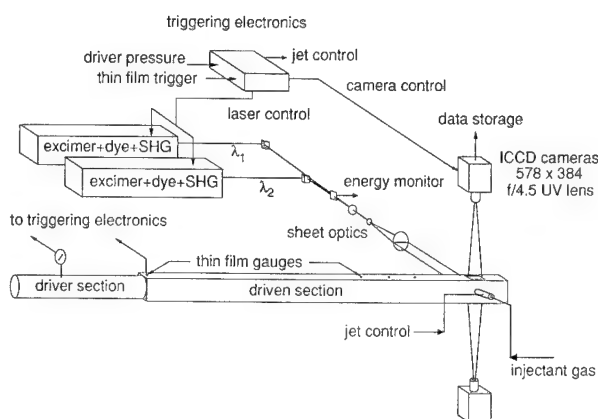

Fig. 7
Schematic of the experimental facility for two-line PLIF imaging of temperature in supersonic flows

A portion of this light is collected with lenses (or mirrors) and focussed onto the front face of an intensified solid-state detector array. For current work, a single-stage microchannel plate (MCP) intensifier is used together with a CCD detector array. The intensifier is time-gated to that light is only collected during a brief period (typically 100–200 nsec), to minimize the effects of extraneous emission or scattered light. Current detector arrays have greater than 10^5 pixels, so that each PLIF image is a record of fluorescence emission from a large number of flowfield points in the illumination plane.

In effect, the PLIF signal is a measure of the light absorbed at each flowfield point, modified by the local fluorescence yield, which is the fraction of absorbed light converted to fluorescence emission. Unfortunately, the PLIF signal can be a complex function of the absorbing species concentration, temperature, pressure and velocity (through the Doppler shift of absorption lines for moving gases). Various strategies have been developed to cope with these problems and to relate the PLIF signals to flowfield properties of interest such as species concentration, temperature [15], pressure, density and velocity [16]; see Refs. 2 and 17 for recent overviews. Here we summarize our approach to quantitative imaging of temperature in a flowfield comprised of a jet in supersonic crossflow; this flow is representative of mixing and combustion of a fuel jet in a scramjet combustor. Specifically, the strategy being pursued, known as two-line PLIF, is based on sequential excitation of two absorption transitions of a single species, presently NO, with the ratio of the two PLIF signal being used to infer temperature. A more complete description of this work may be found in Ref. 15.

The two-line technique used here is based on the ratio of fluorescence signals obtained following sequential laser excitation of two rovibronic transitions, originating from different rotational states in the $A^2\Sigma^+ \leftarrow X^2\Pi(0,0)$ band of NO. This strategy is particularly useful in flows which are compressible or varying in composition, because in taking the ratio of fluorescence signals, the dependence on number density, absorbing species mole fraction, and collisional quenching is removed.

NO is an attractive probe species because it is naturally present in the freestream of many high enthalpy combustion and propulsion facilities, and it can be easily seeded into fuel jets. In reacting flows, the NO may sensitize ignition and may be partially consumed by the combustion process; however, assuming the surviving NO is sufficient for fluorescence detection, accurate two-line temperature measurements are still possible, because the NO mole fraction dependence cancels in the signal ratio. Additional attributes of NO as a flow tracer should be noted: 1) it provides a relatively strong absorption cross-section and good fluorescence efficiency, which is crucial for imaging applications; 2) it exhibits strong nonresonant fluorescence which, when combined with spectral filtering, can alleviate potential problems with radiative trapping and laser scattering; 3) it does not exhibit J-dependent radiative lifetimes or quenching rates that can lead to systematic measurement er-

rors; and 4) its spectroscopy is well characterized, which facilitates modelling and interpretation of the fluorescence signal.

The two-line method requires the use of two lasers and two cameras for instantaneous measurements. In these experiments, the lasers are tuned to different transitions and are fired sequentially, with a delay which is sufficient to temporally separate the respective fluorescence signal decays but less than that which allows blurring of the images due to flow motion. The cameras are gated so that each camera integrates the fluorescence signal induced from only one of the lasers.

For weak laser excitation, the temperature is related to the fluorescence ratio R_{12}, by

$$R_{12} \equiv S_{f1}/S_{f2} = C_{12} \exp\{-\Delta\varepsilon_{12}/kT\}$$

where S_f is the temporally integrated fluorescence signal; the subscripts 1 and 2 refer to the values associated with the respective fluorescence images; $\Delta\varepsilon_{12}$ is the energy difference between the initial absorbing states; k is the Boltzmann constant; T is the gas kinetic/rotational temperature; and C_{12} is a constant, which is dependent upon spectroscopic and experimental parameters, including the laser pulse energies. The constant, C_{12}, can be determined by independent calibration or from the signal ratio directly (in situ), if the temperature is accurately known at some location within the image. Note that in writing this equation we have assumed that the respective fluorescence yields cancel in the ratio. This is a valid assumption for these measurements, because the quenching cross-sections, fluorescence lifetimes and fluorescence branching ratios for the $A^2\Sigma^+, v'=0$ state of NO are known to be insensitive to rotational quantum number. Difference in the overlap integrals of the absorption and laser lineshape functions for the two lines probed are also neglected.

The scramjet model flowfield examined here is shown schematically in Fig. 8. The crossflow is supersonic and is
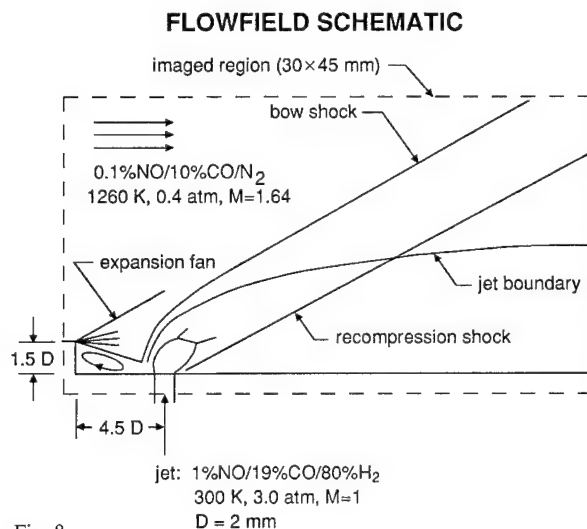
FLOWFIELD SCHEMATIC

Fig. 8
Schematic of the jet-in-crossflow flowfield showing the nominal flow conditions

turned through a Prandtl-Meyer expansion fan as it passes over the rearward facing step. The flow separates as it passes over the step and forms a recirculation zone just downstream of the step. Fuel is injected sonically, using a pulsed valve [15], through a circular orifice (diameter = D) located $4.5\,D$ downstream of a rearward facing step (height = $1.5\,D$). The fuel jet is underexpanded and results in the characteristic barrel shock structure. The barrel shock is swept over due to the momentum of the oncoming crossflow. A bow shock is formed upstream of the fuel jet because the jet acts as an obstruction to the crossflow. Downstream of the fuel jet, the crossflow is turned parallel to the wall by a recompression shock wave. The nominal flowfield conditions for this experiment are listed on the figure and are representative of the inlet conditions for a scramjet combustor. The temperatures and pressures noted in the figure are the static values of the freestream and the stagnation values of the jet gas. Carbon monoxide (CO) was added to the fuel jet to reduce the fluorescence lifetime of NO. This was necessary to ensure adequate temporal resolution of the measurements in this high-speed flowfield.

The lasers used in these experiments were XeCl excimer-pumped dye lasers (Lambda Physik FL 2002 and FL 3002). The pump beams at 308 nm had pulse energies of more than 100 mJ with pulse widths of ~ 20 ns. Coumarin 450 dye mixtures were used and the fundamental dye laser beams were frequently-doubled to ~ 226 nm using BBO crystals. The lasers were fired sequentially with a delay of 250 ns to temporally separate the fluorescence signals. Including transmission losses through the optics, the pulse energy of each laser sheet (in the test section) was ~ 0.5 mJ in a spectral bandwidth of $\sim 0.3\,\mathrm{cm}^{-1}$.

The broadband fluorescence in the spectral range from 225 to 335 nm was collected at right angles to the plane of illumination with $f/4.5$ UV Nikkor lenses (105 mm focal length). UG-5 Schott Glass filters (2 mm thick) were used to block elastic laser scattering. The fluorescence was imaged onto two intensified cooled CCD cameras (Princeton Instruments, with an EEV 578×384 array, 23 µm pixels). The imaged region was 30×45 mm. The images were acquired and processed using two IBM-compatible 486 personal computers. Laser pulses were carefully positioned temporally to occur just after the respective intensifier gates were fully on.

Fig. 9 shows a typical experimental result for the instantaneous temperature (the precision of the measurement is actually much better than apparent in this gray-scale reproduction). The jet boundary is very easily identified in the temperature field, and is indicative of a very sharp scalar gradient in the shear layer. The plume temperature increases with increasing x/D, due to the warmer freestream mixing with the cool jet. Pockets of relatively cool gas persist within the plume for several jet diameters, but the plume reaches a relatively uniform temperature for $x/D \geq 12$. Major pockets of freestream fluid are generally not observed in the lower portion of the plume (adjacent to the wall). The efficient mixing and relatively high temperatures in this boundary layer region make it the most
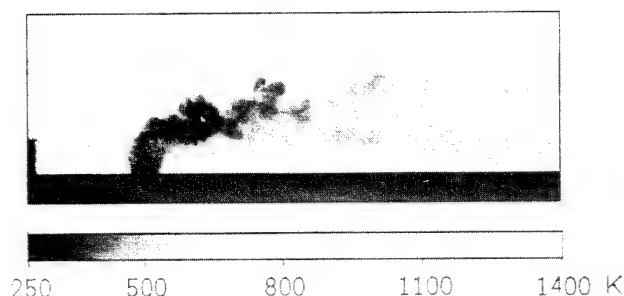

Fig. 9
Instantaneous temperature image for a jet in supersonic crossflow; region shown is 15×45 mm

favorable for autoignition and efficient combustion in a reacting flow. This observation is consistent with previous OH imaging measurements in similar combusting flows [18].

The results obtained for the instantaneous 2-D temperature field via two-line PLIF (see Ref. 15 for details) indicate that shot noise is the dominant source of temperature uncertainty. Single-shot temperature uncertainties varied from a minimum of 5% at low temperatures to as much as 20% at high temperatures for the absorption line pair used. These uncertainties could be reduced, however, by improving the laser pulse energy and efficiency of the collection optics. The good results obtained clearly confirm the potential of PLIF imaging for quantitative thermometry. Other work is in progress in our laboratory to establish quantitative PLIF imaging strategies for velocity [19] and vibrational temperature [20] in high-enthalpy, supersonic flows.

Conclusions

The two laser techniques described in this paper provide capability for simultaneous measurements of multiple parameters or measurements of a single quantity at multiple points. These methods should be viewed as complementary to each other and to other measurements schemes under development in various laboratories. These laser-based diagnostic methods have reached a level of maturity such that they are now suitable for use in industrial applications as well as in basic and applied research. Furthermore, these nonintrusive methods can measure gasdynamic and thermodynamic parameters which are, in many cases, inaccessible with the experimental methods utilized in past decades.

References

[1] R.K. Hanson, "Combustion Diagnostics: Planar Flowfield Imaging," Twenty-First Symposium (International) on Combustion, 1677–1691, The Combustion Institute 1986.

[2] R.K. Hanson, J.M. Seitzman, and P.H. Paul, "Planar Laser-Fluorescence Imaging in Combusion Gases," Appl. Phys. B50, 441 – 454 (1990).

[3] D.F. Davidson, A.Y. Chang, M.D. DiRosa and R.K. Hanson, "Continuous Wave Laser Absorption Techniques for Gasdynamic Measurements in Supersonic Flows," Appl. Opt. 30, 2598 – 2608 (1991).

[4] A.Y. Chang, B.E. Battles, and R.K. Hanson, "Simultaneous Measurements of Velocity, Temperature and Pressure using Rapid cw Wavelength-Modulation LIF of OH," Opt. Lett. 15, 706 – 708 (1990).

[5] A.Y. Chang, M.D. DiRosa, D.F. Davidson, and R.K. Hanson, "Rapid-Tuning CW Laser Technique for Measurements of Gas Velocity, Temperature, Pressure, Density and Mass Flux Using NO," Appl. Opt. 30, 3011 – 3022 (1991).

[6] E.C. Rea, Jr., A.Y. Chang, and R.K. Hanson, "Rapid Laser Wavelength Modulation Spectroscopy Applied as a Fast Temperature Measurement Technique in Hydrocarbon Combustion," Appl. Opt. 27, 4454 – 4464 (1988).

[7] L.C. Phillipe and R.K. Hanson, "Laser-Absorption Mass Flux Sensor for High-Speed Air Flows," Opt. Lett. 16, 2002 – 2004 (1992).

[8] L.C. Philippe and R.K. Hanson, "Sensitive Diode Laser Absorption Technique for Aerodynamic Measurements," paper AIAA 92-0139, AIAA 30th Aerospace Sciences Meeting, Reno, Jan. 1992; also Appl. Opt., in press.

[9] M.P. Arroyo and R.K. Hanson, "Absorption Measurements of Water Vapor Concentration, Temperature and Lineshape Parameters Using a Tunable InGaAsP Diode Laser," Appl. Opt., in press.

[10] M.P. Arroyo, S. Langlois, and R.K. Hanson, "Diode Laser Absorption Technique for Simultaneous Measurements of Multiple Gasdynamic Parameters in High-Speed Flows Containing Water Vapor," Appl. Opt., in press.

[11] M.D. DiRosa, A.Y. Chang, and R.K. Hanson, "CW Dye Laser Technique for Simultaneous, Spatially-Resolved Measurements of Temperature, Pressure and Velocity of NO in an Underexpanded Free Jet," Appl. Opt. 32, 4074 – 4087 (1993).

[12] H.A. Chang, D.S. Baer, and R.K. Hanson, "Semiconductor Laser Diagnostics of Atomic Oxygen for Hypersonic Flowfield Measurements," paper AIAA-93-0628. AIAA 31st Aerospace Sciences Meeting, Reno, Jan. 1993.

[13] D.S. Baer and R.K. Hanson, "Tunable Diode Laser Absorption Diagnostics for Atmospheric Pressure Plasmas," J. Quant. Spectrosc. Radiat. Trans. 47, 455 – 475 (1992).

[14] D.S. Baer, H.A. Chang, and R.K. Hanson, "Fluorescence Diagnostics for Atmospheric-Pressure Plasmas using Semiconductor Lasers," J. Opt. Soc. B 9, 1968 – 1978 (1992).

[15] B.K. McMillin, J.L. Palmer, and R.K. Hanson, "Temporally Resolved, Two-Line Fluorescence Imaging of NO Temperature in a Transverse Jet in Supersonic Crossflow," Appl. Opt., in press.

[16] B. Hiller and R.K. Hanson, "Simultaneous Planar Measurements of Velocity and Pressure Fields in Gas Flows Using Laser-Induced Fluorescence," Appl. Opt. 27, 33 – 48 (1988).

[17] J.M. Seitzman and R.K. Hanson, "Planar Fluorescence Imaging in Gases," Chapter 6 in Experimental Methods for Flows with Combustion, ed. A. Taylor, Academic Press, London 1993.

[18] M.P. Lee, B.K. McMillin, J.L. Palmer, and R.K. Hanson, "Planar Fluorescence Imaging of a Transverse Jet in Supersonic Crossflow," J. Prop. Power 8, 729 – 735 (1992).

[19] J.L. Palmer, B.K. McMillin, and R.K. Hanson, "Planar Laser-Induced Fluorescence Imaging of Velocity and Temperature in Shock Tunnel Free Jet Flows," paper AIAA 92-0762, AIAA 30th Aerospace Sciences Meeting, Reno, Jan. 1992.

[20] J.L. Palmer, B.K. McMillin, and R.K. Hanson, "Planar-Laser-Induced Fluorescence Imaging in Free Jet Flows with Vibrational Nonequilibrium," paper AIAA-93-0046, AIAA 31st Aerospace Sciences Meeting, Reno, Jan. 1993.

Dual diode-laser fiber-optic diagnostic for water-vapor measurements

M. Pilar Arroyo,* Timothy P. Birbeck, Douglas S. Baer, and Ronald K. Hanson

*High Temperature Gasdynamics Laboratory, Department of Mechanical Engineering,
Stanford University, Stanford, California 94305-3032*

We present a novel diode-laser diagnostic for water-vapor measurements based on absorption spectroscopy. Two InGaAsP diode lasers were used to record H_2O absorption line shapes near 1395 nm at a 3-kHz repetition rate along a single path through a water-vapor flow field generated in a shock tube. The use of two lasers permits simultaneous line-shape measurements in different spectral regions and facilitates the selection of appropriate line pairs for thermometry. The wavelength tuning rate was determined by use of a fiber-optic device known as a ring interferometer. Flow-field conditions (1320 K, 0.3 atm) inferred from measured line shapes compared favorably with calculated values.

High-resolution spectroscopy techniques have recently been developed to provide fast, sensitive, and nonintrusive means of measuring multiple quantities such as temperature, pressure, velocity, and concentration in gaseous flows.[1–3] In these methods a constituent species is monitored with a rapid-scanning narrow-linewidth laser by use of absorption spectroscopy techniques. Similar measurements of water vapor would be especially relevant to combustion, propulsion, and aerodynamics facilities since water-vapor concentration can be related to performance parameters such as extent and efficiency of combustion, propulsion efficiency, and heat release. In addition, the water molecule is of interest because it occurs naturally in air flows, represents a primary combustion product, and has absorption bands that may be reached with commercially available diode lasers.[4–6]

In the present investigation two narrow-linewidth diode lasers were tuned independently over multiple H_2O transitions to record spectrally and temporally resolved absorption line shapes. We controlled the diode-laser wavelength by maintaining a constant laser temperature T_{laser} while varying the injection current i_{laser}. Inversion of absorption line shapes from direct transmission measurements is an established tool that has been used to derive local thermodynamic properties of a gas.[1,2,7] Quantities such as pressure and velocity may be determined from a single line shape. However, the determination of temperature requires measurements of at least two profiles that, for optimum sensitivity, have similar transition line strengths at the probed temperature and originate from states with an energy separation of at least kT, where k is Boltzmann's constant.[2,6]

The finite continuous tuning range of individual semiconductor diode lasers without controlled external feedback significantly limits the number of line pairs that may be resolved in a single scan[6] and thus limits the potential temperature sensitivity of the measurement. In the present system this limitation was alleviated through the use of two lasers that were tuned independently over a pair of H_2O vibrational transitions not accessible in a single continuous scan. The beams were combined into a single optical fiber and directed through the probed region over a common path. The spatially coincident, spectrally distinct beams were temporally separated by control of the relative phase of the laser injection currents. A ring interferometer[8,9] instead of a conventional étalon was used to calibrate the wavelength tuning of the laser to present a complete diagnostic system composed almost entirely of fiber-optic components that may be suitable for process monitoring. The design of a system based on fiber-optic components reduces the complexity of alignment, minimizes the optical path length through room air, and demonstrates the ability to record line shapes remotely. The resulting system provides a flexible, fast, and accurate means of measuring multiple quantities in flows containing water vapor.

Figure 1 illustrates the experimental setup. Two distributed-feedback InGaAsP lasers emitting near 1395 nm were used in this study. Laser 1 was packaged in a hermetically sealed package that was mounted on an external thermoelectric cooler. Laser 2 was coupled directly (pigtailed) to a single-mode optical fiber. The case temperature and the injection current of each laser were controlled independently. The beam output from laser 1 was collimated, directed through an optical isolator, and focused into a single-mode optical fiber with a fiber-source coupler. The laser output beams were combined by use of a 2×1 fused fiber coupler into a single-mode fiber. The output was divided into four paths (10/10/40/40 ratio) by a 1×4 splitter. The first beam (I_{ring}) was sent through a ring interferometer to detector 1 (det. 1) to provide a measurement of the laser wavelength tuning rate. The second beam (I_0) was sent directly to detector 2 (det. 2) to record the incident (reference) intensity before entering the flow field. The third beam (I) was collimated through the shock-tube test section and focused onto detector 3 (det. 3). The fourth beam
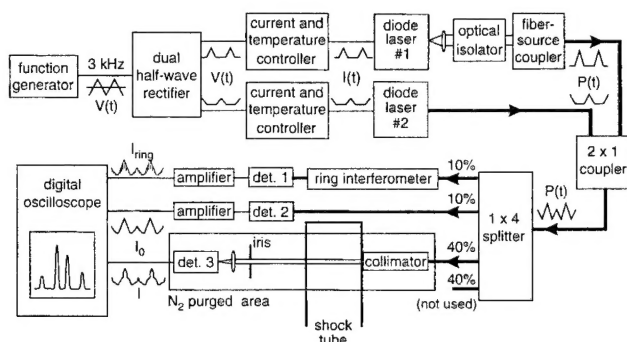
Fig. 1. Schematic of the experimental setup.

was not used in the present investigation. The detector bandwidths were either 1 MHz (detector 1) or 200 kHz (detectors 2 and 3). The I_0 and I_{ring} voltage signals were electronically adjusted to match the I voltage signal by use of amplifiers externally coupled to detectors 1 and 2.

The ring interferometer consisted of a fused-silica coupler with a splitting ratio of 5/95 and with one of its outputs fused to one of the inputs. The device had a 24.5-cm circumference and effectively served as an étalon with a 0.837-GHz free spectral range and a finesse of approximately 100. The measured total width (FWHM) of the ring interferometer fringes was 20 MHz. Hence, accounting for the instrument width, we determined the laser linewidth to be ~18 MHz, significantly narrower than the probed absorption H_2O line shapes.

A 3-kHz triangular function from a function generator is passed through a dual half-wave rectifier. The two outputs of this rectifier are half-triangular functions that are sent to the laser current controllers. The rectifier can change the width and the height of the half-triangles in both outputs. In this way the laser currents are modulated with half-triangular functions, one shifted with respect to the other so as to modulate one laser current while the other laser current is fixed to a value below threshold. Thus the lasers emit alternately, never overlapping in time. Since both lasers may respond in a different way to the modulation in current, respective wavelengths and powers will vary. Laser 2 was run at its maximum power (~150 μW), and the power of laser 1 was adjusted to twice this value by a proper alignment of the optical isolator. As a result of the losses on the fiber-optic devices and the splitting of the beam, the transmitted power through the test section was ~10 μW from laser 2 and 20 μW from laser 1. Higher laser powers would yield higher signal-to-noise ratios and improve measurement accuracy.

The diagnostic was demonstrated in a shock tube. Shock heating is a convenient method for producing high-temperature samples of gases under well-known conditions. The 14.3-cm-long optical path was bounded by a pair of windows attached to the shock tube 1.8 cm from the end wall and oriented perpendicular to the flow direction. The collection lens was preceded by an iris with a diameter slightly greater than the collimated beam and placed 70 cm from the shock-tube window to reduce the emission signal from the hot shock-heated water. The volume

near the collimator, focusing lens, and detector 3 was enclosed and purged continuously with dry N_2 gas to minimize absorption by the water in the room air. The remaining beam paths traveled almost exclusively through optical fibers. The laser power attenuation through a 1-m-long single-mode fiber was less than 0.1% (0.55 dB/km).

We tuned laser 1 across the $2_{02} \leftarrow 3_{03}$ line (7181.156 cm^{-1}) and partially across the $9_{55} \leftarrow 9_{54}$ line (7180.613 cm^{-1}) by varying i_{laser} from 20 to 100 mA and maintaining $T_{laser1} = 35.7$ °C. We tuned laser 2 across the overlapping $8_{63} \leftarrow 8_{62}$ and $8_{62} \leftarrow 8_{63}$ lines near 7173.779 cm^{-1}, using the same current waveform and maintaining $T_{laser2} = 34.5$ °C. These lines were selected because of the relatively strong temperature dependence of their line-strength ratio and the magnitude of each transition line strength for the given test conditions. The measured line-center absorption for each line was nearly 30%.

Figure 2 presents representative data that we recorded by tuning each laser one complete cycle of the injection current waveform. The top curve shows the reference signal I_0. The absorption by the strong $2_{02} \leftarrow 3_{03}$ line on the laser 1 scan was due to residual H_2O in the room-air path between the laser and the fiber-source coupler. The middle curve shows the absorption signal, $\Delta I = I_0 - I$. The bottom curve shows the difference between the reference-beam and the ring-interferometer transmission signals, $I_0 - I_{ring}$. There were several regions during the scan in which the laser wavelength variation was highly nonlinear. As a result, the full tuning range for a particular scan was divided into several regions. These regions could be accurately fitted to individual fifth-order polynomials to relate the time-dependent fringe positions to relative laser wavelength. The tuning characteristics of the lasers used in this study differ from those of a laser used previously[6] because of differences in the lasers and were not due to the fiber-optic components.

The interferometer fringe heights appear to change erratically because of the high finesse of the ring in-
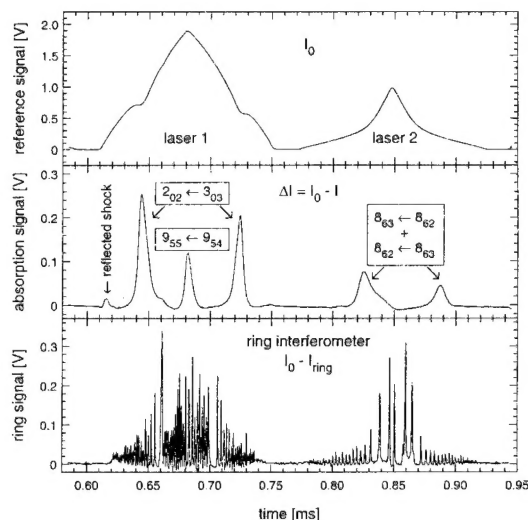

Fig. 2. Absorption traces recorded in a water-vapor flow field. The temperature and pressure in the probed region were 1293 K and 0.311 atm, respectively.
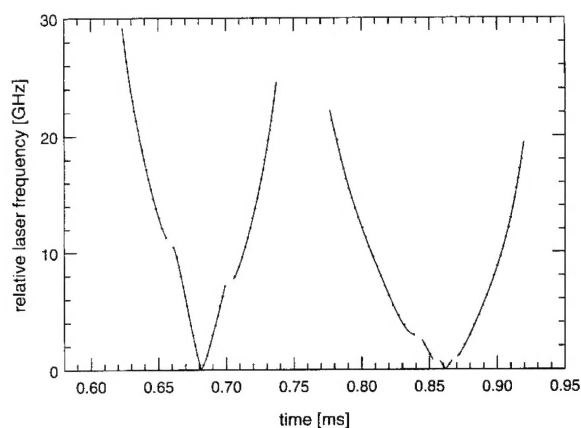
Fig. 3. Polynomial fits (solid curve) of the ring-interferometer transmission peak positions (dots) from the data presented in Fig. 2.
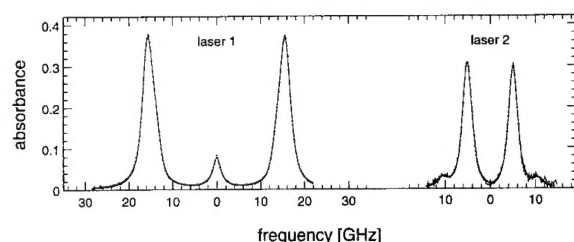

Fig. 4. Comparison of the measured absorbance (solid curve) and best fit (dots) obtained from the traces in Fig. 2. The lower signal-to-noise ratio in the spectral features on the right is due to the lower new power from laser 2.

terferometer and the limited sampling rate of the oscilloscope (500 ns/point). Since the finesse was relatively large, however, the limited sampling rate did not introduce significant errors in the measured fringe positions. Figure 3 shows the measured time-dependent fringe positions (dots) for the data presented in Fig. 2 and the corresponding polynomial fits (solid curves). The maximum difference between the fit and the measured frequency was less than 0.15 GHz.

The transmittance, $-\ln(1 - \Delta I/I_0)$, was obtained from the I_0 and ΔI signals after conversion to a relatively frequency scale. The normalized transmittance for each measured line shape was least-squares fitted to a set of Voigt profiles whose intensity ratios and relative separations were determined from the data.[6,7] The temperature was inferred from the ratio of the integrated intensities of the $2_{02} \leftarrow 3_{03}$ line and the combined intensities of the overlapping $8_{63} \leftarrow 8_{62}$ and $8_{62} \leftarrow 8_{63}$ lines.

Pressure was inferred[6,7] by use of the line strengths measured by Toth,[10] which have been determined[6,11] to be more reliable than the values tabulated in the current HITRAN database.[12] Figure 4 illustrates the results of the fit procedure based on the data in Fig. 2. Two lines with intensity ratios of 0.27 and 1 and fre-

quency separations of -16.3 and -2.0 GHz relative to the $2_{02} \leftarrow 3_{03}$ line, respectively, were used together with the $2_{02} \leftarrow 3_{03}$ line in the fit of the laser 1 scan. The fit of the laser 2 scan required one more line, in addition to the $8_{63} \leftarrow 8_{62}$ and $8_{62} \leftarrow 8_{63}$ lines (which were taken as a single feature), with an intensity ratio of 0.07 and a separation of 5.5 GHz relative to the main feature.

The inferred pressure and temperature (0.3 atm, 1320 K) agree with calculated values (0.311 atm, 1293 K). For the given conditions the estimated uncertainty of the measured intensity ratio is 0.02, and the associated uncertainty in the inferred temperature is 30 K ($\Delta T/T \approx 4\%$).

In conclusion, we have demonstrated a novel laser-absorption-based technique for temperature and pressure measurements of water vapor. The use of optical fibers as a transmission medium and the two-laser design makes the technique flexible, easy to use, fast, accurate, and capable of measuring multiple quantities in flows containing water vapor or other gas species. Furthermore, two different species could be monitored simultaneously if the wavelength of each laser were chosen appropriately. With modest modifications the concept could be extended to permit simultaneous single-path absorption measurements at several wavelengths.

References

1. E. C. Rea and R. K. Hanson, Appl. Opt. **27,** 4454 (1988).
2. A. Y. Chang, M. D. DiRosa, D. F. Davidson, and R. K. Hanson, Appl Opt. **30,** 3011 (1991).
3. L. C. Philippe and R. K. Hanson, Appl. Opt. **32,** 6090 (1993).
4. N. Goldstein, S. Adler-Golden, J. Lee, and F. Bien, Appl. Opt. **31,** 3409 (1992).
5. C. B. Carlisle and D. E. Cooper, Appl. Phys. Lett. **56,** 805 (1990).
6. M. P. Arroyo and R. K. Hanson, Appl. Opt. **32,** 6104 (1993).
7. M. P. Arroyo, S. Langlois, and R. K. Hanson, Appl. Opt. **33,** 3296 (1994).
8. L. F. Stokes, M. Chodorow, and H. J. Shaw, Opt. Lett. **7,** 288 (1982).
9. S. Tai, K. Kyuma, K. Hamanaka, and T. Nakayama, Opt. Acta **33,** 1539 (1986).
10. R. A. Toth, Jet Propulsion Laboratory, 4800 Oak Grove Drive, Pasadena, Calif. 91109 (personal communication, 1992).
11. S. Langlois, T. P. Birbeck, and R. K. Hanson, J. Mol. Spectrosc. **163,** 27 (1994).
12. L. S. Rothmann, J. Quant. Spectrosc. Radiat. Transfer **48,** 469 (1992).